

Doctorate Dissertation
博士論文

Sterile neutrino oscillation studies with the T2K far detector
Super-Kamiokande
(T2K実験におけるスーパーカミオカンデ遠地検出器
を用いたステライルニュートリノ振動の研究)

A Dissertation Submitted for Degree of Doctor of Philosophy
July 2018

平成30年7月博士（理学）申請
Department of Physics, Graduate School of Science,
The University of Tokyo

東京大学大学院理学系研究科物理学専攻

Tsui Ka Ming
徐嘉明

Abstract

The T2K (Tokai-to-Kamioka) experiment is a long-baseline accelerator neutrino experiment in Japan. The muon (anti-) neutrino beam produced at J-PARC is detected by a set of near detectors at 280 m from the target to determine the neutrino flux and interaction rates, and the Super-Kamiokande (SK) water-Cherenkov far detector 295 km apart to measure the oscillated neutrino spectra. The experiment uses an off-axis configuration that the far detector is at an angle of 2.5° from the beam center. This intercepts a narrow neutrino beam of peak energy 0.6 GeV which corresponds to the first minimum (maximum) of ν_μ disappearance (ν_e appearance) probability. T2K is thus optimized to measure the standard 3-flavor oscillation parameters: Δm_{32}^2 , θ_{23} , θ_{13} and δ_{CP} . On the other hand, T2K also has the potential to explore exotic physics like sterile neutrino.

The existence of sterile neutrinos is still an open question. They are singlet fermions which can contribute to weak interactions only through mixing with active neutrinos and may explain some observations which appear anomalous in the standard three-neutrino scenario. In this thesis, we perform a joint oscillation analysis using both charged current (CC) and neutral current (NC) SK samples to constrain the parameters in the 3+1 sterile oscillation model: Δm_{41}^2 , θ_{24} and θ_{34} . With T2K Run 1-8 dataset of 2.22914×10^{21} protons-on-target (POT), we exclude $\sin^2 \theta_{24} > 0.1$

and $\sin^2 \theta_{34} > 0.5$ at 90% limit for $\Delta m_{41}^2 > 0.1\text{eV}^2$.

Preface

In a large experiment like T2K, it is impossible for a person to participate in every single part of the experiment. Therefore, any physics result or discovery is credited to the T2K collaboration as a whole. Indeed, my dissertation topic, sterile neutrino study in T2K far detector, has gone through numerous collaboration discussions and reviews before becoming official, and it is not possible without the efforts of all past and present members. Chapter 3 describes the experimental facility and the analysis software that are developed by this large collaboration. But for the sake of a dissertation, I would like to highlight my personal contributions below.

In the past, T2K has only released results of short baseline sterile neutrino analysis. My study is therefore the first T2K long baseline sterile neutrino analysis, with T2K data collected until 2017.

Before we really initiated the sterile analysis in the collaboration, I had done some preliminary studies, without the use of T2K official fitter, to estimate the sensitive parameter space, and determine the types of samples and variables to be used in the fitting. These included modifying the oscillation probability formulas to see the effects on different samples, correlating the reconstructed variables with neutrino energy, and rough χ^2 fit with event numbers only. After we gained the approval from analysis working group, we moved towards to a strict study.

In Chapter 4 where the oscillation samples are described, I have re-generated the MC data of neutral current oscillation samples in order to obtain all the necessary truth variables for oscillation analysis.

In Chapter 5 where the analysis method is outlined, I have joined the working group which is responsible for the development of the analysis code (P-theta). Specific to my sterile study, I have modified the code to include the sterile oscillation framework, and the additional neutral current (NC) samples. I have implemented the systematic parameters which are dedicated to the NC samples, in which we have spent lots of discussions and efforts to determine what parameters to use and what values to set. I have also changed the fitting strategy (from marginalization to minimization) in order to optimize the usage of computational resource.

In Chapters 6 and 7, I have performed the sensitivity studies and data fit on my own. I have also done lots of checks and alternative studies, which are shown in Appendix B to I.

The analysis result is now official and has been presented in ICHEP 2018. Our long baseline sterile oscillation analysis is a complement to the previously released short baseline analysis in T2K[1], and we have successfully produced the world's best constraint on $\sin^2 \theta_{24}$ for $\Delta m_{41}^2 < 3 \times 10^{-3} \text{eV}^2$.

Acknowledgement

I would like to express my gratitude to my supervisor Prof. Kimihiro Okumura, for his guidance and advices on my studies, and providing me the invaluable opportunity to participate in SK and T2K. He is so nice and accepted me as a foreign student in the group, which led to my fantastic days in Japan.

Also, I wish to thank Prof. Takaaki Kajita, Prof. Yasuhiro Nishimura, Ryosuke Akutsu and other people in RCCN, who makes me feel warm as a family. In particular Ms Keiko Watanabe and Ms Chieko Mashima saved me a lot of troubles for my poor Japanese.

I am grateful to meet Prof. Yasuhiro Nakajima, Prof. Jun Kameda and other people in Kamioka who helped me with my studies in SK; Dr. Wing Ma, Prof. Christophe Bronner, and members in the P-theta group who helped me getting start with oscillation analysis in T2K; Prof. Yusuke Koshio, Dr. Alexander Izmaylov and collaborators in T2K-exotics who helped me developing the sterile analysis. I bless they will continue publishing exciting results in the future.

Finally, I want to express my gratefulness and love to my family, especially my wife, Chiu Tung Cheng, who supports my decision of PhD study, and even came to Japan to live with me one year later (also starting a PhD). She makes my life complete and colorful, and I wish to bring her a wonderful life too.

Contents

1	Introduction	1
2	Standard and sterile neutrino oscillation model	5
2.1	3-flavor neutrino mixing	5
2.1.1	Motivation	5
2.1.2	Formalism	7
2.1.3	Matter effect	10
2.1.4	Current measured values of neutrino mixing parameters	12
2.2	Sterile neutrino model	19
2.2.1	Theoretical interest	19
2.2.2	Experimental hints at eV scale	23
2.2.3	3+1 sterile neutrino model	24
3	The T2K experiment	29
3.1	Neutrino beamline at J-PARC	30
3.1.1	Proton beamline	30
3.1.2	Neutrino beamline	31
3.1.3	Off-axis beam configuration	34
3.1.4	Neutrino flux simulation	35

3.2	Near detector complex	37
3.2.1	INGRID	39
3.2.2	ND280	40
3.2.3	ND280 software	46
3.2.4	BANFF fit	47
3.3	Far detector Super-Kamiokande	48
3.3.1	Cherenkov radiation	49
3.3.2	Detector design	50
3.3.3	Detector simulator SKDETSIM	52
3.3.4	Detector calibration	52
3.3.5	T2K data taking	58
3.3.6	Event reconstruction	62
3.4	Neutrino event generator NEUT	65
3.4.1	Quasi-elastic neutrino-nucleon scattering	65
3.4.2	Single meson production	67
3.4.3	Deep inelastic scattering (DIS)	68
3.4.4	Coherent pion production	69
3.4.5	Multi-nucleon (2p2h) interaction	70
3.4.6	Final state and secondary interactions	70
4	Oscillation samples and event selections at SK	72
4.1	Date set summary	72
4.2	Charged current oscillation samples	75
4.2.1	FHC/RHC $1R\mu$ samples	75
4.2.2	FHC/RHC $1Re$ samples	82

4.2.3	FHC ν_e CC1 π^+ sample	86
4.3	Neutral current oscillation samples	90
4.3.1	FHC/RHC 2R π^0 samples	91
4.3.2	FHC NC γ de-excitation sample	96
4.4	Event summary	106
5	Oscillation analysis framework	107
5.1	Event binning	107
5.2	Monte Carlo Predictions	108
5.2.1	Neutrino propagation modes	109
5.2.2	Neutrino interaction categories	110
5.2.3	True neutrino energy binning	110
5.2.4	Input preparation	111
5.2.5	Oscillation probability calculation	112
5.2.6	Event rate calculation	112
5.3	Systematic parameters	114
5.3.1	Beam flux parameters	114
5.3.2	Neutrino interaction and cross-section parameters	116
5.3.3	Super-K detector uncertainties	120
5.3.4	Effect of systematic parameters	135
5.4	Fitting method	138
5.4.1	Likelihood calculation	138
5.4.2	Confidence level building	142
6	Sensitivity study	143
6.1	3-flavor oscillation fit	146

6.2	3+1 oscillation	148
6.2.1	$\sin^2 \theta_{24}$ - Δm_{41}^2 plane	148
6.2.2	$\sin^2 \theta_{24}$ - $\sin^2 \theta_{34}$ plane	150
6.3	Effect of statistics	151
6.4	Effect of systematics	151
7	Data fit results	155
7.1	Global best fit points	155
7.2	3-flavor oscillation	157
7.3	3+1 sterile oscillation	157
8	Summary and prospect	161
	Appendix	165
A	SK event reconstruction algorithms	165
A.1	apfit	165
A.2	fitQun	170
B	Event rate tables	175
C	Sterile oscillation probability with matter effect	184
D	Differences between NH and IH at $\Delta m_{41}^2 \sim \Delta m_{31}^2$	186
E	Effects of θ_{14}, δ_{14} and δ_{24} on the fit	189
F	Setting Exclusion limits of sterile parameters with the Gaussian CL_s	
	Method	193

G Fitting non-Asimov data sets	198
H Valid Δm_{41}^2 parameter space	202
I Event spectra at sterile exclusion limits	205
J List of abbreviations and symbols	207
Bibliography	211

List of Figures

2.1	The transition probability $P(\nu_\mu \rightarrow \nu_e)$ with matter effect observed at SK as a function of cosine of zenith angle and neutrino energy. The zenith angle can be converted to neutrino propagation length through the Earth's matter, assuming the Earth is a sphere. Top (bottom) shows the normal (inverted) hierarchy case, and left (right) shows the neutrino (anti-neutrino) case (Figure taken from [2]).	11
2.2	Ratio of the observed $\bar{\nu}_e$ spectrum to expected assuming no oscillation for KamLAND, with the 3-flavor best fit oscillation curve superimposed. $L_0=180$ km is the flux-weighted average reactor baseline (Figure taken from [3]).	13
2.3	Predicted solar neutrino spectra[4], overlaid with predicted MSW $P(\nu_e \rightarrow \nu_e)$ (green is from solar best fit, blue is from solar + KamLAND best fit). Shown in red is the 1σ band of $P(\nu_e \rightarrow \nu_e)$ from combined data of SK and SNO. Shown in points are the measurements of $P(\nu_e \rightarrow \nu_e)$ from the ${}^7\text{Be}$ (green), the pep (light green) and the ${}^8\text{B}$ flux (red) by Borexino[5], and the pp (blue) and CNO (gold) extracted from [6–9].(Figure taken from [10]).	14

2.4	Allowed contours of Δm_{21}^2 vs $\sin^2 \theta_{12}$ from solar neutrino data (green), KamLAND data (blue), and the combined result (red). The dashed dotted lines show the SK + SNO result. The filled regions give the 1, 2, 3 σ confidence level contours. For solar analysis, 4, 5 σ confidence level contours are also shown (Figure taken from [10]).	15
2.5	The 90% and 68% confidence levels in the $\sin^2 \theta_{23} - \Delta m_{32}^2$ plane from T2K, SK[11], NO ν A[12], MINOS[13] and IceCube[14], assuming $\Delta m_{32}^2 > 0$ (Figure taken from [15]).	16
2.6	Measured reactor $\bar{\nu}_e$ spectral distortion at Daya Bay (Figure taken from [16]).	17
2.7	Illustration of the two possible mass hierarchies, and the effect of δ_{CP} on the mixing matrix element $U_{\alpha i}$	18
2.8	Schematic of a possible heavy sterile neutrino production at hadron colliders followed by its subsequent decay, suggested in [17].	22
2.9	The disappearance probability $P(\nu_\mu \rightarrow \nu_\mu)$ as a function of neutrino energy at 295 km. The black line shows that standard 3-flavor result, while the red line shows the sterile one with $\Delta m_{41}^2 = 0.1\text{eV}^2$ and $\sin^2 \theta_{24} = 0.2$	27
2.10	The appearance probability $P(\nu_\mu \rightarrow \nu_e)$ as a function of neutrino energy at 295 km. The black line shows that standard 3-flavor result, while the red line shows the sterile one with $\Delta m_{41}^2 = 0.1\text{eV}^2$ and $\sin^2 \theta_{24} = 0.2$	27

2.11	The overall active neutrino survival probability $1 - P(\nu_\mu \rightarrow \nu_s)$ as a function of neutrino energy at 295 km. The black line shows that standard 3-flavor result, while the red line shows the sterile one with $\Delta m_{41}^2 = 0.1\text{eV}^2$, $\sin^2 \theta_{24} = 0.1$ and $\sin^2 \theta_{34} = 0.5$	28
3.1	A schematic diagram of the T2K experiment (Figure taken from [18]).	30
3.2	The J-PARC proton beamline (copyright J-PARC).	31
3.3	Overview of the T2K neutrino beamline (Figure taken from [18]). . .	32
3.4	The predicted ν_μ flux at SK for operation at different horn currents. Top shows the flux histogram from 0 to 3 GeV, bottom shows the ratios from 0 to 10 GeV (Figure taken from [19]).	33
3.5	The T2K unoscillated neutrino flux prediction at SK for the neutrino (left) and antineutrino (right) modes (Figure taken from [20]).	34
3.6	The predicted neutrino flux at SK without oscillation at an off-axis angle 0.0° (black), 2.0° (blue) and 2.5° respectively (red). The y-axis units are different among three angles. On the top and bottom shows $P(\nu_\mu \rightarrow \nu_\mu)$ and $P(\nu_\mu \rightarrow \nu_e)$ at 295km (Figure taken from [19]).	36
3.7	The near detector complex. The on-axis INGRID modules are located on the bottom two levels, while the off-axis ND280 detector is on the upper level (Figure taken from [18]).	38
3.8	INGRID on-axis detector (Figure taken from [18]).	39
3.9	An INGRID module. On the left shows the tracking planes and iron plates, on the right shows the veto planes (black) (Figure taken from [18]).	40
3.10	The Proton module (Figure taken from [18]).	41

3.11	An exploded view of the ND280 off-axis detector (Figure taken from [18]).	42
3.12	A schematic of PØD. The beam is coming from the left to the right (Figure taken from [18]).	43
3.13	Simplified drawing showing the main features of a TPC. The outer dimensions are roughly 2.3 m×2.4 m×1.0 m (Figure taken from [18]).	44
3.14	Distribution of the energy loss as a function of the momentum in the TPCs for negatively charged particles produced in neutrino interactions, compared to the expected curves for muons, electrons, protons and pions (Figure taken from [21]).	45
3.15	Schematic of the package structure of the ND280 Software Suite. Only the most representative packages are shown (Figure taken from [18]).	47
3.16	A schematic diagram of the SK detector (Figure taken from [22]). . .	50
3.17	Event displays of T2K events in SK for (a) a muon-like ring and (b) an electron-like ring. The cylindrical detector is being unrolled onto a plane. Each colored point represents the charge a PMT hit. The white line shows the reconstructed cone. On the top right corner shows the OD hit map. The white crosses are the location of the reconstructed vertex, and the diamond is the location where a ray from the event vertex would intersect the detector wall if it heads in the direction of the beam (Figure taken from [18]).	51
3.18	Typical fitted water coefficient functions used in SK-MC, which are tuned with data taken in April 2009 (Figure taken from [23]).	54
3.19	Momentum distribution of decay electrons (MeV) for the data (black points) and MC (red) (Figure taken from [24]).	55

3.20	Invariant mass distributions of π^0 events for the data (black points) and MC (red). The solid lines show the Gaussian fitting lines (Figure taken from [24]).	56
3.21	Distributions of $p(\text{p.e.})/p(\theta)$ of low energy stopping muons for the data (black points) and MC (red), at three $p(\theta)$ bins: 200 - 280 MeV/c, 280 - 360 MeV/c and 360 - 440 MeV/c (Figure taken from [24]). . .	57
3.22	Distributions of momentum over range of high energy stopping muons for the data (black points) and MC (red) with various ranges. From the top left to bottom right plots, the ranges are 5 - 10 m, 10 - 15 m, 15 - 20 m, 20 - 25 m, 25 - 30 m and 30 - 35 m respectively (Figure taken from [24]).	59
3.23	Time variations of the momentum over range and momentum of decay electrons. The red dotted lines are linear fit functions, and the green lines are the value of MC (Figure taken from [24]).	60
3.24	ΔT_0 distribution of all FC, OD and LE events within $\pm 500 \mu\text{s}$ around the expected beam arrival time for T2K Run 1-7. The histograms are stacked in that order (Figure taken from [20]).	61
3.25	Vertex, direction and momentum resolutions compared between apfit and fitQun for SK-IV fully contained atmospheric neutrino MC. The resolution is defined as the 68 percentile of the respective distributions (Figures taken from [25]).	63
3.26	Event breakdowns for the 1-ring e -like (top), 1-ring μ -like (middle) and $\text{NC}1\pi^0$ (bottom) samples of the SK-IV fully contained atmospheric neutrino MC. fitQun results are on the left and apfit results on the right (Figures taken from [25]).	64

3.27	Feynman diagram of a neutrino CCQE interaction.	66
3.28	CC cross-section predicted by NEUT version 5.3.2 for (a) ν_μ and (b) $\bar{\nu}_\mu$. The T2K flux spectra are shown with arbitrary units (Figures taken from [26]).	66
4.1	Accumulated number of POT as a function of date for beam good spills (blue), SK + beam good spills in neutrino mode (red), SK + beam good spills in antineutrino mode (orange), and the SK dead fraction of POT (green = (blue-red-orange)/blue) (Figure taken from [27]).	74
4.2	The cumulative number of observed FC events as a function of POT in neutrino mode (FHC) and antineutrino mode (RHC) for T2K Run 1-8. The red solid lines refer to expectation in case of constant event rates for all runs (Figures taken from [27]).	74
4.3	Time variation of the SK attenuation length measured by cosmic ray through-going muon data, Gray shaded regions denote the Run 1-8 periods (Figure taken from [27]).	75
4.4	Distributions of FHC (left) and RHC (right) $1R\mu$ event selections at each stage for Run 1-8. Blue arrows denote the selection criteria. The MC expectation is calculated based on 3-flavor oscillation framework with the world best-fit oscillation parameters and BANFF fit corrections (Figures taken from [27]).	77

4.5	Distributions of FHC (left) and RHC (right) $1R\mu$ event selections at each stage for Run 1-8. Middle graphs show the π^+ rejection cut in 2D, with events below the dotted yellow line selected as ν_μ candidates, and bottom graphs show the distance from the cut line (Figures taken from [27]).	78
4.6	Number of events passing each $1R\mu$ selection stage for T2K Runs 1-8. The MC expectation is calculated based on 3-flavor oscillation framework with the world best-fit oscillation parameters and BANFF fit corrections (Figures taken from [27]).	79
4.7	Reconstructed vertex distributions of FHC (left) and RHC (right) $1R\mu$ events for Run 1-8, after passing all selection cuts. Top graphs show the <i>wall</i> distribution with <i>towall</i> > 250 cm applied, and bottom graphs show the <i>towall</i> distribution with <i>wall</i> > 50 cm applied. The blue arrows indicating the full FV cut (Figures taken from [27]). . . .	80
4.8	Reconstructed vertex distributions of FHC (left) and RHC (right) $1R\mu$ events for Run 1-8, after passing all selection cuts. Top graphs show the square of the distance of the vertices from the central vertical axis of the SK tank, and bottom graphs show the vertical position of the vertices (Figures taken from [27]).	81
4.9	The cumulative number of observed $1R\mu$ events (blue) as a function of POT in FHC and RHC for T2K Run 1-8. The red solid lines refer to expectation in case of constant event rates for all runs (Figures taken from [27]).	81
4.10	Reconstructed neutrino energy distribution of $1R\mu$ samples for T2K Runs 1-8 (Figures taken from [27]).	82

4.11	Distributions of FHC (left) and RHC (right) 1Re event selections at each stage for Run 1-8 (Figures taken from [27]).	84
4.12	Distributions of FHC (left) and RHC (right) 1Re event selections at each stage for Run 1-8. Middle graphs show the π^0 rejection cut in 2D, with events below the dotted yellow line selected as ν_e candidates, and bottom graphs show the distance from the cut line (Figures taken from [27]).	85
4.13	Number of events passing each 1Re selection stage for T2K Runs 1-8 (Figures taken from [27]).	86
4.14	Reconstructed vertex distributions of FHC (left) and RHC (right) 1Re events for Run 1-8, after passing all selection cuts. Top graphs show the <i>wall</i> distribution with <i>towall</i> > 170 cm applied, and bottom graphs show the <i>towall</i> distribution with <i>wall</i> > 80 cm applied. The blue arrows indicating the full FV cut (Figures taken from [27]). . . .	87
4.15	Reconstructed vertex distributions of FHC (left) and RHC (right) 1Re events for Run 1-8, after passing all selection cuts. Top graphs show the square of the distance of the vertices from the central vertical axis of the SK tank, and bottom graphs show the vertical position of the vertices (Figures taken from [27]).	88
4.16	The cumulative number of observed 1Re events (blue) as a function of POT in FHC and RHC for T2K Run 1-8. The red solid lines refer to expectation in case of constant event rates for all runs (Figures taken from [27]).	88
4.17	Reconstructed neutrino energy distribution of 1Re samples for T2K Runs 1-8 (Figures taken from [27]).	89

4.18	Feynman diagram of a $CC1\pi^+$ interaction	89
4.19	Distributions of FHC $\nu_e CC1\pi^+$ event selections at each stage for Run 1-8. Bottom left graph shows the π^0 rejection cut in 2D, with events below the dotted yellow line selected as ν_e candidates, and bottom right graph shows the distance from the cut line(Figures taken from [27]).	90
4.20	Number of events passing each FHC $\nu_e CC1\pi^+$ selection stage for T2K Runs 1-8 (Figures taken from [27]).	91
4.21	Reconstructed vertex distributions of FHC $\nu_e CC1\pi^+$ events for Run 1-8, after passing all selection cuts. Left graph shows the <i>wall</i> distribution with <i>towall</i> > 270 cm applied, and right graph shows the <i>towall</i> distribution with <i>wall</i> > 50 cm applied. The blue arrows indicating the full FV cut (Figures taken from [27]).	91
4.22	Reconstructed vertex distributions of FHC (left) and RHC (right) 1Re events for Run 1-8, after passing all selection cuts. Top graphs show the square of the distance of the vertices from the central vertical axis of the SK tank, and bottom graphs show the vertical position of the vertices (Figures taken from [27]).	92
4.23	Reconstructed neutrino energy distribution of FHC $\nu_e CC1\pi^+$ sample for Runs 1-8 (Figures taken from [27]).	92
4.24	Number of ring distribution of all apfit FCFV multi-ring events for Runs 1-8 (Figures taken from [27]).	93
4.25	Reconstructed π^0 invariant mass and momentum of 2R π^0 samples for Runs 1-8 (Figures taken from [27]).	94
4.26	True neutrino energy distribution of 2R π^0 samples.	95

4.27	Correlations between neutrino energy and π^0 invariant mass/momentum for FHC.	95
4.28	The binding energy spectra of ^{16}O spectral function. The two peaks correspond to the $1p_{1/2}$ -hole state (ground state) and $1p_{3/2}$ -hole state respectively. Neutron levels are deeper than protons' by about 3.54 MeV (Figure taken from [28]).	97
4.29	De-excitation modes of the ^{16}O proton hole $(s_{1/2})_p^{-1}$ state. Only gamma rays with $E_\gamma > 3$ MeV are shown (Figure taken from [29]). . .	100
4.30	Distributions of G_V^2 vs. G_A^2 of NC γ de-excitation events with reconstructed energy between 4.5 and 5.0 MeV. The left plot shows the distribution of T2K beam ν_μ simulated events, while the right plot shows that of the off-timing data. The dotted lines show a cut at $\text{ovaQ} \equiv G_V^2 - G_A^2 = 0.2$ (Figures taken from [28]).	103
4.31	Cut threshold of dwall, effwall and ovaQ as a function of reconstructed energy for T2K Run4. Red points show the optimized cut values in each energy bin, while red dash lines show the fitting lines (Figures taken from [28]).	104
4.32	Distributions of reconstructed energy of NC γ de-excitation events for T2K Run 4 before and after selection cuts (Figures taken from [28]). .	104
4.33	Distributions of FHC NC γ de-excitation sample for Runs 1-4.	105
4.34	Correlation between reconstructed gamma energy and true neutrino energy of FHC NC γ de-excitation sample.	106

5.1	Error size and correlations for all the 133 systematic parameters of the analysis. Parameters are 1-50: beam flux, 51-72: neutrino interaction and cross-section, 73-132: Super-K detector, 133: SK p-scale parameters.	116
5.2	The normalized <i>wall</i> distributions of stopping cosmic muons for MC simulation (red) and data (black) (Figures taken from [30]).	124
5.3	Decay electron tagging efficiency and fake rate as a function of muon momentum (left) and <i>towall</i> (right) (Figures taken from [30]).	124
5.4	Muon mis-identification rate for stopping muon data and MC, as a function of muon momentum (left) and <i>towall</i> (right) (Figures taken from [30]).	125
5.5	Graphical representation of the detector region bin as a function of <i>wall</i> and <i>towall</i> , zoomed into small <i>wall</i> and <i>towall</i> regions (Figures taken from [31]).	126
5.6	Overall SK topological cut errors as a function of visible energy. The total error in each bin is the sum in quadrature of the “shift error” (bin content) and “fit error” (error bar). Top left: ν_e CC1e, bottom left: ν_e CC other, top right: ν_μ CC1 μ , bottom right: ν_μ CC other (Figures taken from [31]).	127
5.7	Error size and correlations for the SK detector efficiency uncertainties. Parameters are 1-12: FHC 1Re, 13-18: FHC 1R μ , 19-30: RHC 1Re, 31-36: RHC 1R μ , 37-48: FHC ν_e CC1 π^+ , 49-52: FHC 2R π^0 , 53-56: RHC 2R π^0 , 57-60: FHC NC γ de-excitation.	132

5.8	Error size and correlations for FSI+SI+PN uncertainties. Parameters are 1-12: FHC $1Re$, 13-18: FHC $1R\mu$, 19-30: RHC $1Re$, 31-36: RHC $1R\mu$, 37-48: FHC $\nu_e CC1\pi^+$, 49-52: FHC $2R\pi^0$, 53-56: RHC $2R\pi^0$, 57-60: FHC NC γ de-excitation.	135
5.9	Number of observed events for the $1R\mu$ samples obtained over 50k throws of systematic parameters. On the left shows the predicted number of events in all bins. The dotted lines show the $\pm 1\sigma$ region around the mean value. On the right shows the error envelope in each sample bin. Blue boxes correspond to the $\pm 1\sigma$ region around the mean value, black histograms correspond to the nominal values for default value of the systematic parameters.	137
5.10	Number of observed events for the $1Re$ and $\nu_e CC1\pi^+$ samples obtained over 50k throws of systematic parameters.	138
5.11	Number of observed events for the NC samples obtained over 50k throws of systematic parameters.	139
5.12	Fractional change of number of events when a systematic parameter is increased by 1σ from nominal value. Parameters are 1-50: beam flux, 51-72: neutrino interaction and cross-section, 73-132: Super-K detector, 133: SK p-scale parameters.	140

6.1	Predicted spectra for each sample. Distributions for $1R\mu$ samples are a function of E_{rec} (GeV) whereas distributions for $1Re$ samples and $\nu_e CC1\pi^+$ sample are a function of p_e (MeV) and θ (degree). Distributions for $2R\pi^0$ samples are a function of π^0 momentum (MeV) whereas distributions for NC γ de-excitation sample are a function of reconstructed γ energy (MeV).	145
6.2	Asimov sensitivity 2D confidence level contours in Δm_{32}^2 vs. $\sin^2 \theta_{23}$ for normal and inverted hierarchy. The black cross marks the parameter truth values.	147
6.3	Asimov sensitivity 2D confidence level contours in δ_{CP} vs. $\sin^2 \theta_{13}$ for normal and inverted hierarchy. The black cross marks the parameter truth values.	147
6.4	Asimov sensitivity 1D $\Delta\chi^2$ in δ_{CP} for normal and inverted hierarchy.	148
6.5	Asimov sensitivity 2D confidence level contours in Δm_{41}^2 vs. $\sin^2 \theta_{24}$ for normal and inverted hierarchy. On the right shows our sensitivity overlaid on limits to date from other experiments[32–39] (Figure taken from [32]).	149
6.6	Our analysis.	150
6.7	Asimov sensitivity 2D confidence level contours in Δm_{41}^2 vs. $\sin^2 \theta_{24}$ assuming NH. The exclusion limit is mostly determined by the ν_μ samples at large Δm_{41}^2 , and supplemented by ν_e and NC samples at small Δm_{41}^2	150
6.8	Asimov sensitivity 2D confidence level contours in $\cos^2 \theta_{24} \sin^2 \theta_{34}$ vs. $\sin^2 \theta_{24}$. On the right shows the 90% and 99% upper limits from IceCube[40] and SK[35].	151

6.9	Asimov sensitivity 2D confidence level contours of NH assuming current Run 1-8 POT and future POT.	152
6.10	Asimov sensitivity 2D confidence level contours of NH showing the individual effect of different sources of systematic uncertainty.	153
6.11	Asimov sensitivity 2D confidence level contours of NH in $\sin^2 \theta_{24}$ - Δm_{41}^2 plane, showing the systematic effects of Xsec and SK parameters.	154
7.1	Observed event spectra overlaid on the Asimov prediction.	156
7.2	Data fit 2D confidence level contours in Δm_{32}^2 vs. $\sin^2 \theta_{23}$ for normal and inverted hierarchy.	158
7.3	Data fit 2D confidence level contours in δ_{CP} vs. $\sin^2 \theta_{13}$ for normal and inverted hierarchy.	159
7.4	Data fit 1D $\Delta\chi^2$ plots in δ_{CP} for normal and inverted hierarchy.	159
7.5	Data fit 2D confidence level contours in Δm_{41}^2 vs. $\sin^2 \theta_{24}$ for normal and inverted hierarchy. On the right shows our results overlaid on limit to date from other experiments[32–39] (Figure taken from [32]).	160
7.6	Data fit 2D confidence level contours in $\cos^2 \theta_{24} \sin^2 \theta_{34}$ vs. $\sin^2 \theta_{24}$. On the right shows the 90% and 99% upper limits from IceCube [40] and SK [35].	160
A.1	Illustration of the Hough Transform (Figure taken from [41]).	166
A.2	Illustration of Cherenkov photon emission from a muon. When muon loss energy in a distance dx , photons are emitted in the region $dx \cdot \sin \theta + r \cdot d\theta$ (Figure taken from [42]).	167

A.3	Likelihood separation of single-ring electron (left) and muon (right) events for SK-IV atmospheric neutrino MC. The magenta lines show the cut criteria for electron-muon separation (Figure taken from [25]).	172
A.4	Likelihood separation of ν_μ charged-current quasi-elastic (left) and NC π^+ (right) events for T2K neutrino MC. The black lines show the cut criteria for muon- π^+ separation (Figure taken from [25]).	172
A.5	Likelihood separation of the CC single electron (left) and NC single π^0 (right) events in the SK-IV atmospheric neutrino MC. The magenta lines show the cut criteria for electron- π^0 separation (Figure taken from [25]).	173
A.6	Schematic diagram of ring counting in the multi-ring fitter of fitQun. The fifth and sixth rings are assumed to be e -like only. This diagram shows the procedure assuming the first ring to be e -like, and the same procedure is repeated for the case of first ring being π^+ -like (Figure taken from [24]).	173
C.1	P_{osc} with and without matter effect. Unless specified, all oscillation parameters are the same as in Table 6.2.	185
D.1	P_{osc} with $\sin^2 \theta_{24} = 0.2$, $\Delta m_{41}^2 = \Delta m_{31}^2 = 2.509 \times 10^{-3} \text{eV}^2$ for NH and IH.	187
E.1	“Daya Bay constraint” as a function of Δm_{41}^2 .	190
E.2	Asimov sensitivity 2D confidence level contours assuming NH showing the possible effects of θ_{14} , δ_{14} and δ_{24} .	192

F.1	Exclusion limits of the sterile parameters drawn by CL_s and fixed $\Delta\chi^2$ methods.	197
G.1	Best fit χ^2 distributions of both 3+1 sterile and 3-flavor oscillation models for 2500 non-Asimov data sets.	199
G.2	Best fit standard oscillation parameters for 2500 non-Asimov data sets.	200
G.3	Best fit $\sin^2 \theta_{24}$ - $\sin^2 \theta_{34}$ distribution for 2500 non-Asimov data sets. . .	200
G.4	Exclusion limits in the Δm_{41}^2 - $\sin^2 \theta_{24}$ plane from the Asimov and non-Asimov data sets, assuming NH.	201
G.5	Exclusion limits in the $\cos^2 \theta_{24}$ $\sin^2 \theta_{34}$ - $\sin^2 \theta_{24}$ plane from the Asimov and non-Asimov data sets, assuming NH.	201
H.1	$P(\nu_\mu \rightarrow \nu_\mu)$ at ND at 0.6 GeV, as a function of Δm_{41}^2 with $\sin^2 \theta_{24} = 0.1$.	203
H.2	Asimov sensitivity 2D confidence level contours in Δm_{41}^2 vs. $\sin^2 \theta_{24}$, assuming NH. The blue lines show the nominal sterile analysis, and the red lines show a test study of using $P_{SK}(\nu_\mu \rightarrow \nu_\mu)/P_{ND}(\nu_\mu \rightarrow \nu_\mu)$ and $P_{SK}(\nu_e \rightarrow \nu_e)/P_{ND}(\nu_e \rightarrow \nu_e)$ in event rate calculation. This illustrates that our sterile fit is valid below $\Delta m_{41}^2 = 0.3\text{eV}^2$ where the ND sees little sterile oscillation.	204
I.1	Asimov event spectra (black lines) together event spectra at Points #1 (blue), #2 (red) and #3 (green), assuming NH, overlaid on data points (black points). The ν_e spectra are projected on the electron momentum p_e	206

List of Tables

2.1	Best-fit values for the three-flavor neutrino-mixing parameters from a global analysis [43].	12
4.1	The run period, POT and horn current of each T2K run. Run 5 - Run 7 included periods of beam operation in both neutrino and antineutrino mode. (Table taken from [27]).	73
4.2	The spectroscopic factors of each nucleon state in ^{16}O (Table taken from [28]).	98
4.3	Summary of the energy levels and gamma ray emission branching ratios for the $1p_{3/2}$ hole states (Table taken from [28]).	99
4.4	Number of events observed in each CC and NC oscillation samples.	106
5.1	Binning used for reconstructed energy of $1\text{R}\mu$ samples.	108
5.2	Binning used for reconstructed lepton momentum and angle of 1Re samples and FHC ν_e CC 1π sample.	109
5.3	Binning used for reconstructed π^0 momentum of $2\text{R}\pi^0$ samples.	109
5.4	Binning used for reconstructed γ energy of FHC NC γ de-excitation sample.	109

5.5	Definition of neutrino interaction categories in this analysis. NEUT interaction modes of anti-neutrinos are negative. NCQE events (NEUT mode 51,52) are classified as NC other.	110
5.6	Binning used for true neutrino energy E_ν^{true}	111
5.7	Weights applied to CC coherent pion events.	112
5.8	Binning of beam flux systematic parameters for neutrino mode. . . .	115
5.9	Binning of beam flux systematic parameters for anti-neutrino mode. .	115
5.10	Summary of the neutrino interaction parameters using the results of ND280 fit. * Errors are not constrained by the near detector. ^ Non-BANFF errors added for the sterile analysis. # NCQE error instead of NC other error applies for FHC NC γ de-excitation sample.	117
5.11	Binning of SK detector systematic parameters for 1Re and ν_e CC1 π samples.	120
5.12	Binning of SK detector systematic parameters for 1R μ samples. . . .	121
5.13	Binning of SK detector systematic parameters for 2R π^0 samples. . . .	121
5.14	Binning of SK detector systematic parameters for NC γ de-excitation sample. Beam unrel. refers to background events that are not due to neutrino interactions, e.g. PMT dark noises, radioactive decay, etc. .	121
5.15	Criteria for event categorization based on final state information. The number of charged pions (N_{π^\pm}) and protons (N_P) only includes particles produced with momentum above Cherenkov threshold set at 156.0 MeV/c and 1051.0 MeV/c respectively.	122
5.16	Decay electron efficiency and estimated systematic uncertainties. . . .	123
5.17	List of fitQun cut variables used in the atmospheric neutrino fit. . .	126

5.18	Input systematic errors for the ToyMC of SK detector efficiency uncertainties.	128
5.19	Input systematic errors of topological cuts (ring-counting, PID, π^0 rejection cuts) for $1R_e$ and $\nu_e CC 1\pi^+$ samples.	128
5.20	Input systematic errors of topological cuts (ring-counting, PID) for $1R_\mu$ samples.	129
5.21	Input systematic errors of topological cuts for $2R\pi^0$ samples.	129
5.22	The uncertainties of primary gamma production for NCQE signal events.	130
5.23	The detector response uncertainties for $NC\gamma$ de-excitation sample. . .	131
5.24	The summary of SK detector efficiency errors for $NC\gamma$ de-excitation sample.	132
5.25	NEUT FSI “1-sigma” parameter sets from the fit to π^\pm -C data[44]. .	134
5.26	Percent errors on the predicted event rates of CC samples.	136
5.27	Percent errors on the predicted event rates of NC samples.	136
5.28	Fixed $\Delta\chi_f^2$ values used to build confidence level intervals	142
6.1	Run and POT configuration for the eight oscillation samples.	143
6.2	Oscillation parameters used to generate ToyMC data set.	144
6.3	Allowed values of the 3-flavor parameters in the oscillation fit.	144
7.1	Event rates of T2K Run 1-8 data and Asimov data set generated using parameters in Table 6.2.	155
7.2	Best fit oscillation parameter values for both 3+1 sterile model and 3-flavor model. On the right shows the results from standard oscillation analysis [45].	157
B.1	Event rate table for FHC $1R_\mu$ sample in 3-flavor oscillation analysis.	175

B.2	Event rate table for FHC $1R_e$ sample in 3-flavor oscillation analysis. .	176
B.3	Event rate table for RHC $1R_\mu$ sample in 3-flavor oscillation analysis.	176
B.4	Event rate table for RHC $1R_e$ sample in 3-flavor oscillation analysis. .	177
B.5	Event rate table for FHC $\nu_e CC 1\pi^+$ sample in 3-flavor oscillation analysis.	177
B.6	Event rate table for FHC $2R\pi^0$ sample in 3-flavor oscillation analysis.	178
B.7	Event rate table for RHC $2R\pi^0$ sample in 3-flavor oscillation analysis.	178
B.8	Event rate table for FHC $NC\gamma$ de-excitation sample in 3-flavor oscillation analysis.	179
B.9	Event rate table for FHC $1R_\mu$ sample in 3+1 sterile oscillation analysis.	179
B.10	Event rate table for FHC $1R_e$ sample in 3+1 sterile oscillation analysis.	180
B.11	Event rate table for RHC $1R_\mu$ sample in 3+1 sterile oscillation analysis.	180
B.12	Event rate table for RHC $1R_e$ sample in 3+1 sterile oscillation analysis.	181
B.13	Event rate table for FHC $\nu_e CC 1\pi^+$ sample in 3+1 sterile oscillation analysis.	181
B.14	Event rate table for FHC $2R\pi^0$ sample in 3+1 sterile oscillation analysis.	182
B.15	Event rate table for RHC $2R\pi^0$ sample in 3+1 sterile oscillation analysis.	182
B.16	Event rate table for FHC $NC\gamma$ de-excitation sample in 3+1 sterile oscillation analysis.	183
G.1	Event rates of four non-Asimov data sets.	199

Chapter 1

Introduction

When Wolfgang Pauli first proposed the existence of neutrino in the 1930s to explain the missing energy in radioactive beta decay experiments, he described it as a “desperate remedy” and wrote “I have done something very bad today by proposing a particle that cannot be detected; it is something no theorist should ever do.” Indeed this mysterious “ghost particle” was a puzzle (and still is now). After more than 20 years of technological advancement, the first neutrino, precisely the electron anti-neutrino $\bar{\nu}_e$, was discovered in a reactor-neutrino experiment[46] through the inverse beta decay reaction:

$$\bar{\nu}_e + p \rightarrow e^+ + n. \quad (1.1)$$

Following the first neutrino observations, muon neutrino ν_μ , which couples to muon instead of electron, was discovered in an accelerator neutrino experiment in 1962[47]. While the third charged lepton, tau, was discovered in 1975[48], it takes another 25 years for the DONUT experiment[49] to directly detect tau neutrino in 2000.

Neutrino physics has been advancing very quickly since its discovery. One of

the most interesting topics is the phenomenon of neutrino oscillation, where one neutrino flavor can change its identity on propagation and become another flavor at detection. Actually the concept of neutrino oscillation was first introduced in 1957 by Pontecorvo[50, 51], although at that time he was proposing the oscillation between neutrinos and anti-neutrinos $\nu \leftrightarrow \bar{\nu}$. Subsequently, the ideas of neutrino mixing and flavor oscillations were presented in 1962[52, 53], and the theory of neutrino oscillation was finally developed in 1976[54–57]. Such framework is analogue to quark mixing, and allows the violation of charge-parity (CP) symmetry in the leptonic sector, which might be the answer to the observed matter-antimatter asymmetry in our universe.

Another implication of neutrino oscillation is that neutrino must be massive. This violates the Standard Model of particle physics, so a good understanding of this process can help the development of physics beyond Standard Model.

There are many different types of neutrino oscillation experiments with various neutrino sources and detector designs. They cover a diverse range of neutrino energy and measure different sets of oscillation parameters. Their results are mostly consistent with the standard 3-flavor oscillation model, in which the three active neutrino flavors ν_e , ν_μ and ν_τ can be expanded as superpositions of three mass eigenstates ν_1 , ν_2 and ν_3 . The corresponding mixing angles θ_{ij} and mass splittings $\Delta m_{ij}^2 = m_i^2 - m_j^2$ are measured with a high precision. For example, solar and long baseline reactor neutrino experiments determine the solar mass splittings $\Delta m_{sol}^2 = \Delta m_{21}^2 \simeq 2.3 \times 10^{-3} \text{eV}^2$ and $\sin^2 \theta_{12}$. Atmospheric and long baseline accelerator neutrino experiments quantify the atmospheric mass splittings $\Delta m_{atm}^2 = |\Delta m_{31}^2| \approx |\Delta m_{32}^2| \simeq 7.5 \times 10^{-5} \text{eV}^2$ and $\sin^2 \theta_{23}$. Meanwhile short baseline reactor neutrino experiments give us measurements on Δm_{31}^2 and $\sin^2 \theta_{13}$.

On the other hand, several oscillation experiments have indicated the possibility of the existence of a new mass splittings $\Delta m^2 \sim \mathcal{O}(\text{eV}^2)$ which cannot be accommodated in the 3-flavor model. One possible way to explain this is to introduce one or more additional massive neutrinos which do not participate in the standard weak interactions. They are called sterile neutrinos in contrast to the three “active” neutrino species.

Apart from solving the oscillation problem, sterile neutrinos are also interesting in many aspects because they are present in many extensions of the Standard Model and have important implications on astrophysics, cosmology, etc. In e.g. the Neutrino Minimal Standard Model (νMSM)[58–60], there are three sterile neutrinos which can be dark matter candidate and explain the baryon asymmetry in the Universe.

In this thesis, we perform a search of sterile neutrino in T2K. T2K is a long baseline acceleration neutrino experiment which is designed for precise determination on Δm_{32}^2 and $\sin^2 \theta_{23}$ through muon neutrino disappearance measurement. Combining with simultaneous electron neutrino appearance measurement, recent T2K data have also showed some preference on non-zero CP phases and normal neutrino mass ordering[20]. The high quality data set at T2K has offered us opportunity to study exotic physics, e.g. the existence of sterile neutrinos. We make use of T2K’s data at the far detector Super-Kamiokande (SK) to search for sterile neutrino, specifically under the 3+1 sterile model.

In Chapter 2, we give a brief overview of the standard 3-flavor oscillation model and introduce the 3+1 sterile model. A description of the T2K experiment is presented in Chapter 3, and the oscillation samples collected at SK are described in Chapter 4. We explain our analysis method in Chapter 5, and show the results of sensitivity study with Monte Carlo in Chapter 6. Finally the data fit results are

illustrated in Chapter 7, followed by a summary section in Chapter 8.

Chapter 2

Standard and sterile neutrino oscillation model

2.1 3-flavor neutrino mixing

2.1.1 Motivation

In the charged-current (CC) weak interaction which is mediated by the W boson, the W boson is always coupled to a charged lepton (e, μ, τ) and its corresponding neutrino (ν_e, ν_μ, ν_τ). A neutrino flavor eigenstate is therefore defined by the participating charged lepton in the CC interaction. For example, reactor neutrinos are produced by the beta decay interaction which involves electron, and hence are all electron anti-neutrino,

$$n \rightarrow p + e^- + \bar{\nu}_e. \tag{2.1}$$

On the other hand, the main decay mode of charged pion is to muon and muon neutrino:

$$\begin{aligned}\pi^+ &\rightarrow \mu^+ + \nu_\mu, \\ \pi^- &\rightarrow \mu^- + \bar{\nu}_\mu.\end{aligned}\tag{2.2}$$

Lepton number (+1 for charged lepton and neutrino, -1 for their antiparticles) is conserved in these interactions, so ν and $\bar{\nu}$ are produced correspondingly.

When a pure neutrino flavor is produced at a source, we expect the same flavor interaction anytime/anywhere at detection. However, experiments show that it is not the case. Such behavior was first observed in the Homestake experiment[6] in late 1960s, where only one-third of solar ν_e was detected when compared with theoretical calculations. While there were various possible explanations such as the inaccuracies in the solar model and experimental systematics, one interesting theory stands out: the depletion could be due to the flavor oscillation of ν_e into ν_μ and ν_τ inside the Sun. At first, this theory received little support because it requires a massive neutrino which contradicts the Standard Model. However, as more and more experiments came out, there were stronger evidences on the solar ν_e deficit. Finally the SNO experiment[61] proves that solar neutrino oscillation indeed exists by measuring both the ν_e flux and the total solar neutrino ($\nu_e + \nu_\mu + \nu_\tau$) flux at the same time. A deficit in ν_e flux was observed, while total solar neutrino flux agreed with the standard solar model, which implied ν_e changing flavor into ν_μ and ν_τ .

Independent experiments with different neutrino sources and detector designs, such as Super-Kamiokande[62] and KamLAND[63], also strongly support the theory of neutrino oscillation. The oscillation theory is now well-established, and experiments have moved from discovery of oscillation to precision measurement of oscilla-

tion parameters.

2.1.2 Formalism

The physics of neutrino mixing is similar to quark mixing, where the neutrino flavor states ν_α are not identical to the mass eigenstates ν_i and their transformations are governed by a unitary mixing matrix. In the 3-flavor oscillation framework, ν_α and ν_i are related by a 3×3 matrix called the Pontecorvo-Maki-Nakagawa-Sakata (PMNS) matrix U :

$$\begin{aligned}\nu_i &= \sum_{\alpha} U_{\alpha i} |\nu_{\alpha}\rangle, \\ \nu_{\alpha} &= \sum_i U_{\alpha i}^* |\nu_i\rangle.\end{aligned}\tag{2.3}$$

The PMNS matrix is parametrized by three mixing angles θ_{12} , θ_{13} , θ_{23} , and a CP phase δ_{CP} which allows charge-parity violation in the leptonic sector. It matrix can be decomposed into three rotation matrices depending on θ_{ij} :

$$\begin{aligned}U &= \begin{pmatrix} U_{e1} & U_{e2} & U_{e3} \\ U_{\mu1} & U_{\mu2} & U_{\mu3} \\ U_{\tau1} & U_{\tau2} & U_{\tau3} \end{pmatrix} \\ &= \begin{pmatrix} 1 & 0 & 0 \\ 0 & c_{23} & s_{23} \\ 0 & -s_{23} & c_{23} \end{pmatrix} \begin{pmatrix} c_{13} & 0 & s_{13}e^{-i\delta_{CP}} \\ 0 & 1 & 0 \\ -s_{13}e^{i\delta_{CP}} & 0 & c_{13} \end{pmatrix} \begin{pmatrix} c_{12} & s_{12} & 0 \\ -s_{12} & c_{12} & 0 \\ 0 & 0 & 1 \end{pmatrix} \\ &= \begin{pmatrix} c_{12}c_{13} & s_{12}c_{13} & s_{13}e^{-i\delta_{CP}} \\ -s_{12}c_{23} - c_{12}s_{23}s_{13}e^{i\delta_{CP}} & c_{12}c_{23} - s_{12}s_{23}s_{13}e^{i\delta_{CP}} & s_{23}c_{13} \\ s_{12}s_{23} - c_{12}c_{23}s_{13}e^{i\delta_{CP}} & -c_{12}s_{23} - s_{12}c_{23}s_{13}e^{i\delta_{CP}} & c_{23}c_{13} \end{pmatrix},\end{aligned}\tag{2.4}$$

where $c_{ij} = \cos \theta_{ij}$ and $s_{ij} = \sin \theta_{ij}$.

There is actually an additional diagonal matrix multiplied at the end of U :

$$\begin{pmatrix} e^{i\alpha_1/2} & 0 & 0 \\ 0 & e^{i\alpha_2/2} & 0 \\ 0 & 0 & 1 \end{pmatrix}. \quad (2.5)$$

The Majorana CP-violating phases α_1 and α_2 only matter if neutrinos are Majorana particles, i.e. neutrinos are their own antiparticle, which violate lepton number conservation. These phases are mostly searched by neutrinoless double beta decay experiments. Since they have no effect on the neutrino oscillation probability, they are dropped out for simplicity.

Using U , a neutrino flavor state propagation can be written as

$$|\nu_\alpha(t)\rangle = \sum_i U_{\alpha i}^* |\nu_i\rangle e^{i(\vec{p}_i \cdot \vec{x} - Et)}. \quad (2.6)$$

In the ultra-relativistic limit $E \gg m_i$,

$$\begin{aligned} p_i &= \sqrt{E^2 - m_i^2} \\ &\approx E - \frac{m_i^2}{2E}, \end{aligned} \quad (2.7)$$

and neutrino travels at almost speed of light $L \approx t$, we can simplify Eq. 2.6 as

$$|\nu_\alpha(L)\rangle \approx \sum_i U_{\alpha i}^* |\nu_i\rangle e^{-i\frac{m_i^2 L}{2E}}. \quad (2.8)$$

The probability of detecting ν_β at distance L is therefore

$$\begin{aligned}
P(\nu_\alpha \rightarrow \nu_\beta) &= |\langle \nu_\beta | \nu_\alpha(L) \rangle|^2 \\
&= \sum_i \sum_j U_{\alpha i}^* U_{\beta i} U_{\alpha j} U_{\beta j}^* e^{-i(m_i^2 - m_j^2)L/2E} \\
&= \delta_{\alpha\beta} - 4 \sum_{i>j} \Re(U_{\alpha i}^* U_{\beta i} U_{\alpha j} U_{\beta j}^*) \sin^2 \left(\frac{\Delta m_{ij}^2 L}{4E} \right) \\
&\quad + 2 \sum_{i>j} \Im(U_{\alpha i}^* U_{\beta i} U_{\alpha j} U_{\beta j}^*) \sin \left(\frac{\Delta m_{ij}^2 L}{2E} \right).
\end{aligned} \tag{2.9}$$

For anti-neutrino, we replace U by U^* .

The oscillation behavior is mostly controlled by the $\sin^2 \frac{\Delta m_{ij}^2 L}{4E}$ terms. The oscillation amplitude is determined by the combination of sine and cosine terms of the mixing angles θ_{ij} . The oscillation phase is $\frac{\Delta m_{ij}^2 L}{4E}$, thus by changing the neutrino energy and detection baseline, one can map out the entire oscillation spectrum and measure Δm_{ij}^2 . And if $\Delta m_{ij}^2 = 0$, i.e. all neutrinos are massless, there would be no oscillation.

While δ_{CP} is attached to θ_{13} , it does not enter the formula unless all θ_{ij} are non-zero. If $\delta_{CP} = 0$ or π , there would be no difference between $P(\nu_\alpha \rightarrow \nu_\beta)$ and $P(\bar{\nu}_\alpha \rightarrow \bar{\nu}_\beta)$. Otherwise there would be an asymmetry between neutrino and anti-neutrino:

$$\begin{aligned}
\Delta P(\nu_\alpha \rightarrow \nu_\beta) &= P(\nu_\alpha \rightarrow \nu_\beta) - P(\bar{\nu}_\alpha \rightarrow \bar{\nu}_\beta) \\
&= 4 \sum_{i>j} \Im(U_{\alpha i}^* U_{\beta i} U_{\alpha j} U_{\beta j}^*) \sin \left(\frac{\Delta m_{ij}^2 L}{2E} \right).
\end{aligned} \tag{2.10}$$

2.1.3 Matter effect

When neutrinos propagate in matter, they interact with the materials (mostly electrons) through charged-current (CC) and neutral-current (NC) interactions [64–66].

All neutrino flavors undergo NC interaction with the same amplitude,

$$\nu_\alpha + e^- \rightarrow \nu_\alpha + e^-, \quad (2.11)$$

the corresponding Hamiltonian is diagonal and symmetric, which just introduces an overall phase factors for all flavors and has no physical significance.

On the other hand, only ν_e would experience CC interaction:

$$\nu_e + e^- \rightarrow e^- + \nu_e. \quad (2.12)$$

ν_μ and ν_τ cannot undergo similar CC interactions due to the lack of the corresponding leptons in ordinary matter. This introduces an extra term A in the Hamiltonian of propagating neutrino:

$$H = \frac{1}{2E} \left(U \begin{pmatrix} m_1^2 & 0 & 0 \\ 0 & m_2^2 & 0 \\ 0 & 0 & m_3^2 \end{pmatrix} U^\dagger + \begin{pmatrix} A & 0 & 0 \\ 0 & 0 & 0 \\ 0 & 0 & 0 \end{pmatrix} \right), \quad (2.13)$$

with

$$A = 2\sqrt{2}G_F N_e E, \quad (2.14)$$

where G_F is the Fermi constant and N_e is the number density of electrons. For anti-neutrino, U is replaced by U^* and A is replaced by $-A$.

To calculate the oscillation probability, we need to diagonalize the above Hamil-

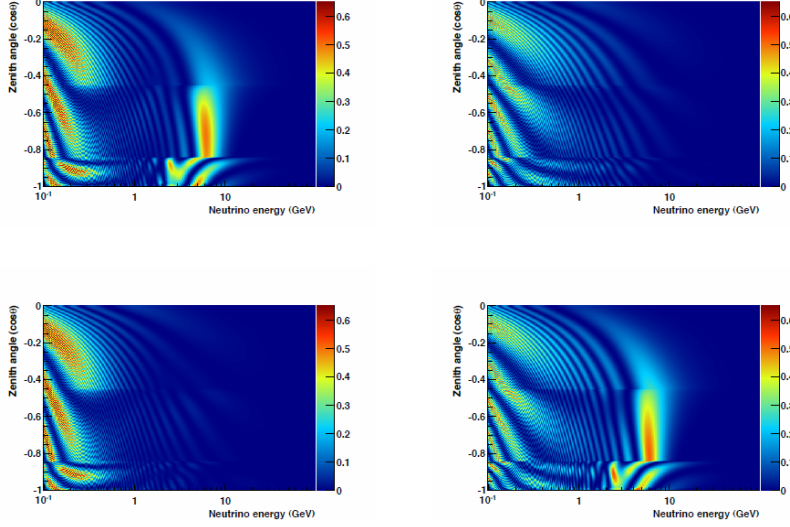


Figure 2.1: The transition probability $P(\nu_\mu \rightarrow \nu_e)$ with matter effect observed at SK as a function of cosine of zenith angle and neutrino energy. The zenith angle can be converted to neutrino propagation length through the Earth’s matter, assuming the Earth is a sphere. Top (bottom) shows the normal (inverted) hierarchy case, and left (right) shows the neutrino (anti-neutrino) case (Figure taken from [2]).

tonian to get a new set of mass eigenvalues $m_i'^2$ and mixing matrix U' which are energy-dependent. Both the oscillation amplitude and oscillation phase are changed. Since the potential term A differs by a negative sign between neutrino and anti-neutrino, this introduces a δ_{CP} -like effect and has to be taken account in δ_{CP} measurement. It can also be shown that the two mass hierarchies are affected in different ways. For example, Fig. 2.1 shows the transition probability $P(\nu_\mu \rightarrow \nu_e)$ with matter effect for a neutrino traveling through Earth’s matter, for normal/inverted hierarchy neutrino/anti-neutrino case.

Matter effect can change the oscillation pattern significantly for high energy neutrinos propagating a long distance, e.g. solar neutrinos and atmospheric neutrino travelling across the Earth. Yet, for T2K’s beam energy and baseline, matter effect is not significant, and is ignored in the sterile neutrino oscillation probability calcu-

Parameter	Best-fit
Δm_{21}^2	$(7.53 \pm 0.18) \times 10^{-5} \text{eV}^2$
$ \Delta m_{32}^2 $	$(2.45 \pm 0.05) \times 10^{-3} \text{eV}^2$
$\sin^2 \theta_{12}$	0.307 ± 0.013
$\sin^2 \theta_{23}$	0.51 ± 0.04
$\sin^2 \theta_{13}$	0.0210 ± 0.0011

Table 2.1: Best-fit values for the three-flavor neutrino-mixing parameters from a global analysis [43].

lation. In Appendix C, we confirm that the matter effect is not important in our sterile analysis.

2.1.4 Current measured values of neutrino mixing parameters

In order to determine all neutrino mixing parameters, θ_{ij} , Δm_{ij}^2 and δ_{CP} , experiments have been done to measure $P(\nu_\alpha \rightarrow \nu_\beta)$ at different L/E regions. Table 2.1 shows the best-fit values of all currently known parameters from a global analysis. Since $|\Delta m_{32}^2| \gg \Delta m_{21}^2$, we have $\Delta m_{32}^2 \approx \Delta m_{31}^2$, and currently no single experiment is able to measure these two different oscillation cycles at the same time.

θ_{12} and Δm_{21}^2

The world's most accurate measurement of θ_{12} and Δm_{21}^2 comes from a combined fit of KamLAND, which is a long baseline reactor neutrino experiment measuring $\bar{\nu}_e$ flux from more than 50 commercial nuclear reactors in Japan and Korea, and global solar neutrino data[10].

For long baseline reactor experiments, the survival probability of $\bar{\nu}_e$ can be written

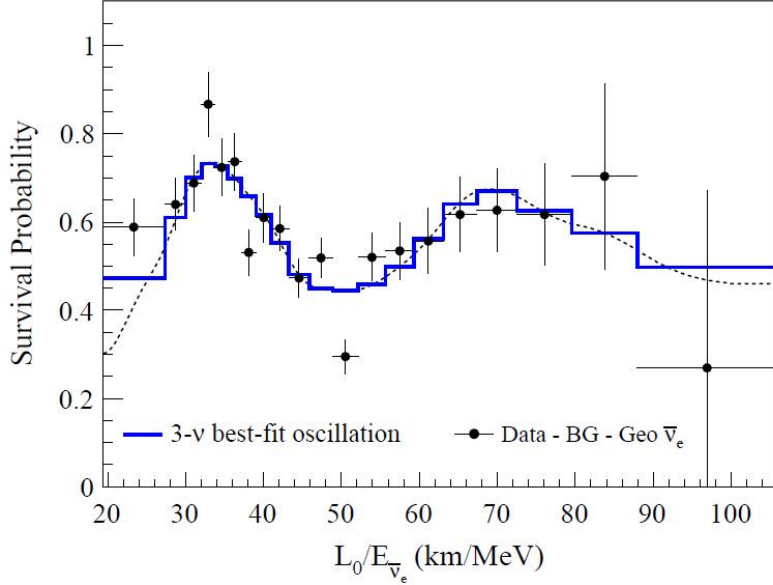


Figure 2.2: Ratio of the observed $\bar{\nu}_e$ spectrum to expected assuming no oscillation for KamLAND, with the 3-flavor best fit oscillation curve superimposed. $L_0=180$ km is the flux-weighted average reactor baseline (Figure taken from [3]).

as:

$$P(\bar{\nu}_e \rightarrow \bar{\nu}_e) \approx 1 - \sin^2 2\theta_{12} \sin^2 \frac{\Delta m_{21}^2 L}{4E}. \quad (2.15)$$

Fig. 2.2 shows the KamLAND's best-fit $P(\bar{\nu}_e \rightarrow \bar{\nu}_e)$ spectrum, with a flux-weighted average baseline of $L_0 = 180$ km.

Solar neutrino experiments measure the solar ν_e flux produced in different proton-proton chain reactions. As ν_e propagates out of the Sun, it experiences matter effects, but with matter density gradually decreasing from the Sun's core to surface. This leads to the MSW effect [64, 66, 67], where the slow decrease of matter density resonantly enhances the neutrino mixing. Fig. 2.3 shows the expected MSW survival probability $P(\nu_e \rightarrow \nu_e)$. The basic idea is, low energy neutrinos suffer little matter effect and travel like those in vacuum, while high energy neutrinos are strongly affected and made mostly ν_2 in production. Whether the energy is low or high depends

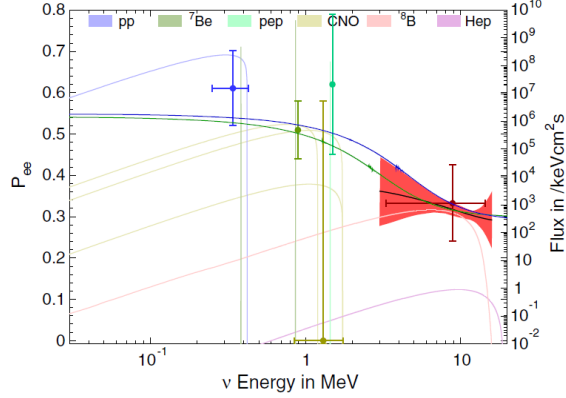


Figure 2.3: Predicted solar neutrino spectra[4], overlaid with predicted MSW $P(\nu_e \rightarrow \nu_e)$ (green is from solar best fit, blue is from solar + KamLAND best fit). Shown in red is the 1σ band of $P(\nu_e \rightarrow \nu_e)$ from combined data of SK and SNO. Shown in points are the measurements of $P(\nu_e \rightarrow \nu_e)$ from the ${}^7\text{Be}$ (green), the pep (light green) and the ${}^8\text{B}$ flux (red) by Borexino[5], and the pp (blue) and CNO (gold) extracted from [6–9].(Figure taken from [10]).

on the relative size the matter potential A in the Hamiltonian in Eq. 2.13. The solar matter density in the center region is $\sim 10^5 \text{ kg/m}^3$, and $\Delta m_{21}^2 \approx 7.5 \times 10^{-5} \text{ eV}^2$, so the transition from “low” to “high” energy regime occurs in the MeV region.

In the low energy limit which is essentially vacuum oscillations,

$$P(\nu_e \rightarrow \nu_e) \approx 1 - \sin^2 2\theta_{12} \sin^2 \frac{\Delta m_{21}^2 L}{4E} \approx 1 - \frac{1}{2} \sin^2 2\theta_{12}, \quad (2.16)$$

where $\sin^2 \frac{\Delta m_{21}^2 L}{4E}$ is averaged out due to the extremely large size of the Sun. In the high energy limit,

$$P(\nu_e \rightarrow \nu_e) \approx |\langle \nu_e | \nu_2 \rangle|^2 \approx \sin^2 \theta_{12}. \quad (2.17)$$

By measuring the transition of $P(\nu_e \rightarrow \nu_e)$ between the low energy and high energy ends, one can then map out $\sin^2 \theta_{12}$ and Δm_{21}^2 .

The KamLAND + solar fit results are shown in Fig. 2.4. There is a slight tension between KamLAND and solar measurements on Δm_{21}^2 , but KamLAND one domina-

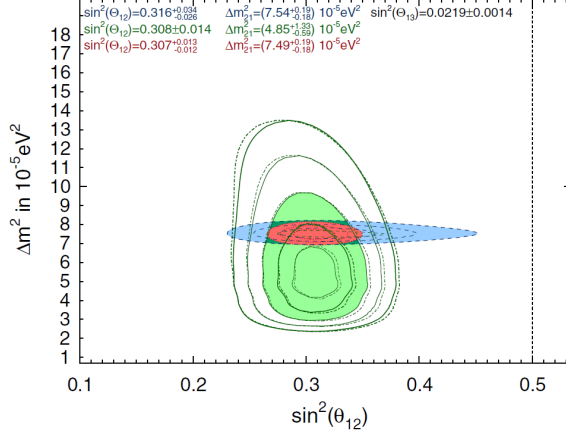


Figure 2.4: Allowed contours of Δm_{21}^2 vs $\sin^2 \theta_{12}$ from solar neutrino data (green), KamLAND data (blue), and the combined result (red). The dashed dotted lines show the SK + SNO result. The filled regions give the 1, 2, 3 σ confidence level contours. For solar analysis, 4, 5 σ confidence level contours are also shown (Figure taken from [10]).

tes in the fit because of its much smaller errors. Also the combined fit gives a much better constraint on $\sin^2 \theta_{12}$.

θ_{23} and Δm_{32}^2

The first observation of atmospheric neutrino oscillation was done by the Kamiokande experiment[68]. It measured the atmospheric neutrino flux due to cosmic ray interaction in the atmosphere. A deficit in muon neutrino flux was observed, which was one of the earliest evidence of the existence of neutrino oscillations. The atmospheric neutrino oscillation is mostly due to $\sin^2 \theta_{23}$ and Δm_{32}^2 , where the survival probability of ν_μ and $\bar{\nu}_\mu$ can be written as:

$$P(\nu_\mu \rightarrow \nu_\mu) = P(\bar{\nu}_\mu \rightarrow \bar{\nu}_\mu) \approx 1 - \sin^2 2\theta_{23} \sin^2 \frac{\Delta m_{32}^2 L}{4E}. \quad (2.18)$$

Following the discovery in Kamiokande, series of atmospheric and long baseline

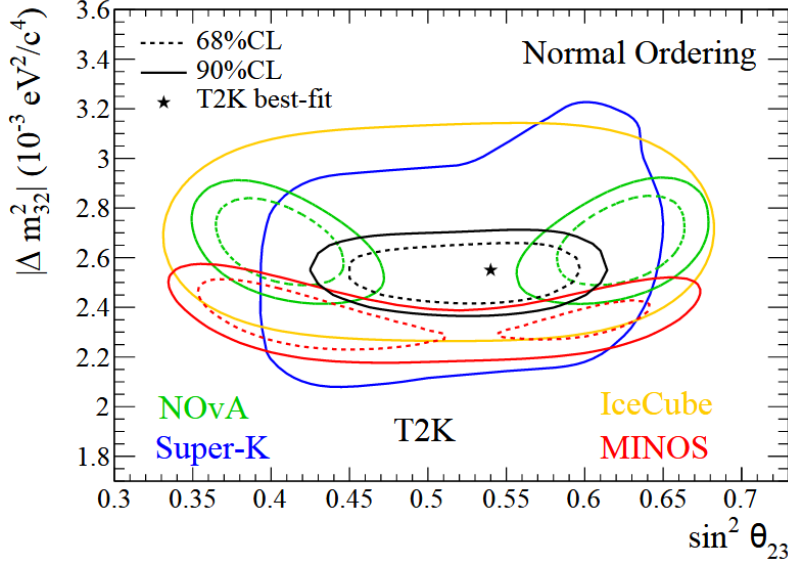


Figure 2.5: The 90% and 68% confidence levels in the $\sin^2 \theta_{23} - \Delta m_{32}^2$ plane from T2K, SK[11], NO ν A[12], MINOS[13] and IceCube[14], assuming $\Delta m_{32}^2 > 0$ (Figure taken from [15]).

accelerator neutrino experiments have been done to constrain $\sin^2 \theta_{23}$ and Δm_{32}^2 . Modern experiments like T2K and SK have measured them to a high precision, as shown in Fig. 2.5. What remain unknown are whether there is maximal mixing of $\sin^2 \theta_{23} = 0.5$, and the sign of Δm_{32}^2 .

θ_{13}

The last mixing angle, θ_{13} , is determined by short baseline reactor experiments such as Daya Bay[16], RENO[69] and Double Chooz[70]. With baseline of ~ 1 km, they are able to detect the $\bar{\nu}_e$ disappearance due to Δm_{31}^2 oscillation:

$$P(\bar{\nu}_e \rightarrow \bar{\nu}_e) \approx 1 - \sin^2 2\theta_{13} \sin^2 \frac{\Delta m_{31}^2 L}{4E}. \quad (2.19)$$

Fig. 2.6 shows, e.g. $\bar{\nu}_e$ survival probability measured at Daya Bay.

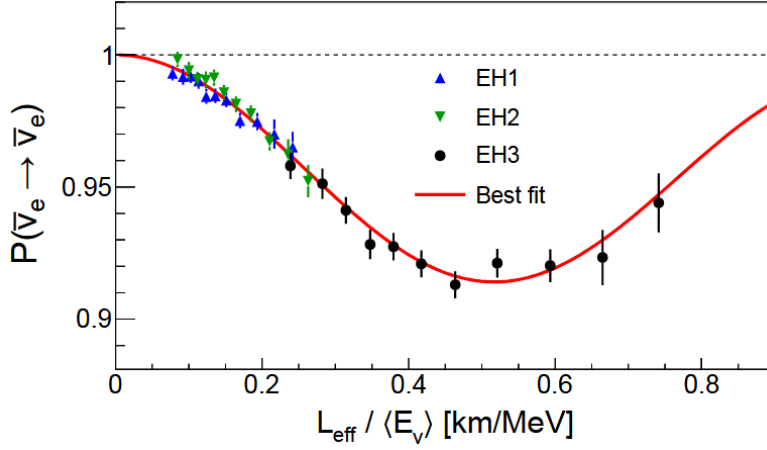


Figure 2.6: Measured reactor $\bar{\nu}_e$ spectral distortion at Daya Bay (Figure taken from [16]).

Long baseline accelerator neutrino experiments like T2K, NO ν A[12], MINOS[13] are also capable of θ_{13} measurements by measuring the electron neutrino appearance from a pure neutrino beam:

$$P_{\nu_\mu \rightarrow \nu_e} \approx \sin^2 2\theta_{13} \sin^2 \theta_{23} \sin^2 \frac{\Delta m_{31}^2}{4E}. \quad (2.20)$$

The precision is, however, a bit worse due to lower statistics and the uncertainty of $\sin^2 \theta_{23}$.

Unknown parameters

While most oscillation parameters are well determined, we have little knowledge about two important variables: neutrino mass hierarchy and δ_{CP} . Fig. 2.7 illustrates the two possible mass hierarchies, and the effect of δ_{CP} on the mixing matrix element $U_{\alpha i}$.

The two possible mass hierarchies are normal hierarchy ($m_1 < m_2 < m_3$) and

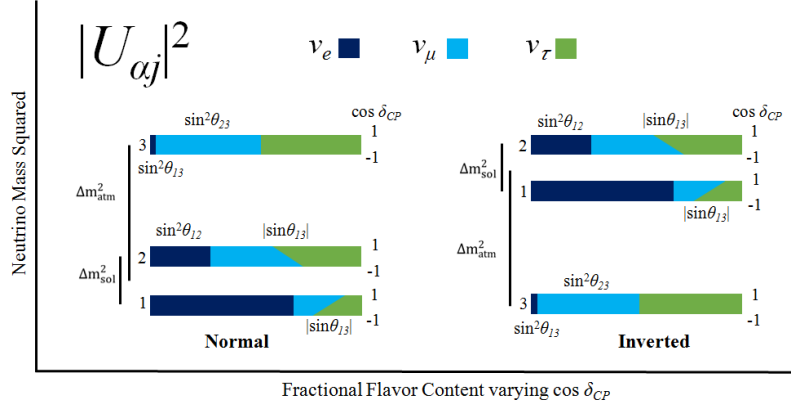


Figure 2.7: Illustration of the two possible mass hierarchies, and the effect of δ_{CP} on the mixing matrix element $U_{\alpha i}$.

inverted hierarchy ($m_3 < m_1 < m_2$). Since $|\Delta m_{32}^2| \gg \Delta m_{21}^2$, normal hierarchy (NH) corresponds to one larger mass and two smaller masses, while inverted hierarchy (IH) corresponds to one smaller mass and two larger masses. Such mass pattern can be crucial in, e.g. examining theory beyond Standard Model (BSM) that leads to the existence of neutrino mass, determining the absolute neutrino mass scale, resolving the Majorana nature of neutrino, etc.

The value of δ_{CP} is, as named, indicating whether there is CP violation in the leptonic sector, which may be used to explain the observed matter-antimatter asymmetry in our universe.

Although these two important parameters are currently unknown, the small but non-zero value of θ_{13} has made it possible to measure them through oscillation experiments. For example, in accelerator experiments, the electron neutrino appearance channel is sensitive to δ_{CP} , which however has some degeneracy with mass hierarchy since matter effect would enhance (suppress) the appearance probability in case of NH (IH). Measurements in both neutrino and antineutrino channels can help break this degeneracy, but current experiments have not reach definitive conclusions yet.

T2K[71], NO ν A[72] and MINOS[73] all seem to have some preference on maximum CP-violation of $\delta_{CP} \simeq \pm \frac{\pi}{2}$, although there are tensions between the published results. Atmospheric neutrino data from SK[74] also showed preference of $\delta_{CP} \simeq -\frac{\pi}{2}$ and favored NH by $> 90\%$. Next generation experiments like Hyper-K[75], T2HKK[76] and DUNE[77] would be capable to unfold the mysteries with their exceptional sensitivity.

2.2 Sterile neutrino model

2.2.1 Theoretical interest

In the Standard Model (SM), the three active neutrinos that participate in weak interactions are all left-handed (spins antiparallel to momenta), and all anti-neutrinos are right-handed. The absence of right-handed neutrinos (left-handed anti-neutrinos) means neutrinos cannot obtain mass through Higgs mechanism and thus neutrinos are massless. Yet, the phenomenon of neutrino oscillation implies neutrinos must be massive. Also, from current experiment data, neutrino mass is at most of eV order[43], which is $> 10^5$ times smaller than the lightest fermion electron. The origin of neutrino mass is by no doubt the missing ingredient in the SM and involves new physics.

To solve the neutrino mass problem, the SM must be extended. One of the simplest solutions would be the introduction of right-handed neutrinos. These right-handed neutrinos, however, are singlet fermions, so they do not interact via weak interactions and are “sterile”. With the right-handed sterile neutrinos, it is possible to include a Dirac mass term or Majorana mass term or both to generate neutrino mass.

In the case of single neutrino, the Dirac mass term is of the form

$$m_D(\bar{n}_L n_R + \bar{n}_R n_L), \quad (2.21)$$

so it is actually the coupling between the left-chiral neutrino state n_L and the right-chiral neutrino state n_R . If only the Dirac mass term exists, the coupling has to be extremely small (compared with other particles) in order to explain the small neutrino mass.

The Majorana mass term is of the form

$$m_L \bar{n}_L^C n_L + m_R \bar{n}_R^C n_R, \quad (2.22)$$

where the superscript C donates charge conjugate. Unlike other fermions, neutrino is electrically neutral, so the Majorana mass term does not violate charge conservation and is allowed. However, the n_L coupling would require a Higgs triplet with hypercharge +2 that does not exist in the SM.

A general mass term with both Dirac and Majoranan masses may be constructed as

$$\begin{pmatrix} \bar{n}_L^C & \bar{n}_R \end{pmatrix} \begin{pmatrix} m_L & m_D \\ m_D & m_R \end{pmatrix} \begin{pmatrix} n_L \\ n_R^C \end{pmatrix}, \quad (2.23)$$

and the mass eigenvalues (m_1, m_2) are

$$m_{1,2} = \frac{1}{2} \left((m_L + m_R) \pm \sqrt{(m_L - m_R)^2 + 4m_D^2} \right). \quad (2.24)$$

In the special case of $m_L = 0$ and $m_R \gg m_D$, we have

$$m_1 \approx -\frac{m_D^2}{m_R},$$

$$m_2 \approx m_R.$$
(2.25)

Therefore we have “light” active neutrino and a “heavy” sterile neutrino. This is the so-called (type-I) seesaw mechanism[78–82] and can be generalized to any number of active and sterile neutrinos by replacing $m_{L/R/D}$ with the corresponding mass matrices.

Because of its beauty and simplicity, sterile neutrino is present in many extensions of SM, and it is in principal possible to have any number of sterile neutrinos with any masses. One famous model is the Neutrino Minimal Standard Model (ν MSM)[58–60], where there are three right-handed neutrinos with masses smaller than the electro-weak scale. In this model, the lightest sterile neutrino is a dark matter candidate with O(keV) mass, and the two heavier sterile neutrinos need to have roughly degenerate masses of O(MeV) or O(GeV). The decay of heavy Majorana neutrinos would generate a violation of lepton number conservation in the universe, which could then converted to baryon number non-conservation (sphalerons[83]) and therefore explain the matter-antimatter asymmetry observed nowadays.

There are various possible ways to search for sterile neutrinos over a wide range of mass scale. In collider experiments like LHC, heavy sterile neutrinos could be produced and decay into e.g. $W^\pm l^\mp$ pairs (see Fig. 2.8). The search for the opposite-sign di-lepton signal in association with the hadronic decay of W^\pm is one possible strategy[17]. Sterile neutrino dark matter may be searched directly by looking for a narrow decay line in X-ray spectra of dark matter dominated astrophysical

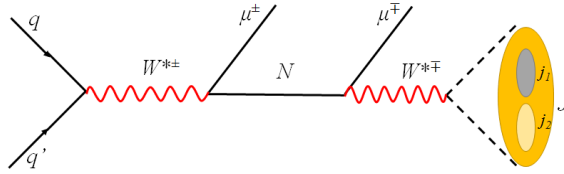


Figure 2.8: Schematic of a possible heavy sterile neutrino production at hadron colliders followed by its subsequent decay, suggested in [17].

objects[84–87], or indirect constraints can be formed through observations of structure formation at different spatial scales[88, 89]. Neutrinoless double decay experiments might give some hints too because the decay rate is sensitive to $m_N|U_{eN}|^2$, where $N \geq 4$ donates the sterile neutrino index. Nevertheless, we are particularly interested in O(eV) sterile neutrinos because of their observable signatures in oscillation spectra, which could be used to resolve some observed anomalies in oscillation experiments.

For eV scale sterile neutrinos to exist, the type-I seesaw models need to assume very small (10^{-12}) Yukawa couplings between the active and sterile neutrinos, and at least two sterile neutrinos are needed to explain the observed mass splittings of active neutrinos. There are therefore extensions to the usual seesaw models that allow light sterile neutrinos to appear “more naturally”, e.g. the flavor symmetry models[90–92] where sterile neutrinos of eV and keV masses can co-exist by the split seesaw mechanism[93] or Froggatt-Nielsen mechanism[94], and the “minimal extended type-I seesaw” model that adds a fermion singlet in addition to three sterile neutrinos[91, 95, 96]. Apart from the correct mass-splittings, these models also provide sizable active-sterile mixing that matches experimental observations. Our long baseline sterile neutrino oscillation search is sensitive to those models that produce light sterile neutrinos (< 1 eV) with a small but measurable mixing with active neutrinos ($\sin^2 \theta \lesssim 0.1$).

2.2.2 Experimental hints at eV scale

While sterile neutrinos could possibly explain neutrino masses, fill the gap in SM, and account for dark matter and matter-antimatter asymmetry, there are still no concrete evidence to prove their existence. Here we briefly describe the neutrino oscillation experiments that suggest O(eV) masses sterile neutrinos, which was the starting ground of sterile neutrino theory. These eV sterile neutrinos could affect the oscillation spectra through mixing with the active neutrinos.

The first and most well-known hint came from the accelerator experiment LSND[97, 98], where there was excess of $\bar{\nu}_e$ events from a pure $\bar{\nu}_\mu$ beam. Such excess cannot be explained by the 3-flavor transition of $\bar{\nu}_\mu \rightarrow \bar{\nu}_e$, and suggests a new $\Delta m^2 \sim 1\text{eV}^2$ which could be due to sterile neutrinos. The same parameter space has been studied by subsequent experiments like MiniBooNE[38] and MINOS[32]. Although most parameter space has been ruled out, it's still possible that a small sterile mixing of $\sin^2 \theta \sim 10^{-3}$ exists.

There are also some interesting findings from reactor neutrino experiments[99]. Reactor experiments like Daya Bay have reported deficit in measured $\bar{\nu}_e$ flux with respect to predictions. It is possible to explain this so-called reactor anomaly with eV sterile neutrino in addition to flux model inefficiency. Similarly, the GALLEX and SAGE Gallium solar neutrino experiments reported deficit in ν_e events during calibration processes with radioactive sources[100, 101].

While the Planck cosmological data is consistent with no sterile neutrino[102], it does not completely rule out massive sterile neutrinos with small mixing angles. Oscillation experiments are still promising way to search for eV sterile neutrinos.

2.2.3 3+1 sterile neutrino model

If eV scale sterile neutrinos indeed exist, we might be able to discover them through neutrino oscillation experiments. As motivated by the results of LSND and subsequent sterile oscillation searches, we focus on the simplest 3+1 sterile neutrino model with $\Delta m_{41}^2 \lesssim 1\text{eV}^2$. This is a good approximation of the general 3+N models with one eV scale sterile neutrino and multiple heavy sterile neutrinos ($>\text{keV}$) in Sec. 2.2.1, where we can only see the spectral distortions due to additional m_4 (unless the heavy neutrinos constitute another $\Delta m^2 \lesssim 1\text{eV}^2$ which is very unlikely). In the future we may extend our study to 3+2 or any 3+N model which has more oscillation parameters and needs extra care on treating different combinations/scenarios.

In the 3+1 model, the flavor state ν_α would be written as a superposition of four mass states ν_i , where ν_4 is the sterile neutrino with mass m_4 . The transformation requires a 4×4 unitary matrix similar to the PMNS matrix. We use the

parameterization in [103] to decompose the matrix into constituent mixing angles:

$$\begin{aligned}
U_{3+1} &= \begin{bmatrix} U_{e1} & U_{e2} & U_{e3} & U_{e4} \\ U_{\mu1} & U_{\mu2} & U_{\mu3} & U_{\mu4} \\ U_{\tau1} & U_{\tau2} & U_{\tau3} & U_{\tau4} \\ U_{s1} & U_{s2} & U_{s3} & U_{s4} \end{bmatrix} \\
&= \begin{bmatrix} 1 & 0 & 0 & 0 \\ 0 & 1 & 0 & 0 \\ 0 & 0 & c_{34} & s_{34} \\ 0 & 0 & -s_{34} & c_{34} \end{bmatrix} \begin{bmatrix} 1 & 0 & 0 & 0 \\ 0 & c_{24} & 0 & s_{24}e^{-i\delta_{24}} \\ 0 & 0 & 1 & 0 \\ 0 & -s_{24}e^{i\delta_{24}} & 0 & c_{24} \end{bmatrix} \begin{bmatrix} c_{14} & 0 & 0 & s_{14}e^{-i\delta_{14}} \\ 0 & 1 & 0 & 0 \\ 0 & 0 & 1 & 0 \\ -s_{14}e^{i\delta_{14}} & 0 & 0 & c_{14} \end{bmatrix} \\
&\quad \begin{bmatrix} 1 & 0 & 0 & 0 \\ 0 & c_{23} & s_{23} & 0 \\ 0 & -s_{23} & c_{23} & 0 \\ 0 & 0 & 0 & 1 \end{bmatrix} \begin{bmatrix} c_{13} & 0 & s_{13}e^{-i\delta_{13}} & 0 \\ 0 & 1 & 0 & 0 \\ -s_{13}e^{i\delta_{13}} & 0 & c_{13} & 0 \\ 0 & 0 & 0 & 1 \end{bmatrix} \begin{bmatrix} c_{12} & s_{12} & 0 & 0 \\ -s_{12} & c_{12} & 0 & 0 \\ 0 & 0 & 1 & 0 \\ 0 & 0 & 0 & 1 \end{bmatrix}, \tag{2.26}
\end{aligned}$$

where δ_{13} is the usual δ_{CP} in the 3-flavor case. In addition to three new sterile mixing angles θ_{14} , θ_{24} and θ_{34} , there are also two new CP phases δ_{14} and δ_{24} . In accelerator experiments like T2K, we are mostly sensitive to θ_{24} and θ_{34} but not the sterile CP phases. Also, from solar and reactor neutrino analysis [104], $\sin^2 \theta_{14} = |U_{e4}|^2 < 0.041$ at 90% CL. We may conveniently set $\theta_{14} = \delta_{14} = \delta_{24} = 0$ and simplify the sterile

mixing matrix to

$$U_{3+1} = \begin{bmatrix} c_{12}c_{13} & c_{13}s_{12} & s_{13}e^{-i\delta_{13}} & 0 \\ -c_{23}c_{24}s_{12} - c_{12}c_{24}s_{13}s_{23}e^{i\delta_{13}} & c_{12}c_{23}c_{24} - c_{24}s_{12}s_{13}s_{23}e^{i\delta_{13}} & c_{13}c_{24}s_{23} & s_{24} \\ s_{12}(c_{34}s_{23} + c_{23}s_{24}s_{34}) & -c_{12}(c_{34}s_{23} + c_{23}s_{24}s_{34}) & c_{13}(c_{23}c_{34} - s_{23}s_{24}s_{34}) & c_{24}s_{34} \\ -c_{12}s_{13}(c_{23}c_{34} - s_{23}s_{24}s_{34})e^{i\delta_{13}} & -s_{12}s_{13}(c_{23}c_{34} - s_{23}s_{24}s_{34})e^{i\delta_{13}} & -c_{13}(c_{23}s_{34} + c_{34}s_{23}s_{24}) & c_{24}c_{34} \\ s_{12}(-s_{23}s_{34} + c_{23}c_{34}s_{24}) & c_{12}(s_{23}s_{34} - c_{23}c_{34}s_{24}) & & \\ +c_{12}s_{13}(c_{23}s_{34} + c_{34}s_{23}s_{24})e^{i\delta_{13}} & +s_{12}s_{13}(c_{23}s_{34} + c_{34}s_{23}s_{24})e^{i\delta_{13}} & & \end{bmatrix}. \quad (2.27)$$

The oscillation probability can be calculated by the same formula in Eq. 2.9, with U replaced by U_{3+1} and raise the summation limit from $i = 3$ to $i = 4$.

In T2K, we are interested in 3 probability values: $P(\nu_\mu \rightarrow \nu_\mu)$, $P(\nu_\mu \rightarrow \nu_e)$ and $1 - P(\nu_\mu \rightarrow \nu_s)$, where ν_s may be regarded as a ‘‘sterile flavor state’’.

The survival probability $P(\nu_\mu \rightarrow \nu_\mu)$ strongly affects the muon neutrino disappearance samples. Eq. 2.28 shows $P(\nu_\mu \rightarrow \nu_\mu)$ in an approximated form. With non-zero θ_{24} , the overall Δm_{31}^2 oscillation amplitude would be reduced, and it’s in principle possible to probe the value of Δm_{41}^2 from the fast oscillation.

$$P_{\mu\mu} \approx 1 - \sin^2 2\theta_{23} \cos 2\theta_{24} \sin^2 \frac{\Delta m_{31}^2 L}{4E} - \sin^2 2\theta_{24} \sin^2 \frac{\Delta m_{41}^2 L}{4E} \quad (2.28)$$

As an illustration, Fig. 2.9 shows $P(\nu_\mu \rightarrow \nu_\mu)$ at the T2K-SK baseline $L = 295$ km with and without sterile neutrino, where $\Delta m_{41}^2 = 0.1\text{eV}^2$ and $\sin^2 \theta_{24} = 0.2$.

The transition probability $P(\nu_\mu \rightarrow \nu_e)$ impacts the ν_e appearance samples. The oscillation amplitude is reduced a bit with non-zero θ_{24} , as shown in Eq. 2.29 and Fig. 2.10.

$$P_{\mu e} \approx \sin^2 2\theta_{13} \cos^2 \theta_{24} \sin^2 \theta_{23} \sin^2 \frac{\Delta m_{31}^2 L}{4E}. \quad (2.29)$$

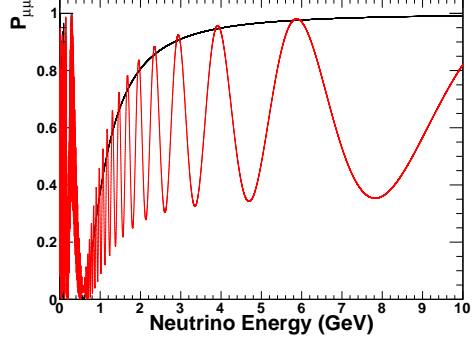


Figure 2.9: The disappearance probability $P(\nu_\mu \rightarrow \nu_\mu)$ as a function of neutrino energy at 295 km. The black line shows that standard 3-flavor result, while the red line shows the sterile one with $\Delta m_{41}^2 = 0.1 \text{eV}^2$ and $\sin^2 \theta_{24} = 0.2$.

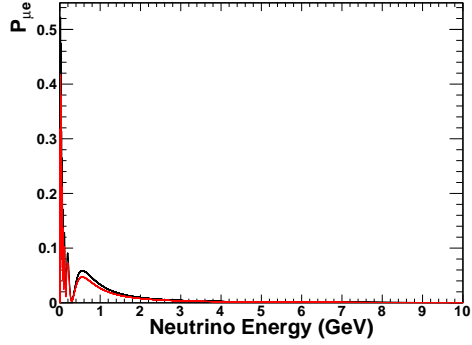


Figure 2.10: The appearance probability $P(\nu_\mu \rightarrow \nu_e)$ as a function of neutrino energy at 295 km. The black line shows that standard 3-flavor result, while the red line shows the sterile one with $\Delta m_{41}^2 = 0.1 \text{eV}^2$ and $\sin^2 \theta_{24} = 0.2$.

The probability $1 - P(\nu_\mu \rightarrow \nu_s) = P(\nu_\mu \rightarrow \nu_\mu) + P(\nu_\mu \rightarrow \nu_e) + P(\nu_\mu \rightarrow \nu_\tau)$ measures the total amount of all three active neutrinos that are not oscillated into sterile neutrino. It is possible to measure this probability with the neutral current (NC) interaction samples as active neutrinos shall interact at the same rate. Any deficit in such samples may be inferred as the sign of sterile neutrino oscillation. As shown in Eq. 2.30, two oscillation modes can be seen (similar to $P(\nu_\mu \rightarrow \nu_\mu)$). An

important reason to consider this probability is that it is a channel sensitive to θ_{34} .

$$1 - P(\nu_\mu \rightarrow \nu_s) \approx 1 - \sin^2 \theta_{34} \sin^2 2\theta_{23} \sin^2 \frac{\Delta m_{31}^2 L}{4E} - \cos^2 \theta_{34} \sin^2 2\theta_{24} \sin^2 \frac{\Delta m_{41}^2 L}{4E}. \quad (2.30)$$

Fig. 2.11 shows how the sterile neutrino might change the oscillation pattern.

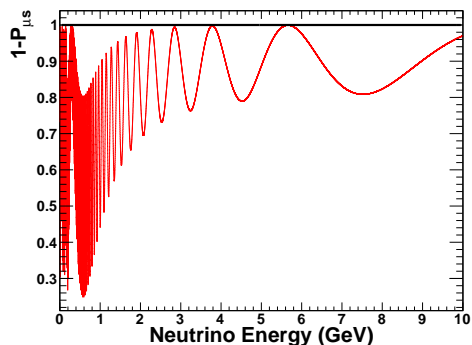


Figure 2.11: The overall active neutrino survival probability $1 - P(\nu_\mu \rightarrow \nu_s)$ as a function of neutrino energy at 295 km. The black line shows that standard 3-flavor result, while the red line shows the sterile one with $\Delta m_{41}^2 = 0.1\text{eV}^2$, $\sin^2 \theta_{24} = 0.1$ and $\sin^2 \theta_{34} = 0.5$.

In order to constrain θ_{24} and θ_{34} , it is preferable to measure multiple oscillation probabilities at the same time. T2K provides a suitable environment for such measurement because of the rich sets of oscillation samples available at the far detector SK.

Chapter 3

The T2K experiment

The T2K (Tokai-to-Kamioka) experiment is a long baseline accelerator neutrino oscillation experiment in Japan (Fig. 3.1). A high intensity muon neutrino beam is produced by a 30 GeV proton beam hitting a graphite target, inside the J-PARC facility in Tokai (Ibaraki Prefecture, east Japan). The neutrino beam is first measured by a set of near detectors at 280 m to determine the non-oscillated neutrino flux and interaction cross-sections. Then the far detector Super-Kamiokande (SK) at Kamioka detects the oscillated neutrino events at 295 km away.

The neutrino beam is tuned in an off-axis configuration that its peak energy 0.6 GeV is at the first minimum of the ν_μ survival probability at 295 km. This allows an accurate measurement of $\sin^2 \theta_{23}$ and Δm_{32}^2 with the ν_μ disappearance samples. The ν_e appearance samples also give us some sensitivity on $\sin^2 \theta_{13}$ and δ_{CP} . There are oscillation samples based on neutral current event selections as well, but they are not used in standard oscillation analysis because of the lack of sensitivities on the 3-flavor oscillation parameters.

In the following, we describe in more details the T2K configuration, including

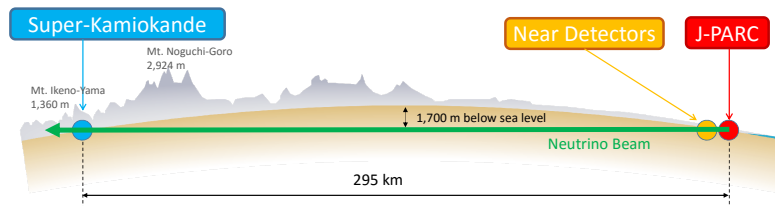


Figure 3.1: A schematic diagram of the T2K experiment (Figure taken from [18]).

the neutrino beamline in Sec. 3.1, the two near detectors in Sec. 3.2, and the far detector SK in Sec. 3.3. A brief description of the neutrino event generator, NEUT, is provided in Sec. 3.4.

3.1 Neutrino beamline at J-PARC

3.1.1 Proton beamline

J-PARC (Japan Proton Accelerator Research Complex) is a multi-purpose facility that makes use of high-intensity proton beam to generate various secondary particle beams for a wide range of scientific purposes. The proton beam consists of three parts: a linear accelerator (LINAC), a rapid-cycling synchrotron (RCS) and a main ring (MR) (Fig. 3.2). The 330 m long LINAC accelerates negative hydrogen ions H^- to 181 MeV and injects into the RCS. Upon injection, the RCS converts H^- to protons by a charge-stripping foil, and accelerates them to 3 GeV at 25 Hz repetition

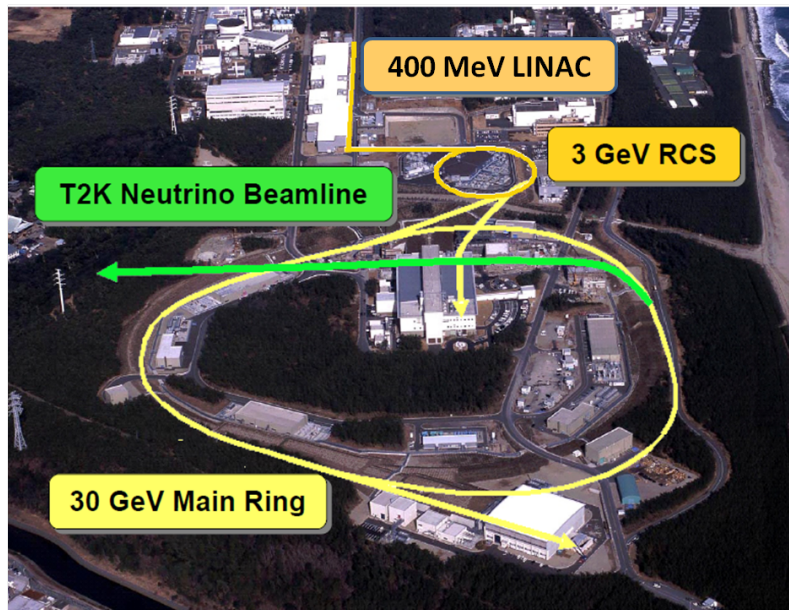


Figure 3.2: The J-PARC proton beamline (copyright J-PARC).

rate and two bunches per cycle. About 5% of these bunches are further sent to the MR for acceleration up to 30 GeV. For the neutrino beamline, a single extraction of protons, known as a “spill”, happens at a frequency of 0.5 Hz. Each spill spans over $5 \mu\text{s}$, which contains 8 proton bunches of length 100 ns separated from each other by 560 ns. This narrow spill width helps reducing the detector background rate by a factor of 10^5 .

3.1.2 Neutrino beamline

The neutrino beamline (Fig. 3.3) is further divided into two sequential sections: primary and secondary beamlines. The primary beamline bends the proton beam towards the direction of Kamioka and focuses it at the target by a set of normal and superconducting magnets. Beam monitors are installed along the beamline to examine the beam intensity, profile and loss during operation.

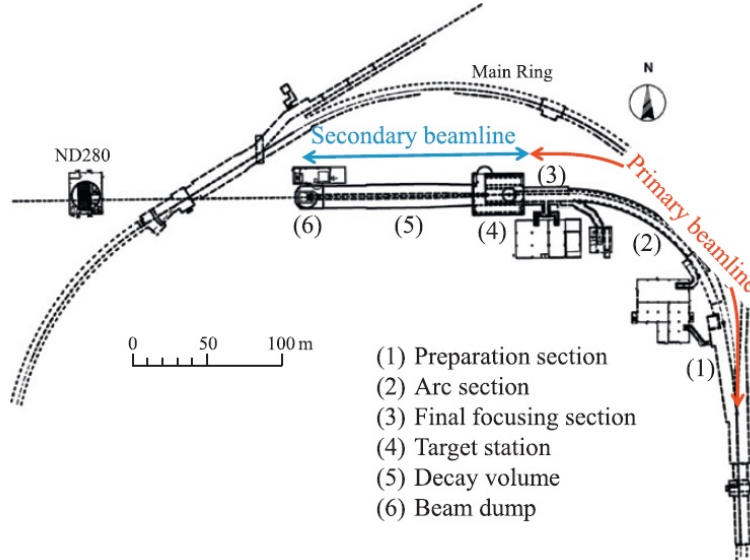


Figure 3.3: Overview of the T2K neutrino beamline (Figure taken from [18]).

In the secondary beamline, protons hit the graphite target to produce mostly secondary pions (and few kaons). Right after the targets, there are three magnetic horns that guide the pions into a decay volume. The horns are powered by a 250 kA pulsed current which can be either positive or negative. The +250 kA “Forward Horn Current” (FHC) is used to focus π^+ and produce mostly ν_μ beam:

$$\pi^+ \rightarrow \mu^+ + \nu_\mu.$$

The -250 kA “Reverse Horn Current” (RHC), on the other hand, focuses π^- and produces mostly $\bar{\nu}_\mu$ beam:

$$\pi^- \rightarrow \mu^- + \bar{\nu}_\mu.$$

Fig. 3.4 illustrates that when the horns are operated at 250 kA, a maximum magnetic field of 1.7 T is generated and increases the neutrino flux at SK by a factor of ~ 17 at the peak energy.

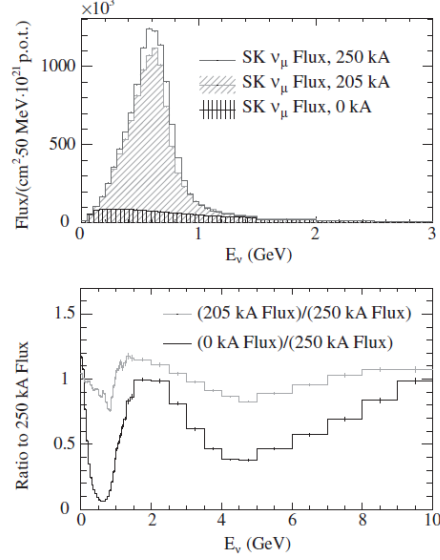


Figure 3.4: The predicted ν_μ flux at SK for operation at different horn currents. Top shows the flux histogram from 0 to 3 GeV, bottom shows the ratios from 0 to 10 GeV (Figure taken from [19]).

At the end of the decay volume, there is a beam dump that made up of thick layers of graphite and iron. While neutrinos can go through it easily, hadrons and low energy muons are stopped. Muons with momentum above ~ 5.0 GeV, however, can pass through the beam dump and reach the muon monitor. The muon monitor is used to measure the muon distribution profile. Based on the knowledge of two-body decay into muon and neutrino, the neutrino beam intensity and direction can be deduced from the muon kinematics on a bunch-by-bunch basis.

The intense proton beam inevitably produces some unwanted contaminations. For example, in the FHC mode, interactions like

$$K^+ \rightarrow \pi^0 + e^+ + \nu_e$$

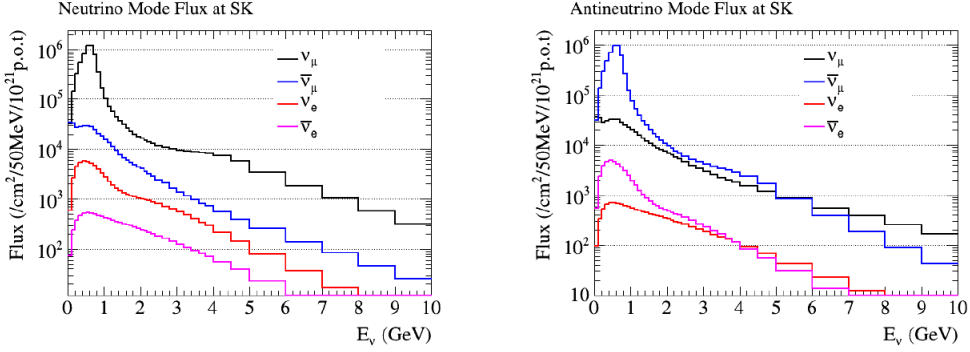


Figure 3.5: The T2K unoscillated neutrino flux prediction at SK for the neutrino (left) and antineutrino (right) modes (Figure taken from [20]).

and

$$\mu^+ \rightarrow e^+ + \nu_e + \bar{\nu}_\mu$$

exist. The $\nu_\mu/\bar{\nu}_\mu$ flux and $\nu_e/\bar{\nu}_e$ contaminations are more precisely measured at the near detectors. Fig. 3.5 shows the predicted neutrino and antineutrino flux at the far detector.

3.1.3 Off-axis beam configuration

Interestingly, the neutrino beam is not pointing exactly towards the far detector (and one of the near detectors), but at an off-axis angle of 2.5° . This off-axis angle is used to tune the peak energy and the width of the neutrino beam.

From relativistic kinematics, the neutrino energy E_ν from a two-body $\pi \rightarrow \mu + \nu_\mu$ decay is related to the pion momentum p_π , pion mass m_π and muon mass m_μ by:

$$E_\nu = \frac{m_\pi^2 - m_\mu^2}{2(\sqrt{p_\pi^2 + m_\pi^2} - p_\pi \cos \theta)}, \quad (3.1)$$

where θ is the neutrino emission angle relative the pion direction. Given a fixed p_π , increasing θ reduces the outgoing E_ν . Also, by differentiating Eq. 3.1 with respect

to p_π , there is an upper bound of E_ν that can be obtained for non-zero θ , where:

$$p_\pi^{\max} = \frac{m_\pi \cos \theta}{\sin \theta}, \quad (3.2)$$

$$E_\nu^{\max} = \frac{m_\pi^2 - m_\mu^2}{2m_\pi \sin \theta}. \quad (3.3)$$

The existence of upper bound thus narrows the E_ν distribution with respect to zero off-axis angle.

Fig. 3.6 shows the unoscillated neutrino flux predicted at SK, comparing the spectra at three different off-axis angles. Although the total neutrino flux is reduced, the choice of the 2.5° off-axis angle shifts the neutrino energy peak to 0.6 GeV and makes the spectrum much narrower which maximizes our sensitivity to measured oscillation parameters.

3.1.4 Neutrino flux simulation

The neutrino flux simulation is done in three parts.

First, the primary interaction between the proton beam and the graphite target is simulated by FLUKA[105], which agrees the best with external hadron production data. Protons of 30 GeV are pointed to the target based on the measured proton beam spatial distribution and divergence. All interactions and secondary particles are tracked until they leave the target region.

Next, the particles are input into a GEANT3[106] simulation code called JNU-BEAM, with hadronic interactions modeled by GCALOR[107, 108]. The particles are propagated through the horns, where they are affected by the magnetic field and may interact with the horn material, then through the decay volume until they inte-

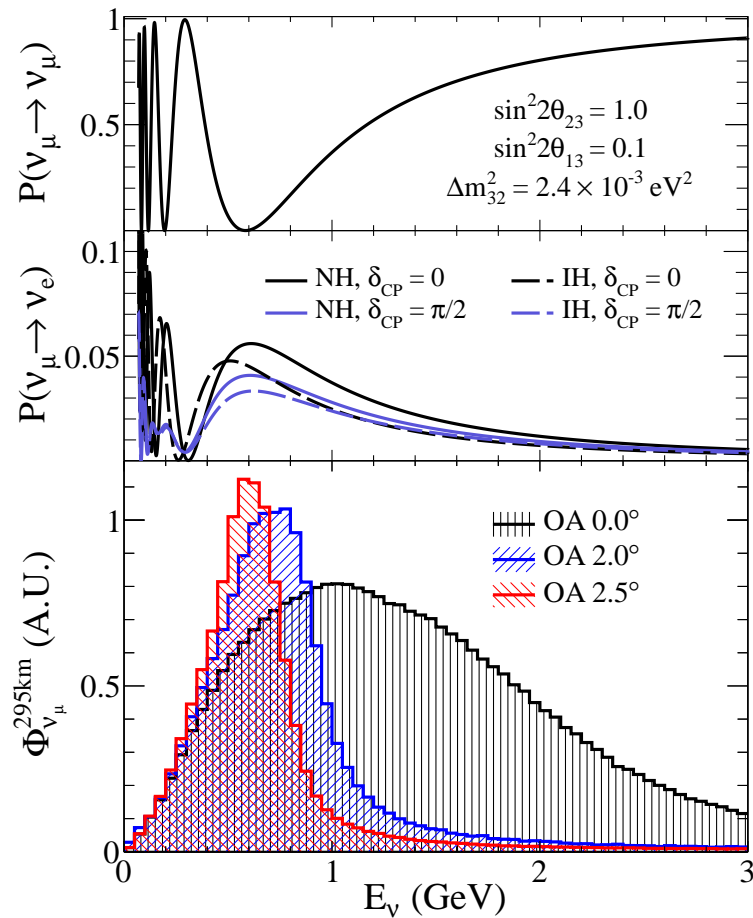


Figure 3.6: The predicted neutrino flux at SK without oscillation at an off-axis angle 0.0° (black), 2.0° (blue) and 2.5° respectively (red). The y-axis units are different among three angles. On the top and bottom shows $P(\nu_\mu \rightarrow \nu_\mu)$ and $P(\nu_\mu \rightarrow \nu_e)$ at 295km (Figure taken from [19]).

ract or decay. When a neutrino is produced, it is forced to point to the direction of SK or a random point in the near detector plane. The neutrino event information is stored, and the probability of pointing to that direction is saved as an event weight.

Finally, an event-by-event reweighting process is applied to all neutrino events, which incorporates various hadron production datasets, including the NA61/SHINE measurements on charged pion and kaon[109–111]. NA61/SHINE (SPS Heavy ion and Neutrino physics Experiment) at the CERN SPS (Super Proton Synchrotron) makes use of a 2 cm “thin target” and the 90 cm “T2K replica target” delivered by the T2K Collaboration to measure the production cross-section of secondary particles. The reweighting process properly corrects the production rates of secondary pions and kaons at target materials, and their subsequent interaction rates which may further produce tertiary hadrons or attenuate hadrons that decay to neutrino. The neutrino flux and energy spectrum are obtained by summing the events with the assigned event weights.

3.2 Near detector complex

The neutrino beam is first measured by two near detectors at 280 m from the proton target: INGRID and ND280. This baseline is short compared to the 3-flavor oscillation length, so we assume the measurements are on the unoscillated beam that can be used to constrain the neutrino flux and interaction models. The two detectors are situated in a pit of depth 37 m (Fig. 3.7).

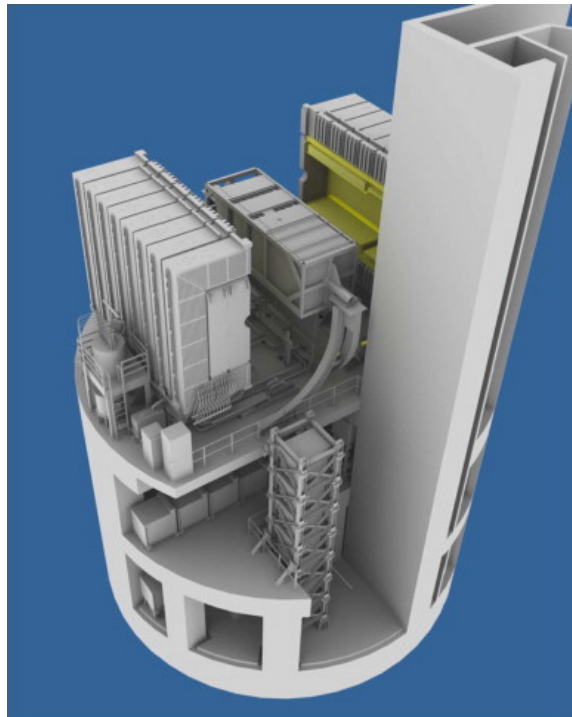


Figure 3.7: The near detector complex. The on-axis INGRID modules are located on the bottom two levels, while the off-axis ND280 detector is on the upper level (Figure taken from [18]).

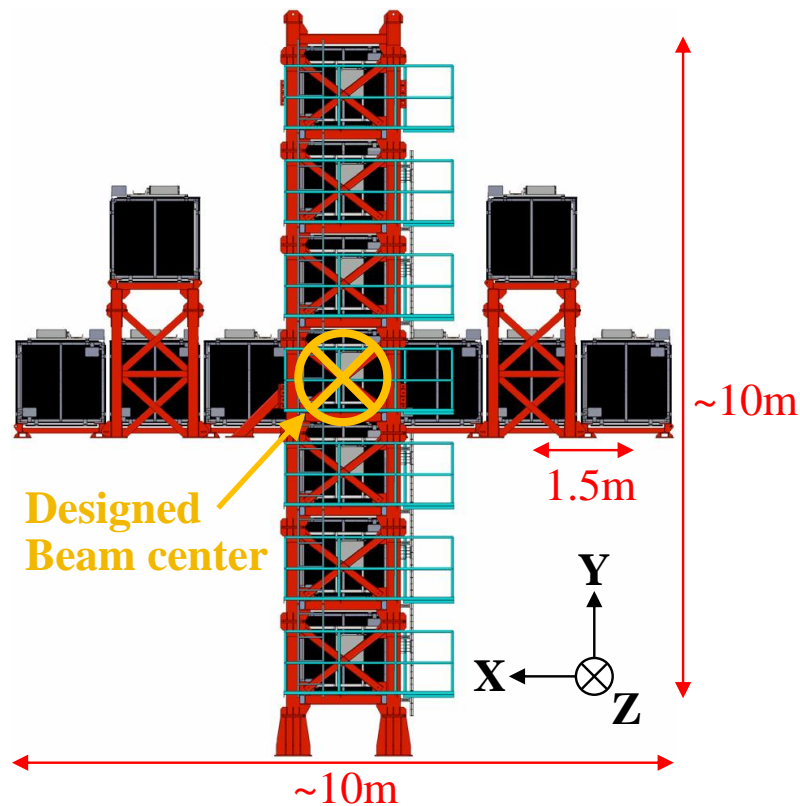


Figure 3.8: INGRID on-axis detector (Figure taken from [18]).

3.2.1 INGRID

INGRID (Interactive Neutrino GRID) is an array of iron/scintillator detectors that is set on the center of the neutrino beam axis. The purpose of this on-axis detector is to measure precisely the neutrino beam direction and intensity with the large statistics of interaction events in iron. The beam center can be measured with a precision better than 10 cm, which correspond to an angular precision of 0.4 mrad.

As shown in Fig. 3.8, the INGRID detector is composed of 14 identical modules arranged in a cross along the vertical and horizontal axes. The center of the cross, with two overlapping modules, sits at the center of the beam. There are also two separate modules located at off-axis directions to measure the beam axial symmetry.

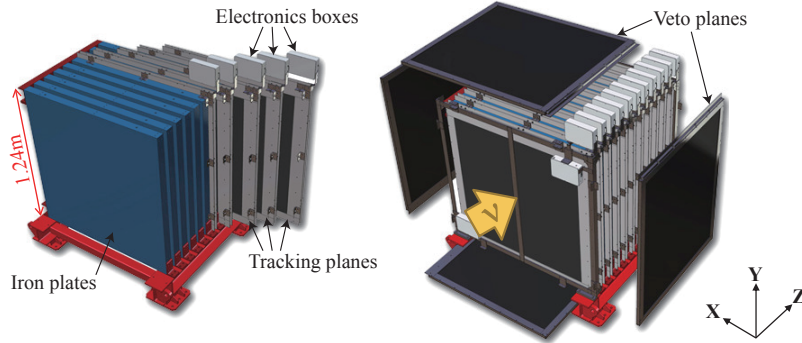


Figure 3.9: An INGRID module. On the left shows the tracking planes and iron plates, on the right shows the veto planes (black) (Figure taken from [18]).

In an INGRID module (Fig. 3.9), there are nine iron plates and 11 tracking scintillator planes arranged in a sandwich structure. Interactions outside the module are rejected by the surrounding veto scintillator planes. The modules are calibrated by cosmic ray, both on the ground surface and the ND280 pit underground.

In between the vertical and horizontal modules, there is an extra Proton Module that efficiently detects the muons and protons produced in neutrino interactions, especially in the quasi-elastic channel that can be compared with Monte Carlo simulations. It consists of scintillator planes but no iron plate so that most neutrino interactions are on a carbon target (see Fig. 3.10). Also, it has finer grain scintillator to improve tracking efficiency.

3.2.2 ND280

ND280 is the primary off-axis detector at the near detector complex. It is a magnetized tracking detector placed exactly on the SK direction. It serves three important purposes. First, it measures the off-axis ν_μ flux for event rate prediction at SK. Second, it determines the beam ν_e content which is a non-reducible background for ν_e appearance search. Third, it measures the ν_μ interaction cross-sections to reduce

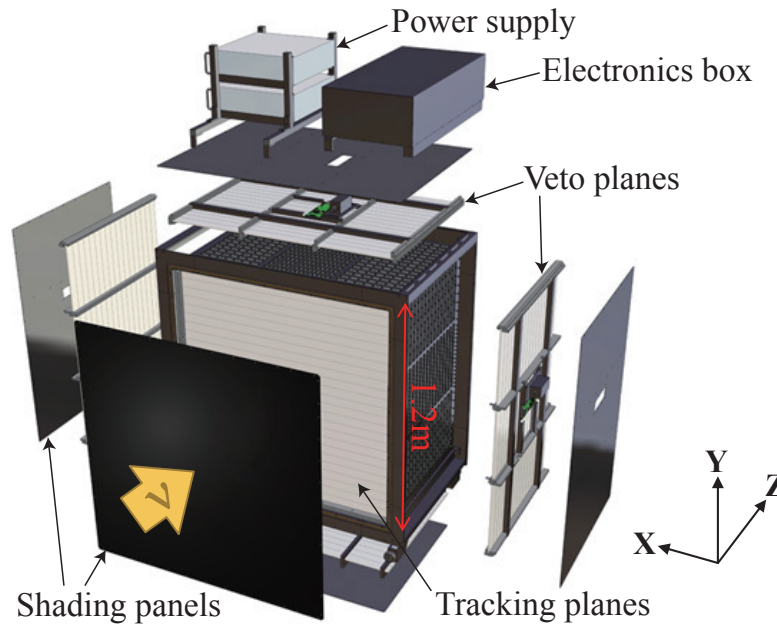


Figure 3.10: The Proton module (Figure taken from [18]).

the errors due neutrino interaction models. To fulfill these purposes, the ND280 detector is designed carefully to reconstruct both the ν_μ and ν_e charged current (CC) and neutral current (NC) interaction events.

The detector is drawn schematically in Fig. 3.11. It consists of the PØD followed by the tracker TPC/FGD sandwich. They are surrounded by a metal frame container called the “basket” and ECalan electromagnetic calorimeter (ECal). The outermost part is a recycled UA1 magnet with scintillator which acts as a side muon range detector (SMRD).

UA1 magnet

ND280 makes use of the old CERN UA1/NOMAD magnet to provide a dipole magnetic field of 0.2 T. This magnetic field bends the trajectory of charged particles and allows the TPC to determine their momenta and signs through measurement of track

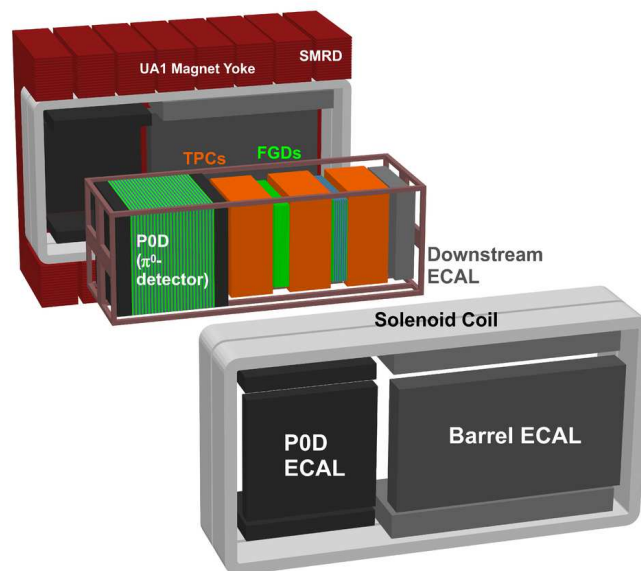


Figure 3.11: An exploded view of the ND280 off-axis detector (Figure taken from [18]).

curvature. The magnet consists of water-cooled aluminum coils and a flux return yoke. The field uncertainty is around 2 G at the nominal field of 0.2 T, helping to reduce the systematic uncertainty of momentum determination down to 2% for charged particles below 1 GeV/c.

P0D

The Pi-zero detector (P0D) is used to measure the rate of the neutral current interaction process with π^0 production,

$$\nu_\mu + N \rightarrow \nu_\mu + N + \pi^0 + X,$$

on a water (H_2O) target which is the same detector material at SK. The π^0 then decays two gammas to give visible signals in the detector. Such NC single π^0 pro-

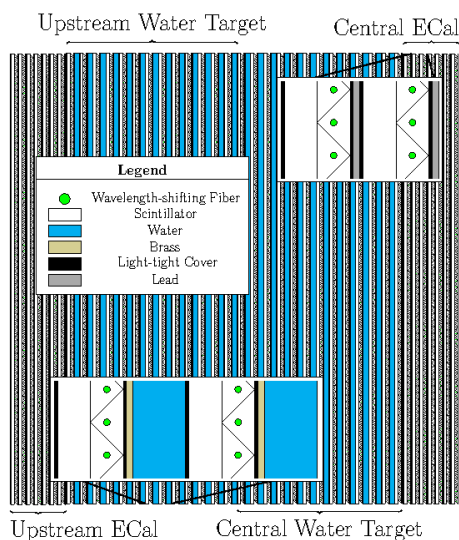


Figure 3.12: A schematic of PØD. The beam is coming from the left to the right (Figure taken from [18]).

duction forms an important background in the ν_e appearance oscillation samples at SK, when only one gamma is reconstructed in the event.

The schematic design of PØD is shown in Fig. 3.12. The central section is composed of planes of scintillator bars interleaved with fillable water target bags and brass sheets. The water target can be filled or emptied, providing a subtraction method to calculate the water cross-sections. The front (upstream ECal) and rear (central ECal) sections are alternating scintillator planes and lead sheets that improves containment of electromagnetic showers and creates a veto region to reject particles entering from interactions outside the PØD.

TPCs

The three time projection chambers (TPCs) are designed to have excellent resolution in charged particle track reconstruction, momentum determination and particle

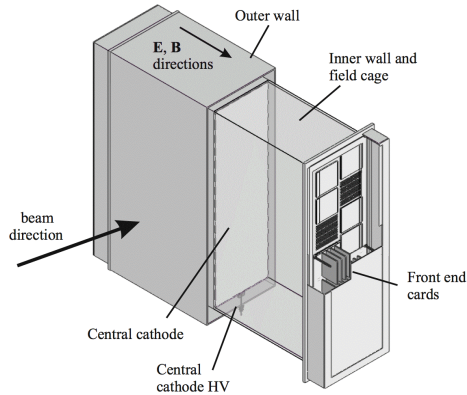


Figure 3.13: Simplified drawing showing the main features of a TPC. The outer dimensions are roughly $2.3 \text{ m} \times 2.4 \text{ m} \times 1.0 \text{ m}$ (Figure taken from [18]).

identification. With these capabilities, they can measure event rate of ν_μ and ν_e in different interaction channels.

A simplified drawing of the TPC is shown in Fig. 3.13. Each TPC uses an argon-based mixture as drift gas, contained in an inner box. The surrounding outer box contains CO_2 as an insulating gas. A uniform electric field is formed by the copper strip pattern on the inner box panels and the central cathode panel, roughly aligned with the magnetic field provided by the UA1 magnet. When charged particles pass through the TPCs, ionization electrons produced drift from the central cathode to one of the readout planes. The readout planes are instrumented with bulk micromegas detectors that multiply and sample the electrons. The pattern and arrival time of the signals can be used to reconstruct the particle trajectory in the active drift volume.

Particle identification in TPCs is facilitated by measuring the energy loss per distance by charged particles in the gas. From Monte Carlo simulation and test beam studies, the relationships between energy loss and momentum for various charged particles are determined. Fig. 3.14 shows, e.g. such distribution for negatively charged particles. With an energy resolution of about 7.8% for minimum ionizing

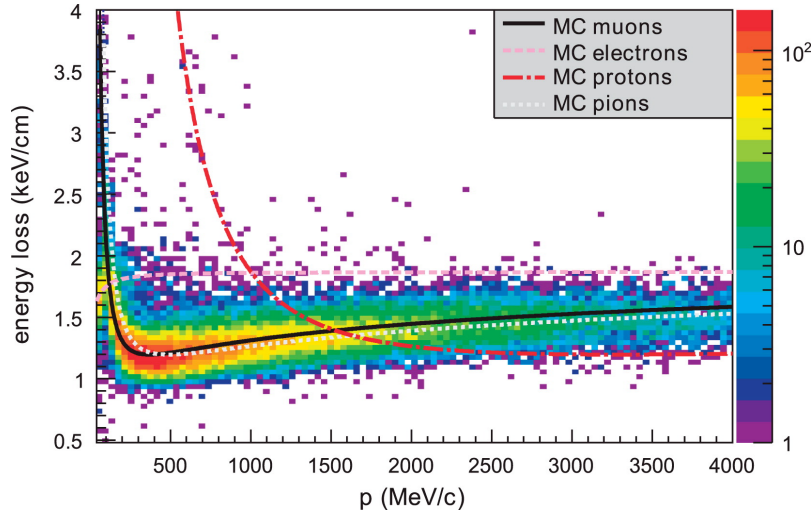


Figure 3.14: Distribution of the energy loss as a function of the momentum in the TPCs for negatively charged particles produced in neutrino interactions, compared to the expected curves for muons, electrons, protons and pions (Figure taken from [21]).

particles (MIPs), the TPCs can identify the particle identity with quite a high accuracy.

FGDs

The two fine grained detectors (FGDs) serve the purposes to provide target mass for neutrino interactions and, at the same time, trajectory reconstruction of charged particles from interaction vertex. The dimensions and weight of target material are the same for the two FGDs: 2300 mm×2400 mm×365 mm and 1.1 tons. However, the first FGD is made up entirely of scintillators (total 5760) which act as both target and tracker, while the second one only contains 2688 scintillator bars, with rest of the space filled by 15 cm thickness of water. By comparing the interaction rates in the two FGDs, cross-section measurements can be done on both carbon and water targets.

ECal

The ND280 ECal that surrounds the inner detectors (PØD, TPCs and FGDs) are electromagnetic calorimeter aiming to reconstruct photons and other high energy particles that exit the inner detector volume. It is made up of plastic scintillator bars as active material and lead absorber sheets between layers to provide a near-hermetic coverage.

According to its usage, the 13 independent ECal modules are classified into 3 types. The six Barrel-ECal modules that surround the tracker volume and the downstream module (Ds-ECal) that covers the downstream exit of the tracker volume are used to extract information for particle identification (electron-muon-pion separation). The six PØD-ECal modules that surround the PØD volume is for detecting gammas that either do not convert in PØD active volume or produce showers only partially contained with PØD. They also confirm the passage of charged tracks, identify MIPs and veto incoming backgrounds that make reconstruction of π^0 easier.

SMRD

The SMRD consists of 440 scintillator modules being inserted into the air gaps inside the UA1 magnet flux return yokes. It measures the momenta of muons at large angles with respect to the beam, triggers cosmic ray muons that enter or penetrate the detector, and identify events that occur in or around the magnet.

3.2.3 ND280 software

The ND280 software structure is shown schematically in Fig. 3.15. In the simulation part, there are interfaces with the neutrino beam simulation and the neutrino

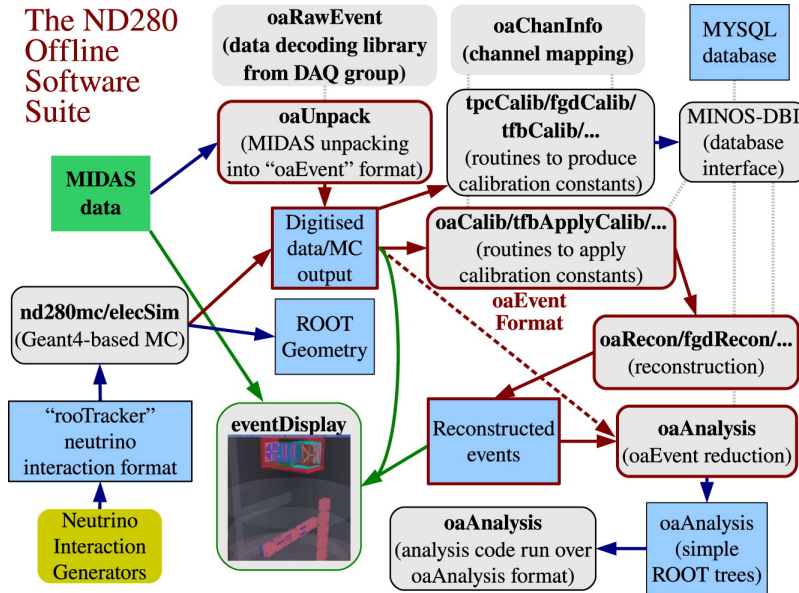


Figure 3.15: Schematic of the package structure of the ND280 Software Suite. Only the most representative packages are shown (Figure taken from [18]).

interaction generation packages to generate events in the ND280 region based on the neutrino flux and the geometry and materials in the detector. A Geant4[112]-based Monte Carlo software is used to simulate the particle interaction inside the detector and also the detector response. For both data and MC, neutrino events are stored in the format of “oaEvent” and pass through reconstruction processes under the framework of RecPack toolkit[113]. The full event information in the oaEvent files is further compiled into the ROOT[114] object “tree”, making it easier for end-users to perform analysis.

3.2.4 BANFF fit

The BANFF fit is a fit to ND280 data to constrain the neutrino flux and cross-section uncertainties propagated to the oscillation analysis, developed by the Beam And ND280 Flux extrapolation task Force (BANFF). The fit is done in two steps.

First, the priors for flux and cross-section model parameters are calculated based on external data, and beam data from proton beam monitors and INGRID. Then, a maximum likelihood fit is performed on selected ND280 samples to constrain the flux and cross-section uncertainties.

The use of external data to extract priors of cross-section parameters is necessary because the ND280 measurements do not cover the full phase spaces of the cross-section models, and do not provide enough information on the kinematics of secondary tracks, especially charged and neutral pions. MiniBooNE[115] and MINER ν A[116] data are appropriate choices because they span similar neutrino energies on carbon-like targets.

A number of ND280 samples are chosen to measure the observed muon momentum and cosine of muon angle. In neutrino beam mode, the ν_μ samples are divided into CC0 π , CC1 π and CCOther. In anti-neutrino mode, there are $\bar{\nu}_\mu$ CC 1-Track and CC N-Track samples, and also ν_μ CC 1-Track and CC N-Track samples to study the ν_μ contamination.

The parameterizations of the flux and cross-section uncertainties are described detailedly in Sec. 5.3.

3.3 Far detector Super-Kamiokande

Super-Kamiokande (SK) is the world's largest land-based, 50kton water Cherenkov detector located deep under Mt. Ikenoyama, Gifu Prefecture, Japan. The mean rock overburden is around 1000 m (2700 m water-equivalent) which reduces the cosmic ray background by a factor of 10^5 . SK is 295 km west of the neutrino beam source in J-PARC and acts as the far detector in the T2K experiment.

Since its operation in 1996, SK has been running stably through four data-taking periods SK-I to IV, and T2K takes place in SK-IV period. In addition to accelerator produced-neutrinos, SK has also released numerous important results on measuring the proton decay lifetime, atmospheric and solar neutrino oscillations, and dark matter searches. Such rich scientific results can be credited to SK's extremely large detector size and satisfactory photo-coverage achieved with 13000 photomultiplier tubes (PMTs).

3.3.1 Cherenkov radiation

When charged particle travels faster than speed of light in water (refractive index $n_w = 1.34$),

$$v \geq \frac{c}{n_w}, \quad (3.4)$$

it emits cone of Cherenkov photons which is light shock wave. Charged particles of different masses have their corresponding momentum threshold to emit Cherenkov light. Electrons, muons and charged pions, which are of lighter masses, have smaller momentum thresholds of 0.57 MeV/c, 118 MeV/c and 156 MeV/c respectively. Proton is much more massive and has a large momentum threshold of 1.07 GeV/c.

The Cherenkov opening angle θ_c is determined by the ratio of photon speed and particle speed in water, i.e.

$$\cos \theta_c = \frac{c}{n_w v} \quad (3.5)$$

For highly relativistic particle, $v \approx c$, we have the characteristic $\theta_c \approx 42^\circ$ in water.

The Cherenkov photons produce a ring-shaped hit pattern when they reach the detector walls. By looking at the time and charge information of the PMT hits, one can deduce variables like event vertex, particle momenta and directions.

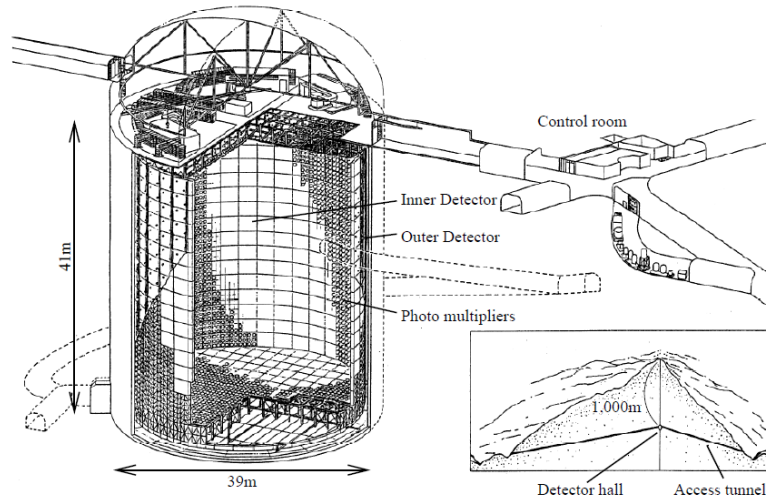


Figure 3.16: A schematic diagram of the SK detector (Figure taken from [22]).

3.3.2 Detector design

The SK detector consists of the inner and outer detectors which are both cylindrical in shape and filled with pure water. Fig. 3.16 gives a schematic diagram of the detector. The inner detector (ID) has a diameter of 33.8 m and a height of 36.2 m which houses 11129 inward-facing 50 cm diameter PMTs. The outer detector (OD) encloses the ID and is about 2 m thicker both radially and on the axis at both ends. The OD contains 1885 outward-facing PMTs of 20 cm diameter mounted on the inner walls. The ID and OD are separated by a 50 cm wide stainless steel scaffolded covered by plastic sheets to ensure optical isolation between ID and OD. The ID wall is lined with black plastic sheets to absorb photons that minimize scattering. The OD walls, on the other hand, are lined with a highly reflective material called Tyvek® which reflects photons and increases their chance of entering OD PMTs.

The ID has a 40% PMT cathode surface coverage, and the PMTs have a combined quantum and collection efficiency of about 20%. This enables the ID to reconstruct a number of physical observables to infer the corresponding neutrino interactions.

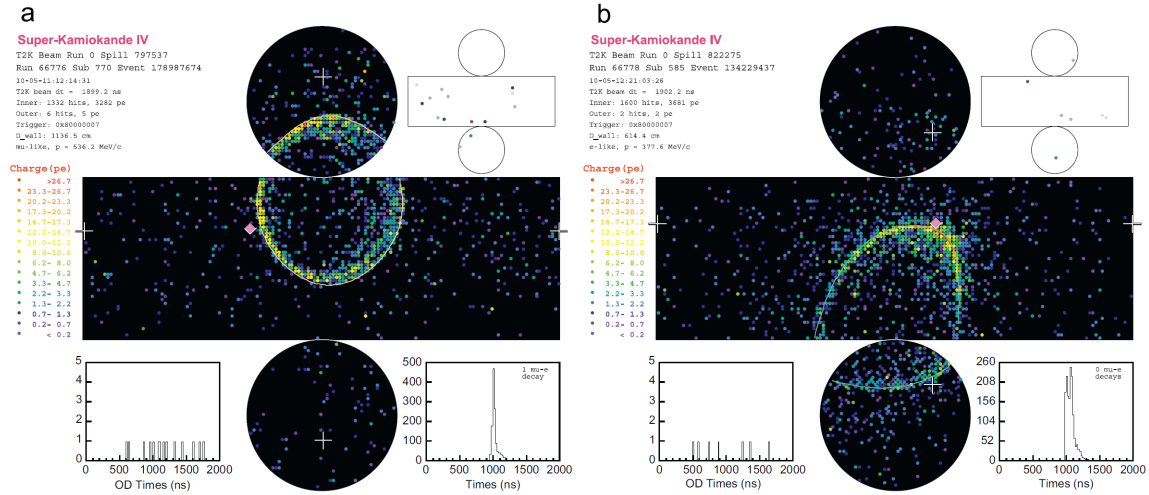


Figure 3.17: Event displays of T2K events in SK for (a) a muon-like ring and (b) an electron-like ring. The cylindrical detector is being unrolled onto a plane. Each colored point represents the charge a PMT hit. The white line shows the reconstructed cone. On the top right corner shows the OD hit map. The white crosses are the location of the reconstructed vertex, and the diamond is the location where a ray from the event vertex would intersect the detector wall if it heads in the direction of the beam (Figure taken from [18]).

Also, the ID is capable of identifying the neutrino flavor in interactions. When ν_μ and ν_e undergo charged current quasi-elastic (CCQE) interaction, they produce muons and electrons respectively. Muons have large mass that travel through the detector almost straightly. This produces a clear, sharp ring pattern of PMT hits. On the contrary, electrons with much lighter mass scatter more easily and produce electromagnetic showers. The resulting Cherenkov light cones displace slightly with respect to each other and produce a “fuzzy” ring pattern on the PMTs. Fig. 3.17 shows the event displays of a “muon-like” and a “electron-like” events due to T2K neutrino beam.

The OD is mostly used for vetoing cosmic ray muons and other backgrounds, and identifies high energy particles that escapes the ID. Also, the 2 m thick of water acts as a shield to attenuate gammas and neutrons from the radioactive decays in

surrounding rock. Due to its sparsely spaced PMTs, the OD cannot perform detailed event reconstruction. Yet, events observed in OD can still be used for different purposes, such as data-MC event rate comparison.

3.3.3 Detector simulator SKDETSIM

SKDETSIM is the full detector simulator of SK that propagates particles across the detector, simulates PMT responses and produces MC digitized PMT hit data. It is a GEANT3 based program in which most hadronic interactions are handled by the GCALOR physics package. The propagation of Cherenkov light is taken by custom package which considers absorption, Rayleigh scattering (symmetric) and Mie scattering (asymmetric, very forward angular distribution), with the model parameters calibrated by laser measurements. The PMT photocathode surfaces are constructed in the detector geometry. When photon reach the PMT surfaces, the PMT responses are simulated with the measured quantum efficiency, gain and other electronic properties. The overall performance of SKDETSIM is checked by comparing with cosmic ray samples, and discrepancy between MC and data is only of percent level.

3.3.4 Detector calibration

To properly describe the data collected in such a large detector, various calibration processes have to been done to understand the detector performance. Here we describe three typical items: PMT, water and energy calibrations.

PMT

There are two gain calibrations for the PMTs: relative and absolute. The relative gain is adjusted by changing the high voltage supply of each PMT so that they give approximately the same responses to a Xe lamp light source. The absolute gain calibration is to determine the conversion factor between the charges collected by the PMTs to the number of incident photo-electrons (p.e.). The calibration source contains nickel wires that capture neutrons emitted from a ^{252}Cf neutron source. The process generates low energy gamma rays of 6 - 9 MeV. When placed in the calibration portholes, the source only produces 50 - 80 PMT hits in the whole ID, so each PMT hit is most probably due to one photon. This gives the single photo-electron charge distribution to calibrate the PMT absolute gain.

Another PMT relevant calibration is the relative timing calibration. Since each PMT is connected to the DAQ system with slightly different lengths of cable, the signal time is offset by various amounts. Also, it takes shorter time for strong signals to exceed the detection threshold than the weak signals, this introduces a second timing offset. The calibration uses a diffuser ball to emit uniform light in the center of the tank, and records the time-charge (photon-electron) distributions for all PMTs, which provides information for timing correction.

Finally, daily monitoring of the PMT performance can be done with cosmic ray muon samples. Vertically downward going muons transversing the full length of the ID are selected. Their energy depositions in water are roughly constant of around 2 MeV/cm. The observed charges in the PMTs, after taking into account the light attenuation in water and the PMT acceptance, are fit to measure the water transparency and tune the PMT charge scale (gain).

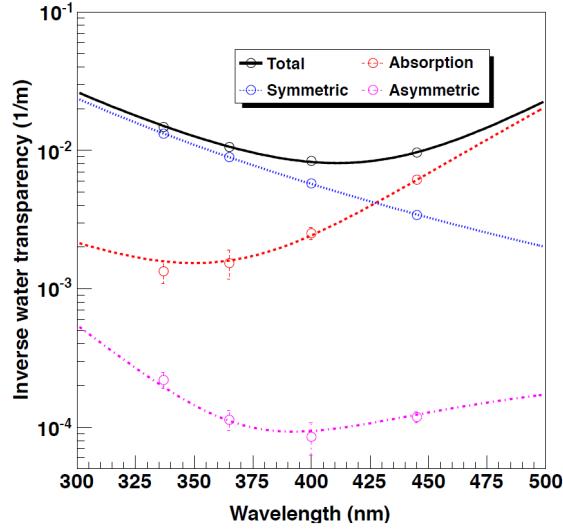


Figure 3.18: Typical fitted water coefficient functions used in SK-MC, which are tuned with data taken in April 2009 (Figure taken from [23]).

Water parameters

There are three parameters describing the light attenuation in water: photon absorption, symmetric scattering due to Rayleigh scattering, and asymmetric scattering due to Mie scattering. The light attenuation length L is a function of wavelength λ which can be described as:

$$L(\lambda) = \frac{1}{\alpha_{abs}(\lambda) + \alpha_{sym}(\lambda) + \alpha_{asy}(\lambda)}, \quad (3.6)$$

where α_{abs} , α_{sym} , α_{asy} are the absorption, symmetric scattering and asymmetric scattering coefficients respectively. While the light attenuation length is also measured by the cosmic muon data, more accurate measurements are performed with a laser source which can give both the wavelength dependency and contributions from each of the three processes. Fig. 3.18 shows a typical result of the measurement of absorption and scattering coefficients.

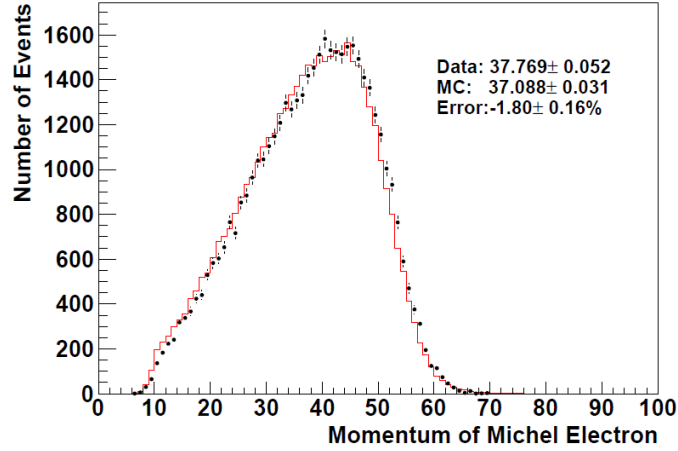


Figure 3.19: Momentum distribution of decay electrons (MeV) for the data (black points) and MC (red) (Figure taken from [24]).

Energy calibration

The momenta (and thus energy) of the detected, charged particles are reconstructed from the PMT collected charges. To better understand the accuracy and uncertainty of the absolute energy scale, different sources of particles with a wide range of energy are used in the calibration study.

The lowest energy source comes from decay electrons (~ 50 MeV/c). Decay electrons are searched in a time window of $1.5 \mu\text{s}$ to $8.0 \mu\text{s}$ after a stopping muon event. Low energy (~ 6 MeV) gamma rays from μ^- capture on a nucleon are rejected by imposing a cut on the number of PMT hits. There are also higher momentum events (~ 70 MeV/c) which are due to μ^- capture on the 1st shell (K-shell) of an oxygen atom. Fig. 3.19 shows the momentum distribution of the decay electrons, in which a good agreement is obtained between data and MC.

The second source is from NC single π^0 events, where the decay $\pi^0 \rightarrow \gamma\gamma$ gives two electron-like rings in the detector. The invariant mass of the π^0 events are

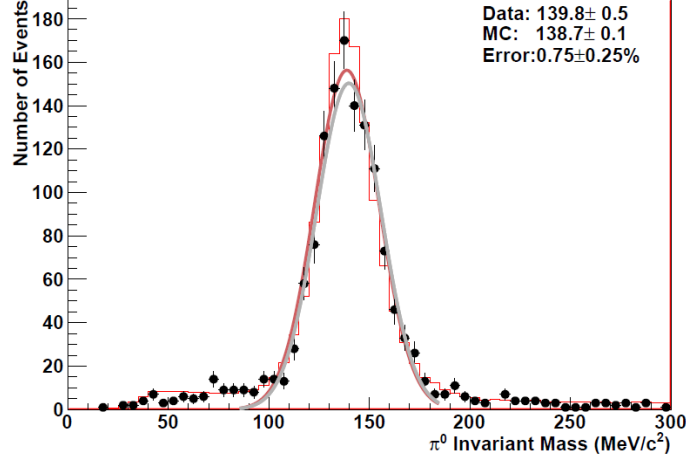


Figure 3.20: Invariant mass distributions of π^0 events for the data (black points) and MC (red). The solid lines show the Gaussian fitting lines (Figure taken from [24]).

reconstructed by the formula:

$$m_{inv} = \sqrt{2p_{\gamma 1}p_{\gamma 2}(1 - \cos \theta)}, \quad (3.7)$$

where $p_{\gamma 1}$ and $p_{\gamma 2}$ are the momenta of the two gamma rays, and θ is the angle between them. The mass distribution is compared with MC prediction (see Fig. 3.20). The difference in Gaussian fitted peak positions estimates the error as $(0.75 \pm 0.25)\%$.

The third source is the low energy stopping muons in the detector ($< 500 \text{ MeV}/c$). For these low energy muons, momentum can also be reconstructed from the Cherenkov opening angle θ_c :

$$p(\theta) = \frac{m}{\sqrt{n_w^2 \cos^2 \theta - 1}}. \quad (3.8)$$

Fig. 3.21 shows the ratios of the nominal reconstructed momentum $p(\text{p.e.})$ to $p(\theta)$ at several $p(\theta)$ bins, both for data and MC. The maximum error is $(-1.905 \pm 0.402)\%$.

The final, highest energy source is the high energy stopping muons (around 1 to

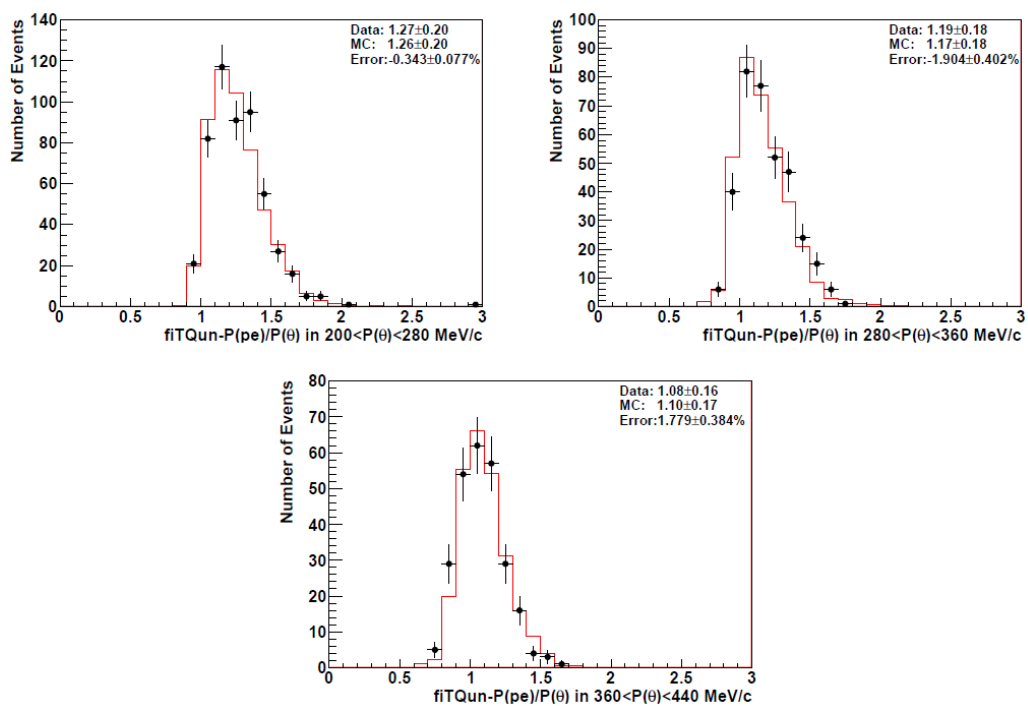


Figure 3.21: Distributions of $p(p.e.)/p(\theta)$ of low energy stopping muons for the data (black points) and MC (red), at three $p(\theta)$ bins: 200 - 280 MeV/c, 280 - 360 MeV/c and 360 - 440 MeV/c (Figure taken from [24]).

10 GeV/c). Downward muon tracks with track length greater than 5 m are selected, in which the track length is approximately proportional to the muon momentum. Fig. 3.22 shows the momentum over range distributions of the data and MC, between the range of 5 m and 35 m in 5 m bins. A momentum loss of ~ 2.2 MeV/c/cm is observed in every bin. The errors are evaluated by comparing the fitted peak positions assuming Gaussian distributions, and are all less than 1%.

The overall absolute energy scale error is defined as the largest error of all the errors described above, which is 1.90%. Meanwhile, time variations of the energy scale are monitored by the decay electrons and momentum over range measurements (see Fig. 3.23). While the momentum over range is almost stable, the decay electron momentum is increasing yearly by $(0.21 \pm 0.03)\%$. A time variation error is assigned as the ratio of the RMS over mean and is 0.88%. The final energy scale error is $\sqrt{(1.90\%)^2 + (0.88\%)^2} = 2.1\%$.

3.3.5 T2K data taking

To record the T2K induced neutrino events, the SK's DAQ system has a trigger in time with the beam spills produced at J-PARC. Each beam spill has a GPS timestamp that is accessible by SK, where the DAQ system defines a software trigger to record all the PMT hit information in a 1 ms time window around the beam arrival time. The spill events are then stored for offline analysis later. Fig. 3.24 shows event timing (ΔT_0) distribution for all categories of events.

An event is triggered if the ID detects ≥ 47 PMT hits in a 200 ns time window, which roughly corresponds to a 5 MeV electron, or the OD detector has ≥ 22 PMT hits in a 200 ns time window. The event includes all the PMT hits within $-5 \sim +35\mu\text{s}$ from the detected trigger timing.

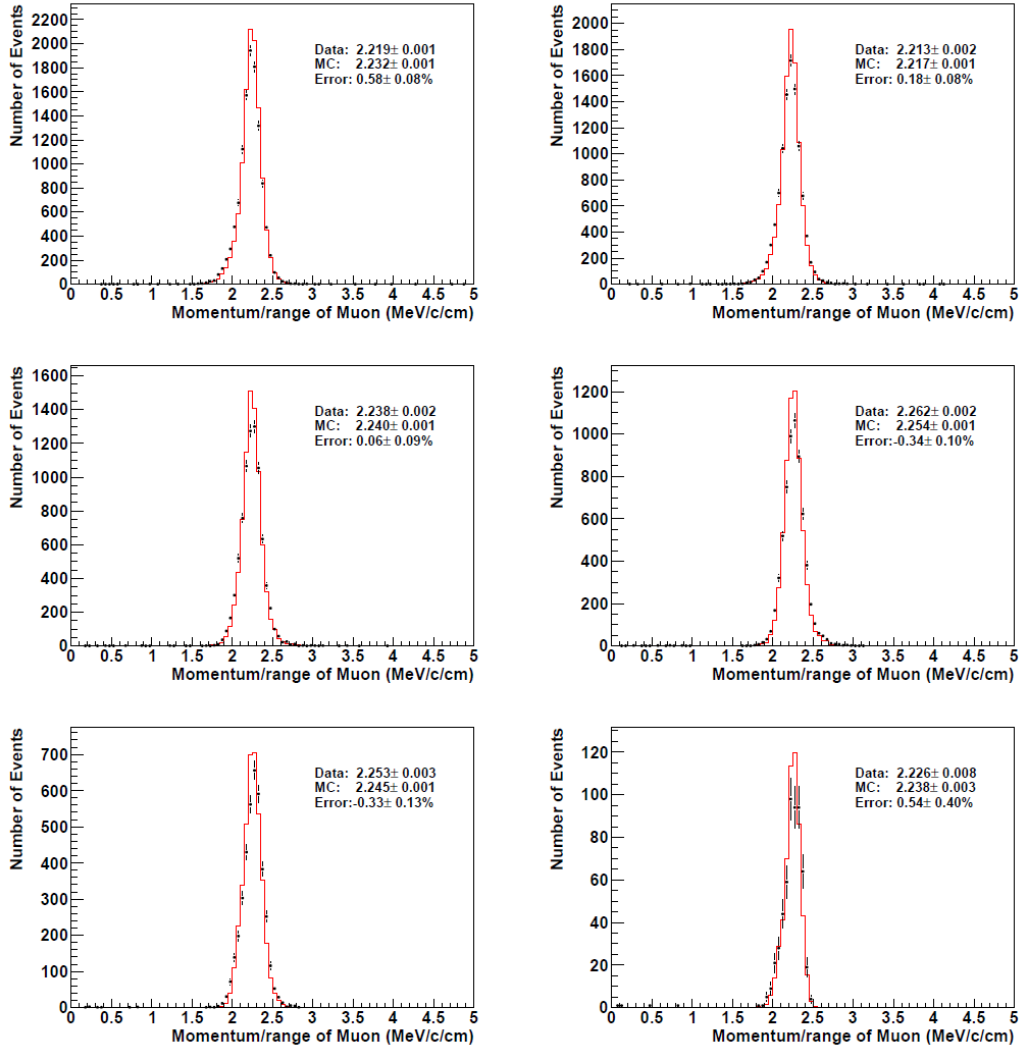


Figure 3.22: Distributions of momentum over range of high energy stopping muons for the data (black points) and MC (red) with various ranges. From the top left to bottom right plots, the ranges are 5 - 10 m, 10 - 15 m, 15 - 20 m, 20 - 25 m, 25 - 30 m and 30 - 35 m respectively (Figure taken from [24]).

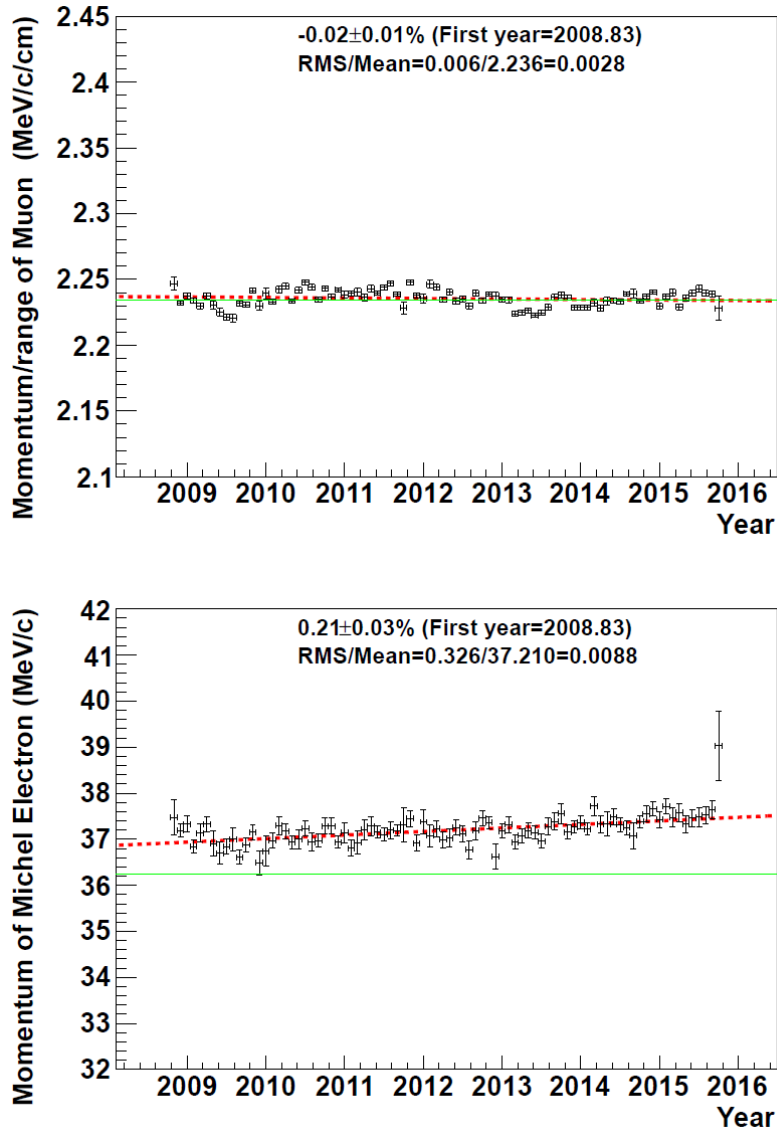


Figure 3.23: Time variations of the momentum over range and momentum of decay electrons. The red dotted lines are linear fit functions, and the green lines are the value of MC (Figure taken from [24]).

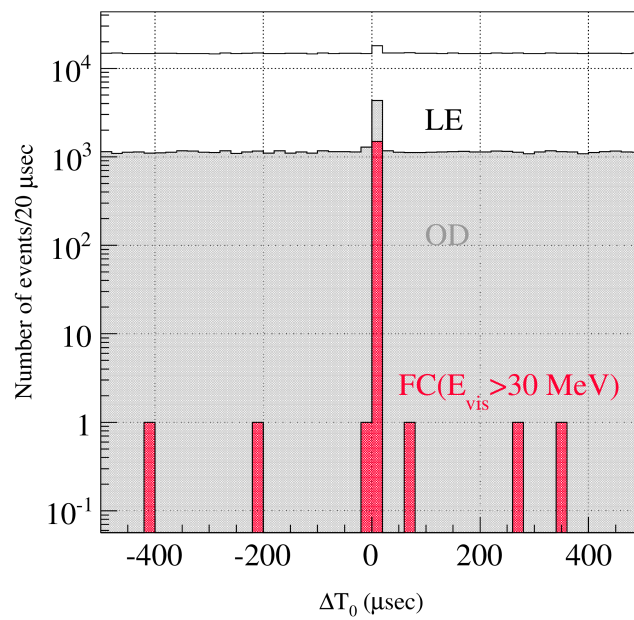


Figure 3.24: ΔT_0 distribution of all FC, OD and LE events within $\pm 500 \mu\text{s}$ around the expected beam arrival time for T2K Run 1-7. The histograms are stacked in that order (Figure taken from [20]).

The T2K events are categorized into three mutually exclusive samples. If OD activities are identified, i.e. number of PMT hits is greater than 15 in the largest OD hit cluster, it is classified as an OD event. Then, low energy (LE) events are extracted if the total charge of ID PMT hits in 300 ns time window is less than 200 p.e., which roughly corresponds to a 20 MeV electron. An event is also classified as LE if a single ID PMT hit constitutes more than half of the total p.e. observed. Such events are usually due to radioactivity near the PMT. Finally, all remaining events are classified as fully contained (FC) events which have Cherenkov light deposited extensively in the ID.

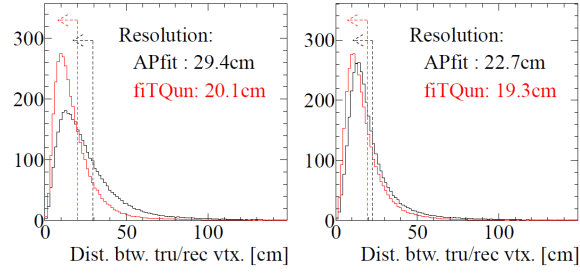
3.3.6 Event reconstruction

The conventional event reconstruction algorithm in SK is called *apfit*, which was developed back in the late 1990's at the beginning of SK operation. The physical properties of a event are reconstructed in a step-by-step process that uses only the time and charge information from hit PMTs.

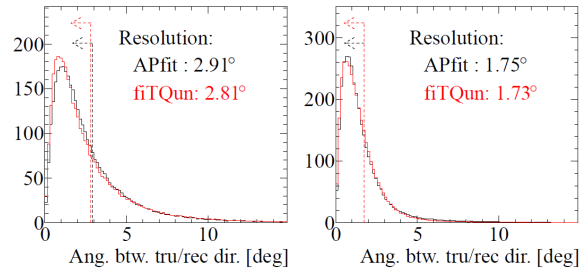
Recently T2K has developed a new fitter called *fitQun*, which employs a maximum likelihood method and uses information from both hit and non-hit PMTs. It has better performance in reconstructing multi-ring events, and dedicated fitters for π^0 and π^+ respectively. Now T2K oscillation samples are gradually switching from *apfit*-based to *fitQun* based reduction. Details of the two reconstruction algorithms can be found in Appendix A.

Comparison between *apfit* and *fitQun* performance

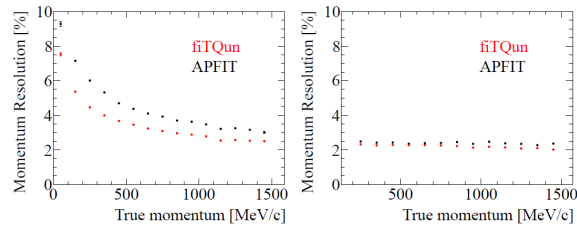
Fig. 3.25 shows the vertex, direction and momentum resolutions compared between *apfit* and *fitQun*, based on SK-IV fully contained atmospheric neutrino MC. Clearly



(a) Single-ring electron (left) and muon (right) vertex resolution.



(b) Single-ring electron (left) and muon (right) direction resolution.



(c) Single-ring electron (left) and muon (right) momentum resolution as a function of true momentum.

Figure 3.25: Vertex, direction and momentum resolutions compared between apfit and fitQun for SK-IV fully contained atmospheric neutrino MC. The resolution is defined as the 68 percentile of the respective distributions (Figures taken from [25]).

fitQun is better in every perspective.

Fig. 3.26 shows the event breakdowns of the 1-ring e -like, 1-ring μ -like and NC1 π^0 events by fitQun and apfit. While the single ring event reconstruction efficiencies are about the same for both fitters, it is obvious that fitQun performs much better on identifying NC1 π^0 events. In generally fitQun has better performance in

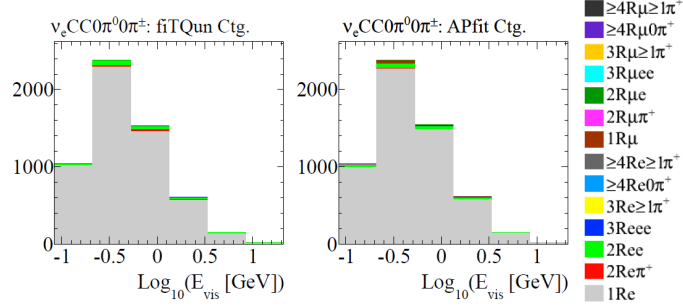
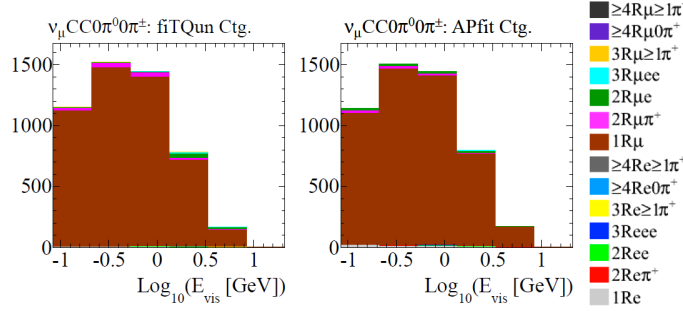
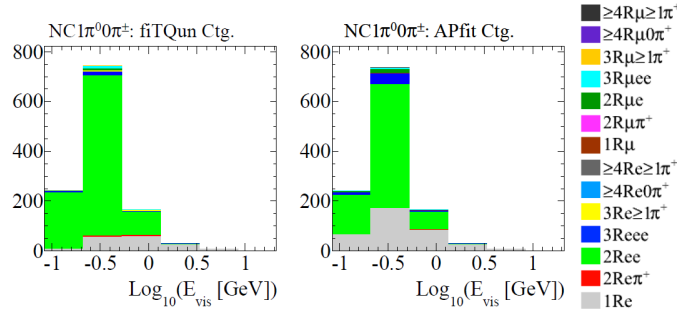
(a) 1-ring e -like events.(b) 1-ring μ -like events.(c) NC1 π^0 events.

Figure 3.26: Event breakdowns for the 1-ring e -like (top), 1-ring μ -like (middle) and NC1 π^0 (bottom) samples of the SK-IV fully contained atmospheric neutrino MC. fitQun results are on the left and apfit results on the right (Figures taken from [25]).

reconstructing multi-ring events. Also the π^+ fitter makes it possible to reconstruct $\text{CC}1\pi^+$ events explicitly. Currently T2K has already used the fitQun 1-ring e -like and μ -like samples as the official oscillation analysis samples, and more fitQun based samples are under development.

3.4 Neutrino event generator NEUT

NEUT[117] is a neutrino interaction simulation library that generates primary neutrino-nucleon interactions and handles subsequent secondary interactions within the interacting nuclei. Its results are used as an input for both the ND280 and SK simulation codes to simulate the detector responses. This library was originally developed for the Kamiokande experiment but has been continuously updated to support the Super-Kamiokande and T2K experiments.

In NEUT, the following primary neutrino interactions are simulated: (quasi-) elastic scattering, single meson production, coherent pion production, and deep inelastic scattering. Recently a multi-nucleon neutrino interaction model has been added to NEUT as well. The secondary interactions between the nucleus and any products of the primary interactions, including both mesons and recoiling nucleons, are modeled by a particle cascade routine.

3.4.1 Quasi-elastic neutrino-nucleon scattering

Among all the primary interactions, the charged current quasi-elastic (CCQE) interactions constitute the majority of the events in the SK oscillation samples, where a neutrino scatters off from an entire nucleon and resembles an elastic scattering kinematics (see Fig. 3.27). Fig. 3.28 shows the total CC cross-sections predicted by NEUT, where we can see CCQE interaction dominates at the beam flux peak.

The CCQE cross-sections on free protons (or hydrogen atoms in water) are based on the Llewellyn Smith Model[118]. For CCQE interactions on bound nucleons in ^{16}O , the NEUT default is the relativistic Fermi gas model (RFG) in [119], where the momentum distribution of the nucleons follows the Fermi gas model, and the out-

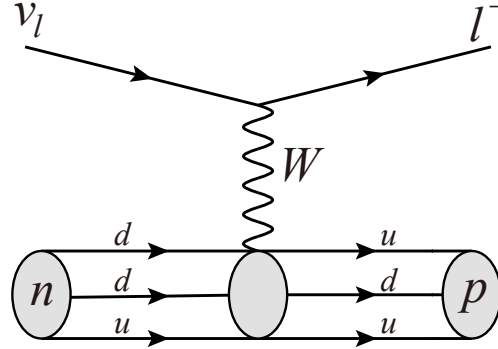
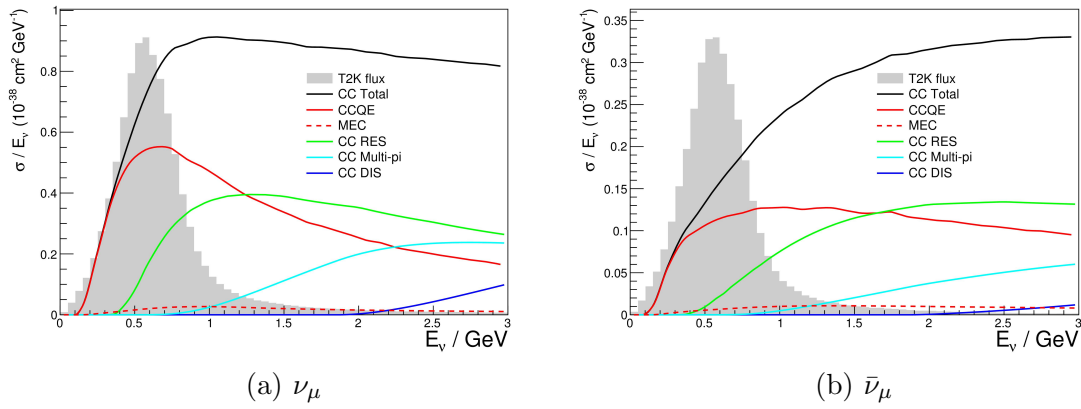


Figure 3.27: Feynman diagram of a neutrino CCQE interaction.

Figure 3.28: CC cross-section predicted by NEUT version 5.3.2 for (a) ν_μ and (b) $\bar{\nu}_\mu$. The T2K flux spectra are shown with arbitrary units (Figures taken from [26]).

going nucleon has to escape the nuclear potential and experience the Pauli blocking effects that forces its momentum to be greater than the Fermi surface momentum. Alternative models are later added to improve data-MC agreement. The spectral function (SF) model in [120] uses the impulse approximation, where the neutrino interacts with a single nucleon but takes into account the short-range correlations between nucleons and affects the energy and momenta of outgoing particles. The random phase approximation (RPA) model in [121] introduces medium polarization effect that affects the propagation of particle-hole (ph) pair by the long range correlation induced by residual ph excitation.

On the other hand, the cross-sections for NC elastic scattering are related to the CC cross-sections by the following relations[122, 123]:

$$\sigma(\nu p \rightarrow \nu p) = 0.153 \times \sigma(\nu n \rightarrow e^- p), \quad (3.9)$$

$$\sigma(\bar{\nu} p \rightarrow \bar{\nu} p) = 0.218 \times \sigma(\bar{\nu} p \rightarrow e^+ n), \quad (3.10)$$

$$\sigma(\nu n \rightarrow \nu n) = 1.5 \times \sigma(\nu p \rightarrow \nu p), \quad (3.11)$$

$$\sigma(\bar{\nu} n \rightarrow \bar{\nu} n) = 1.0 \times \sigma(\bar{\nu} p \rightarrow \bar{\nu} p). \quad (3.12)$$

3.4.2 Single meson production

Single pion production is simulated by the Rein and Sehgal's method[124], in which the process is split into two parts:

$$\nu + N \rightarrow l + N^*,$$

$$N^* \rightarrow \pi + N',$$

where N and N' are the nucleons, N^* is the baryon resonance. The cross-sections are obtained by multiplying the amplitude of each resonance production with the probability of pion decay. The excited resonances are included up to an invariant mass of 2 GeV. The pion angular distribution is calculated by the Rein and Sehgal's method for the $\Delta(1232)$ resonance, while it is assumed to be isotropic in the resonance rest frame for others. The Pauli blocking effect is considered in the baryon decay, where the knocked-off nucleon is required to have momentum greater than Fermi surface momentum. The pion-less Δ decay (Δ resonances being directly absorbed by nuclei) is also simulated which accounts for 20% of the events.

The cross-sections for single η and K productions can be obtained by substituting the corresponding decay probability instead.

3.4.3 Deep inelastic scattering (DIS)

For DIS,

$$\nu + N \rightarrow l + N' + \text{hadrons},$$

the cross-section is calculated for hadronic system with an invariant mass energy W greater than 1.3 GeV. To avoid double-counting of the single pion production process, only processes with pion multiplicities greater than 1 are included for $1.3 \text{ GeV} < W < 2 \text{ GeV}$. The nucleon structure functions are taken from the parton distributions functions by Glück et al.[125], with corrections in the lower Q^2 region by Bodex and Yang[126].

The relations between NC and CC cross-sections are determined from the expe-

rimental results[127, 128]:

$$\frac{\sigma(\nu N \rightarrow \nu X)}{\sigma(\nu N \rightarrow \mu^- X)} = \begin{cases} 0.26, & E_\nu < 3\text{GeV} \\ 0.26 + 0.04(E_\nu/3 - 1), & 3\text{GeV} \leq E_\nu < 6\text{GeV} \\ 0.30, & E_\nu \geq 6\text{GeV} \end{cases} \quad (3.13)$$

$$\frac{\sigma(\bar{\nu} N \rightarrow \bar{\nu} X)}{\sigma(\bar{\nu} N \rightarrow \mu^+ X)} = \begin{cases} 0.39, & E_\nu < 3\text{GeV} \\ 0.39 - 0.02(E_\nu/3 - 1), & 3\text{GeV} \leq E_\nu < 6\text{GeV} \\ 0.37, & E_\nu \geq 6\text{GeV} \end{cases} \quad (3.14)$$

Events with $W > 2$ GeV are simulated by the CERN PYTHIA/JetSet package[129]. The forward-backward asymmetry of pion multiplicity (n_π^F/n_π^B) in the center of mass frame of the hadronic system is obtained from the BEBC experimental results[130]:

$$\frac{n_\pi^F}{n_\pi^B} = \frac{0.35 + 0.41 \ln(W^2)}{0.5 + 0.09 \ln(W^2)}. \quad (3.15)$$

3.4.4 Coherent pion production

The coherent pion production model is from [131], where the neutrino interacts with the entire ^{16}O nucleus as a whole:

$$\nu + {}^{16}\text{O} \rightarrow l + {}^{16}\text{O} + \pi.$$

The outgoing pion has the same charge as the incoming weak-current, and pion production is enhanced in the forward direction as the outgoing pion carries away most of the incoming neutrino momentum.

3.4.5 Multi-nucleon (2p2h) interaction

A multi-nucleon neutrino interaction model by Nieves et al.[121, 132] has been recently added to NEUT. This '2p2h' (2 particle-2 hole), or in general 'nph', model describes multiple nucleon interaction with a single neutrino. The 2p2h event topology has a charged lepton and no pions, so is indistinguishable from CCQE interactions and significantly enhances CCQE-like cross-section.

The cross-sections are calculated by a multi-body expansion of the weak propagator in the medium. While the first-order expansion predicts the standard CCQE interaction, the second-order and higher order terms involve additional nucleons or Δ resonances in the hadronic current. Since pion-less delta decay (PDD) is also a multi-nucleon process, it is possible to include it in the 2p2h model. The 2p2h PDD cross-sections are confirmed to be similar to the NEUT original implementation in Sec. 3.4.2, therefore only the 2p-2h PDD process is turned on to avoid double-counting.

3.4.6 Final state and secondary interactions

After the primary interaction processes, leptons and hadrons must escape the nuclear matter before they can be observed. The final state interactions (FSI) between the hadrons and nuclei can dramatically change the observable particles. In addition, hadrons can still undergo secondary interactions (SI) somewhere in the detector even after leaving the nucleus, making them invisible in detection. Among all particles, the FSI and SI of pions are the most important, because of both its large production and interaction cross-section. For example, the charged pion produced in a $CC1\pi$ interaction can be absorbed by the nucleus and not be detected, mimicking

a CCQE interaction. The neutrino energy reconstruction can be messed up due to the wrongly-assumed 2-body kinematics.

NEUT simulates the FSI by an intra-nuclear cascade model. To begin with, the initial position of the neutrino interaction is generated based on the Woods-Saxon type nucleon density distribution[133]:

$$\rho(r) = \frac{Z}{A} \rho_0 \frac{1}{1 + \exp(\frac{r-c}{a})}, \quad (3.16)$$

where $Z = 8$ is the atomic number and $A = 16$ is the mass number for the ^{16}O nucleus, with the average nuclear density $\rho_0 = 0.48m_\pi^3$, and density parameters $a = 0.41$ fm and $c = 2.69$ fm. The reaction products are then propagated “classically” in finite steps in the nuclear medium. Fermi motion and Pauli blocking are considered.

For pion momentum $p_\pi < 500$ MeV/c, the quasi-elastic, single charge exchange and absorption probabilities are calculated by the Oset et al. model[134]. For $p_\pi > 500$ MeV/c, the interaction probability are computed from PDG cross-section data[135] of π^\pm scattering off from free proton and deuteron.

Moreover, nucleon-nucleon elastic scattering is considered, which may produce Δ resonances and pion decays. Cross-section measurements from [136] are used, with the isobar production model by Lindenbaum et al.[137] included.

Chapter 4

Oscillation samples and event selections at SK

In order to constrain all the interesting parameters in the sterile neutrino mixing model, we have to measure multiple oscillation probabilities at the same time. Luckily the SK detector is able to construct different oscillation samples based on observed event topology. Apart from the standard CC oscillation samples, we have also included two new sets of NC samples ($2R\pi^0$ and $NC\gamma$ de-excitation) to enhance the sterile sensitivity. Below we outline all the oscillation samples that are used in this sterile analysis and their selection criteria.

4.1 Data set summary

In this analysis, we make use of data collected during T2K beam periods Runs 1-8. The duration, proton-on-target (POT) and horn current of each run are summarized in Table 4.1. The POT for physics analysis only includes good beam spills selected

T2K Run	Start	End	POT($\times 10^{20}$)	Horn current set (kA)
Run 1	23/Jan. 2010	26/Jun. 2010	0.326	+250
Run 2	18/Nov. 2010	11/Mar. 2011	1.122	+250
Run 3b	08/Mar. 2012	21/Mar. 2012	0.217	+200
Run 3c	08/Apr. 2012	09/Jun. 2012	1.382	+250
Run 4	19/Oct. 2012	08/May. 2013	3.596	+250
Run 5	16/May. 2014	24/Jun. 2014	0.245/0.512	+250/-250
Run 6	30/Oct. 2014	03/Jun. 2015	0.192/3.547	+250/-250
Run 7	01/Feb. 2016	27/May. 2016	0.485/3.499	+250/-250
Run 8	27/Oct. 2016	12/Apr. 2017	7.170	+250

Table 4.1: The run period, POT and horn current of each T2K run. Run 5 - Run 7 included periods of beam operation in both neutrino and antineutrino mode. (Table taken from [27]).

by the SK DAQ status and a number of data quality parameters. Fig. 4.1 shows the accumulated number of POT as a function of date. The total data for T2K oscillation analysis is 22.2914×10^{20} POT, with 14.7341×10^{20} POT in neutrino mode and 7.5573×10^{20} POT in antineutrino mode.

Fig. 4.2 shows the cumulative number of observed fully contained (FC) events as a function of POT. The stability of event rates is examined by the Kolmogorov-Smirnov (KS) test. The largest vertical distance D between the data and constant event rate hypothesis (red line) in Fig. 4.2 is computed for each plot. For neutrino (antineutrino) running, D is found to be 38.05 (12.10) with a normalization factor of $1/1232$ ($1/263$). The KS probability to obtain values larger than D from statistical fluctuations is 18.43% (61.08%), which is consistent with constant event rate.

The SK detector stability is continuously monitored. For details see Sec. 3.3.4. Fig. 4.3 shows the time variation of the attenuation length of detector water measured by cosmic ray through-going muon data, which has remained constant within 90 ± 5 m. The absolute energy scale is also stable, with the energy scale uncertainty be 2.1%.

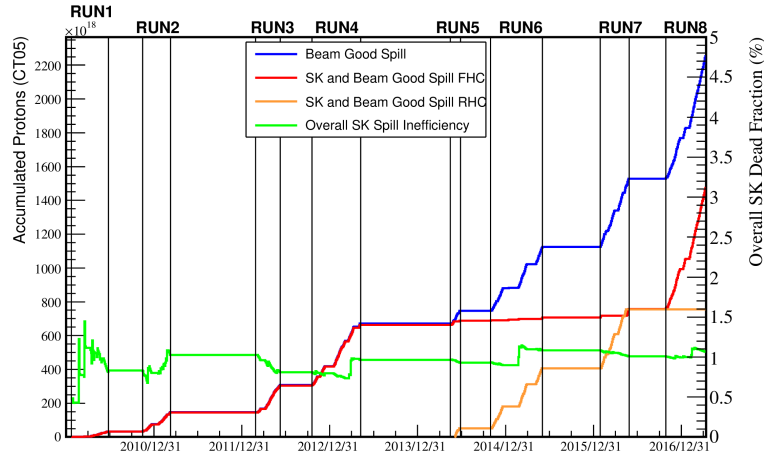
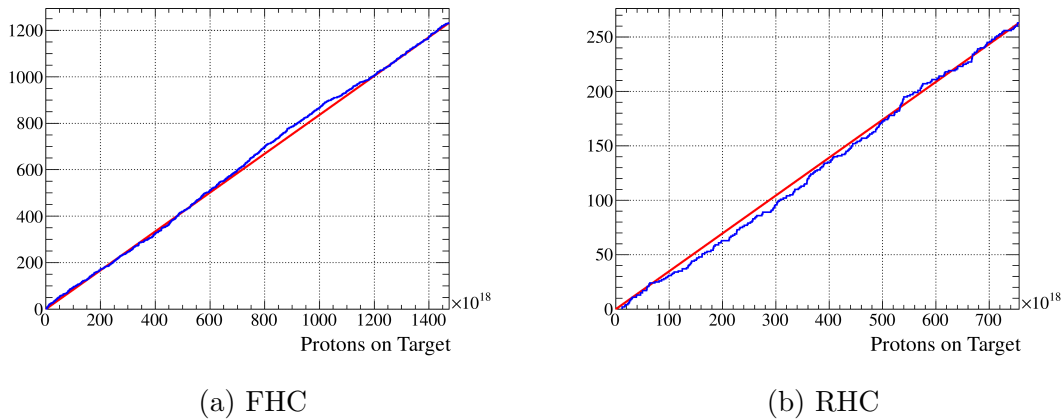


Figure 4.1: Accumulated number of POT as a function of date for beam good spills (blue), SK + beam good spills in neutrino mode (red), SK + beam good spills in antineutrino mode (orange), and the SK dead fraction of POT (green = (blue-red-orange)/blue) (Figure taken from [27]).



(a) FHC

(b) RHC

Figure 4.2: The cumulative number of observed FC events as a function of POT in neutrino mode (FHC) and antineutrino mode (RHC) for T2K Run 1-8. The red solid lines refer to expectation in case of constant event rates for all runs (Figures taken from [27]).

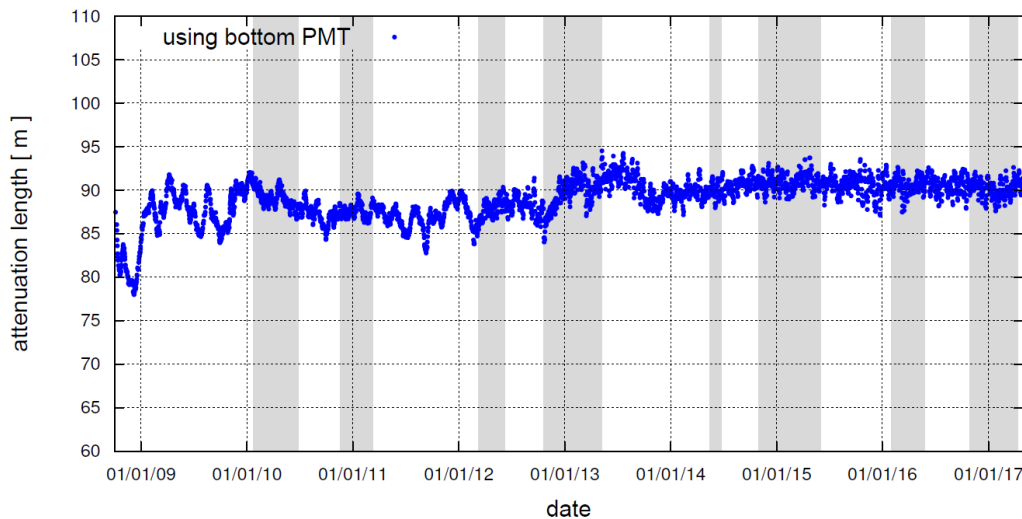


Figure 4.3: Time variation of the SK attenuation length measured by cosmic ray through-going muon data, Gray shaded regions denote the Run 1-8 periods (Figure taken from [27]).

The MC neutrino events are generated with NEUT 5.3.2, SKDETSIM 13.90 and reweighted by flux 13av1.2. Both the data and MC are reconstructed by apfit version 14b and fitQun v4r0.

4.2 Charged current oscillation samples

T2K has several standard CC oscillation samples that are sensitive to the 3-flavor oscillation parameters. In the 3+1 sterile neutrino model that we are interested in, the CC samples can also put constraints on θ_{24} . All these samples have been switched to fitQun-based reconstruction selection.

4.2.1 FHC/RHC 1R μ samples

The 1-ring μ -like samples (1R μ) are the standard T2K ν_μ disappearance samples that are available in both neutrino (FHC) and anti-neutrino (RHC) beam modes.

The event selection criteria are listed below:

1. Fully-contained (FC) in the SK inner detector (ID) and reconstructed inside the fiducial volume (FV):
 - (a) $n_{hitac} < 16$ (number of PMT hits in the largest outer detector hit cluster)
 - (b) $wall > 50$ cm (closest distance between vertex and detector wall),
 - (c) $towall > 250$ cm (particle track length in ID).
2. Number of rings found by fitQun multi-ring fitter is one.
3. The ring is identified as muon-like by the PID algorithm.
4. Reconstructed momentum > 200 MeV/c.
5. Number of decay electrons is less than or equal to one.
6. Pass the two-dimensional π^+ cut.

Figs. 4.4 and 4.5 show the distributions of the variables used in the selection cuts 2 to 6. Data of T2K Run 1-8 are overlaid on the MC expectation, which show very good agreement. The numbers of events passing each selection cut are shown in Fig. 4.6. After all selection cuts, 240 events are selected as ν_μ candidate for FHC and 68 events for RHC.

Fig. 4.7 show the 1D distributions of the variables $wall$ and $towall$, and the spatial distributions of event vertices in R^2 and Z of the detector coordinates in Fig. 4.8. The event rate increases with R from the tank center to the tank wall, due to the increase in interaction volume, and decreases close to the detector wall due to poorer reconstruction efficiency. The event rate is flat in the Z direction, except the tank top/bottom regions.

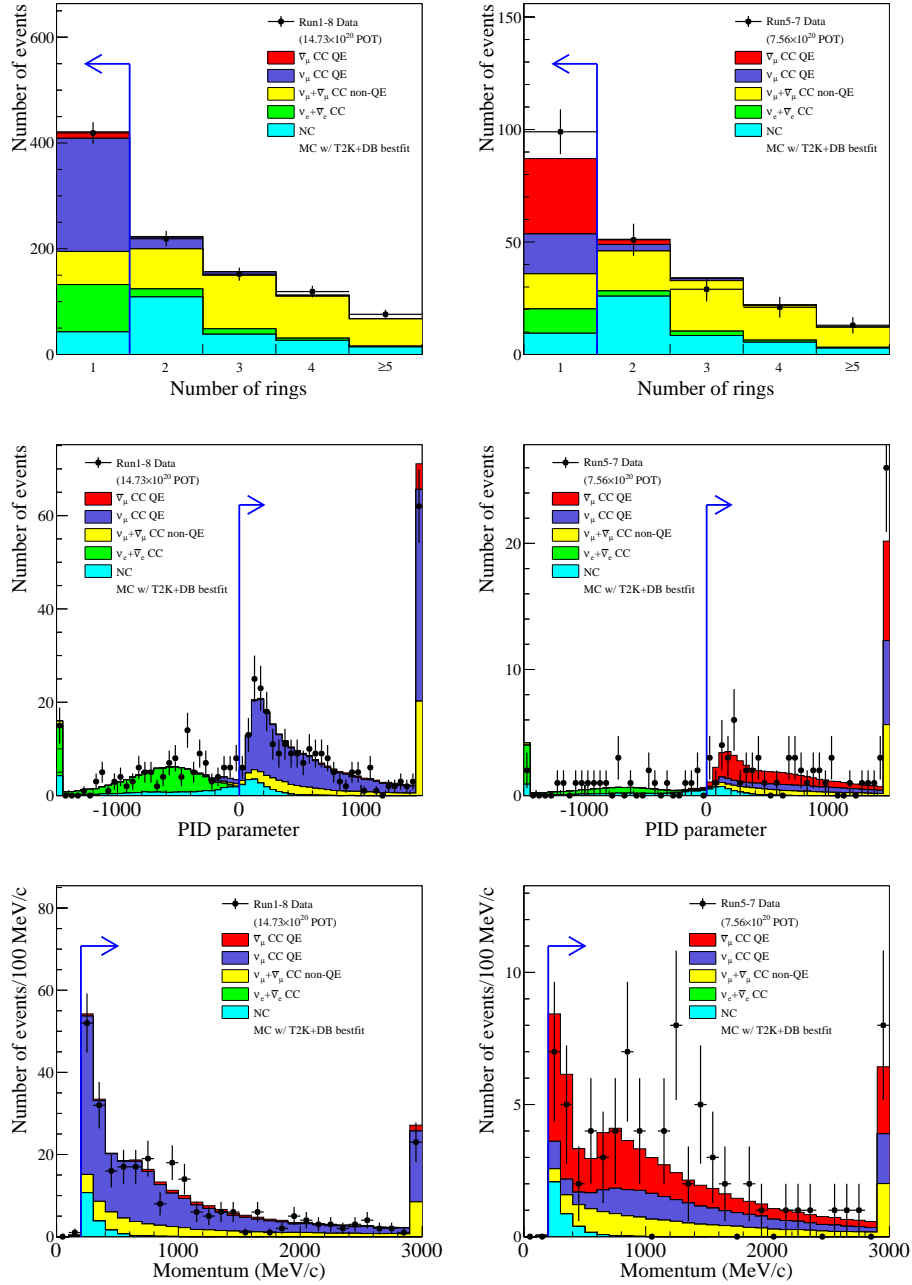


Figure 4.4: Distributions of FHC (left) and RHC (right) $1R\mu$ event selections at each stage for Run 1-8. Blue arrows denote the selection criteria. The MC expectation is calculated based on 3-flavor oscillation framework with the world best-fit oscillation parameters and BANFF fit corrections (Figures taken from [27]).

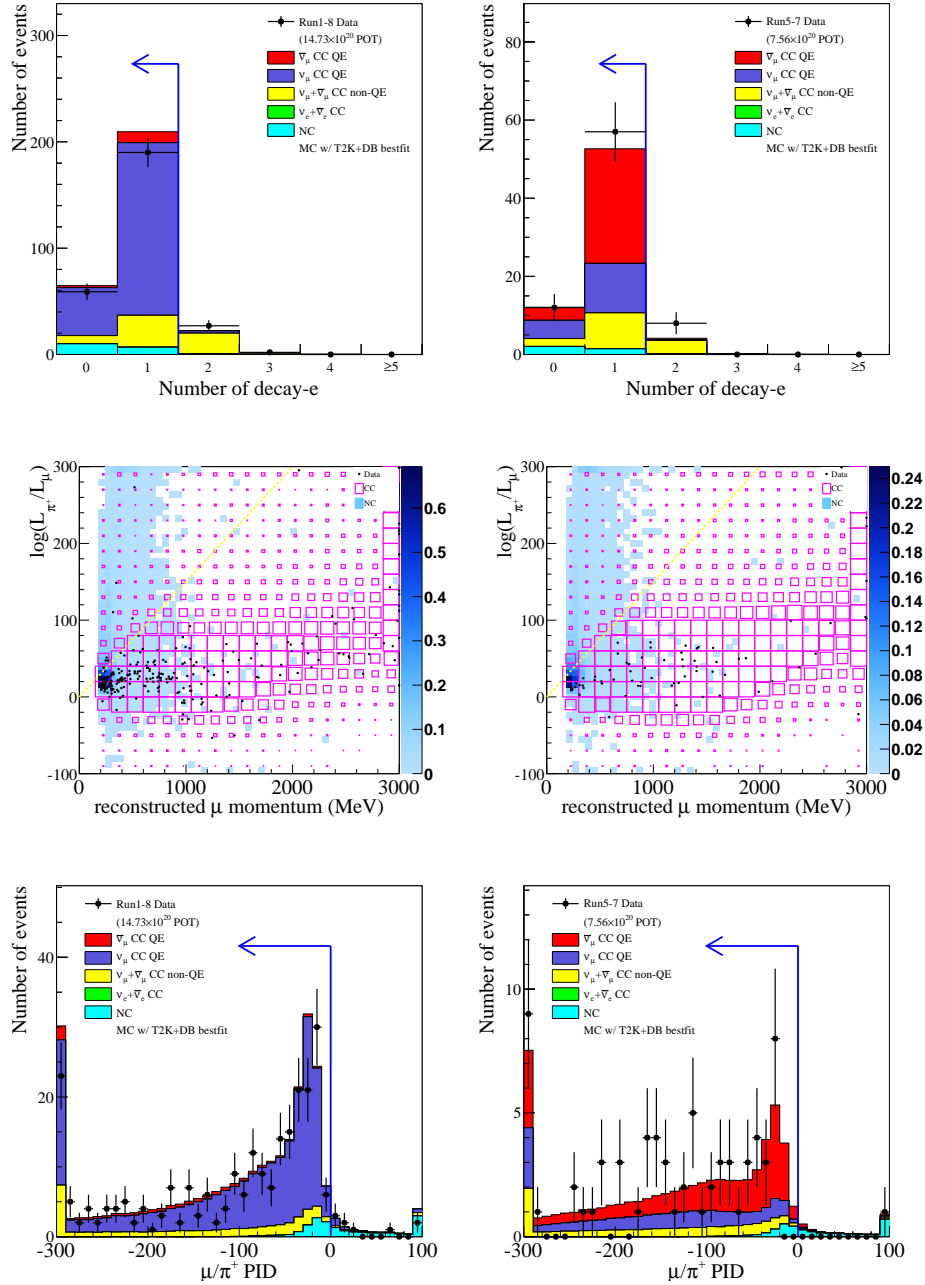


Figure 4.5: Distributions of FHC (left) and RHC (right) $1R\mu$ event selections at each stage for Run 1-8. Middle graphs show the π^+ rejection cut in 2D, with events below the dotted yellow line selected as ν_μ candidates, and bottom graphs show the distance from the cut line (Figures taken from [27]).

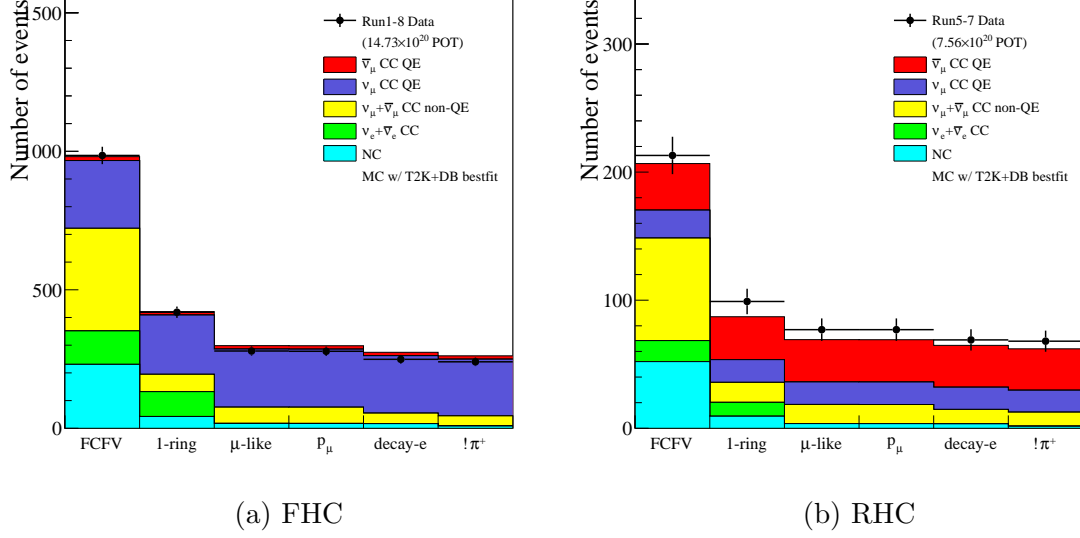


Figure 4.6: Number of events passing each $1R\mu$ selection stage for T2K Runs 1-8. The MC expectation is calculated based on 3-flavor oscillation framework with the world best-fit oscillation parameters and BANFF fit corrections (Figures taken from [27]).

Fig. 4.9 shows the cumulative number of observed ν_μ events as a function of POT. For FHC (RHC) data, the greatest distance D between observation and a constant event rate hypothesis is 0.028 (0.091). The KS probability to obtain large values due to statistical fluctuations is 98.85% (59.2%). The event rates are stable over the experimental periods.

From the reconstructed muon momentum p_μ , and the angle between the neutrino beam and the outgoing muon θ_{beam} , the reconstructed neutrino energy E_ν^{rec} is calculated by

$$E_\nu^{\text{rec}} = \frac{(M_n - V_{\text{nuc}}) \cdot E_\mu - m_\mu^2/2 + M_n \cdot V_{\text{nuc}} - V_{\text{nuc}}^2/2 + (M_p^2 - M_n^2)/2}{M_n - V_{\text{nuc}} - E_\mu + p_\mu \cos(\theta_{\text{beam}})}, \quad (4.1)$$

where M_n (M_p) is the neutron (proton) mass, $V_{\text{nuc}} = 27$ MeV is the binding energy of

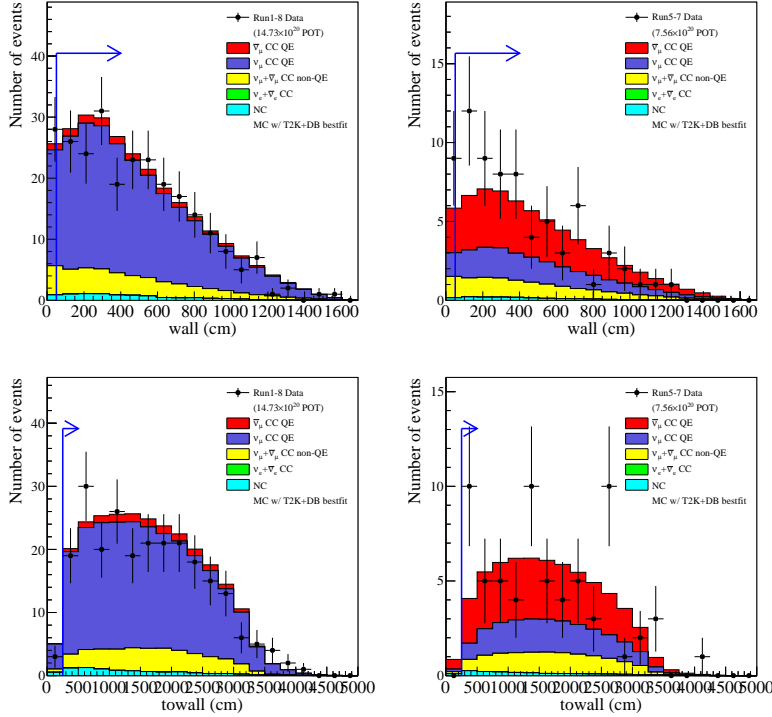


Figure 4.7: Reconstructed vertex distributions of FHC (left) and RHC (right) $1R\mu$ events for Run 1-8, after passing all selection cuts. Top graphs show the $wall$ distribution with $towall > 250$ cm applied, and bottom graphs show the $towall$ distribution with $wall > 50$ cm applied. The blue arrows indicating the full FV cut (Figures taken from [27]).

neutron in oxygen, m_μ is the muon mass and E_μ is its total energy.

In the $1R\mu$ samples, the main contribution is from $\nu_\mu(\bar{\nu}_\mu)$ charged current quasi-elastic (CCQE) events with no pion observed in the final state. Fig. 4.10 shows the reconstructed neutrino energy distribution for T2K Runs 1-8, with data overlaid on MC. The biggest background is from CC non-QE interactions such as $2p2h$ and $CC1\pi$. There are also contributions from the wrong sign backgrounds, especially in the RHC data (ν_μ interaction in RHC mode and vice versa).

The high statistics disappearance samples give us strong sensitivity on $\sin^2\theta_{23}$ and Δm_{31}^2 . At the same time they also constrain $\sin^2\theta_{24}$ as a function Δm_{41}^2 .

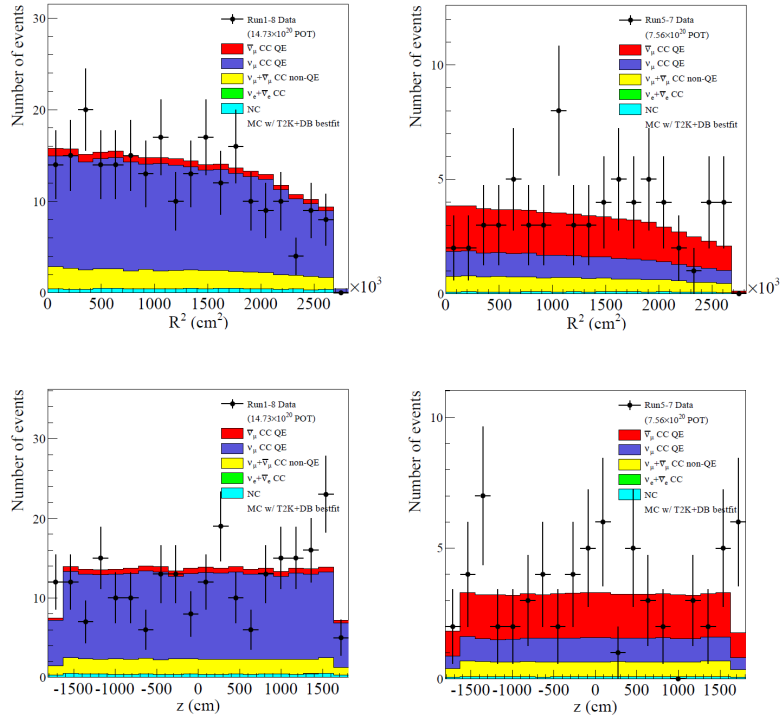


Figure 4.8: Reconstructed vertex distributions of FHC (left) and RHC (right) $1R\mu$ events for Run 1-8, after passing all selection cuts. Top graphs show the square of the distance of the vertices from the central vertical axis of the SK tank, and bottom graphs show the vertical position of the vertices (Figures taken from [27]).

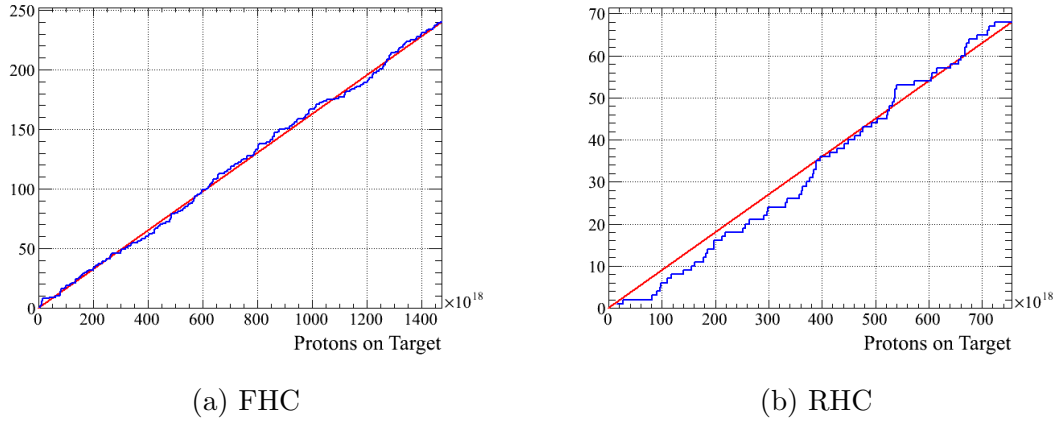


Figure 4.9: The cumulative number of observed $1R\mu$ events (blue) as a function of POT in FHC and RHC for T2K Run 1-8. The red solid lines refer to expectation in case of constant event rates for all runs (Figures taken from [27]).

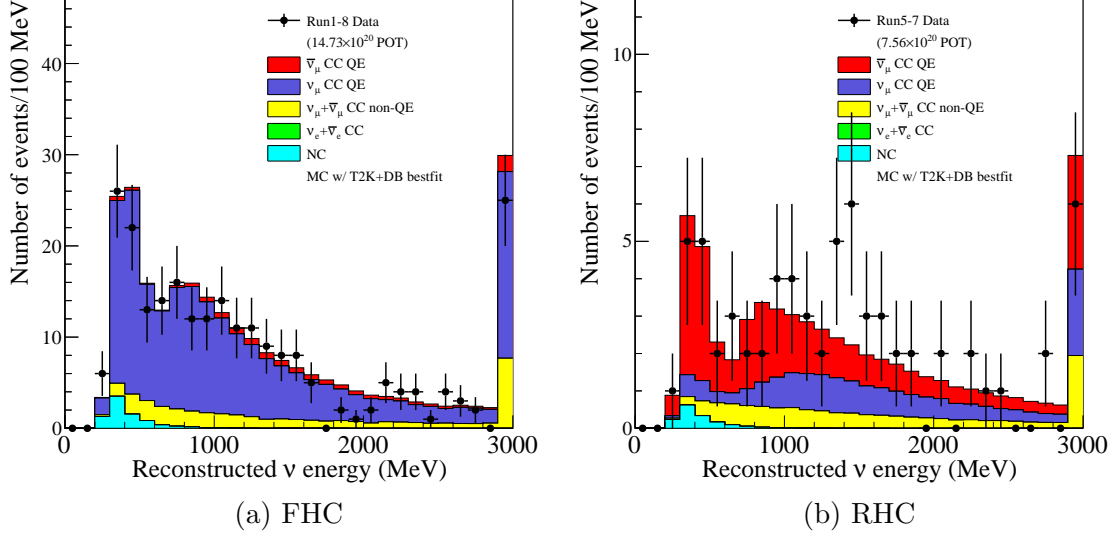


Figure 4.10: Reconstructed neutrino energy distribution of $1R\mu$ samples for T2K Runs 1-8 (Figures taken from [27]).

4.2.2 FHC/RHC $1Re$ samples

The 1-ring e -like ($1Re$) samples are the standard T2K ν_e appearance samples that are available in both neutrino (FHC) and anti-neutrino (RHC) beam mode. The event selection criteria are listed below:

1. FCFV condition:
 - (a) $n_{hitac} < 16$,
 - (b) $wall > 80$ cm,
 - (c) $towall > 170$ cm.
2. Number of rings found by fitQun multi-ring fitter is one.
3. The ring is identified as electron-like by the PID algorithm.
4. Visible energy $E_{vis} > 100$ MeV.

5. No decay electrons.
6. Reconstructed neutrino energy $E_\nu^{rec} < 1250$ MeV.
7. Pass the π^0 rejection cut.

E_ν^{rec} is calculated by replacing the muon mass m_μ with electron mass m_e in Eq. 4.1, and E_{vis} is the sum of momentum of each ring.

Figs. 4.11 and 4.12 show the distributions of the variables used in the selection cuts 2 to 7. Data of T2K Run 1-8 are overlaid on the MC expectation, which show very good agreement. The numbers of events passing each selection cut are shown in Fig. 4.13. After all selection cuts, 74 events are selected as ν_μ candidate for FHC and 7 events for RHC.

Fig. 4.14 show the 1D distributions of the variables $wall$ and $towall$, and Fig. 4.15 shows the spatial distributions of event vertex in R^2 and Z of the detector coordinates.

Fig. 4.16 shows the cumulative number of observed ν_e events as a function of POT. For FHC (RHC) data, the greatest distance D between observation and a constant event rate hypothesis is 0.099 (0.143). The KS probability to obtain large values due to statistical fluctuations is 43.8% (99.4%). The event rates are stable over the experimental periods.

Fig. 4.17 shows the reconstructed neutrino energy distribution for T2K Runs 1-8. The 1Re samples have a high purity of oscillated $\nu_e(\bar{\nu}_e)$ events. The biggest background comes from the intrinsic $\nu_e/\bar{\nu}_e$ components in the beam. Another important background is due to NC π^0 events where only one gamma from the $\pi^0 \rightarrow \gamma\gamma$ decay is reconstructed and wrongly classified as ν_e events.

The samples are optimized to achieve best sensitivity on the conventional δ_{CP} .

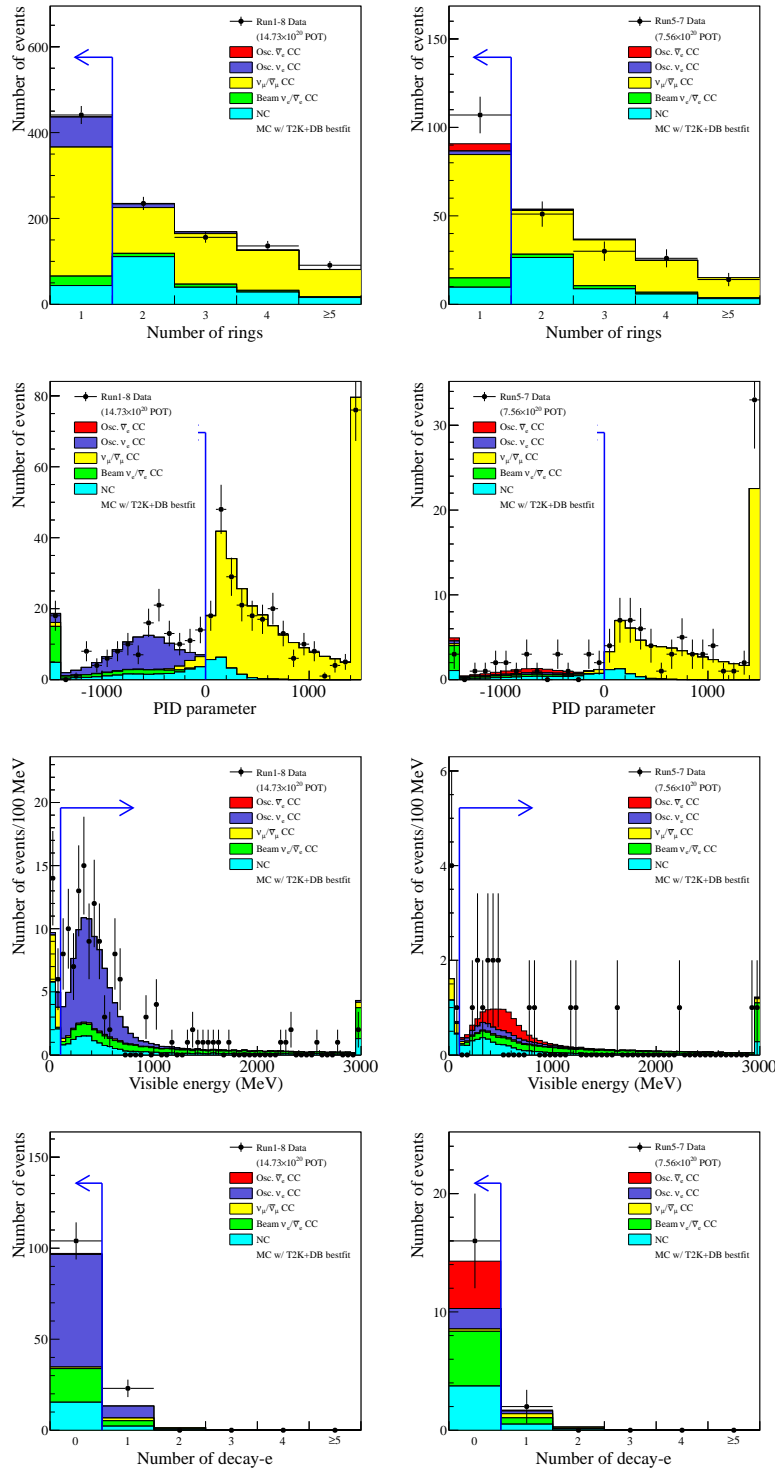


Figure 4.11: Distributions of FHC (left) and RHC (right) 1Re event selections at each stage for Run 1-8 (Figures taken from [27]).

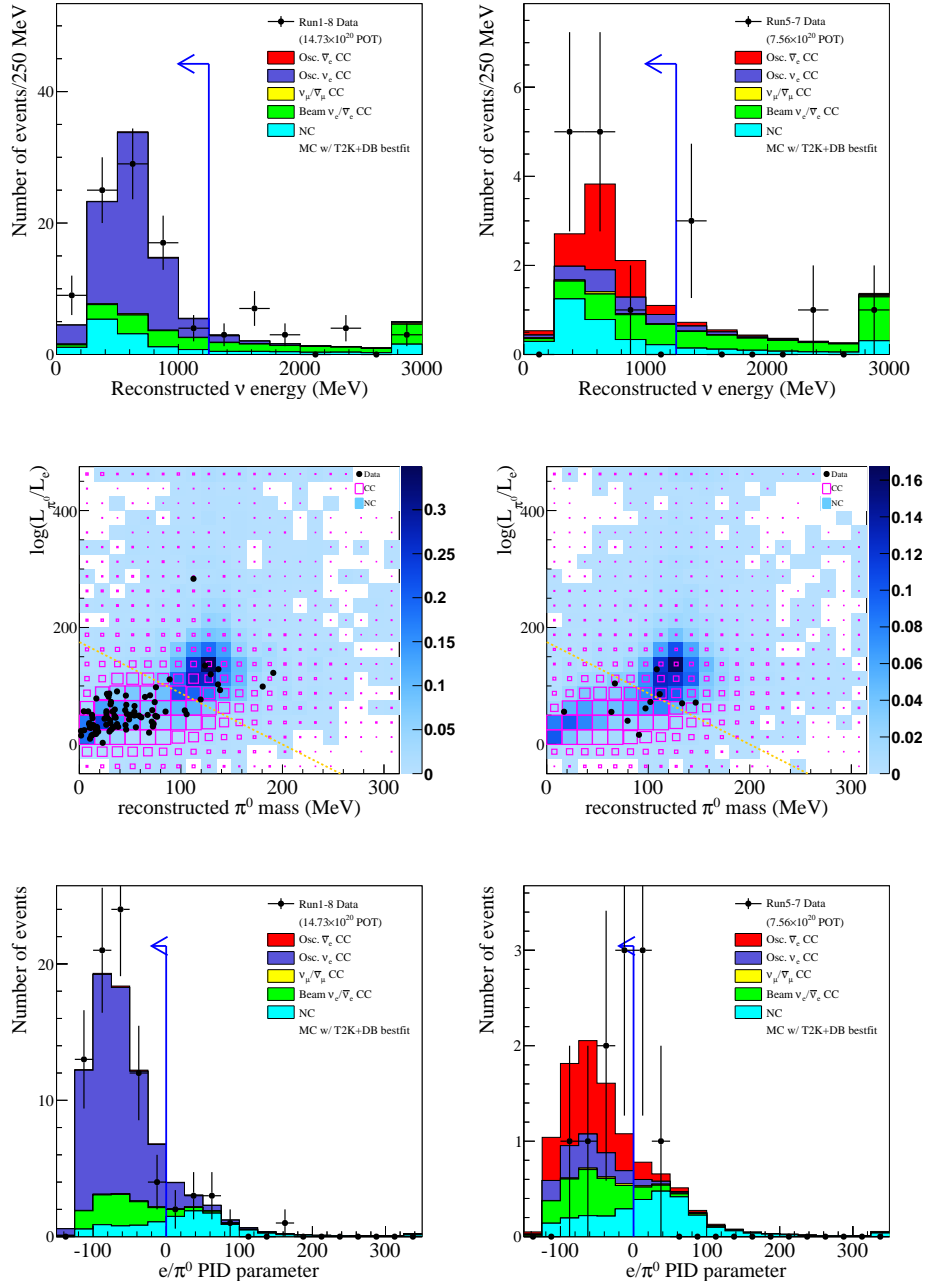


Figure 4.12: Distributions of FHC (left) and RHC (right) 1Re event selections at each stage for Run 1-8. Middle graphs show the π^0 rejection cut in 2D, with events below the dotted yellow line selected as ν_e candidates, and bottom graphs show the distance from the cut line (Figures taken from [27]).

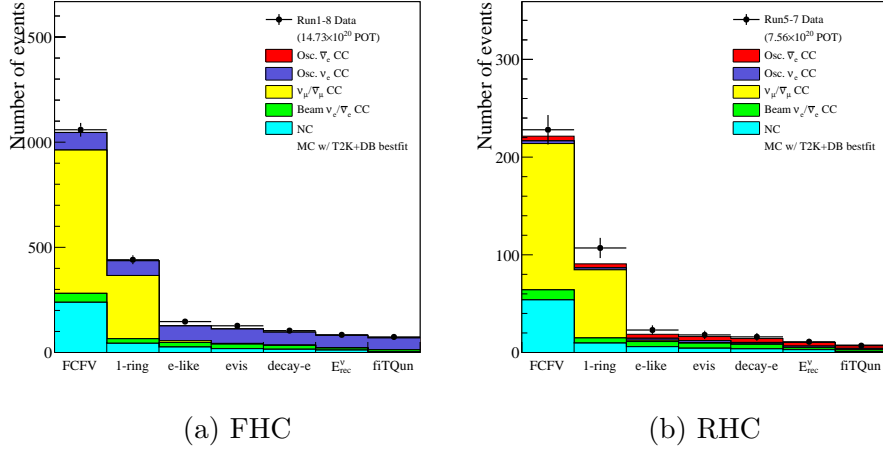


Figure 4.13: Number of events passing each 1Re selection stage for T2K Runs 1-8 (Figures taken from [27]).

On the other hand, they also put some constraints on θ_{24} .

4.2.3 FHC ν_e CC1 π^+ sample

The ν_e CC1 π^+ sample focuses on selecting CC1 π^+ instead of CCQE events. The Feynman diagram of CC1 π^+ interaction is shown in Fig. 4.18. The π^+ is searched by identifying its decay electron in event. The reconstructed neutrino energy $E_{\nu_e CC\Delta}^{\text{rec}}$ is given by:

$$E_{\nu_e CC\Delta}^{\text{rec}} = \frac{2M_p E_e + M_{\Delta^{++}}^2 - M_p^2 - M_e^2}{2(M_p - E_e + p_e \cos \theta_{\text{beam}})}, \quad (4.2)$$

with $M_{\Delta^{++}} = \Delta^{++}$ resonance mass (1232.0 MeV/c²).

The selection criteria of CC1 π^+ sample are thus very similar to 1Re samples, except that it requires exactly one decay electron reconstructed in event. Currently only neutrino mode data of Runs 1-8 is available for this sample.

1. FCFV condition:

- (a) $n_{\text{hitac}} < 16$,

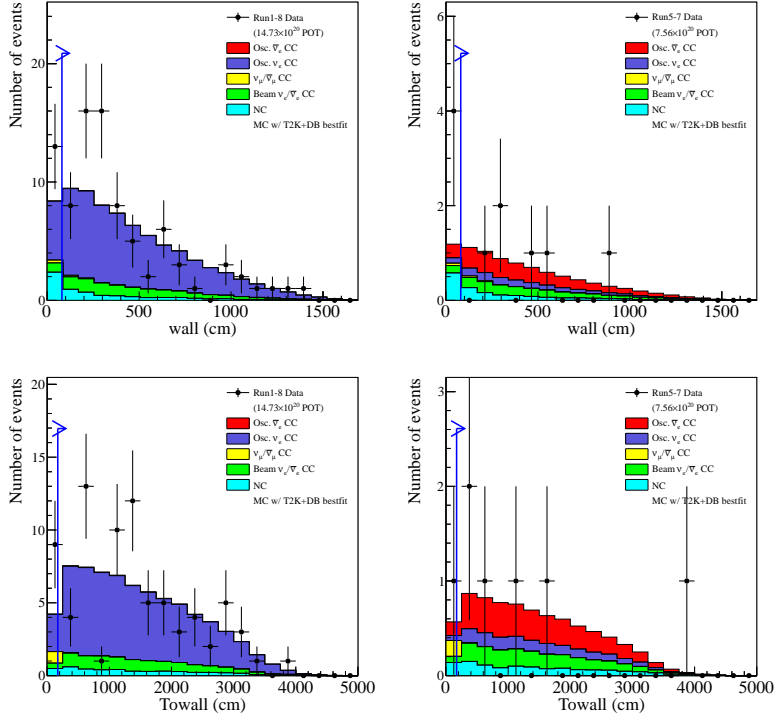


Figure 4.14: Reconstructed vertex distributions of FHC (left) and RHC (right) 1Re events for Run 1-8, after passing all selection cuts. Top graphs show the $wall$ distribution with $towall > 170$ cm applied, and bottom graphs show the $towall$ distribution with $wall > 80$ cm applied. The blue arrows indicating the full FV cut (Figures taken from [27]).

(b) $wall > 50$ cm,

(c) $towall > 270$ cm.

2. Number of rings found by fitQun multi-ring fitter is one.
3. The ring is identified as electron-like by the PID algorithm.
4. Visible energy $E_{vis} > 100$ MeV.
5. One decay electron.
6. Reconstructed neutrino energy $E_{\nu_e CC\Delta}^{rec} < 1250$ MeV.

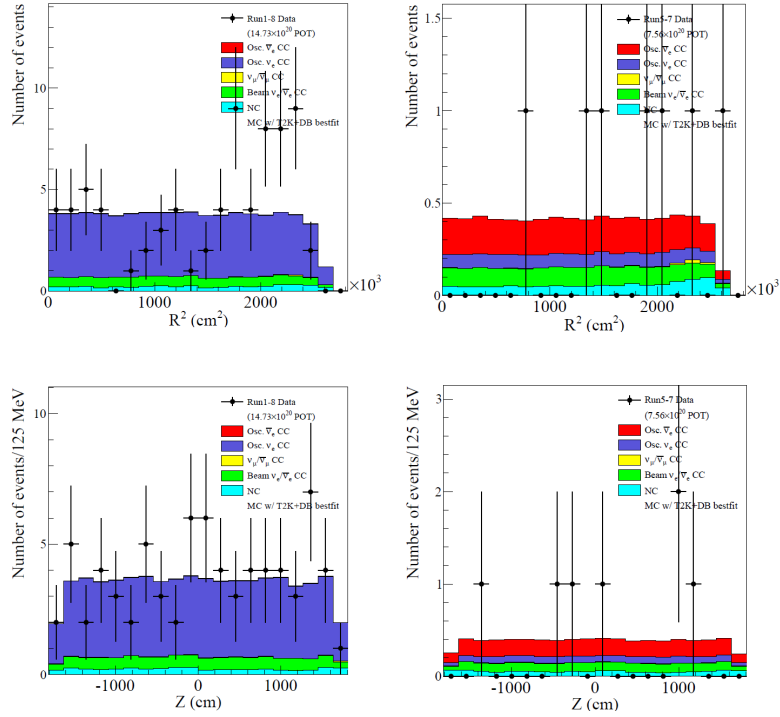


Figure 4.15: Reconstructed vertex distributions of FHC (left) and RHC (right) 1Re events for Run 1-8, after passing all selection cuts. Top graphs show the square of the distance of the vertices from the central vertical axis of the SK tank, and bottom graphs show the vertical position of the vertices (Figures taken from [27]).

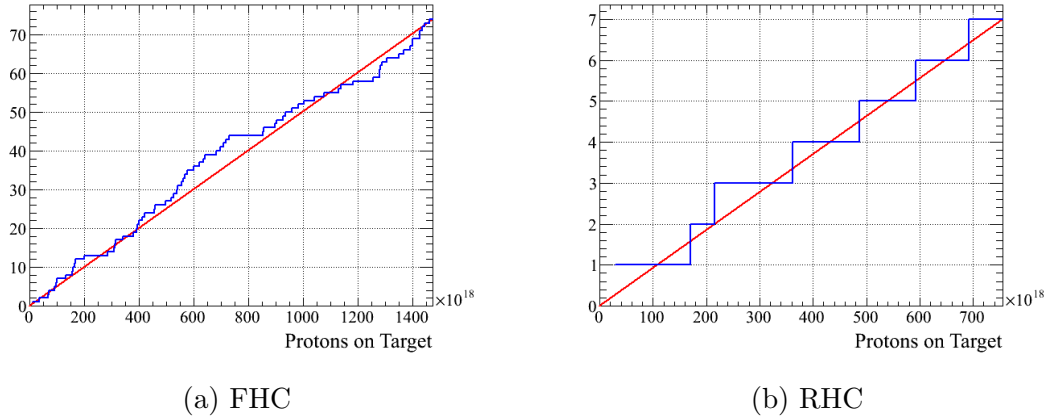


Figure 4.16: The cumulative number of observed 1Re events (blue) as a function of POT in FHC and RHC for T2K Run 1-8. The red solid lines refer to expectation in case of constant event rates for all runs (Figures taken from [27]).

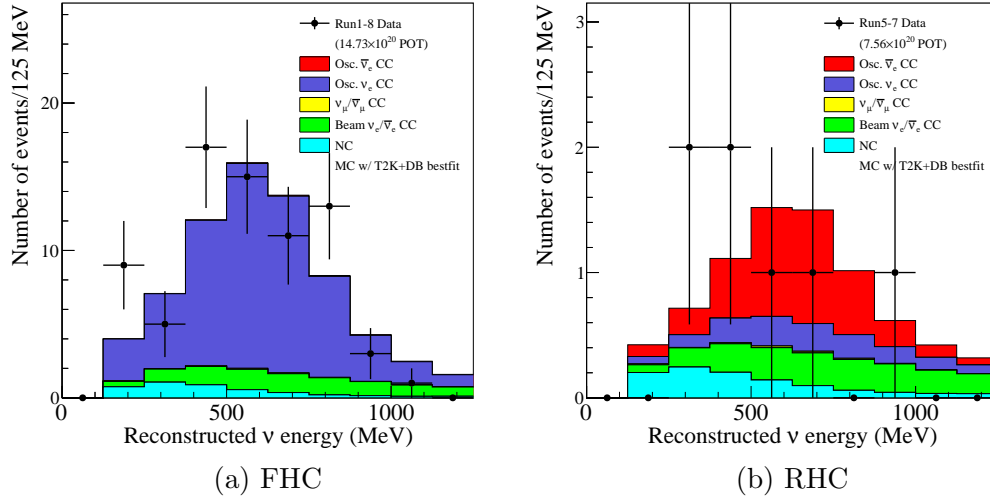


Figure 4.17: Reconstructed neutrino energy distribution of 1Re samples for T2K Runs 1-8 (Figures taken from [27]).

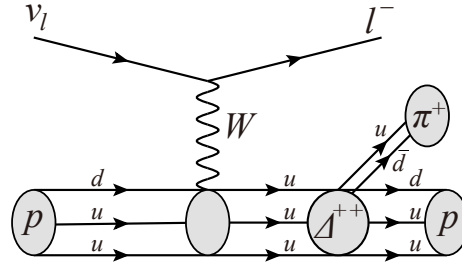


Figure 4.18: Feynman diagram of a $CC1\pi^+$ interaction

7. Pass the π^0 rejection cut.

The distributions of variables from the decay electron cut are shown in Fig. 4.19. Fig. 4.20 shows the number of events passing each selection cut. After all selection cuts, 15 events are found.

Fig. 4.21 and 4.22 show the distributions of the 1D vertex variables.

The reconstructed neutrino energy distribution is shown in Fig. 4.23. As an extension to the 1Re samples, the ν_e $CC1\pi^+$ sample is also a very pure oscillated ν_e

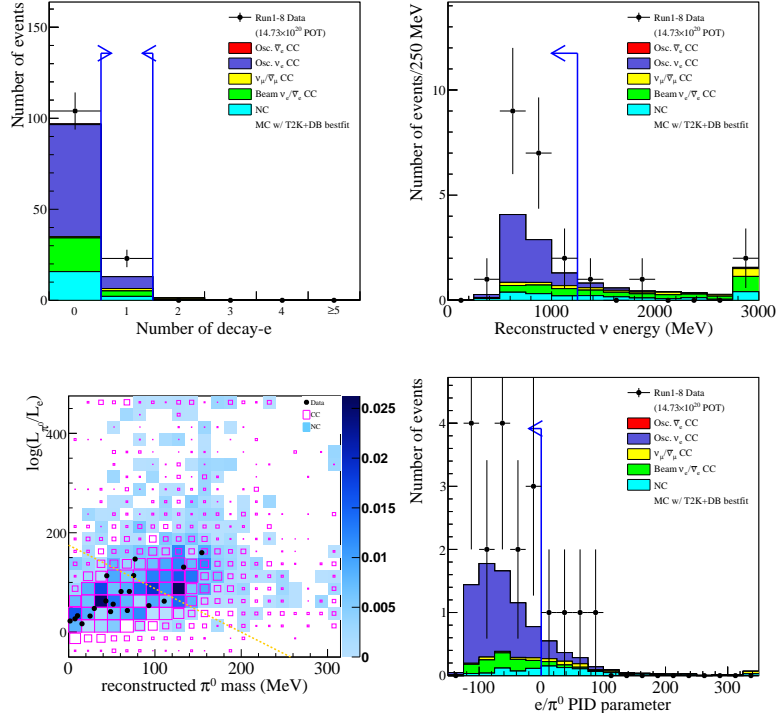


Figure 4.19: Distributions of FHC ν_e CC $1\pi^+$ event selections at each stage for Run 1-8. Bottom left graph shows the π^0 rejection cut in 2D, with events below the dotted yellow line selected as ν_e candidates, and bottom right graph shows the distance from the cut line (Figures taken from [27]).

CC interaction sample, although it has lower statistics.

4.3 Neutral current oscillation samples

Apart from the CC oscillation samples mentioned above, SK also provides few NC oscillation samples that are sensitive to θ_{24} and θ_{34} . While these NC samples have already been published before, this is the first time to use them in oscillation analysis.

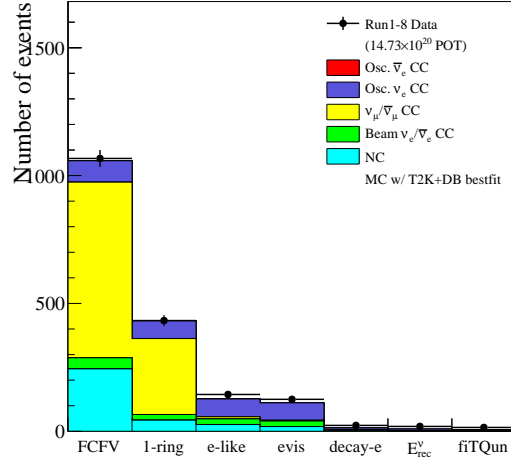


Figure 4.20: Number of events passing each FHC $\nu_e CC1\pi^+$ selection stage for T2K Runs 1-8 (Figures taken from [27]).

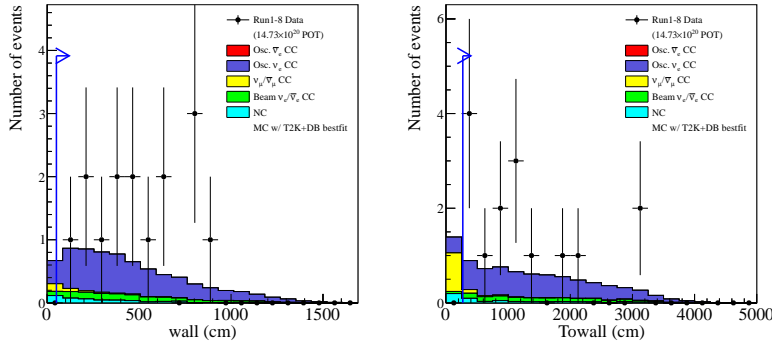


Figure 4.21: Reconstructed vertex distributions of FHC $\nu_e CC1\pi^+$ events for Run 1-8, after passing all selection cuts. Left graph shows the *wall* distribution with *towall* > 270 cm applied, and right graph shows the *towall* distribution with *wall* > 50 cm applied. The blue arrows indicating the full FV cut (Figures taken from [27]).

4.3.1 FHC/RHC $2R\pi^0$ samples

The 2-ring pi-zero ($2R\pi^0$) sample events are reconstructed by apfit instead of fitQun. This sample searches for neutral current (NC) interaction events with a single π^0 production. Data are available in both neutrino and antineutrino beam mode. The selection criteria are as follows:

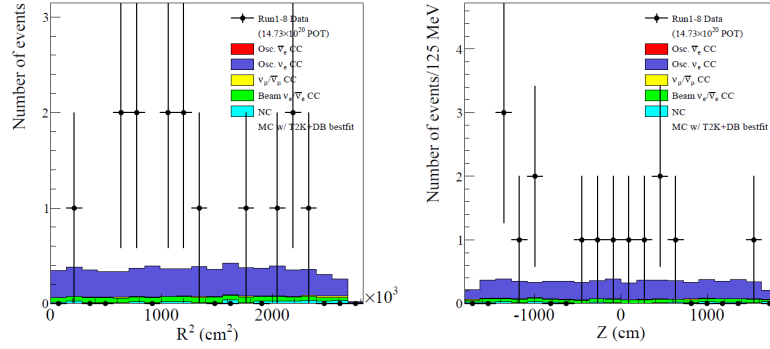


Figure 4.22: Reconstructed vertex distributions of FHC (left) and RHC (right) 1Re events for Run 1-8, after passing all selection cuts. Top graphs show the square of the distance of the vertices from the central vertical axis of the SK tank, and bottom graphs show the vertical position of the vertices (Figures taken from [27]).

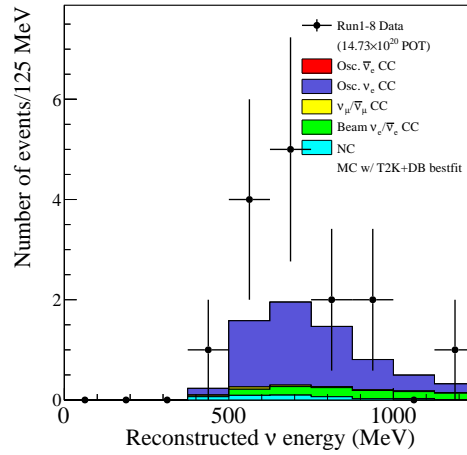


Figure 4.23: Reconstructed neutrino energy distribution of FHC ν_e CC $1\pi^+$ sample for Runs 1-8 (Figures taken from [27]).

1. FCFV condition:

- (a) $n_{hitac} < 16$,
- (b) $wall > 200$ cm,
- (c) $towall > 200$ cm.

2. Number of rings found by apfit is two.

3. Both rings are identified as electron-like by the PID algorithm.
4. No decay electrons.
5. Reconstructed invariant mass $85 \text{ MeV} < m_{inv} < 185 \text{ MeV}$.

Fig. 4.24 shows the number of ring distribution for all FCFV multi-ring events. The two-ring selection contains quite a lot of CC and NC non- 1π backgrounds. The subsequent cuts 3-5 successfully remove most background with a high selection efficiency of NC 1π events. After all selection cuts, 53 events are found in FHC data, and 9 events in RHC data.

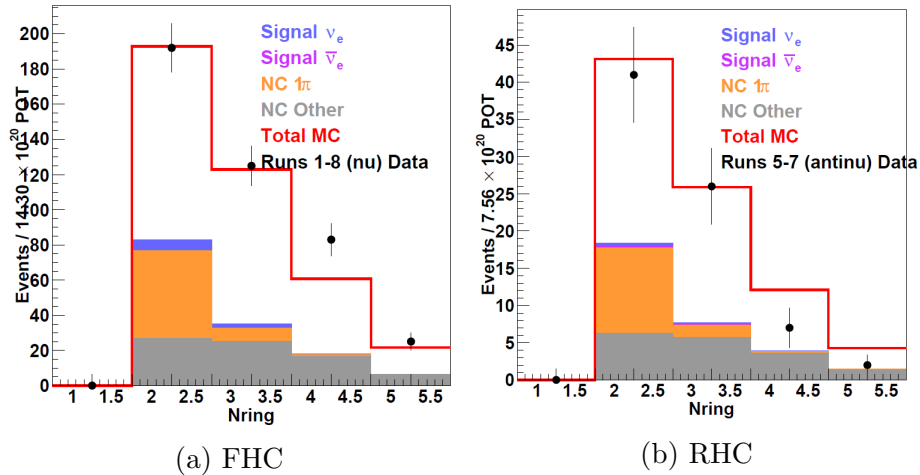


Figure 4.24: Number of ring distribution of all apfit FCFV multi-ring events for Runs 1-8 (Figures taken from [27]).

From MC simulations, 88% of events originate from NC interactions where a single π^0 is produced, either from Δ resonance or coherent pion production, and decays into 2γ . If we count all NC events, the overall NC purity reaches over 97%. Figs. 4.25 and 4.26 shows the reconstructed π^0 invariant mass, reconstructed π^0 momentum and true neutrino energy distributions.

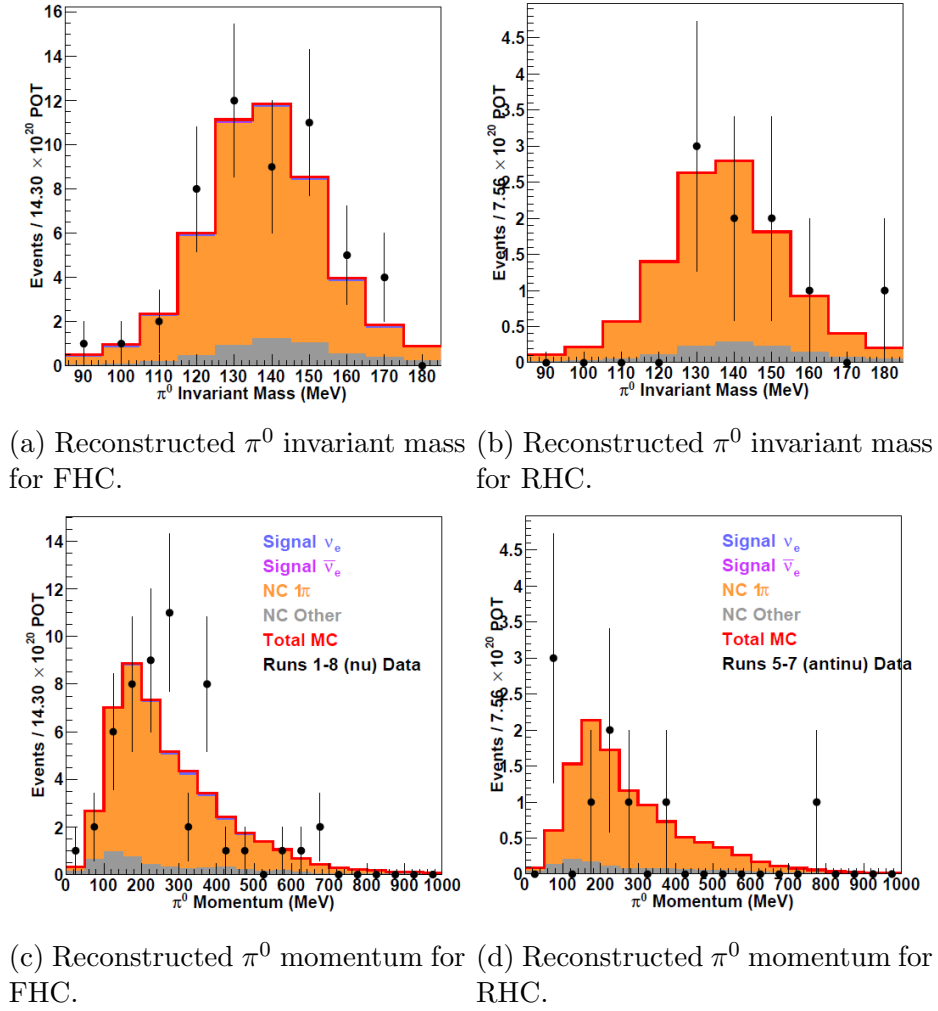
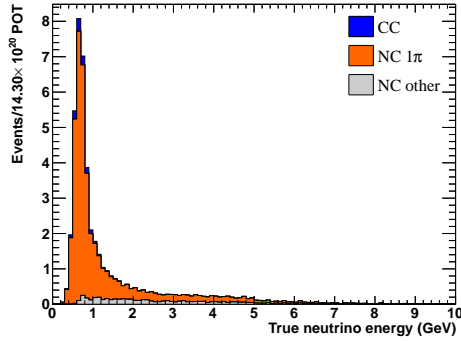


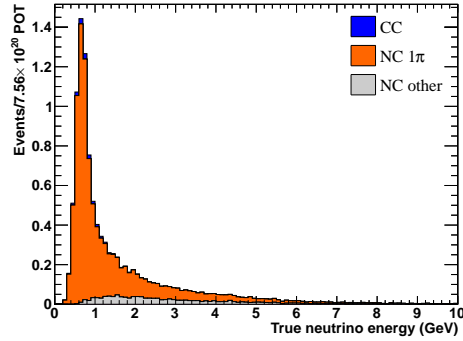
Figure 4.25: Reconstructed π^0 invariant mass and momentum of $2R\pi^0$ samples for Runs 1-8 (Figures taken from [27]).

The NC $2R\pi^0$ samples are actually useful in both 3-flavor and sterile oscillation analysis. For the 3-flavor analysis, the $2R\pi^0$ samples can help constraining π^0 background in the $1R\pi$ samples. On the other hand, any deficit in the NC samples might be regarded as the direct evidence of active-sterile neutrino oscillation.

Fig. 4.26 shows the true neutrino energy of the $2R\pi^0$ events, which spans over the whole T2K beam energy range. One important difference compared with the

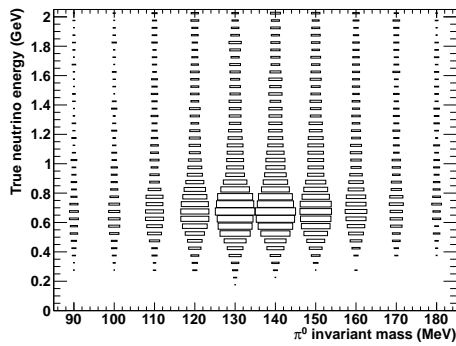


(a) True neutrino energy for FHC.

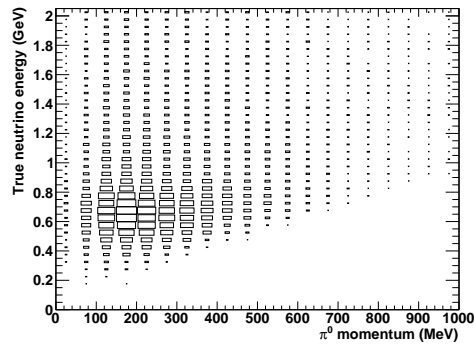


(b) True neutrino energy for RHC.

Figure 4.26: True neutrino energy distribution of $2R\pi^0$ samples.



(a) True neutrino energy vs. π^0 invariant mass.



(b) True neutrino energy vs. π^0 momentum.

Figure 4.27: Correlations between neutrino energy and π^0 invariant mass/momentum for FHC.

CC samples is that, we can only reconstruct the π^0 kinematics, which has little information about the neutrino energy. Fig. 4.27 shows, e.g. the correlations between reconstructed π^0 invariant mass/momentum and true neutrino energy. The $2R\pi^0$ samples are thus sensitive to θ_{24} and θ_{34} but not Δm_{41}^2 .

4.3.2 FHC NC γ de-excitation sample

This is another NC oscillation sample that searches for neutral current quasi-elastic (NCQE) interaction. In a neutrino-nucleus (^{16}O) NCQE interaction, usually a single nucleon is knock out:

$$\nu + {}^{16}\text{O} \rightarrow \nu + {}^{15}\text{N}^* + p,$$

$$\nu + {}^{16}\text{O} \rightarrow \nu + {}^{15}\text{O}^* + n.$$

The excited ^{15}N or ^{15}O atom emits a primary gamma of around 6 MeV, while the knocked-out nucleon (proton or neutron) further interacts to emit secondary gammas. These low energy events are reconstructed using special techniques instead of the standard algorithm `apfit` or `fitQun`.

NCQE cross-section

The NC γ de-excitation MC are generated separately from other samples. In the simulation, the total NCQE cross-sections $\sigma_{\nu^{16}\text{O}}$ are calculated by the impulse approximation and spectral function (SF):

$$\frac{d^2\sigma_{\nu^{16}\text{O}}}{d\Omega dE'_\nu} = \sum_{N=p,n} \int d\mathbf{p} dE P_N(\mathbf{p}, E) \frac{M}{E_N} \frac{d^2\sigma_{\nu N}}{d\Omega dE'_\nu}, \quad (4.3)$$

where E'_ν is the energy of the outgoing neutrino, $E_N = \sqrt{M^2 + \mathbf{p}^2}$, and $M = 0.938$ GeV is the nucleon mass. The total cross-section is written as an incoherent sum of the individual cross-sections on free nucleons $\frac{d^2\sigma_{\nu N}}{d\Omega dE'_\nu}$, weighted by the spectral function $P_N(\mathbf{p}, E)$.

The spectral function $P_N(\mathbf{p}, E)$ defines the probability of removing a nucleon of momentum \mathbf{p} and leaving the residual nucleus with energy $E + E_0 - M$, where E_0 is the ground state energy. In the nuclear shell model, the spectral function can be written as

$$P_N(\mathbf{p}, E) = \sum_i n_i |\phi_i(\mathbf{p})|^2 f_i(E - E_i), \quad (4.4)$$

where $\phi_i(\mathbf{p})$ and E_i are the wave function and the binding energy of the i -th state respectively. The occupation probability n_i and the probability density function $f_i(E - E_i)$ take into account the nucleon-nucleon (NN) correlations. Without NN correlations, $n_i = 1$ and $f_i(E - E_i) = \delta(E - E_i)$.

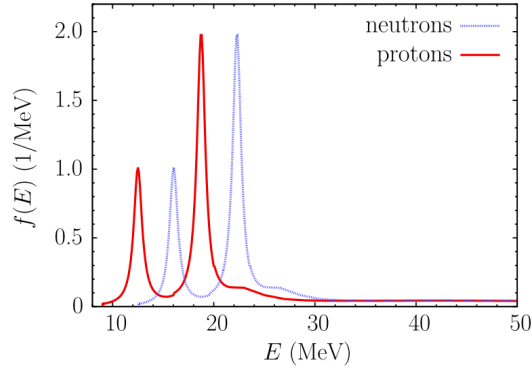


Figure 4.28: The binding energy spectra of ^{16}O spectral function. The two peaks correspond to the $1p_{1/2}$ -hole state (ground state) and $1p_{3/2}$ -hole state respectively. Neutron levels are deeper than protons' by about 3.54 MeV (Figure taken from [28]).

The oxygen spectral function is adopted from Benhar et al. [138, 139], calculated by the local density approximation (LDA) [140] with data from $(e, e'p)$ experiments [141].

Residual nucleus	$1p_{1/2}$	$1p_{3/2}$	$1s_{1/2}$	others
^{15}N	0.158	0.3515	0.1055	0.385
^{15}O	0.158	0.3515	0.1055	0.385

Table 4.2: The spectroscopic factors of each nucleon state in ^{16}O (Table taken from [28]).

Fig. 4.28 shows the energy spectra obtained by integrating $P_N(\mathbf{p}, E)$ over \mathbf{p} . The $1p_{1/2}$ and $1p_{3/2}$ states have sharp peaks but the $1s_{1/2}$ state is spread over very high energy due to NN correlations. The neutron and proton levels have the same shape with energy shifted by 3.54 MeV.

The probability of finding the residual nucleus in a specific shell state, called the spectroscopic factor, is obtained by integrating the energy spectra in Fig. 4.28. The factors for $1p_{1/2}$, $1p_{3/2}$ and $1s_{1/2}$ are integrated between $11.0 \leq E \leq 14.0$ MeV, $17.25 \leq E \leq 22.75$ MeV and $22.75 \leq E \leq 62.25$ MeV respectively. Table 4.2 summarizes the values for residual nuclei ^{15}N (proton-hole states) and ^{15}O (neutron-hole states).

Nuclear de-excitation

Following the NCQE nucleon knock-out, the residual nucleus may be excited and emit de-excitation gamma rays (and other particles) afterwards. The de-excitation branching ratios are mostly obtained from experimental data.

The $1p_{1/2}$ is the ground state, so no decay happens.

For the $1p_{3/2}$ proton hole state, there are three possible energy levels: 6.32 MeV, 9.93 MeV and 10.70 MeV. The branching ratios are assigned according to the experimental data of the $^{16}\text{O}(e, e'p)^{15}\text{N}$ [142]. The de-excitation gamma branching ratios are taken from [143]. The 6.32 MeV level only emits single gamma ray, while the 9.93

Residual nucleus	Energy level (MeV)	J_i^π	Ratio	E_γ (MeV)	E_p (MeV)	Ratio	$\text{Br}(X_i^* \rightarrow \gamma + Y)$
^{15}N	6.32	$\frac{3}{2}^-$	0.869	6.32	—	1.0	0.869
	9.93	$\frac{3}{2}^-$	0.049	9.93	—	0.776 ± 0.019	0.038
				5.27+5.30	—	0.154 ± 0.015	0.008
				6.32	—	0.049 ± 0.012	0.002
				7.30	—	0.021 ± 0.008	0.001
	10.70	$\frac{3}{2}^-$	0.082	—	0.5	—	—
^{15}O	6.18	$\frac{3}{2}^-$	0.869	6.18	—	1.0	0.869
	9.61	$\frac{3}{2}^-$	0.049	—	0.5	—	—
	10.48	$\frac{3}{2}^-$	0.082	—	0.5	—	—

Table 4.3: Summary of the energy levels and gamma ray emission branching ratios for the $1p_{3/2}$ hole states (Table taken from [28]).

MeV level has several emission channels. The 10.70 MeV does not emit gamma but a free nucleon instead. For the $1p_{3/2}$ neutron hole state, there is no experimental data so the spectroscopic factors are assigned to be same as that of proton hole. However, only the 6.18 MeV level emits gamma ray at 86.9% branching ratio. Table 4.3 lists the branching ratio of the $1p_{3/2}$ hole states.

For the $1s_{1/2}$ proton hole state ($^{15}\text{N}^*$), the branching ratios are measured by the E148 experiment on $^{16}\text{O}(p, 2p)^{15}\text{N}$ reactions at the Research Center for Nuclear Physics (RCNP)[144–146]. The neutron-hole state ($^{15}\text{O}^*$), again, has not been measured intensively yet, so the branching ratios are assigned the same as that of the proton hole state. Since the energy levels of the $1s_{1/2}$ hole state are higher than the nucleon emission level, usually a nuclear fragmentation happens instead of gamma emission. The decay particles are further simulated to check whether there is de-excitation gamma. Fig. 4.29 shows, e.g. the branching ratios of $^{15}\text{N}^*$ for gamma rays with $E_\gamma > 3$ MeV.

Residual isotope	Energy level (MeV)	J^π	E_γ (MeV)	Ratio	Br($^{15}\text{N}^* \rightarrow \gamma + \text{Y}$)
^{13}C	3.09	$1/2^+$	3.09	100%	3.0%
	3.68	$3/2^+$	3.68	99.3%	4.2%
	3.85	$1/2^+$	3.09	1.20%	< 0.1%
			3.68	36.3%	1.7%
			3.85	62.5%	2.9%
^{12}C	4.44	2^+	4.44	100%	5.8%
^{14}N	g.s.	2^+	—	—	6.7%
	4.92	0^-	4.92	97%	5.0%
	5.11	2^-	5.11	79.9%	< 0.1%
	5.69	1^-	3.38	63.9%	2.9%
			5.69	36.1%	1.6%
	5.83	3^-	5.11	62.9%	0.3%
			5.83	21.3%	0.1%
	6.20	1^+	3.89	76.9%	< 0.1%
			6.20	23.1%	< 0.1%
	6.45	3^+	5.11	8.1%	0.2%
			6.44	70.1%	2.0%
^{14}C	7.03	2^+	7.03	98.6%	(6.6%)
	g.s.	2^+	—	—	1.1%
	6.09	1^-	6.09	100%	< 0.1%
	6.59	0^+	6.09	98.9%	< 0.1%
	6.73	3^-	6.09	3.6%	< 0.1%
			6.73	96.4%	0.4%
	6.90	0^-	6.09	100%	< 0.1%
	7.01	2^+	6.09	1.4%	< 0.1%
			7.01	98.6%	(6.6%)
	7.34	2^-	6.09	49.0%	2.8%
6.73			34.3%	2.0%	
			7.34	16.7%	1.0%

Figure 4.29: De-excitation modes of the ^{16}O proton hole $(s_{1/2})_p^{-1}$ state. Only gamma rays with $E_\gamma > 3$ MeV are shown (Figure taken from [29]).

Event reconstruction

To reconstruct a NCQE event, the SK low energy analysis tools[147] are used. The fitter, BONSAI (branch optimization navigating successive annealing iterations), performs a maximum likelihood fit to each vertex candidate against both Cherenkov signal and dark noise background hypotheses. The reconstructed energy threshold is set as 4 MeV which is the same as SK-IV solar neutrino analysis. The energy spectrum of signal events has a peak at around 6 MeV, so the 4 MeV threshold has a trigger efficiency above 99.5%. An upper limit of 30 MeV is set to eliminate the decay electron background.

Next, a timing cut is applied to select “in-timing” events that are within ± 100 ns from the beam bunch centers. A sample of “off-timing” background is also constructed by selecting events that are 5 to 500 μ sec before each neutrino spill arriving edge, and is used for the estimation of beam-unrelated background.

After that, a series of wall distance cuts and BONSAI fit goodness cuts are applied to remove the radioactivity background. Since most backgrounds appear near the ID wall, the vertex wall distance cuts should remove most of them. A FV cut is applied to reject events with vertices < 2 m away from the ID wall, and then two wall variables are defined: *dwall* is the distance from the reconstructed vertex to the nearest ID wall, and *effwall* is the distance from the reconstructed vertex along the backward of the reconstructed direction to the ID wall.

The vertex goodness parameter G_V and direction goodness parameter G_A from BONSAI fit are used to remove events with mis-reconstructed vertices. G_V is defined by the timing information of the PMT hits:

$$G_V = \frac{\sum_i w_i e^{-\frac{1}{2}\left(\frac{\Delta t_i}{\sigma}\right)^2}}{\sum_i w_i}, \quad (4.5)$$

with Δt_i be the PMT hit residual time:

$$\Delta t_i = t_i - \frac{|\vec{h}_i - \vec{x}|}{c'}, \quad (4.6)$$

where t_i is the PMT time, \vec{h}_i is the PMT position, \vec{x} is the reconstructed vertex and c' is the light velocity in water. Ideally we have $\Delta t_i \approx 0$ for all PMT hits for perfect vertex reconstruction. $\sigma = 3.0$ ns is the characteristic PMT timing resolution for a single photo-electron. The weighting factor w_i of the i -th hit PMT is used to reduce accidental dark noise:

$$w_i = e^{-\frac{1}{2}(\frac{\Delta t_i}{\sigma_w})^2}, \quad (4.7)$$

where $\sigma_w = 60$ ns is a much wider effective time resolution. A large G_V implies that Δt_i has narrow distribution and the vertex is reconstructed very precisely.

The direction (angular) goodness G_A assesses the azimuthal uniformity of the PMT hits relative to the reconstructed direction. It uses the KS test to calculate the maximum distance between the PMT data and uniform azimuthal emission hypothesis:

$$G_A = \frac{\max\{\angle_{uni}(i) - \angle_{data}(i)\}}{2\pi}, \quad (4.8)$$

where $\angle_{data}(i)$ is the azimuthal angle of the i -th PMT hit, $\angle_{uni}(i) = \frac{2\pi}{N_{50}} \times i$ is the angle of uniform azimuthal emission, and N_{50} is the number of PMT hits within a 50 ns time window.

The total event fit goodness is defined as $\text{ovaQ} \equiv G_V^2 - G_A^2$. Fig. 4.30 shows the G_V^2 vs. G_A^2 distributions for simulated beam events and beam-unrelated events which are mostly radioactive background. A cut at, e.g. $\text{ovaQ} = 0.2$ can effectively separate the signal from background events.

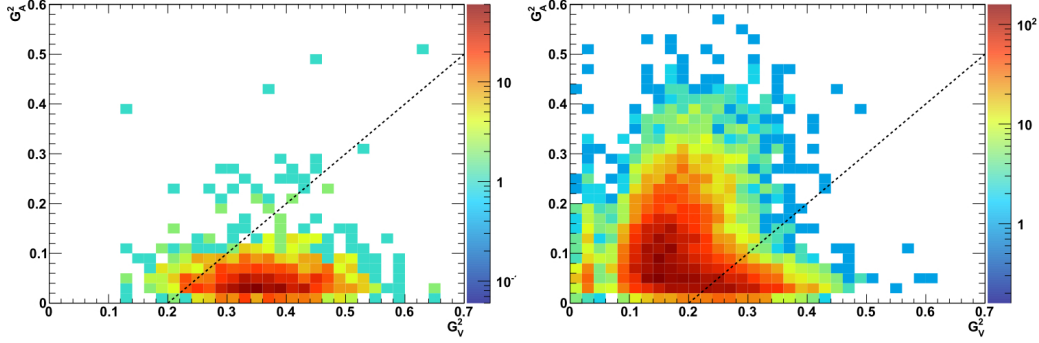


Figure 4.30: Distributions of G_V^2 vs. G_A^2 of NC γ de-excitation events with reconstructed energy between 4.5 and 5.0 MeV. The left plot shows the distribution of T2K beam ν_μ simulated events, while the right plot shows that of the off-timing data. The dotted lines show a cut at $ovaQ \equiv G_V^2 - G_A^2 = 0.2$ (Figures taken from [28]).

The cut values of d_{wall} , e_{fwall} and $ovaQ$ are optimized from run to run based on SK detector conditions, e.g. radioactive impurities of ID wall and water transparency, and the T2K beam power. This is done by maximizing the following figure-of-merit over the cut parameters:

$$FOM = \frac{N_{signal}}{\sqrt{N_{signal} + N_{background}}}. \quad (4.9)$$

Fig. 4.31 shows, e.g. the cut thresholds for T2K Run 4.

Finally, an event pre-activity cut is applied 0.2-20 μs before the event to reject low energy cosmic or atmospheric neutrino muons and their decay electrons. Only events with N_{30} (maximum number of PMT hits in 30 ns time window) less than 22 are accepted. A Cherenkov angle cut of $\theta_C > 34^\circ$ is used to reject low energy muon or pion that are produced in beam-related CC and NC others interactions, since they have smaller Cherenkov opening angle.

Fig. 4.32 shows the reconstructed gamma energy distributions of event candidates before and after the selection cuts for T2K Run 4. The selection efficiency of beam

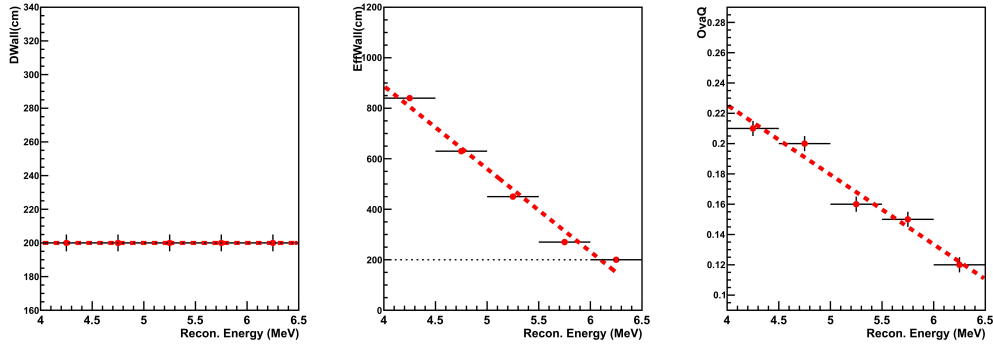
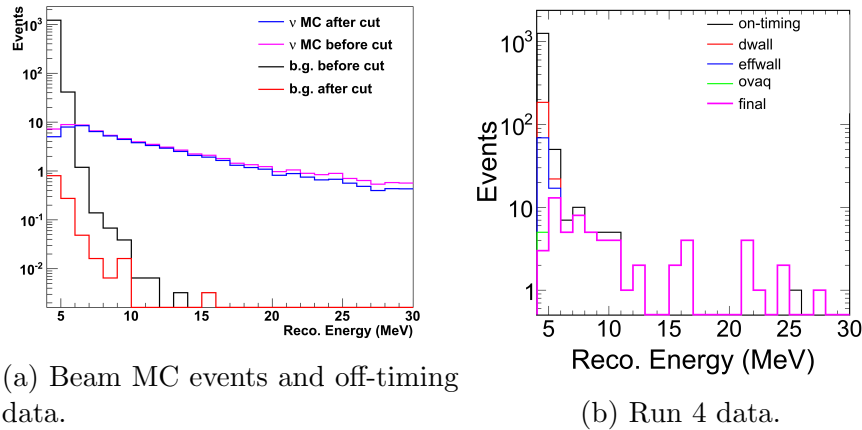


Figure 4.31: Cut threshold of d_{wall} , e_{fwall} and o_{vaQ} as a function of reconstructed energy for T2K Run4. Red points show the optimized cut values in each energy bin, while red dash lines show the fitting lines (Figures taken from [28]).

events is 89.6%, and the rejection rate of beam-unrelated background is more than 99.9%.



(a) Beam MC events and off-timing data.

(b) Run 4 data.

Figure 4.32: Distributions of reconstructed energy of $\text{NC}\gamma$ de-excitation events for T2K Run 4 before and after selection cuts (Figures taken from [28]).

Fig. 4.33 shows the reconstructed gamma energy and true neutrino energy distributions of the $\text{NC}\gamma$ de-excitation sample for T2K Run 1-4. The biggest background in this sample is the $\text{NC}1\pi^0$ production from Δ resonance, where the π^0 is absorbed in final state interaction and the excited nucleus emits de-excitation gamma similar

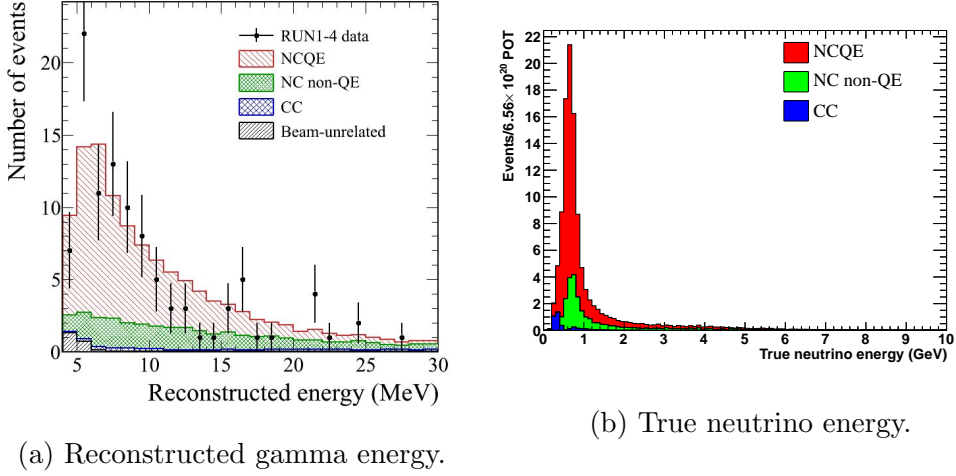


Figure 4.33: Distributions of FHC NC γ de-excitation sample for Runs 1-4.

to that in NCQE interaction. There are also a small amount of CC interaction backgrounds due to charged lepton production with a low momentum. The lepton might be mis-identified as a γ -ray event due to mis-constructed Cherenkov angle. Or, when a nucleon knock-out happens in a CCQE interaction, primary de-excitation γ -ray is emitted from the excited nucleus, and secondary γ -rays are produced by the free nucleon.

Currently only neutrino beam mode data from T2K Run 1-4 data are processed, and 102 events are found. From MC simulations, around 70% of events are from NCQE interactions, 25% from other NC interactions, and the rest are from CC interactions and beam-unrelated background.

Fig. 4.34 shows the correlation between reconstructed gamma energy and true neutrino energy. Again the reconstructed gamma energy distribution has no information about incoming neutrino energy, so it has no sensitivity on Δm_{41}^2 .

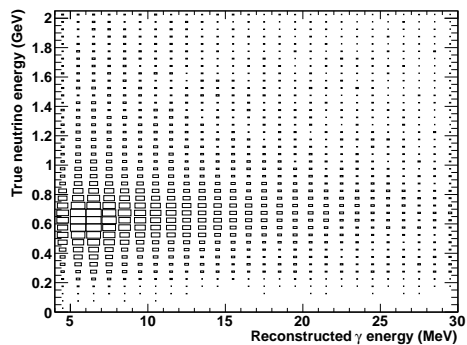


Figure 4.34: Correlation between reconstructed gamma energy and true neutrino energy of FHC NC γ de-excitation sample.

4.4 Event summary

Table 4.4 summarizes the number of events for each CC and NC sample.

Sample	1R μ		1R e		ν_e CC1 π^+	2R π^0		NC γ de-excitation
Beam mode	FHC	RHC	FHC	RHC	FHC	FHC	RHC	FHC
No. of events	240	68	74	7	15	53	9	102

Table 4.4: Number of events observed in each CC and NC oscillation samples.

Chapter 5

Oscillation analysis framework

The objective of our study is to constrain the sterile mixing parameters. We do this by performing a joint oscillation analysis with all the SK samples discussed above. While we only explicitly use SK data, many of the systematic parameters are actually constrained by the BANFF fit with the near detector data and propagated to the far detector. Below we describe our analysis strategy and the systematic parameters applied to this analysis.

5.1 Event binning

In order to maximize the sensitivity to various oscillation parameters, events in different oscillation samples are binned uniquely.

For the $1R\mu$ samples, events are binned one-dimensionally in reconstructed energy E_ν^{rec} . The binning is dense in the first few GeV in order to map out accurately the first oscillation minimum at 0.6 GeV. The event rate is much lower in the high energy region due to the off-axis, narrow beam energy spectrum, and the bin width

Range	Size of one bin	Number of bins
0 - 3 GeV	0.05 GeV	60
3 - 4 GeV	0.25 GeV	4
4 - 6 GeV	0.5 GeV	4
6 - 10 GeV	1 GeV	4
10 - 30 GeV	20 GeV	1

Table 5.1: Binning used for reconstructed energy of 1R μ samples.

is therefore larger.

For the 1Re and ν_e CC1 π^+ samples, events are binned two-dimensionally in electron momentum p_e and scattering angle θ_{beam} with respect to the beam. The p - θ distribution is different between signal and background categories, hence providing additional discrimination power between signal and background events.

For the 2R π^0 and FHC NC γ de-excitation examples, events are binned in π^0 momentum and reconstructed gamma energy respectively. However, since the event distributions have little dependence on neutrino energy, these samples mostly matter in the overall rate but not shape.

The full binning scheme for all samples is shown in Table 5.1 - 5.4.

5.2 Monte Carlo Predictions

The oscillation fit mainly works by comparing real data with MC expectations assuming certain oscillation parameters. The MC used for prediction is generated by feeding NEUT neutrino interaction products into SKDETSIM, then processing the results by the standard reconstruction algorithm and storing the neutrino events in dedicated format. Some important features are discussed here.

Range	Size of one bin	Number of bins
0 - 1500 MeV/c	100 MeV/c	15
0 - 140 degree	10 degree	14
140 - 180 degree	40 degree	1

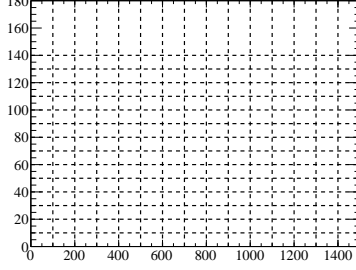


Table 5.2: Binning used for reconstructed lepton momentum and angle of 1Re samples and FHC ν_e CC1 π sample.

Range	Size of one bin	Number of bins
0 - 1500 MeV/c	100 MeV/c	15

Table 5.3: Binning used for reconstructed π^0 momentum of 2R π^0 samples.

5.2.1 Neutrino propagation modes

Neutrino events are classified into six types of neutrino propagation modes: $\nu_\mu \rightarrow \nu_\mu$, $\bar{\nu}_\mu \rightarrow \bar{\nu}_\mu$, $\nu_e \rightarrow \nu_e$, $\bar{\nu}_e \rightarrow \bar{\nu}_e$, $\nu_\mu \rightarrow \nu_e$, $\bar{\nu}_\mu \rightarrow \bar{\nu}_e$. $\nu_\tau(\bar{\nu}_\tau)$ oscillations are ignored because of the relatively high energy CC interaction threshold. $\nu_e \rightarrow \nu_\mu$ and $\bar{\nu}_e \rightarrow \bar{\nu}_\mu$ transitions are also negligible. Since all neutrino flavors undergo NC interactions at the same rate, we only consider NC events in $\nu_\mu \rightarrow \nu_\mu$ and $\bar{\nu}_\mu \rightarrow \bar{\nu}_\mu$ modes.

Range	Size of one bin	Number of bins
4 - 30 MeV	1 MeV	26

Table 5.4: Binning used for reconstructed γ energy of FHC NC γ de-excitation sample.

5.2.2 Neutrino interaction categories

In MC files, NEUT neutrino interaction modes are stored for each neutrino event. For analysis purpose, we group the NEUT modes into nine categories: charged-current quasi-elastic interactions (CCQE), 2p2h, charged-current interactions associated with single-pion resonant production (CC1 π), charged-current coherent pion production (CC coherent), other charged-current processes (CC other), neutral current interactions with single pion production (NC1 π), NC coherent pion production (NC coherent), NC1 γ (NC1 γ), and other neutral current interactions (NC other). Table 5.5 shows the relationship between the NEUT modes and the nine interaction categories.

NEUT interaction mode	Category in analysis
1	CCQE
2	2p2h
11-13	CC1 π
16	CC coherent
17-29	CC other
31-34	NC1 π
36	NC coherent
38,39	NC1 γ
37,40-52	NC other

Table 5.5: Definition of neutrino interaction categories in this analysis. NEUT interaction modes of anti-neutrinos are negative. NCQE events (NEUT mode 51,52) are classified as NC other.

5.2.3 True neutrino energy binning

The true neutrino energy E_ν^{true} has 84 bins. Again it has more bins around the oscillation minimum at 0.6 GeV (see Table. 5.6).

Range	Size of one bin	Number of bins
0 - 0.3 GeV	0.05 GeV	6
0.3 - 1 GeV	0.025 GeV	28
1 - 3 GeV	0.05 GeV	40
3 - 3.5 GeV	0.1 GeV	5
3.5 - 4 GeV	0.5 GeV	1
4 - 5 GeV	1 GeV	1
5 - 7 GeV	2 GeV	1
7 - 10 GeV	3 GeV	1
10 - 30 GeV	20 GeV	1

Table 5.6: Binning used for true neutrino energy E_ν^{true} .

5.2.4 Input preparation

To reduce the computation time for an oscillation fit, MC neutrino events are grouped into histograms based on propagation modes, interaction categories and true energies as described above. In each histogram, events are binned according to sample type as in Sec. 5.1. In order to correctly account for the event contribution, different weights are applied to the MC events.

First, the near detector measures accurately the neutrino beam flux as a function of neutrino flavors and energy. The run to run beam power variations are taken into account to provide an overall weight at a certain beam energy.

The second weight is related to the neutrino interaction model. The default CCQE MC events are generated using the spectral function (SF) cross-section model, while later studies found that the use of relativistic Fermi gas (RFG) model and the Bernstein parameterization of random phase approximation (BeRPA) gives better agreement with external data. Therefore a reweighting is applied to correct the cross-section weight (see Sec. 5.3.2).

Finally, two extra weights are applied: true NC1 γ events are given double weight based on recent findings [148], and CC coherent pion events (NEUT code 16) have

$E_\pi(\text{GeV})$	Weight
0-0.25	0.135
0.25-0.5	0.4
0.5-0.75	0.294
0.75-1.0	1.206

Table 5.7: Weights applied to CC coherent pion events.

been tuned as a function of the pion energy to the Berger-Sehgal model [149] following recent MINER ν A results (see Table 5.7).

5.2.5 Oscillation probability calculation

The standard analysis uses the Prob3++[150] software package for probability calculation. The package employs the Barger et al.[151] model to calculate the full three-flavor oscillation probability analytically. Matter effect in the Earth is included with the radial density structure given by the PREM model[152].

For the sterile analysis, the vacuum “3+1” oscillation probability without approximation in Sec. 2.2.3 is added, assuming eV scale sterile neutrino with $\Delta m_{41}^2 \lesssim 1\text{eV}^2$. Also, with four mass eigenstates, the matter effect included Hamiltonian (similar to Eq. 2.13) cannot be diagonalized analytically, so numerical methods has to be employed. However, for T2K beam energy and baseline, matter effect has little impacts on the oscillation spectra. We simply use the vacuum probability in this study.

5.2.6 Event rate calculation

In the oscillation analysis, the expected event rates of all samples can be calculated for a specific set of oscillation parameters and systematic parameters. To do this,

the input produced in Sec. 5.2.4 is first loaded:

$$M_b(C, I, E_\nu^{\text{true}}), \quad (5.1)$$

where b is the sample-specific event bin, C is the neutrino propagation mode, I is the interaction mode, E_ν^{true} is the true neutrino energy.

Oscillation probabilities $P_{osc}(C, I, E_\nu^{\text{true}}; o)$ are then applied to produce the event templates $T_b(C, I, E_\nu^{\text{true}}; o)$:

$$T_b(C, I, E_\nu^{\text{true}}; o) = M_b(C, I, E_\nu^{\text{true}}) P_{osc}(C, I, E_\nu^{\text{true}}; o), \quad (5.2)$$

where o are the oscillation parameters. For $\bar{\nu}_\mu \rightarrow \bar{\nu}_\mu$ mode, $P(\bar{\nu}_\mu \rightarrow \bar{\nu}_\mu)$ is applied on CC interactions and $1 - P(\bar{\nu}_\mu \rightarrow \bar{\nu}_s)$ is applied on NC interactions:

$$\begin{aligned} P_{osc}(\bar{\nu}_\mu \rightarrow \bar{\nu}_\mu, \text{CC}, E_\nu^{\text{true}}; o) &= P(\bar{\nu}_\mu \rightarrow \bar{\nu}_\mu) \\ &\approx 1 - \sin^2 2\theta_{23} \cos 2\theta_{24} \sin^2 \frac{\Delta m_{31}^2 L}{4E_\nu^{\text{true}}} - \sin^2 2\theta_{24} \sin^2 \frac{\Delta m_{41}^2 L}{4E_\nu^{\text{true}}}, \end{aligned} \quad (5.3)$$

$$\begin{aligned} P_{osc}(\bar{\nu}_\mu \rightarrow \bar{\nu}_\mu, \text{NC}, E_\nu^{\text{true}}; o) &= 1 - P(\bar{\nu}_\mu \rightarrow \bar{\nu}_s) \\ &\approx 1 - \sin^2 \theta_{34} \sin^2 2\theta_{23} \sin^2 \frac{\Delta m_{31}^2 L}{4E_\nu^{\text{true}}} - \cos^2 \theta_{34} \sin^2 2\theta_{24} \sin^2 \frac{\Delta m_{41}^2 L}{4E_\nu^{\text{true}}}. \end{aligned} \quad (5.4)$$

For $\bar{\nu}_e \rightarrow \bar{\nu}_e$ mode, $P(\bar{\nu}_e \rightarrow \bar{\nu}_e)$ is applied on CC interactions:

$$P_{osc}(\bar{\nu}_e \rightarrow \bar{\nu}_e, \text{CC}, E_\nu^{\text{true}}; o) = P(\bar{\nu}_e \rightarrow \bar{\nu}_e) \approx 1 - \sin^2 2\theta_{13} \sin^2 \frac{\Delta m_{31}^2 L}{4E}. \quad (5.5)$$

For $\bar{\nu}_\mu \rightarrow \bar{\nu}_e$ mode, $P(\bar{\nu}_\mu \rightarrow \bar{\nu}_e)$ is applied on CC interactions:

$$P_{osc}(\bar{\nu}_\mu \rightarrow \bar{\nu}_e, \text{CC}, E_\nu^{\text{true}}; o) = P(\bar{\nu}_\mu \rightarrow \bar{\nu}_e) \approx \sin^2 2\theta_{13} \cos^2 \theta_{24} \sin^2 \theta_{23} \sin^2 \frac{\Delta m_{31}^2 L}{4E}. \quad (5.6)$$

In addition, when systematic parameters f are varied from their nominal values, there will be an extra reweighting factor $R_b(C, I, E_\nu^{\text{true}}; f)$ applied to the templates. Therefore the predicted number of event in the bin b is given by

$$N_{\text{pred}}^b = \sum_{C, I, E_\nu^{\text{true}}} T_b(C, I, E_\nu^{\text{true}}; o) R_b(C, I, E_\nu^{\text{true}}; f). \quad (5.7)$$

5.3 Systematic parameters

In our sterile neutrino analysis, a large number of systematic parameters are implemented. In general, they can be classified into three categories: beam flux, neutrino interaction and cross-section, and Super-K detector uncertainties. Many of them are well-constrained by the near detector and devoted SK studies. A covariance matrix taking into account the correlation of these parameters is input into the analysis code, and is used in the calculation of likelihood values. Fig. 5.1 shows the error size and correlation of all the 133 systematic parameters.

5.3.1 Beam flux parameters

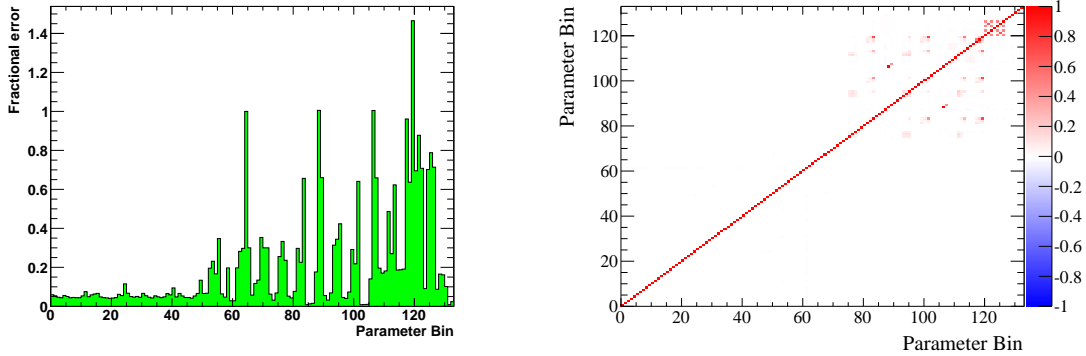
The uncertainties on the neutrino flux are divided into 50 parameters by neutrino flavor, true energy and beam mode (see Table 5.8 and 5.9). The beam parameters are incorporated into the BANFF framework and the uncertainties are reduced through constraints from the near detector data.

Event category	Beam ν flavor	Energy binning (GeV)	# of bins
Oscillated ν_e, ν_μ	ν_μ flavor	0-0.4, 0.4-0.5, 0.5-0.6, 0.6-0.7, 0.7-1.0, 1.0-1.5, 1.5-2.5, 2.5-3.5, 3.5-5.0, 5.0-7.0, 7.0-30.0	11
Oscillated $\bar{\nu}_e, \bar{\nu}_\mu$	$\bar{\nu}_\mu$ flavor	0-0.7, 0.7-1.0, 1.0-1.5, 1.5-2.5, 2.5-30.0	5
ν_e	ν_e flavor	0-0.5, 0.5-0.7, 0.7-0.8, 0.8-1.5, 1.5-2.5, 2.5-4.0, 4.0-30.0	7
$\bar{\nu}_e$	$\bar{\nu}_e$ flavor	0-2.5, 2.5-30.0	2

Table 5.8: Binning of beam flux systematic parameters for neutrino mode.

Event category	Beam ν flavor	Energy binning (GeV)	# of bins
Oscillated ν_e, ν_μ	ν_μ flavor	0-0.7, 0.7-1.0, 1.0-1.5, 1.5-2.5, 2.5-30.0	5
Oscillated $\bar{\nu}_e, \bar{\nu}_\mu$	$\bar{\nu}_\mu$ flavor	0-0.4, 0.4-0.5, 0.5-0.6, 0.6-0.7, 0.7-1.0, 1.0-1.5, 1.5-2.5, 2.5-3.5, 3.5-5.0, 5.0-7.0, 7.0-30.0	11
ν_e	ν_e flavor	0-2.5, 2.5-30.0	2
$\bar{\nu}_e$	$\bar{\nu}_e$ flavor	0-0.5, 0.5-0.7, 0.7-0.8, 0.8-1.5, 1.5-2.5, 2.5-4.0, 4.0-30.0	7

Table 5.9: Binning of beam flux systematic parameters for anti-neutrino mode.



(a) Error (square root of diagonal terms) (b) Uncertainties correlation matrix

Figure 5.1: Error size and correlations for all the 133 systematic parameters of the analysis. Parameters are 1-50: beam flux, 51-72: neutrino interaction and cross-section, 73-132: Super-K detector, 133: SK p-scale parameters.

5.3.2 Neutrino interaction and cross-section parameters

The BANFF fit has parameterized 20 parameters to describe the uncertainties in neutrino interaction model. Although all these parameters are included in the near detector fit, not all receive a significant constraint. On the other hand, we have added two non-BANFF parameters to take care the cross-section normalization error for NC1 π and NCQE interactions. A full list of these parameters can be found in Table 5.10. The type “shape” means its effect is energy-dependent, while “norm” is energy-independent normalization parameter.

As mentioned in Sec. 5.2.4, CCQE interactions are described by the RFG model with relativistic RPA applied. The two fundamental parameters, axial mass M_A^{QE} and Fermi momentum p_F on oxygen, are allowed to vary. The axial mass enters the formula of CCQE cross-section for free nucleon in the form of axial vector form factor:

$$F_A = g_A \left(1 + \frac{Q^2}{(M_A^{QE})^2} \right)^{-2}, \quad (5.8)$$

Parameter	interaction categories applied	type	Nominal value & uncertainty
M_A^{QE}	CCQE	shape	1.13 ± 0.08 (GeV/c ²)
p_F	CCQE	shape	204.98 ± 15.08 (MeV/c)
2p2h norm. ν	2p2h	norm	1.50 ± 0.20
2p2h norm. $\bar{\nu}$	2p2h	norm	0.73 ± 0.23
2p2h norm. C to O	2p2h	norm	0.96 ± 0.17
2p2h shape O	2p2h	shape	1.00 ± 0.35
C_A^{RES}	CC π and NC1 π	shape	0.98 ± 0.06
M_A^{RES}	CC π and NC1 π	shape	0.81 ± 0.04 (GeV/c ²)
BG_A^{RES}	CC π and NC1 π	shape	1.31 ± 0.26
$\sigma_{\nu_e} / \sigma_{\nu_\mu}$	CC	norm*	1.00 ± 0.03
$\sigma_{\bar{\nu}_e} / \sigma_{\bar{\nu}_\mu}$	CC	norm*	1.00 ± 0.03
CC other shape	CC other	shape	0.39 ± 0.20
CC coherent	CC coherent	norm	0.87 ± 0.28
NC coherent	NC coherent	norm	0.94 ± 0.30
NC 1 γ	NC 1 γ	norm*	1.00 ± 1.00
NC other	NC other	norm*	1.00 ± 0.30
BeRPA A	CCQE	shape	0.69 ± 0.06
BeRPA B	CCQE	shape	1.60 ± 0.12
BeRPA C	CCQE	shape	0.96 ± 0.13
BeRPA D	CCQE	shape	0.87 ± 0.35
NC1 π	NC1 π	norm [^]	1.00 ± 0.30
NCQE	NC other [#]	norm [^]	1.00 ± 0.30

Table 5.10: Summary of the neutrino interaction parameters using the results of ND280 fit. * Errors are not constrained by the near detector. [^] Non-BANFF errors added for the sterile analysis. [#] NCQE error instead of NC other error applies for FHC NC γ de-excitation sample.

where Q^2 is the four-momentum transfer and $g_A = -1.267$ is the axial-vector weak coupling constant. The Fermi momentum is a parameter in the Fermi gas model, where the knocked-out nucleon needs to have large enough momentum to escape the nucleus.

Since it is found that one correction term for relativistic RPA is not flexible enough, an effective RPA function (BeRPA) is developed to have the same Q^2 dependence as the Nieves RPA model[121] and cover the theoretical errors at the same time. The parameterization is given as

$$f(x) = \begin{cases} A(1 - x')^3 + 3B(1 - x')^2x' + 3(C - 1)(1 - x')x'^2 + Cx'^3, & x < U \\ 1 + (C + \frac{UD(C-1)}{3}) \exp(-D(x - U)), & x > U \end{cases} \quad (5.9)$$

where $x = Q^2$, $x' = x/U$. Five parameters named A, B, C, D and U allows variation of various Q^2 region of the RPA function but $U = 1.2 \text{ GeV}^2$ is fixed in the analysis. A nominal BeRPA weight is assigned in the cross-section weight, and the variation from the nominal value is taken care by the four parameters.

The 2p2h interactions have four parameters. There is one overall normalization parameter for ν and $\bar{\nu}$ interactions respectively. A normalization parameter (2p2h norm. C to O) of 20% is introduced to take into account the difference between carbon and oxygen. A shape parameter is introduced to test the effects of artificially redistributing the 2p2h cross section strength between “non-Delta like” to “Delta like” 2p2h model.

For CC1 π and NC1 π interactions, there are systematic parameters that change the scaling factor for the axial form factor C_A^5 , the resonant axial vector mass M_A^{RES} , and the isospin-1/2 ($I_{1/2}$) continuum background (BG_A^{RES}). C_A^5 affects the scale of

the axial form factor at $Q^2 = 0$, and M_A^{RES} affects both the rate and Q^2 shape of interactions. BG_A^{RES} is responsible for the scaling of the non-resonance process in $I_{1/2}$ interaction channels. In addition MiniBooNE and MINER ν A data, the parameters are also tuned against bubble chamber experiments ANL[153, 154] and BNL[155–157] to provide priors for BANFF.

There are separated normalization parameters for CC coherent, NC coherent, NC1 γ and NC other interactions, and shape parameter for CC other interactions. The cross-section ratio uncertainties $\sigma_{\nu_e}/\sigma_{\nu_\mu}$ and $\sigma_{\bar{\nu}_e}/\sigma_{\bar{\nu}_\mu}$ are applied to ν_e and $\bar{\nu}_e$ events, because only ν_μ and $\bar{\nu}_\mu$ cross-sections are directly constrained by the near-detector fit.

In our sterile analysis, the 2R π^0 and NC γ de-excitation samples contain mostly NC1 π and NCQE events respectively (NCQE interaction is classified into NC other interaction category), therefore two relevant cross-section normalization parameters are added. They are not constrained by the BANFF fit, and we determined to assign them a conservative value of 30% because there are no accurate data constraining the cross-section values.

The NC1 π normalization error is set as the same size as NC coherent normalization error, where these two parameters are usually correlated in measurements. The value of 30% is the also same as in previous oscillation analysis[158, 159]. Comparison of NEUT with experimental data such as MiniBooNE[160] shows that it is a reasonable value. The T2K off-axis Pi-zero detector (P \emptyset D) is designed to measure the NC1 π^0 events in water, and we expect the cross-section error can be reduced with more data in the future.

For the NCQE interactions, there is publication that estimates the theoretical uncertainty of NCQE cross-sections by comparing the cross-section values calculated

Neutrino flavor	Interaction mode	Momentum Binning (GeV/c)
Osc. $\nu_e/\bar{\nu}_e$	CC	0-0.3, 0.3-0.7, 0.7-1.5
$\nu_\mu/\bar{\nu}_\mu$	CC	0-0.3, 0.3-0.7, 0.7-1.5
Beam $\nu_e/\bar{\nu}_e$	CC	0-0.3, 0.3-0.7, 0.7-1.5
All	NC	0-0.3, 0.3-0.7, 0.7-1.5

Table 5.11: Binning of SK detector systematic parameters for 1Re and ν_e CC1 π samples.

by different models[161]. Among them, the biggest difference is around 30%, between spectral function (SF) and relativistic Green's functions (RGF). The same author has also published results that compare SF cross-section with several experimental data sets [162]. The reported difference is around 20% when compared to MiniBooNE, but the measurement is on carbon but not oxygen, so we may need to scale up the error. Based on above findings, we determined to set the error as 30%. MiniBooNE has also reported measurements on NCQE/CCQE cross-section ratio on CH₂[163], but the reported errors are quite large that it does not help much in reducing our error size. There is analysis going on within T2K to measure the NCQE cross-section with ND280 FGD, and we might expect error reduction by then.

5.3.3 Super-K detector uncertainties

The SK detector uncertainties contain detector efficiency uncertainties, final state interaction (FSI) and secondary interaction (SI) model uncertainties, photo-nuclear (PN) effect uncertainties, and energy scale uncertainty. All these uncertainties (except energy scale) are combined by summing the corresponding covariance matrices. Events are divided into different modes and bins based on sample type. This gives us a total of $12 \times 3 + 6 \times 2 + 4 \times 2 + 4 = 60$ bins which are summarized in Table 5.11 - 5.14.

Neutrino flavor	Interaction mode	Energy Binning (GeV/c)
$\nu_\mu/\bar{\nu}_\mu$	CCQE	0-0.4, 0.4-1.1, 1.1-30.0
$\nu_\mu/\bar{\nu}_\mu$	CC Other	0-30.0
$\nu_e/\bar{\nu}_e$	CC	0-30.0
All	NC	0-30.0

Table 5.12: Binning of SK detector systematic parameters for $1R\mu$ samples.

Neutrino flavor	Interaction mode
Osc. $\nu_e/\bar{\nu}_e$	CC
$\nu_\mu/\bar{\nu}_\mu$	CC
Beam $\nu_e/\bar{\nu}_e$	CC
All	NC

Table 5.13: Binning of SK detector systematic parameters for $2R\pi^0$ samples.

Neutrino flavor	Interaction mode
All	NC other (NCQE)
All	All NC interactions except NC other
All	CC
Beam unrel.	-

Table 5.14: Binning of SK detector systematic parameters for $NC\gamma$ de-excitation sample. Beam unrel. refers to background events that are not due to neutrino interactions, e.g. PMT dark noises, radioactive decay, etc.

Event Type	Selection criteria
ν_e CC1e	ν_e CC && $N_{\pi^0}==0$ && $N_{\pi^\pm}==0$ && $N_P==0$
ν_e CC other	ν_e CC && $!(\nu_e$ CC1e)
ν_μ CC1 μ	ν_μ CC && $N_{\pi^0}==0$ && $N_{\pi^\pm}==0$ && $N_P==0$
ν_μ CC	ν_μ CC && $N_{\pi^0}==0$ && $!(\nu_\mu$ CC1 μ)
ν_μ CC $\mu\pi^0$ other	ν_μ CC && $N_{\pi^0} > 0$
NC 1 π^0	NC && $!($ NC γ) && $N_{\pi^0}==1$ && $N_{\pi^\pm}==0$ && $N_P==0$
NC π^0 other	NC && $!($ NC γ) && $N_{\pi^0} \geq 1$ && $!($ NC 1 π^0)
NC γ	NEUT mode == 38 NEUT mode == 39
NC 1 π^\pm	NC && $!($ NC γ) && $N_{\pi^0}==0$ && $N_{\pi^\pm}==1$ && $N_P==0$
NC other	NC && $!($ NC 1 π^0) && $!($ NC π^0 other) && $!($ NC γ) && $!($ NC 1 π^\pm)

Table 5.15: Criteria for event categorization based on final state information. The number of charged pions (N_{π^\pm}) and protons (N_P) only includes particles produced with momentum above Cherenkov threshold set at 156.0 MeV/c and 1051.0 MeV/c respectively.

SK detector efficiency uncertainties

For all samples except NC γ de-excitation, the SK detector efficiency uncertainties are calculated by evaluating the fractional change of the number of events and correlation between event categories when the selection cut parameters are varied with a ToyMC method. These uncertainties describe the mis-identification of the observed event topologies (final state FS) with designed topological cuts. The FS modes are listed in Table 5.15. The errors for different FS modes are evaluated by cosmic muon control samples, atmospheric neutrino samples and hybrid- π^0 samples.

Cosmic muon control samples The cosmic muon samples are to used assess both vertex and decay electron cut uncertainties. For vertex uncertainty, the *wall* distributions of the entering cosmic muon events are studied. We know the true *wall* value should be 0 cm, so the reconstructed *wall* values give the vertex residual

	Data	Reweighted MC	Uncertainty
Tagging efficiency (η_{tag})	$84.7 \pm 0.2 \%$	$86.0 \pm 0.2 \%$	1%
Decay electron cut	$0.21 \pm 0.02 \%$	$(9.5 \pm 0.6) \times 10^{-3} \%$	0.2%

Table 5.16: Decay electron efficiency and estimated systematic uncertainties.

distribution. Comparing between data and MC in Fig. 5.2, a 2.5 cm difference is observed. Simulations are done to shift the reconstructed *wall* values by ± 2.5 cm to see the change in the number of events in each sample, and less than 0.5% uncertainty is observed. The decay electron cut uncertainty is studied by the stopping muon sample that is reweighed to better match T2K's kinematics. The tagging efficiency and fake rate are evaluated for MC and data (see Fig. 5.3), and the uncertainties are summarized in Table 5.16. The uncertainty for ν_e samples is calculated by attributing both the fake rate systematic of events without a true decay electron and the tagging efficiency of events with a true decay electron:

$$\sigma_{\text{decay-e}}^2 = (P_{\text{true decay-e}} \times \sigma_{\text{tag}})^2 + ((1 - P_{\text{true decay-e}}) \times \sigma_{\text{fake}})^2, \quad (5.10)$$

where σ_{tag} and σ_{fake} are the values given in Table 5.16, and this gives a systematic uncertainty of 0.2% for both beam and signal ν_e samples. Furthermore, the systematic uncertainty on the mis-identification (mis-ID) of muons as electrons is estimated. The muon mis-ID rate is defined as

$$\eta_{\mu\text{-misID}} = \frac{N_{e\text{-like}}^{1d\text{cye}}}{N_{e\text{-like}}^{1d\text{cye}} + N_{\mu\text{-like}}^{1d\text{cye}}}, \quad (5.11)$$

where $N_{e\text{-like}}^{1d\text{cye}}$ ($N_{\mu\text{-like}}^{1d\text{cye}}$) is the number of e -like (μ -like) events with 1 decay electron. The muon mis-ID rate is measured to be $3.9 \pm 0.2\%$ for data and $3.0 \pm 0.2\%$ for reweighted MC (see Fig. 5.4), so the systematic uncertainty is around 30%.

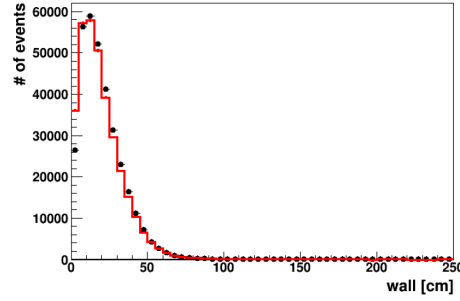


Figure 5.2: The normalized *wall* distributions of stopping cosmic muons for MC simulation (red) and data (black) (Figures taken from [30]).

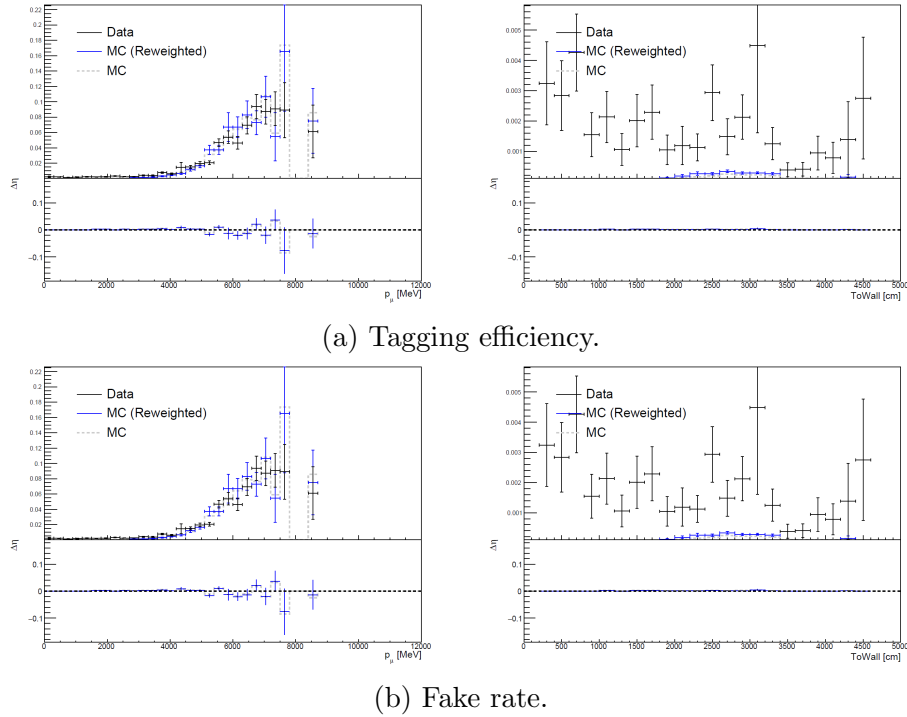


Figure 5.3: Decay electron tagging efficiency and fake rate as a function of muon momentum (left) and *towall* (right) (Figures taken from [30]).

Atmospheric neutrino fit The atmospheric neutrino data in SK is used to estimate the systematic parameters \mathbf{d}_{SK} related to the fitQun reconstruction performance. The \mathbf{d}_{SK} parameters are varied to maximize the likelihood between MC

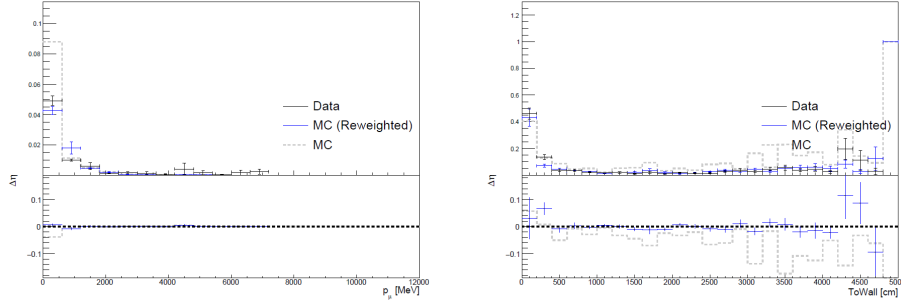


Figure 5.4: Muon mis-identification rate for stopping muon data and MC, as a function of muon momentum (left) and *towall* (right) (Figures taken from [30]).

predictions and SK atmospheric data:

$$\mathcal{L}(\mathbf{a}, \mathbf{x}_{atm}, \mathbf{d}_{SK} | \mathbf{M}_{SK}) = P(\mathbf{M}_{SK} | \mathbf{a}, \mathbf{x}_{atm}, \mathbf{d}_{SK}) \times \pi(\mathbf{a}) \times \pi(\mathbf{x}_{atm}) \times \pi(\mathbf{d}_{SK}), \quad (5.12)$$

where \mathbf{a} are the atmospheric neutrino flux parameters, \mathbf{x}_{atm} are the atmospheric neutrino cross-section parameters, \mathbf{M}_{SK} is the observed SK atmospheric neutrino data, and π are the parameter prior distributions. \mathbf{d}_{SK} contains parameters that modify the fitQun topological cuts, listed in Table 5.17. Each parameter is parametrized in the following way:

$$L'_m = \beta^1 L_m + \beta^0, \quad (5.13)$$

where β^0 is a bias parameter to the L_m distribution, and β^1 is a smearing parameter that adjusts the width of the distribution. The flux and cross-section uncertainties are separated from the detector systematics so that only the detector components are propagated to the T2K analyses. Also, the detector is divided into six regions by the *wall* and *towall* variables (see Fig. 5.5) to allow spatial variation of the reconstruction efficiency in the detector. The fitting results in each sample bin are specified by the “shift error” which is the fractional deviation of number of events from nominal, and

Cut Variable m	Cut Variable Name
0	fitQun e/μ PID
1	fitQun e/π^0 PID
2	fitQun μ/π PID
3	fitQun Ring-Counting Parameter

Table 5.17: List of fitQun cut variables used in the atmospheric neutrino fit.

the “fit error” which represents the uncertainty of measurements. Fig. 5.6 shows the results of SK topological errors for FS modes of ν_e CC1 e , ν_e CC other, ν_μ CC1 μ and ν_μ CC other.

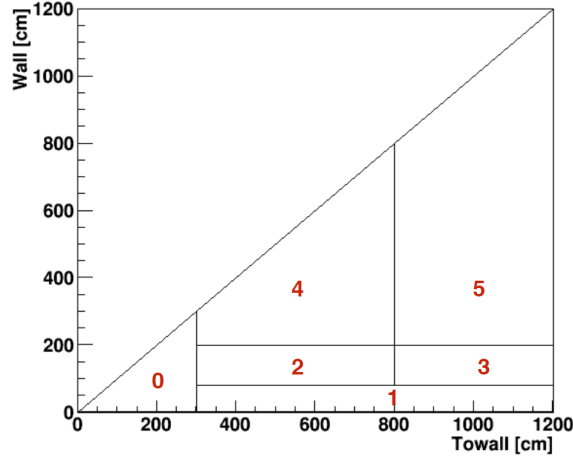


Figure 5.5: Graphical representation of the detector region bin as a function of $wall$ and $towall$, zoomed into small $wall$ and $towall$ regions (Figures taken from [31]).

Hybrid- π^0 fit A set of hybrid- π^0 samples are constructed to evaluate the modelling of π^0 events in SK. The hybrid- π^0 events are built by overlaying a electron-like ring from SK atmospheric samples or a decay electron ring from a stopping cosmic ray muon with a simulated photon ring, where the rings are chosen such that they match the momenta and opening angle of the T2K-MC NC π^0 decay kinematics. They are further divided into primary and secondary samples in which the electron constitutes

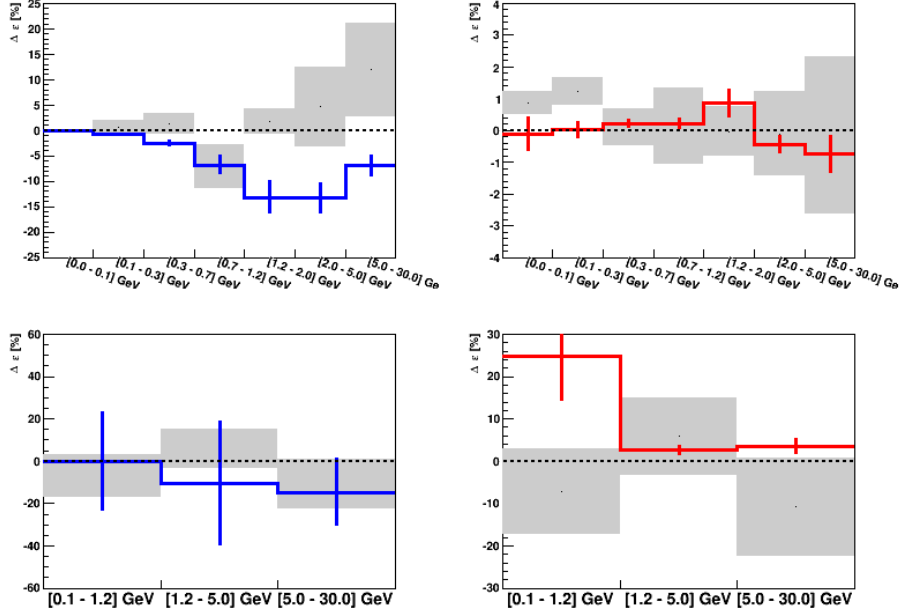


Figure 5.6: Overall SK topological cut errors as a function of visible energy. The total error in each bin is the sum in quadrature of the “shift error” (bin content) and “fit error” (error bar). Top left: ν_e CC1e, bottom left: ν_e CC other, top right: ν_μ CC1 μ , bottom right: ν_μ CC other (Figures taken from [31]).

the higher and lower energy rings respectively. The hybrid- π^0 MC samples with both rings from simulation are compared with the hybrid- π^0 data samples to study the difference in the fraction of events that pass the ν_e selection. The relative difference between data and MC is defined as:

$$R = \frac{\epsilon_{\text{MC}} - \epsilon_{\text{data}}}{\epsilon_{\text{data}}}, \quad (5.14)$$

where ϵ_{data} (ϵ_{MC}) is the remaining efficiency after selections for data (MC). The statistical error on the ratio is calculated assuming the data and MC are independent:

$$\delta R = \frac{\epsilon_{\text{MC}}}{\epsilon_{\text{data}}} \times \sqrt{\left(\frac{\delta\epsilon_{\text{MC}}}{\epsilon_{\text{MC}}}\right)^2 + \left(\frac{\delta\epsilon_{\text{data}}}{\epsilon_{\text{data}}}\right)^2}. \quad (5.15)$$

Error source	$1R\nu_e$	$\nu_e\text{CC}1\pi^+$	$1R\mu$
Vertex		0.5%	
Decay electron cut	$0.1\%\oplus 0.2\%$	$1\%\oplus 2\%$	$0.1\%\oplus 0.2\%$
Topological cuts	Tables 5.19, 5.20, 5.21		

Table 5.18: Input systematic errors for the ToyMC of SK detector efficiency uncertainties.

Event type	Ring-counting	Particle ID	π^0 rejection
ν_e CC1e		atm- ν fit	
ν_e CC other		atm- ν fit	
ν_μ CC DIF (19%)		16%	
ν_μ CC non-DIF (81%)		36.1%	
ν_μ CC other		150%	
ν_μ CC π^0 other		fitQun hybrid- π^0	
NC $1\pi^0$		fitQun hybrid- π^0	
NC π^0 other		fitQun hybrid- π^0	
NC γ		ν_e CC1e+1%	
NC $1\pi^\pm$	100%	100%	100%
NC other	100%	100%	100%

Table 5.19: Input systematic errors of topological cuts (ring-counting, PID, π^0 rejection cuts) for $1R\nu_e$ and $\nu_e\text{CC}1\pi^+$ samples.

The final systematic error is obtained by adding the data/MC differences in the primary and secondary samples independently in quadrature, i.e.

$$\sqrt{R_{\text{primary}}^2 + \delta R_{\text{primary}}^2 + R_{\text{secondary}}^2 + \delta R_{\text{secondary}}^2}. \quad (5.16)$$

Table 5.18 shows the systematic error inputs to the ToyMC. In the ToyMC, each event is assigned with a weight derived from the random fluctuations of the estimated systematic errors. The weighted events are then summed by the output bin and the fractional shift from the nominal value is calculated. The process is repeated by 10^6 times, and the errors and correlations between the output bins are calculated.

Event type	Ring-counting	Particle ID
ν_μ CC1 μ		atm- ν fit
ν_μ CC other		atm- ν fit
ν_e CC1 μ		100%
NC		atm- ν fit = 64.5%

Table 5.20: Input systematic errors of topological cuts (ring-counting, PID) for 1R μ samples.

Event type	Topological cut errors
NC 1 π^0	apfit hybrid- π^0 = 6.49%
NC π^0 other	apfit hybrid- π^0 = 25.37%
Other NC	100%
CC	100%

Table 5.21: Input systematic errors of topological cuts for 2R π^0 samples.

SK detector efficiency uncertainties for NC γ de-excitation sample

For the NC γ de-excitation sample, the SK errors are estimated by separated study because the event selection processes are very different from other samples. We are interested in three error sources: primary gamma production, secondary gamma production and detector responses.

The primary gamma emission from NCQE events are determined by the spectroscopic factors of each shell states and the branching ratios of de-excitation gammas. The spectroscopic factors control the probability of appearance of the hole states ($1p_{1/2}$, $1p_{3/2}$, $1s_{1/2}$) after single nucleon knock out. Among them, only the $1p_{3/2}$ and $1s_{1/2}$ states are excited, and their branching ratios of de-excitation gammas are quite precisely measured. For $1p_{3/2}$ hole states, the dominant error is from the spectroscopic factor and branching ratios 9.93 MeV level, which induces a 3% change in event number. The uncertainties of the $1s_{1/2}$ states are small, but there are continuum excited states above $1s_{1/2}$ that are not simulated. They are treated in a similar way as $1s_{1/2}$

Source	Uncertainties (%)
continuum states	3
$1p_{3/2}$	3
$1s_{1/2}$	1
$E_\gamma < 3$ MeV	1
multi-holes	9
total	10

Table 5.22: The uncertainties of primary gamma production for NCQE signal events.

since they both have high enough energy compared to particle emission thresholds. Because more than 70% of $1s_{1/2}$ states do not emit gamma, the change in event number is small. Gamma rays with $E_\gamma < 3$ MeV are not simulated in NEUT because there are very few available experimental data, but they can hardly produce high enough energy Compton electrons for Cherenkov emission. The biggest uncertainty, however, comes from multi-nucleon hole states, because there are no experimental data about the de-excitation of these multi-hole states. This uncertainty is estimated by completely switching off gamma emission for these states, and the expected event rate drops by 9%. Table 5.22 lists the contribution from different sources of errors, and the overall primary gamma production error is determined to be 10%.

For events due to NC 1π interaction, where de-excitation gammas are produced from π absorption in nucleus, the uncertainty is evaluated by switching the branching ratios from default to two different scenarios: zero gamma emission which reduces event rates by 0.6%, and branching ratios be the same as NCQE events which increases event rates by 2.5%. So the uncertainty is set as 3%.

Secondary gamma productions are mainly due to knocked-out neutrons. The neutrons can further interact with oxygen or be captured by hydrogen. Since there are no experimental constrain on gamma ray emission from neutron-oxygen interaction, the uncertainties are calculated by comparing the simulation results of different si-

Source	Uncertainty (%)
Energy scale	0.4
Energy resolution	1
Trigger efficiency	1
dwall	1
effwall	0.2
ovaQ	0.2
Pre-activity	< 0.1
Cherenkov angle	1
Total	2.1

Table 5.23: The detector response uncertainties for NC γ de-excitation sample.

mulators. The nominal simulation uses MICAP[164, 165] (NMTC[166]) simulator for neutrons energy T_n below (above) 20 MeV, while the alternative simulation uses MICAP (NEUT) for T_n below (above) 30 MeV. In the region $T_n > 30$ MeV, the average energy of secondary gammas from NEUT is higher than that from NMTC, which changes the expected number of events by 12%.

The detector response uncertainties are those related to event selection cut parameters. Table 5.23 lists all items. Energy scale and energy resolution are calibrated precisely in SK, and they introduce around 1% change in event number. Trigger efficiency is evaluated by calibration data and MC, and uncertainty is 1%. The cut values of parameters dwall, effwall and ovaQ change from run to run for selection optimization. Shifts in the cut parameters change the event numbers by less than 1% for each item. The pre-activity cut of $N_{30} < 22$ is tight, and the uncertainties of dark noise or low momentum muons that pass the cut are below 0.1%. The Cherenkov angle cut is shifted by the difference of Cherenkov angle distributions from calibration source and MC, and the resultant changes of remaining events is 1%.

Table 5.24 summarizes the systematic uncertainties of the NC γ de-excitation sample. The uncertainty of the number of beam-unrelated background events is just

Category	NCQE	Other NC	CC	beam-unrelated
Primary γ production	10%	3%	6%	-
Secondary γ production	13%	13%	7.6%	-
Detector response	2.1%	2.1%	2.1%	-
Total	16.5%	13.5%	9.9%	0.8%

Table 5.24: The summary of SK detector efficiency errors for NC γ de-excitation sample.

statistical uncertainty of the accidental events in the 23 hours off-timing data.

Fig. 5.7 shows the size and correlation of the SK detector efficiency parameters for all the oscillation samples. Note that the correlations between the CC and NC samples are weak because they are reconstructed by different algorithm (fitQun, apfit, BONSAI).

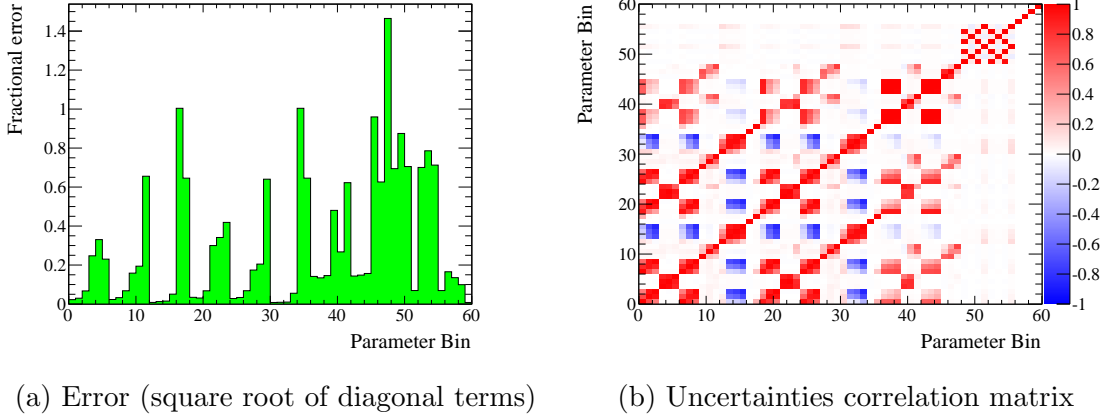


Figure 5.7: Error size and correlations for the SK detector efficiency uncertainties. Parameters are 1-12: FHC $1R_e$, 13-18: FHC $1R_\mu$, 19-30: RHC $1R_e$, 31-36: RHC $1R_\mu$, 37-48: FHC $\nu_e\text{CC}1\pi^+$, 49-52: FHC $2R\pi^0$, 53-56: RHC $2R\pi^0$, 57-60: FHC NC γ de-excitation.

FSI and SI model uncertainties

The FSI and SI model is parameterized by six scale factors. There are three parameters that scale the NEUT microscopic cascade interaction mechanism probabilities

for absorption (FSIABS), low energy QE scattering (FSIQE) and the low energy single charge exchange (SCX) branching fraction (FSICX). Additionally, there are three parameters chosen to span the errors in the high energy data: QE scattering (FSIQEH), SCX (FSICXH) and pion production (FSIINEL).

Pion scattering data are used to tune and constrain the model parameters. Constraints for the low momentum parameters (FSIABS, FSIQE, FSICX) are obtained by fitting the NEUT model to π^\pm -C data[44]. A grid search is performed on the three parameters. The best fit parameter set is found, and 8 parameter sets from the corner of each octant of the 3-parameter space that intersects the $1\text{-}\sigma$ surface of the fit are chosen to represent the constraints and correlations between the parameters.

For the high energy parameters (FSIQEH, FSICXH, FSIINEL), two parameter sets are chosen to span the errors in high momentum (up to 1500 MeV/c) external data. This gives us a total of $8 \times 2 = 16$ parameter sets to propagate the FSI uncertainties. Table 5.25 shows the nominal and 16 variations of NEUT FSI parameters for error estimation.

The NEUT cascade implementation in the SK detector simulator SKDETSIM allows the simultaneous estimation of FSI and SI uncertainties by reweighting the cross-section weights of MC events with the parameters in Table 5.25. The fraction change of events in each output bin and the correlations are calculated in the form of covariance matrix.

PN model uncertainties

SKDETSIM contains a model of photo-nuclear effect: a γ -ray photon could be absorbed by a nucleus so that it would not be reconstructed. This can lead to a $\pi^0 \rightarrow \gamma\gamma$ decay being mis-identified as a $\nu_e/\bar{\nu}_e$ event. A conservative 100% uncertainty is

Par. Set	FSIQE	FSIQEH	FSIINEL	FSIABS	FSICX	FSICXH
Nominal	1.0	1.8	1.0	1.1	1.0	1.8
1	0.6	1.1	1.5	0.7	0.5	2.3
2	0.6	1.1	1.5	0.7	1.6	2.3
3	0.7	1.1	1.5	1.6	0.4	2.3
4	0.7	1.1	1.5	1.6	1.6	2.3
5	1.4	1.1	1.5	0.6	0.6	2.3
6	1.3	1.1	1.5	0.7	1.6	2.3
7	1.5	1.1	1.5	1.5	0.4	2.3
8	1.6	1.1	1.5	1.6	1.6	2.3
23	0.6	2.3	0.5	0.7	0.5	1.3
24	0.6	2.3	0.5	0.7	1.6	1.3
25	0.7	2.3	0.5	1.6	0.4	1.3
26	0.7	2.3	0.5	1.6	1.6	1.3
27	1.4	2.3	0.5	0.6	0.6	1.3
28	1.3	2.3	0.5	0.7	1.6	1.3
29	1.5	2.3	0.5	1.5	0.4	1.3
30	1.6	2.3	0.5	1.6	1.6	1.3

Table 5.25: NEUT FSI “1-sigma” parameter sets from the fit to π^\pm -C data[44].

applied to this type of events in 1Re and ν_e CC1 π^+ samples.

Fig. 5.8 shows the size and correlation of FSI+SI+PN parameters.

SK energy uncertainty

The SK energy uncertainty is applied after all other nuisance parameters to see how the sample spectrum changes if we multiply E_{rec}/p of all the events by the energy scale parameter. We assume that events are uniformly distributed in each bin and thus if a fraction of $\alpha\%$ of the energy range covered by the bin i moves into the range of bin $i+1$, that $\alpha\%$ of events would behave in the same manner. The final event rates used in likelihood calculation is produced after this event migration has been calculated.

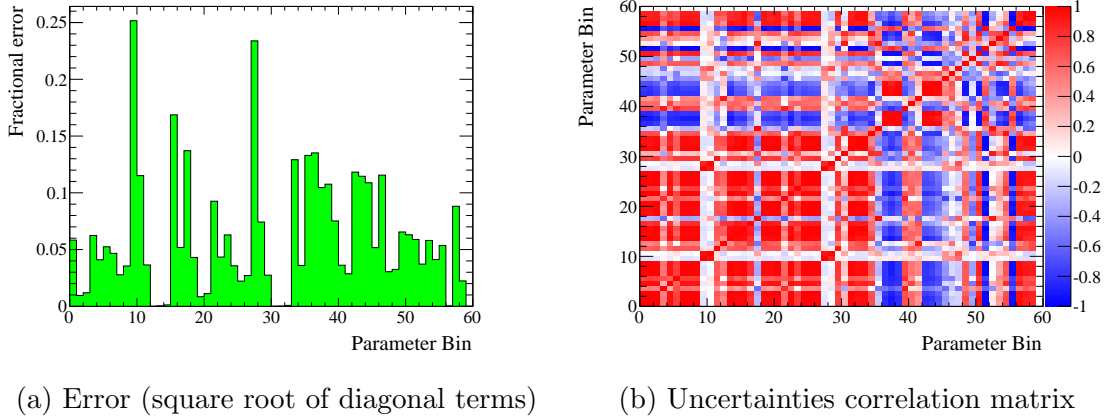


Figure 5.8: Error size and correlations for FSI+SI+PN uncertainties. Parameters are 1-12: FHC $1R_e$, 13-18: FHC $1R_\mu$, 19-30: RHC $1R_e$, 31-36: RHC $1R_\mu$, 37-48: FHC $\nu_e\text{CC}1\pi^+$, 49-52: FHC $2R\pi^0$, 53-56: RHC $2R\pi^0$, 57-60: FHC $\text{NC}\gamma$ de-excitation.

5.3.4 Effect of systematic parameters

In this section we study the effects of systematic parameters on event rates of the eight oscillation samples. For each error category, we make 10k throws of the systematic parameters based on the covariance matrix and calculate the RMS of the predicted event rates among the throws. The total systematic errors are calculated by making 50k throws of all parameters. Table 5.26 summarizes the error contributions for the standard CC samples, assuming oscillation parameter set in Table 6.2, and Table 5.27 summarizes that for the newly added NC samples. We can clearly see that the total errors for CC samples are only a few percent (except $\nu_e\text{CC}1\pi^+$), while the errors are over 20% for NC samples due to the larger contribution in cross-section and SK errors. Note that the cross-section errors for the NC samples are roughly 20%, because the errors are dominated by the $\text{NC}1\pi/\text{NCQE}$ normalization parameters that affects about 70% of events in the samples.

Fig. 5.9, 5.10 and 5.11 show the event distribution variations due to systematic parameters. The distributions are quite symmetric around the nominal values, and

Error Source	$1R\mu$		$1Re$		$\nu_e CC1\pi^+$
	FHC	RHC	FHC	RHC	FHC
Beam	4.1	3.8	4.3	3.9	4.3
Neutrino interaction and cross-section	4.7	4.0	5.5	5.2	5.0
SK Detector	3.3	2.9	3.8	4.3	17.1
Syst. Total	4.7	4.0	5.8	6.4	17.7

Table 5.26: Percent errors on the predicted event rates of CC samples.

Error Source	$2R\pi^0$		NC γ de-excitation
	FHC	RHC	FHC
Beam	4.2	3.8	4.1
Neutrino interaction and cross-section	20.1	19.1	21.1
SK Detector	8.8	8.6	13.2
Syst. Total	21.3	20.4	23.3

Table 5.27: Percent errors on the predicted event rates of NC samples.

the size of error envelopes are consistent with the tables above.

To understand better the error contribution, we vary the systematic parameter one by one (keeping others at nominal) and see how the number of events of the each sample changes accordingly. From Fig. 5.12, we can clearly see that indeed the NC 1π (bin 71) and NCQE (bin 72) cross-section normalization errors contribute most to the $2R\pi^0$ and NC γ de-excitation samples respectively. Also the SK errors are relatively larger for the NC (and $\nu_e CC1\pi^+$) samples.

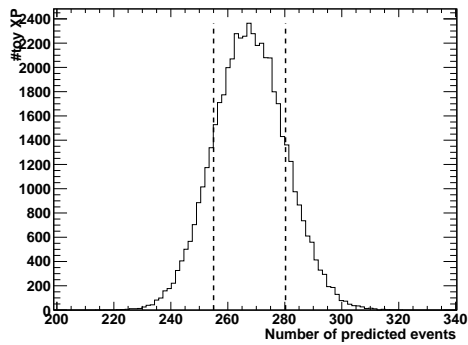
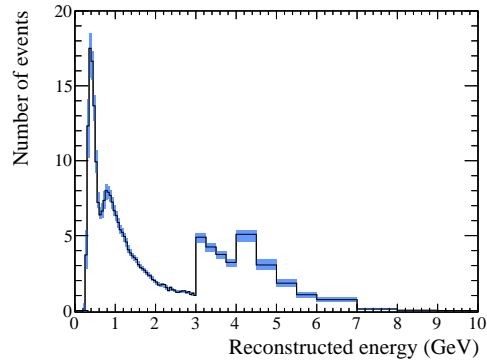
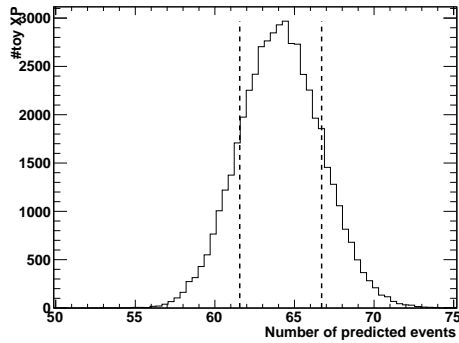
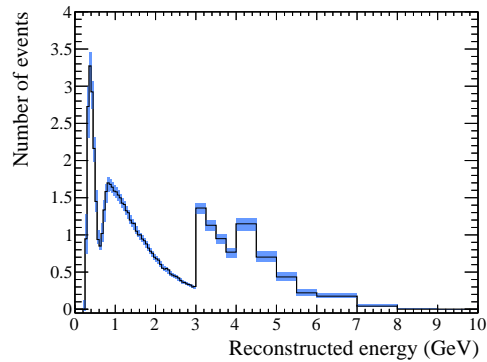
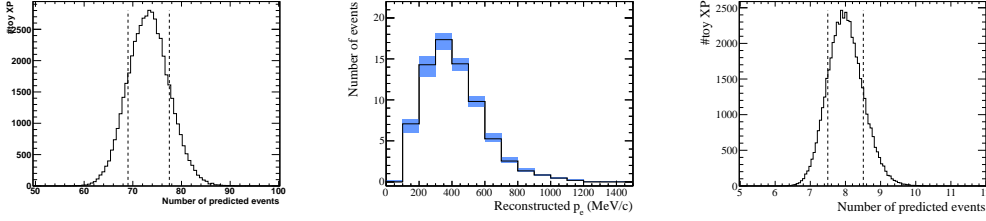
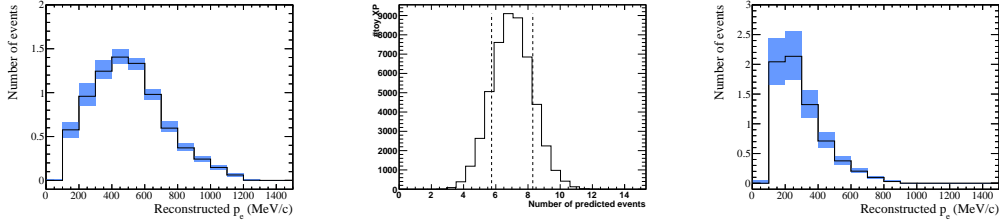
(a) Number of predicted events for FHC $1R\mu$ sample.(b) Number of predicted events in each bin for FHC $1R\mu$ sample.(c) Number of predicted events for RHC $1R\mu$ sample.(d) Number of predicted events in each bin for RHC $1R\mu$ sample.

Figure 5.9: Number of observed events for the $1R\mu$ samples obtained over 50k throws of systematic parameters. On the left shows the predicted number of events in all bins. The dotted lines show the $\pm 1\sigma$ region around the mean value. On the right shows the error envelope in each sample bin. Blue boxes correspond to the $\pm 1\sigma$ region around the mean value, black histograms correspond to the nominal values for default value of the systematic parameters.



(a) Number of predicted events for FHC 1Re sample. (b) Number of predicted events in each p_e bin for FHC 1Re sample. (c) Number of predicted events for RHC 1Re sample.



(d) Number of predicted events in each p_e bin for FHC $\nu_e CC 1\pi^+$ sample. (e) Number of predicted events for RHC $\nu_e CC 1\pi^+$ sample. (f) Number of predicted events in each p_e bin for RHC $\nu_e CC 1\pi^+$ sample.

Figure 5.10: Number of observed events for the 1Re and $\nu_e CC 1\pi^+$ samples obtained over 50k throws of systematic parameters.

5.4 Fitting method

5.4.1 Likelihood calculation

Suppose in an experiment we observe the numbers of events in each sample bin

$\vec{N}_{\text{obs}} := \langle N_{\text{obs}}^b \rangle$, we define the joint likelihood function as

$$\mathcal{L}(\vec{N}_{\text{obs}}, \vec{N}_{\text{pred}}, o, f) = \mathcal{L}_{\text{sample}}(\vec{N}_{\text{obs}}, \vec{N}_{\text{pred}}(o, f)) \times \mathcal{L}_{\text{sys.}}(f) \times \mathcal{L}_{\text{external}}(o), \quad (5.17)$$

where o and f are the oscillation and systematic parameters.

In the sample likelihood part $\mathcal{L}_{\text{sample}}$, we quantify the difference between N_{obs}^b

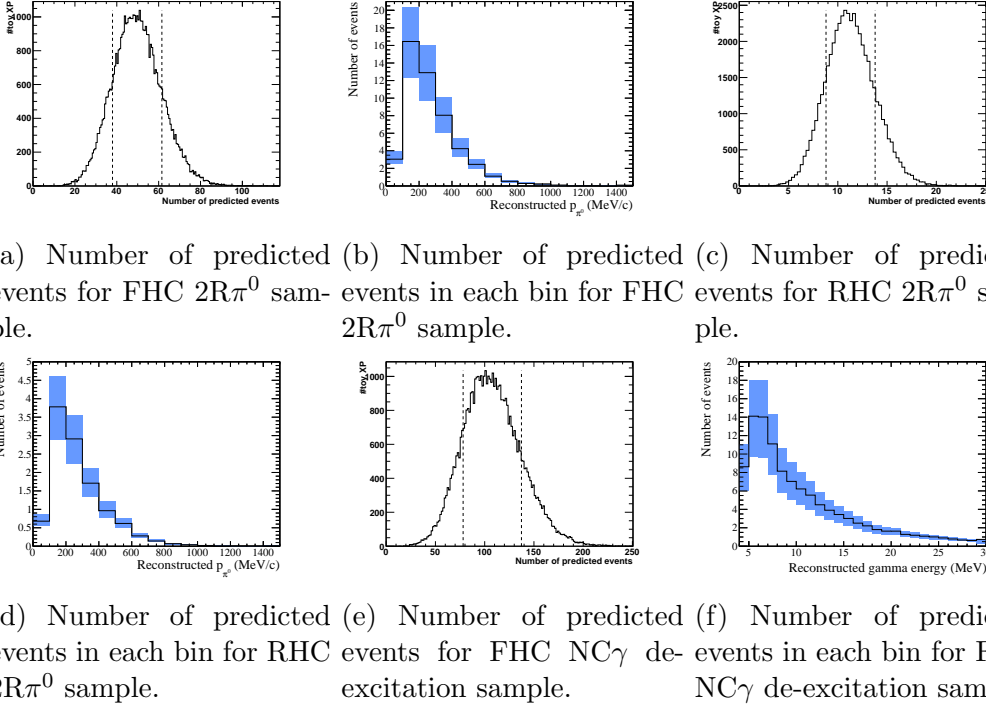


Figure 5.11: Number of observed events for the NC samples obtained over 50k throws of systematic parameters.

and N_{pred}^b in the form of binned Poisson likelihood:

$$-\ln \mathcal{L}_{\text{sample}} = \sum_b N_{\text{pred}}^b - N_{\text{obs}}^b + N_{\text{obs}}^b \ln \frac{N_{\text{obs}}^b}{N_{\text{pred}}^b}, \quad (5.18)$$

where b is summed over the event bins from all samples. The oscillation parameters and systematic parameters enter in the calculation of \vec{N}_{pred} :

$$\vec{N}_{\text{pred}}(o, f) = \sum_{C, I, E_\nu^{\text{true}}} M_b(C, I, E_\nu^{\text{true}}) P_{\text{osc}}(C, I, E_\nu^{\text{true}}; o) R_b(C, I, E_\nu^{\text{true}}; f), \quad (5.19)$$

where M_b , P_{osc} and R_b are the non-oscillated event rates, oscillation probabilities and systematic reweighting factors respectively (see Sec. 5.2.6). Here, the oscillation parameters o , which are being fit, correspond to θ_{23} , Δm_{31}^2 , θ_{13} , δ_{CP} , θ_{24} , θ_{34} and

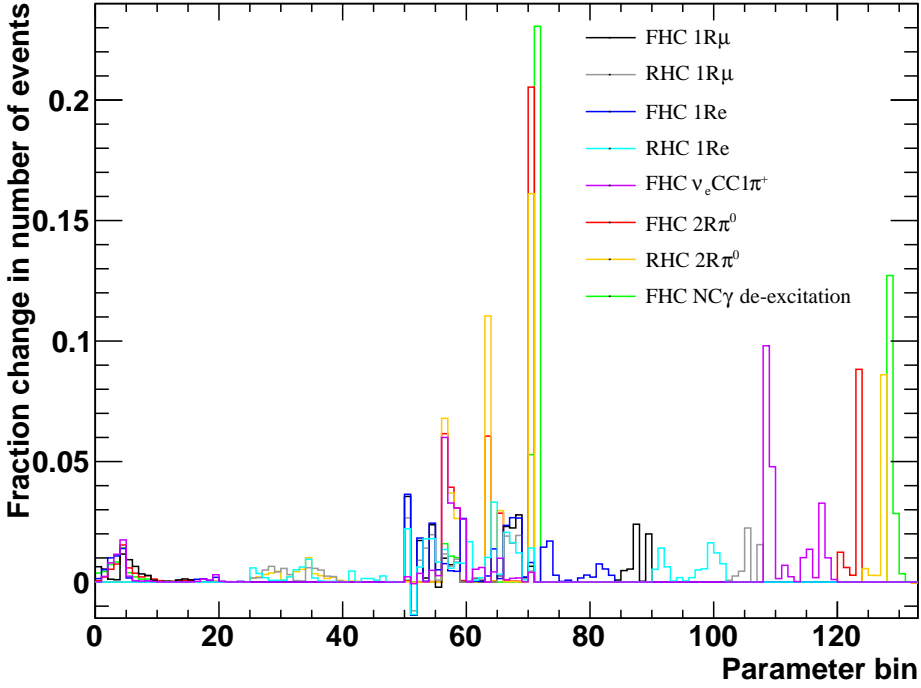


Figure 5.12: Fractional change of number of events when a systematic parameter is increased by 1σ from nominal value. Parameters are 1-50: beam flux, 51-72: neutrino interaction and cross-section, 73-132: Super-K detector, 133: SK p-scale parameters.

Δm_{41}^2 .

The systematic part $\mathcal{L}_{\text{syst.}}(f)$ is calculated as

$$\mathcal{L}_{\text{syst.}} = \exp(-0.5 \sum_{i,j} v_i M_{ij} v_j), \quad (5.20)$$

where v_i is the difference of the i -th systematic parameter from its central value and M_{ij} is the (i, j) element of the inverted covariance matrix.

We use $\mathcal{L}_{\text{external}}$ to include any external constraint on the oscillation parameters. For example, in this study, $\sin^2 2\theta_{13}$ is constrained by reactor measurements, and a

Gaussian penalty ($\bar{x} = 0.0857, \sigma = 0.0046$) is used:

$$\mathcal{L}_{external} = \exp\left(-0.5 \frac{(\sin^2 2\theta_{13} - \bar{x})^2}{\sigma^2}\right) \quad (5.21)$$

In the oscillation analysis, we usually fit for one or two oscillation parameters at once, and the un-fitted oscillation parameters and systematic parameters are treated as nuisance parameters. There are several different ways to handle these nuisance parameters.

The standard way in T2K is to use the method of Bayesian marginalization, i.e. the marginal likelihood is computed by integrating the full likelihood over the nuisance parameters λ :

$$\mathcal{L}_{marg}(\vec{N}_{\text{obs}}, \vec{N}_{\text{pred}}, o^{fit}) = \int \mathcal{L}(\vec{N}_{\text{obs}}, \vec{N}_{\text{pred}}, o, f) p(\lambda(o^{un-fit}, f)) d\lambda, \quad (5.22)$$

where o^{fit} (o^{un-fit}) are the fitted (un-fitted) oscillation parameters.

A numerical integration technique is used to estimate the integral, where λ are thrown $N = 10000$ times according to their prior distributions, and the average \mathcal{L} is computed:

$$\mathcal{L}_{marg}(\vec{N}_{\text{obs}}, \vec{N}_{\text{pred}}, o^{fit}) \approx \frac{1}{N} \sum_{i=1}^N \mathcal{L}(\vec{N}_{\text{obs}}, \vec{N}_{\text{pred}}, o(o^{fit}, o_i^{un-fit}), f_i). \quad (5.23)$$

On the other hand, in our sterile oscillation analysis, there are three more oscillation parameters in the fit: θ_{24} , θ_{34} and Δm_{41}^2 . If we use the same method of marginalization, a much larger number of throws $N \gg 10000$ is required for the fit to converge. This takes much more computation time and is not desirable. Therefore we determine to use the method of minimization instead.

Target coverage	1 parameter	2 parameters
68.3%	1	2.3
90%	2.71	4.61
95%	3.84	5.99
99%	6.63	9.21

Table 5.28: Fixed $\Delta\chi_f^2$ values used to build confidence level intervals

We use Minuit2 ROOT package to minimize $-\ln \mathcal{L}$ with respect to all nuisance parameters. The Migrad algorithm is used for this minimization, and in case it fails to converge the Simplex method is used instead.

$$-\ln \mathcal{L}_{\min}(\vec{N}_{\text{obs}}, \vec{N}_{\text{pred}}, o^{fit}) = \min_{o^{un-fit}, f} (-\ln \mathcal{L}(\vec{N}_{\text{obs}}, \vec{N}_{\text{pred}}, o, f)). \quad (5.24)$$

5.4.2 Confidence level building

A simple way to estimate the confidence level (C.L.) is to use the Wilks's theorem[167].

We define the $\Delta\chi^2$ function as:

$$\Delta\chi^2(o^{fit}) = -2 \times \ln\left(\frac{\mathcal{L}_{\min}(o^{fit})}{\max_{o^{fit}}(\mathcal{L}_{\min}(o^{fit}))}\right). \quad (5.25)$$

The confidence level intervals are the region of parameter space for which the $\Delta\chi^2$ is inferior to a certain fixed value of $\Delta\chi_f^2$ (see Table 5.28).

Chapter 6

Sensitivity study

This section describes the sensitivity studies with MC data assuming T2K-SK Run1-8 proton-on-target (POT), i.e. 1.47341×10^{21} POT in FHC and 0.75573×10^{21} POT in RHC. For FHC NC γ de-excitation sample, only Run1-4 POT (0.656×10^{21}) is used. Table 6.1 lists the Run and POT configuration of the eight samples.

We generated a toy MC data set using the set of “true” oscillation parameters in Table 6.2, with all the systematic parameters set at their nominal values. All statistical fluctuations are suppressed and the numbers of events in each sample bin are equal to their expected values. This is referred to as the Asimov data set, which is a representative of all possible data sets. The “Asimov Sensitivity” calculated in this

Sample	1R μ	1Re	2R π^0	ν_e CC1 π^+	NC γ de-excitation
FHC					
Run		1-8		1-8	1-4
POT		1.47341×10^{21}		1.47341×10^{21}	0.656×10^{21}
RHC					
Run		5-7		-	-
POT		0.75573×10^{21}		-	-

Table 6.1: Run and POT configuration for the eight oscillation samples.

Parameters	True values
Δm_{21}^2	$7.53 \times 10^{-5} \text{eV}^2$
Δm_{32}^2	$2.509 \times 10^{-3} \text{eV}^2$
$\sin^2 \theta_{23}$	0.528
$\sin^2 \theta_{12}(\sin^2 2\theta_{12})$	0.304 (0.846)
$\sin^2 \theta_{13}(\sin^2 2\theta_{13})$	0.0219 (0.0857)
δ_{CP}	-1.601
Earth matter density	2.6 g/cm ³
Baseline length	295 km
Mass hierarchy	Normal
$\Delta m_{41}^2, \sin^2 \theta_{24}, \sin^2 \theta_{34}$	0

Table 6.2: Oscillation parameters used to generate ToyMC data set.

Parameters	Allowed values
Δm_{21}^2	$7.53 \times 10^{-5} \text{eV}^2$
$\sin^2 2\theta_{12}$	0.846
$\sin^2 2\theta_{13}$	0.0857 ± 0.0046
Δm_{32}^2	$[0.002, 0.003] \text{eV}^2$
$\sin^2 \theta_{23}$	$[0.3, 0.7]$
δ_{CP}	$[-\pi, \pi]$

Table 6.3: Allowed values of the 3-flavor parameters in the oscillation fit.

way can be used to estimate the median significance of many toy MC experiments which saves a lot of computation time.

Fig. 6.1 shows the predicted event spectra for all samples generated with the assumed POT and oscillation parameters.

In the fitting process, $\sin^2 \theta_{12} = 0.304$ and $\Delta m_{21}^2 = 7.53 \times 10^{-5} \text{eV}^2$ are held fixed because T2K lacks sensitivity on them. A penalty term is added to use the constrains of $\sin^2 2\theta_{13} = 0.0857 \pm 0.0046$ from [168]. $\sin^2 \theta_{23}$, Δm_{32}^2 and δ_{CP} are allowed to vary in certain intervals. Table 6.3 summarizes the fitter settings for the 3-flavor parameters.

We perform oscillation fits for both 3-flavor oscillation and 3+1 sterile oscillation

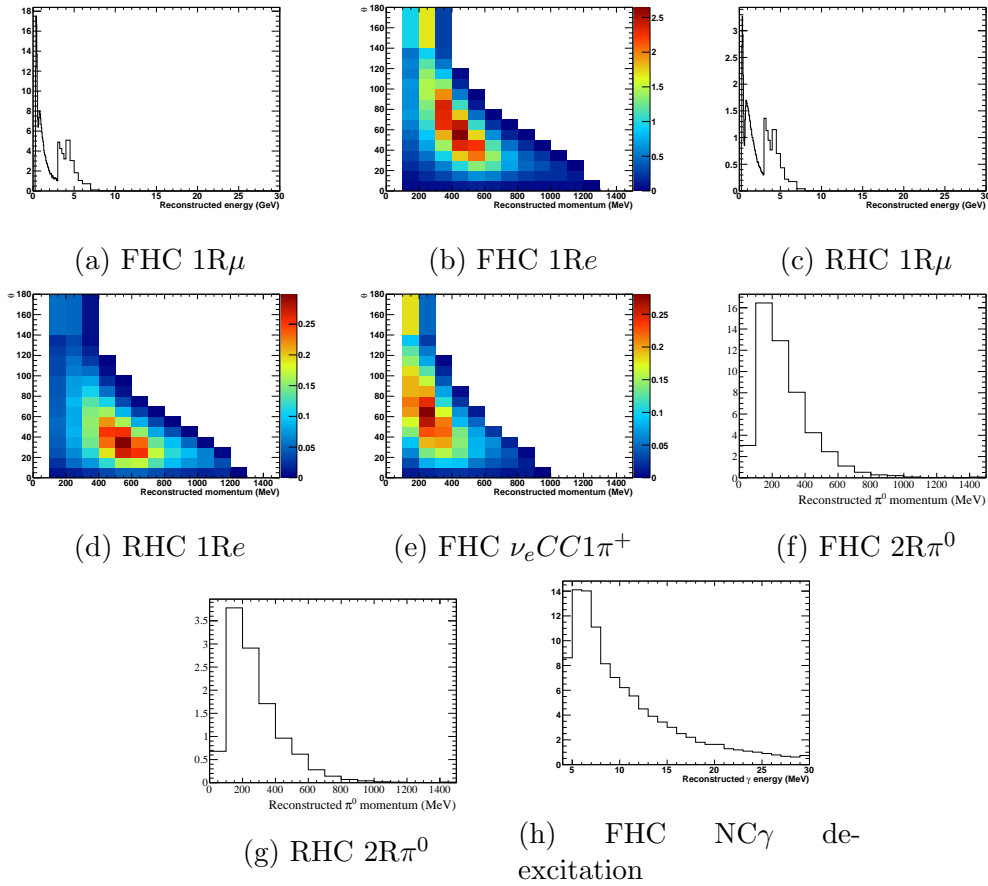


Figure 6.1: Predicted spectra for each sample. Distributions for $1R\mu$ samples are a function of E_{rec} (GeV) whereas distributions for $1Re$ samples and $\nu_e CC 1\pi^+$ sample are a function of p_e (MeV) and θ (degree). Distributions for $2R\pi^0$ samples are a function of π^0 momentum (MeV) whereas distributions for NC γ de-excitation sample are a function of reconstructed γ energy (MeV).

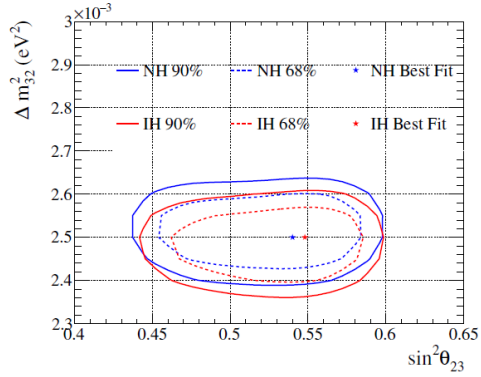
scenarios.

6.1 3-flavor oscillation fit

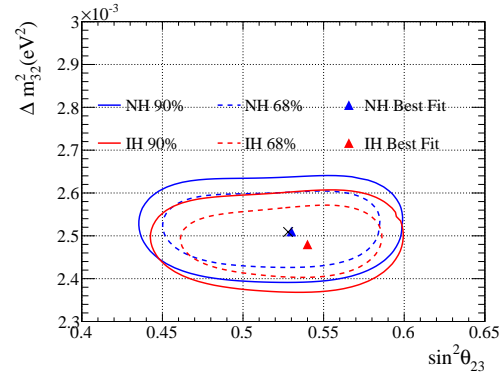
A 3-flavor oscillation fit with only the standard CC samples is first done to check the fitter consistency, then a fit with all eight samples is done to make sure the additional NC samples do not introduce any strange effect or bias. The 3-flavor oscillation probability with matter effect is used in the event rate calculation. Details of the event breakdowns can be found in Table B.1 - B.8 in Appendix B.

Interestingly, the confidence levels with and without the NC samples lay nearly the same on each other. That means under the current statistics, the NC background of the CC samples is already well constrained by the systematic parameters. For simplicity, in the following we just show the fit results with all the eight oscillation samples. The best fit point is indicated by the triangle marker. For the two-dimensional contours, the normal and inverted hierarchy $\Delta\chi^2$ are calculated with respect to their own χ^2_{\min} . For the one-dimensional case, a single global χ^2_{\min} is used.

The sensitivity plots from our analysis are shown in Fig. 6.2-6.4, all together with the plots from standard analysis[45]. Compared with standard results, our fits have a best-fit point closer to truth, but slightly looser constraints on the fitted oscillation parameters. This is mostly due to the difference in the likelihood calculation method, i.e. marginalization of \mathcal{L} vs. minimization of $-\ln\mathcal{L}$ over all nuisance parameters. Yet the two different fitted results are consistent with each other and we conclude that the introduction of the three NC samples does not have any side-effect on the oscillation analysis.

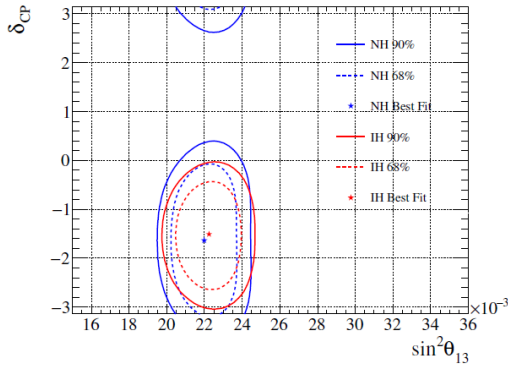


(a) Standard T2K analysis.

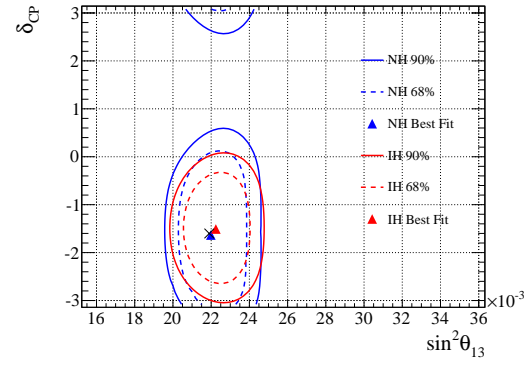


(b) Our analysis.

Figure 6.2: Asimov sensitivity 2D confidence level contours in Δm_{32}^2 vs. $\sin^2 \theta_{23}$ for normal and inverted hierarchy. The black cross marks the parameter truth values.



(a) Standard T2K analysis.



(b) Our analysis.

Figure 6.3: Asimov sensitivity 2D confidence level contours in δ_{CP} vs. $\sin^2 \theta_{13}$ for normal and inverted hierarchy. The black cross marks the parameter truth values.

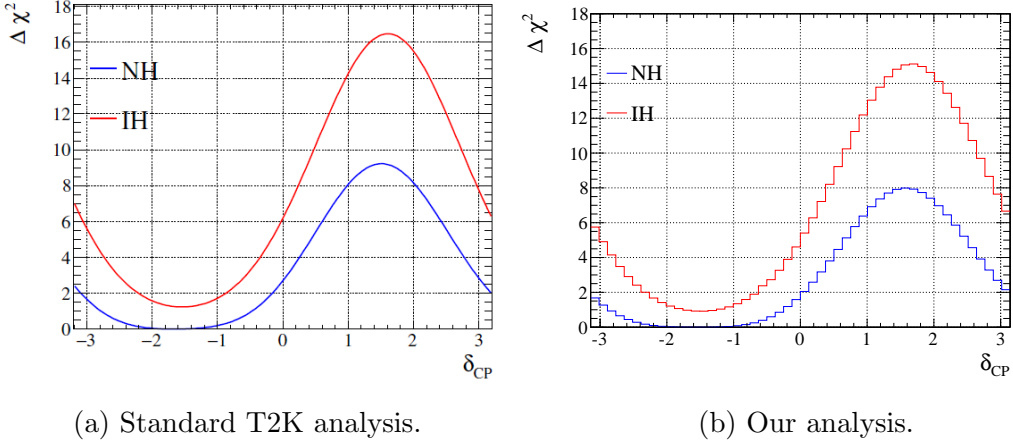


Figure 6.4: Asimov sensitivity 1D $\Delta\chi^2$ in δ_{CP} for normal and inverted hierarchy.

6.2 3+1 oscillation

In this fit, we use the 3+1 sterile vacuum oscillation probability to calculate the event rates. With the same set of oscillation parameters in Table 6.2, the 1Re and $\nu_e\text{CC}1\pi^+$ event numbers are a few percent different from that in 3-flavor case, while other event numbers are similar. Table B.9-B.16 in Appendix B shows the corresponding event breakdowns.

6.2.1 $\sin^2\theta_{24}$ - Δm_{41}^2 plane

We scan the $(\sin^2\theta_{24}, \Delta m_{41}^2)$ parameter space from 10^{-3} to 1 in $\sin^2\theta_{24}$ and 10^{-4}eV^2 to 10^3eV^2 in Δm_{41}^2 . $\sin^2\theta_{34}$ is allowed to float freely from 0 to 1. The best-fit point is at $(\sin^2\theta_{24}, \Delta m_{41}^2) = (0.0040(0.0023), 0.0048(0.0024)\text{eV}^2)$ for NH (IH).

Fig. 6.5 shows our expected sensitivity, together with constraints from other experiments. We have a better sensitivity on $\sin^2\theta_{24}$ for $\Delta m_{41}^2 \leq 0.003\text{eV}^2$ than other existing results, because of T2K's specific design for Δm_{32}^2 - $\sin^2\theta_{23}$ precision measurement. The NH outward bump (worse sensitivity) at around $\Delta m_{41}^2 = 0.0025\text{eV}^2$ is

due to the degeneracy between m_4 and m_3 , which does not exist in IH case.

For larger Δm_{41}^2 values, we are not that competitive due to statistics and the lack of near detector data. Also, if $\Delta m_{41}^2 > 0.3\text{eV}^2$, sterile oscillation would have impacts on ND280 at neutrino beam energy peak 0.6 GeV (see Appendix H), and near detector data needs to be included in the fit (which is not done in this analysis) to give proper constrains in this region. We therefore only show data fit results only up to $\Delta m_{41}^2 = 0.3\text{eV}^2$, to avoid any contradiction to BANFF fit assumptions.

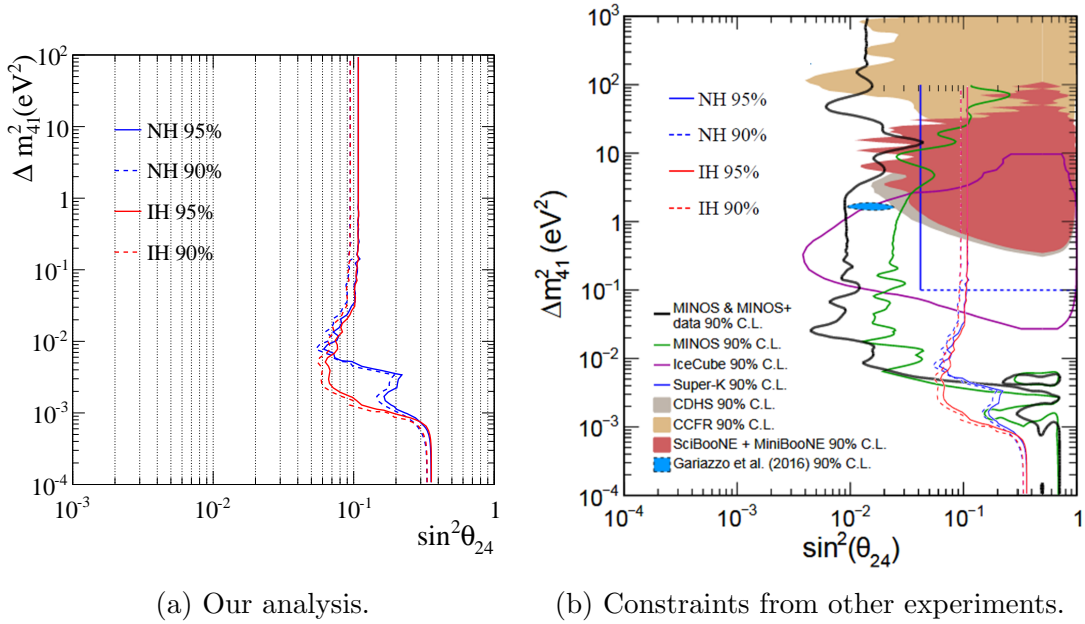


Figure 6.5: Asimov sensitivity 2D confidence level contours in Δm_{41}^2 vs. $\sin^2 \theta_{24}$ for normal and inverted hierarchy. On the right shows our sensitivity overlaid on limits to date from other experiments[32–39] (Figure taken from [32]).

Fig. 6.7 illustrates the contribution of different oscillation samples to the fit. At large Δm_{41}^2 , the fit is dominated by the large statistics of $1R\mu$ events. The ν_e samples resolves part of the $\Delta m_{41}^2 \sim \Delta m_{31}^2$ degeneracy, and together with the NC samples, improves the sensitivity at small Δm_{41}^2 .

In Appendix I, we show the event spectra at several test points of the 90% limit

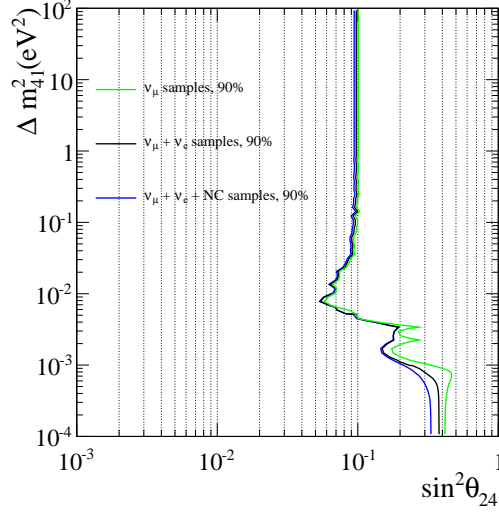


Figure 6.7: Asimov sensitivity 2D confidence level contours in Δm_{41}^2 vs. $\sin^2 \theta_{24}$ assuming NH. The exclusion limit is mostly determined by the ν_μ samples at large Δm_{41}^2 , and supplemented by ν_e and NC samples at small Δm_{41}^2 .

to illustrate the fitter features.

6.2.2 $\sin^2 \theta_{24}$ - $\sin^2 \theta_{34}$ plane

We scan the $(\sin^2 \theta_{24}, \sin^2 \theta_{34})$ parameter space from 10^{-3} to 1 in $\sin^2 \theta_{24}$ and 0 to 1 in $\sin^2 \theta_{34}$. In the region of $\Delta m_{41}^2 > 0.01 \text{eV}^2$, the fit has little dependence on Δm_{41}^2 , and we set a fixed $\Delta m_{41}^2 = 0.1 \text{eV}^2$. The best-fit point is $(\sin^2 \theta_{24}, \sin^2 \theta_{34}) = (0.001, 0)$ for both NH and IH.

Fig. 6.8 shows our expected sensitivity, together with constraints from IceCube[40] and SK[35]. We have looser exclusion limits, especially for $\sin^2 \theta_{34}$. Since $\sin^2 \theta_{34}$ sensitivity comes mostly from NC samples, improvement of NC systematics or development of additional NC samples would be needed if we want to enhance $\sin^2 \theta_{34}$ sensitivity significantly.

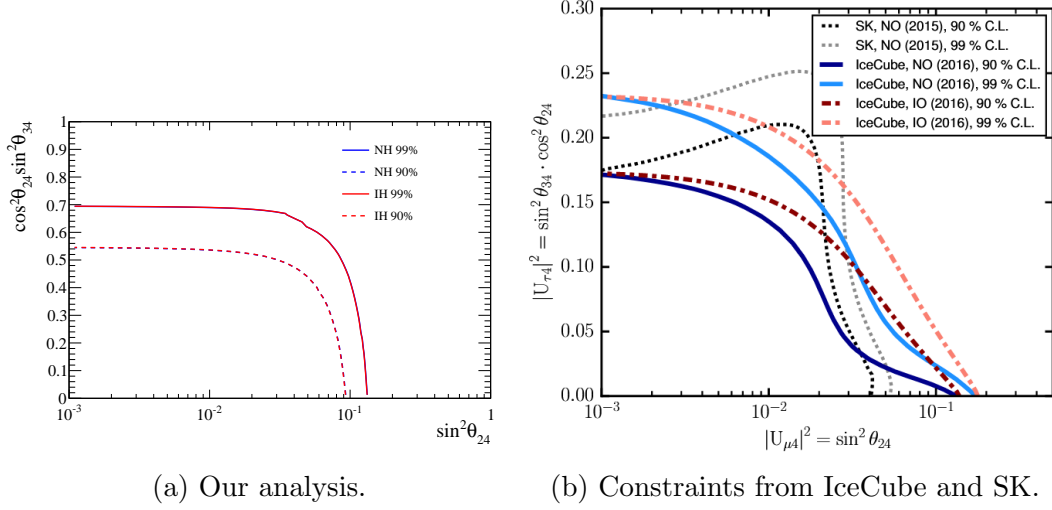


Figure 6.8: Asimov sensitivity 2D confidence level contours in $\cos^2 \theta_{24} \sin^2 \theta_{34}$ vs. $\sin^2 \theta_{24}$. On the right shows the 90% and 99% upper limits from IceCube[40] and SK[35].

6.3 Effect of statistics

Our sterile neutrino analysis is still statistically limited at current POT. Fig. 6.9 shows our expected sensitivity with T2K full POT (7.8×10^{21}) and T2K-II proposed POT (20×10^{21}), where a significant improvement can be seen on the sterile parameter bounds. Also, more oscillation samples are in development by the T2K-SK working group, e.g. multi-ring ν_μ/ν_e samples, and full release of NC γ de-excitation data in both neutrino and anti-neutrino beam modes. This further increases the statistics and certainly helps the analysis.

6.4 Effect of systematics

To study the impacts of systematic uncertainties on the analysis, we perform the oscillation fit with different categories of uncertainties switched on and off. Fig. 6.10 shows the effects of systematics due to each of the three error categories. We further

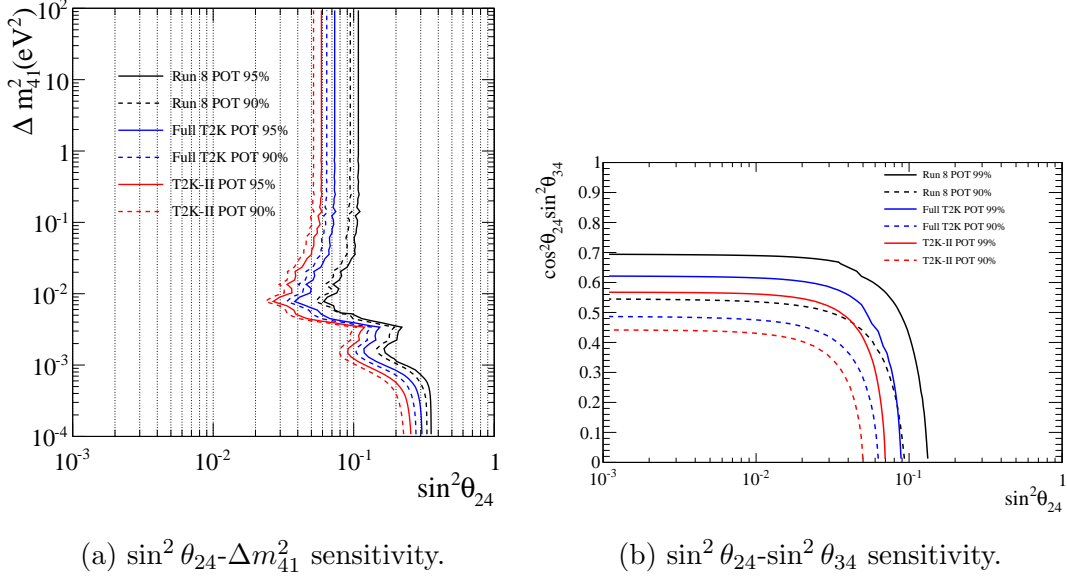


Figure 6.9: Asimov sensitivity 2D confidence level contours of NH assuming current Run 1-8 POT and future POT.

break down the neutrino interaction and cross-section (Xsec) parameters and the SK parameters into specific groups and study their relative contributions in Fig. 6.11.

As discussed in Sec. 5.3.4, Xsec and SK parameters have the largest effects on the newly added NC samples, and affect the sterile sensitivity most. In particular, the NC1 π and NCQE normalization parameters dominate in the Xsec errors. Future cross-section analysis at ND280 would definitely contribute to systematic reduction.

On the other hand, there will be improvements on the SK errors of NC samples too. For example, we expect there would be both statistic and systematic enhancements when fitQun selections of $2R\pi^0$ samples are ready for oscillation analysis. For the NC γ de-excitation sample, the biggest SK error comes from secondary gamma production induced by knocked-out neutrons. There is an experiment being performed in RCNP, Osaka University [169] to measure the gamma ray emission from neutron-oxygen interaction, and the results can be used constrain the uncertainties

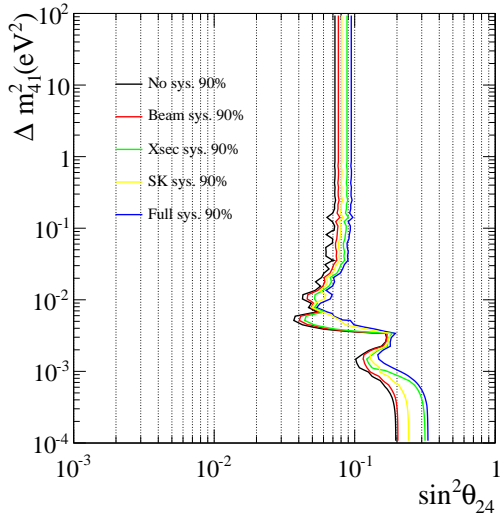
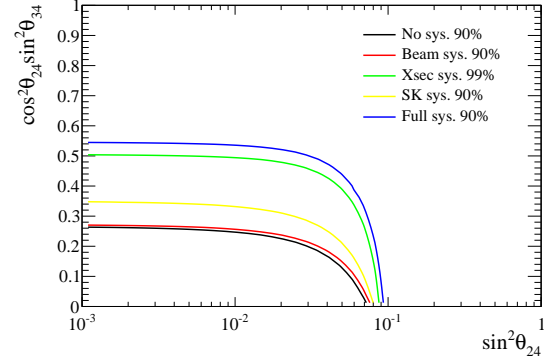
(a) $\sin^2 \theta_{24}$ - Δm_{41}^2 sensitivity.(b) $\sin^2 \theta_{24}$ - $\sin^2 \theta_{34}$ sensitivity.

Figure 6.10: Asimov sensitivity 2D confidence level contours of NH showing the individual effect of different sources of systematic uncertainty.

on secondary gamma.

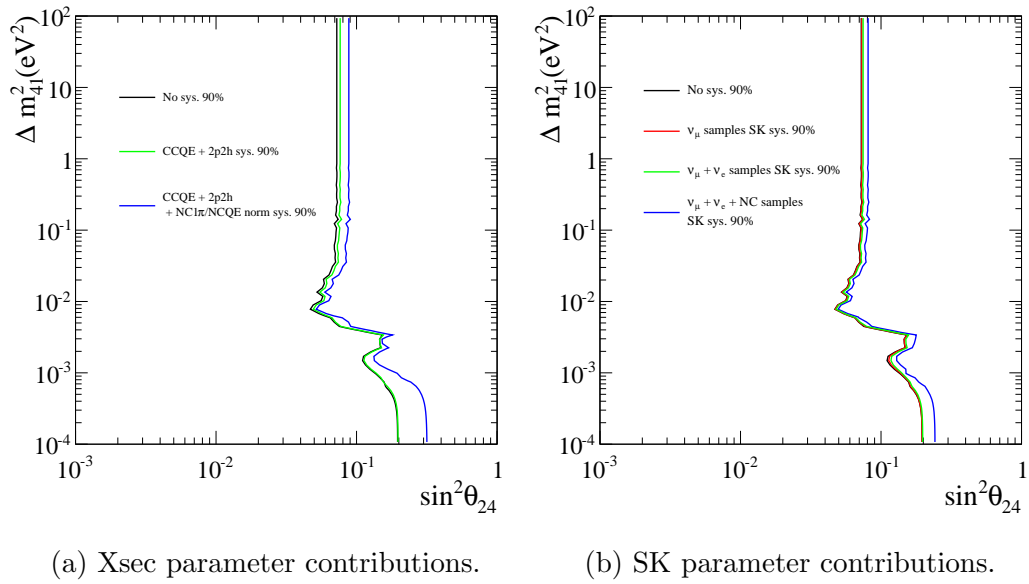


Figure 6.11: Asimov sensitivity 2D confidence level contours of NH in $\sin^2 \theta_{24}$ - Δm^2_{41} plane, showing the systematic effects of Xsec and SK parameters.

Chapter 7

Data fit results

In this chapter, we fit for both the 3-flavor and 3 + 1 sterile oscillation models using T2K Run 1-8 data. Table 7.1 shows the observed event numbers together with the Asimov predicted ones. Fig. 7.1 shows observed event spectra overlaid on Asimov predictions. The two sets of numbers and spectra agree quite well, so we expected the data fit results would be similar to the Asimov fits.

Sample	1R μ		1R e		ν_e CC1 π^+	2R π^0		NC γ de-excitation
	FHC	RHC	FHC	RHC	FHC	FHC	RHC	FHC
Data	240	68	74	7	15	53	9	102
Asimov	268.4	64.3	73.5	7.9	6.9	49.5	11.3	107.7

Table 7.1: Event rates of T2K Run 1-8 data and Asimov data set generated using parameters in Table 6.2.

7.1 Global best fit points

The 3+1 sterile NH (IH) best fit point has a $\chi^2 = 343.8(343.6)$, while the 3-flavor NH (IH) best fit $\chi^2 = 344.8(348.5)$. Table 7.2 shows the best fit oscillation parameter

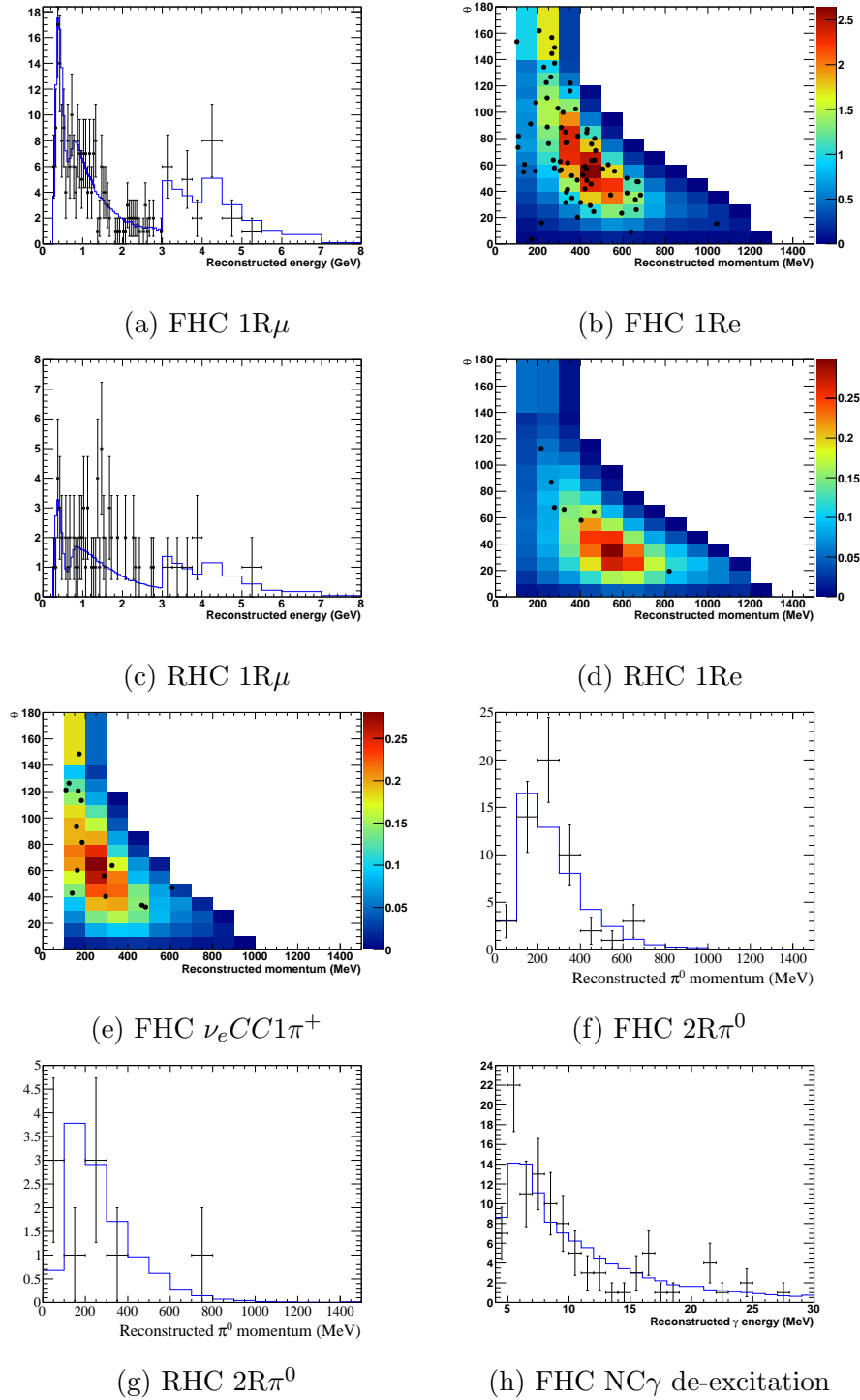


Figure 7.1: Observed event spectra overlaid on the Asimov prediction.

Parameters	3 + 1 sterile		3-flavor		Standard Ptheta	
$ \Delta m_{32}^2 (\times 10^{-3}\text{eV}^2)$	2.43	2.41	2.46	2.43	2.46	2.44
$\sin^2 \theta_{23}$	0.538	0.542	0.526	0.531	0.528	0.533
$\sin^2 2\theta_{13}$	0.088	0.088	0.087	0.088	0.087	0.088
δ_{CP}	-1.69	-1.45	-1.75	-1.46	-1.77	-1.44
Mass hierarchy	Normal	Inverted	Normal	Inverted	Normal	Inverted
$\Delta m_{41}^2(\text{eV}^2)$	0.012	0.009	-	-	-	-
$\sin^2 \theta_{24}$	0.045	0.047	-	-	-	-
$\sin^2 \theta_{34}$	0.000	0.002	-	-	-	-

Table 7.2: Best fit oscillation parameter values for both 3+1 sterile model and 3-flavor model. On the right shows the results from standard oscillation analysis [45].

values for all cases. The 3-flavor best fit point are consistent with that of the standard Ptheta analysis. The 3+1 sterile model has a larger $\sin^2 \theta_{23}$ to allow non-zero $\sin^2 \theta_{24/34}$.

7.2 3-flavor oscillation

Fig. 7.2 and 7.3 show the 2D confidence level intervals in Δm_{32}^2 vs. $\sin^2 \theta_{23}$ and δ_{CP} vs. $\sin^2 \theta_{13}$ respectively, and Fig. 7.4 shows the 1D $\Delta\chi^2$ plots in δ_{CP} . They are all consistent with the standard oscillation analysis results in Ref.[45].

7.3 3+1 sterile oscillation

Fig. 7.5 shows the confidence level contours in the $\sin^2 \theta_{24}$ vs. Δm_{41}^2 plane. Compared to the Asimov fit, the data fit has slightly better exclusion limits on $\sin^2 \theta_{24}$ for $\Delta m_{41}^2 < 5 \times 10^{-3}\text{eV}^2$. For NH, at $\Delta m_{41}^2 \sim 2.5 \times 10^{-3}\text{eV}^2$, the data fit and Asimov fit have different shapes (data is inward but Asimov is outward), which seems to be due to the slight deficit of FHC $1R\mu$ events in the sub-GeV region (see Fig. 7.1a). Basi-

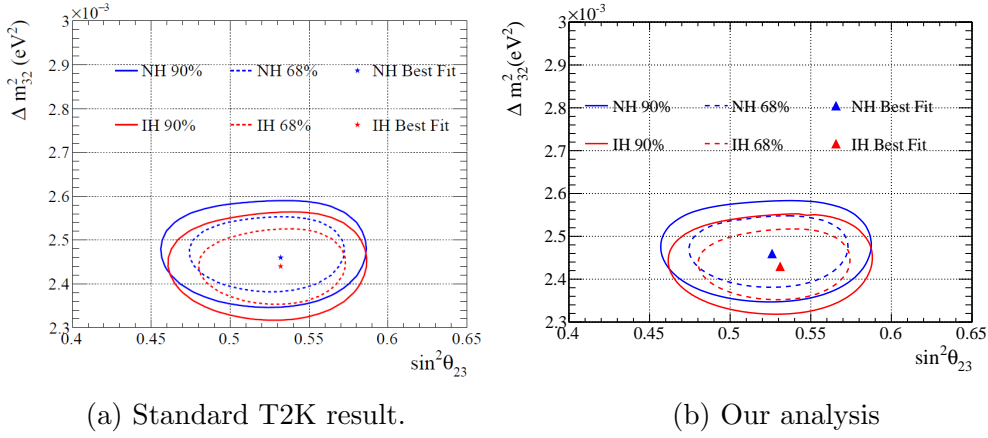
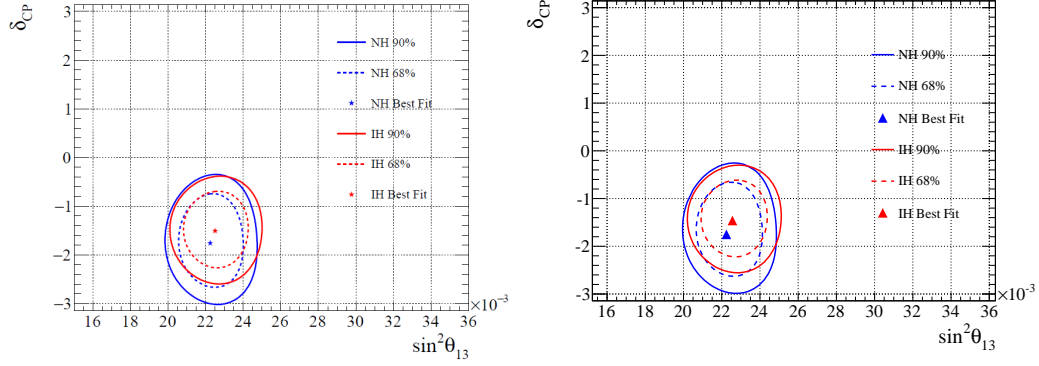


Figure 7.2: Data fit 2D confidence level contours in Δm_{32}^2 vs. $\sin^2 \theta_{23}$ for normal and inverted hierarchy.

cally the data fit is consistent with the Asimov fit, with certain statistical fluctuations that gradually stabilize as $\Delta m_{41}^2 > 0.1 \text{eV}^2$.

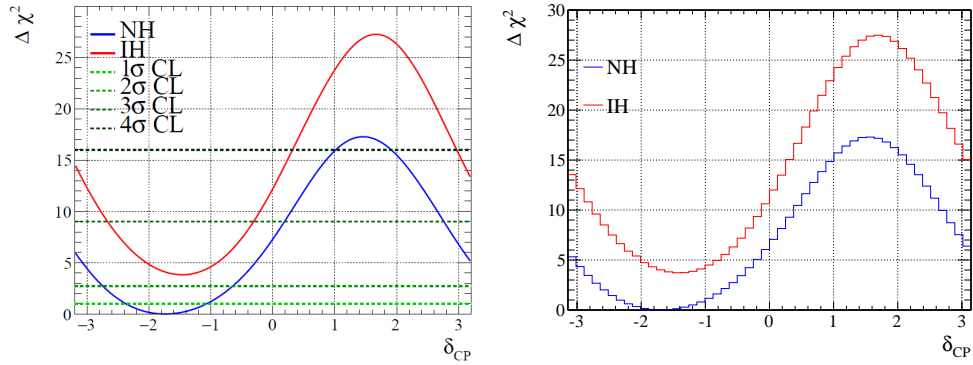
Fig. 7.6 shows the confidence level contours in the $\cos^2 \theta_{24} \sin^2 \theta_{34}$ vs. $\sin^2 \theta_{24}$ plane, with $\Delta m_{41}^2 = 0.1 \text{eV}^2$. The NH and IH contours overlay on each other. Again the data fit result is consistent with the Asimov ones.



(a) Standard T2K result.

(b) Our analysis

Figure 7.3: Data fit 2D confidence level contours in δ_{CP} vs. $\sin^2 \theta_{13}$ for normal and inverted hierarchy.



(a) Standard T2K result.

(b) Our analysis

Figure 7.4: Data fit 1D $\Delta \chi^2$ plots in δ_{CP} for normal and inverted hierarchy.

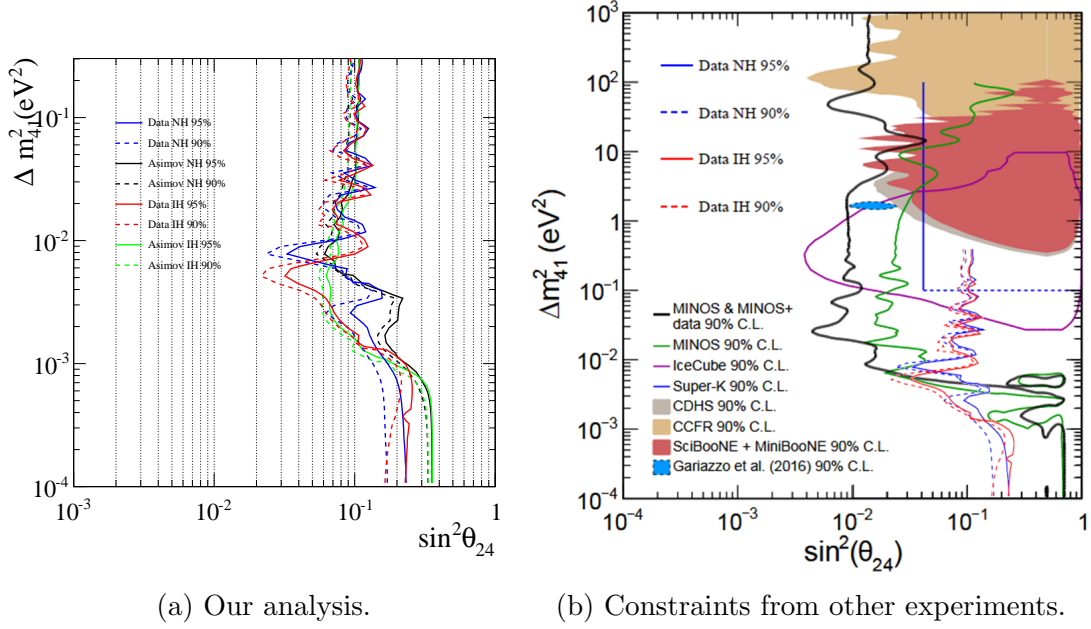


Figure 7.5: Data fit 2D confidence level contours in Δm_{41}^2 vs. $\sin^2 \theta_{24}$ for normal and inverted hierarchy. On the right shows our results overlaid on limit to date from other experiments[32–39] (Figure taken from [32]).

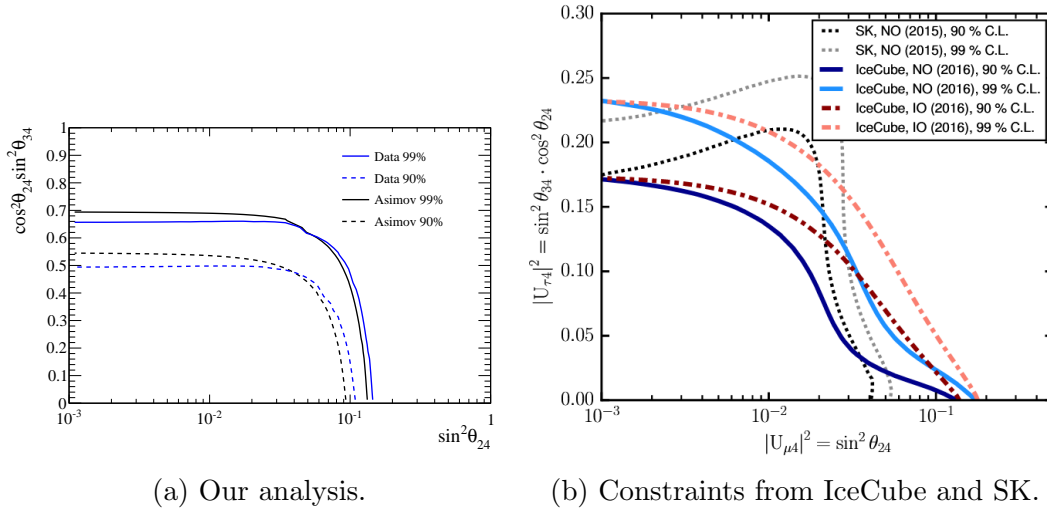


Figure 7.6: Data fit 2D confidence level contours in $\cos^2 \theta_{24} \sin^2 \theta_{34}$ vs. $\sin^2 \theta_{24}$. On the right shows the 90% and 99% upper limits from IceCube [40] and SK [35].

Chapter 8

Summary and prospect

There are interesting hints from experiments, like LSND and Daya Bay, which suggest a third mass splitting $\Delta m^2 \sim 1\text{eV}^2$ in neutrino oscillation. Such results might be explained by the existence of sterile neutrinos, which are present in many extensions of the Standard Model. Sterile neutrinos are neutral singlet fermions which do not participate in the weak interaction, making direct detection difficult. But if eV-scale sterile neutrinos exist, they can affect the oscillation spectra through mixing with the three active neutrinos.

In the T2K experiment, the high intensity neutrino beam produces large statistics of neutrino events which are useful in searching for sterile neutrino. We utilize the oscillation samples in the far detector SK to constrain the sterile mixing parameters under the 3+1 sterile neutrino model (3 active neutrinos + 1 sterile neutrino). In particular, we include the NC interaction samples in the oscillation analysis for the first time to enhance the sterile sensitivity.

The sterile mixing parameters have different effects on the oscillation spectra. T2K is mostly sensitive to the sterile mixing angles θ_{24} and θ_{34} . We modify the T2K

official fitter to include the sterile oscillation probability and NC oscillation samples. A joint analysis with both the standard CC oscillation samples and new NC samples is performed to constrain θ_{24} and θ_{34} for a range of Δm_{41}^2 .

We include both the CC samples and NC samples in the oscillation analysis. The standard CC samples, ν_μ disappearance samples (FHC/RHC 1R μ) and ν_e appearance samples (FHC/RHC 1Re, FHC ν_e CC1 π^+), are sensitive to θ_{24} . The new NC samples, FHC/RHC 2R π^0 samples (mainly NC1 π^0 resonant production) and FHC NC γ de-excitation sample (mainly NCQE events), measure the NC interaction rates of all three active neutrinos, and give us sensitivity on θ_{24} and θ_{34} .

Most systematic parameters inherit from the standard 3-flavor analysis. Two NC cross-section errors and twelve SK detector errors are added to describe the uncertainties on the newly added NC samples. The SK detector uncertainties are calculated based on separate studies, with FSI and SI model uncertainties handled by a reweighting software package.

The fit goodness is described by a joint likelihood function for all samples:

$$\mathcal{L}(\vec{N}_{\text{obs}}, \vec{N}_{\text{pred}}, o, f) = \mathcal{L}_{\text{sample}}(\vec{N}_{\text{obs}}, \vec{N}_{\text{pred}}(o, f)) \times \mathcal{L}_{\text{syst.}}(f) \times \mathcal{L}_{\text{external}}(o),$$

where $\mathcal{L}_{\text{sample}}$ is the binned Poisson likelihood between the number of observed events \vec{N}_{obs} and the number of predicted events \vec{N}_{pred} calculated with oscillation parameters o and systematic parameters f . The systematic penalty $L_{\text{syst.}}$ is evaluated with the input covariance matrix, and $\mathcal{L}_{\text{external}}$ is used to include any external constraint on the oscillation parameters.

An Asimov data set (event rates predicted without any statistical or systematic fluctuations) is generated assuming T2K-SK Run1-8 POT (except NC γ de-excitation

sample, only Run1-4), no sterile mixing. The expected sensitivity of the sterile mixing parameters are evaluated by fitting the Asimov data.

Data fits are performed in two sterile parameter planes: $\sin^2 \theta_{24}$ vs Δm_{41}^2 , and $\sin^2 \theta_{24}$ vs $\sin^2 \theta_{34}$. The data fit results are consistent with the Asimov sensitivity. Our constraint on $\sin^2 \theta_{24}$ is better than any existing results for $\Delta m_{41}^2 < 0.003\text{eV}^2$. However we are not competitive for larger Δm_{41}^2 values, or in the $\sin^2 \theta_{34}$ constraint. We exclude $\sin^2 \theta_{24} > 0.1$ and $\sin^2 \theta_{34} > 0.5$ at 90% limit for $\Delta m_{41}^2 > 0.1\text{eV}^2$.

The current analysis is still statistically limited, and future T2K data will definitely improve our results (shown in Sec. 6.3). Additional oscillation samples are in development to provide extra statistics: multi-ring samples which contain higher neutrino energy events and benefit searches at large Δm_{41}^2 , and RHC NC γ de-excitation sample which improves θ_{34} constraint.

Among the systematic parameters, the newly added NC cross-section errors (NC1 π and NCQE) turn out to be the greatest systematic limitations in the fit. Future cross-section analysis from T2K (or other experiments) might help reduce these errors. The SK errors of NC samples can also be reduced by: the transition from apfit to fitQun reconstruction for $2R\pi^0$ samples (together with a slight increase in statistics), and the reduction of secondary γ production error with measurements in RCNP for NC γ de-excitation samples. The extent of improvement can be estimated from the studies in Sec. 6.4.

Another possible improvement strategy is the joint fit analysis with other data sets. At present, the ND280 (near detector) samples act as the input of BANFF fit which constrain the neutrino flux and cross-section systematic parameters propagated to the oscillation analysis. The SK detector uncertainties are characterized by the atmospheric neutrino samples, which include some built-in cross-section uncertain-

ties. Therefore the cross-section errors are somewhat double-counted and inflate the detector systematics. A joint analysis that utilizes the T2K-SK oscillation samples, ND280 samples, and SK atmospheric neutrino samples will both increase the statistics and reduce the systematics. The ND280 samples also provide sterile sensitivity for Δm_{41}^2 up to 100 eV^2 . Such analysis framework is now under development by both T2K and SK members, and will definitely benefit both the standard oscillation fit and the sterile oscillation fit.

There are some long scale projects related to the T2K. These include the ND280 upgrades[170] and construction of new near detectors in J-PARC (WAGACI/Baby-MIND[171], NINJA[172], E61[173–175]) which improves cross-section measurements and provides new samples for short baseline sterile analysis. In the far detector aspect, we have the SK-Gd upgrade with better neutrino/anti-neutrino discrimination, and the proposed T2HK which uses Hyper-Kamiokande as a new far detector[176] (or T2HKK with one more detector in Korea) to gain larger event statistics with smaller detector errors. The combination of all these efforts contribute to both standard 3-flavor oscillation and sterile oscillation analysis. We look forward to their realizations, together with the upcoming short baseline oscillation experiments, that would lead to major discoveries in the next five or ten years.

Appendix A

SK event reconstruction algorithms

The section describes in details the two reconstruction algorithms, apfit and fitQun, used in SK.

A.1 apfit

In apfit, the reconstruction process goes through a series of steps:

1. Vertex reconstruction

The event vertex is first approximated by assuming the PMT hits are due to a single point source. The point vertex, \vec{A} , is found by minimizing the time residual t_i for all PMT hits:

$$t_i = t_i^0 - \frac{n_w}{c} |\vec{P}_i - \vec{A}|, \quad (\text{A.1})$$

where t_i^0 is raw hit time, and \vec{P}_i is the position of the i -th PMT. The particle

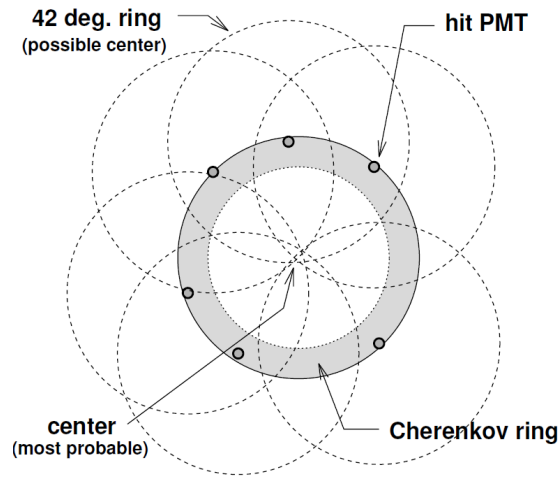


Figure A.1: Illustration of the Hough Transform (Figure taken from [41]).

direction is estimated by summing the PMT hit vectors.

Then, the Cherenkov ring edge is searched by tuning the ring opening angle to match the observed charge pattern and improve direction construction.

Finally, the vertex position is refined by considering a line-source of photons and accounting for scattering effects.

2. Ring counting

After the 1st ring is identified in previous step, the algorithm searches for other ring candidates by applying the method of Hough Transform[177]. Fig. A.1 illustrates the idea. A 42° cone is drawn around each PMT hit, and the intersection of these cones give the ring center.

The ring candidate is then tested by a likelihood function which compares the observed charge pattern with the N -ring and $N+1$ -ring hypotheses. If the $N+1$ -ring hypothesis is favored, the process repeats to find the next ring candidate. Otherwise it is stopped and the number of rings is determined to be N . A maximum of 5 rings can be identified.

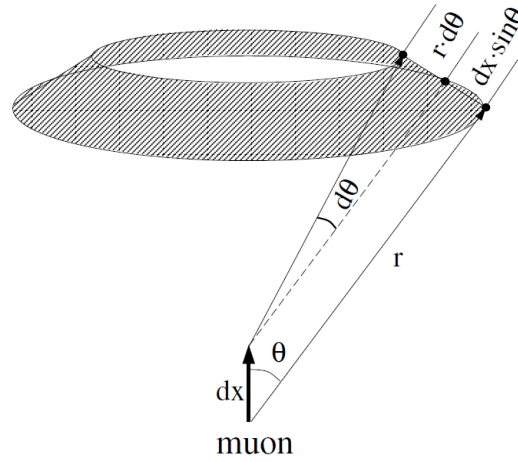


Figure A.2: Illustration of Cherenkov photon emission from a muon. When muon loss energy in a distance dx , photons are emitted in the region $dx \cdot \sin \theta + r \cdot d\theta$ (Figure taken from [42]).

3. Particle identification

A particle identification (PID) algorithm is applied on each identified Cherenkov ring. The observed charge pattern is compared with the prediction from a showering event (e -like) and a non-showering event (μ -like) respectively.

The showering events are mostly due to electrons or gammas, where the electromagnetic showers or multiple scattering produce a diffuse charge pattern. The expected charge distributions are prepared in advance by Monte Carlo simulations, which are characterized by the electron momentum and the PMT angle relative to the electron direction.

For muon rings, muons are assumed to travel in a straight line with no scattering, and the expected charge distribution can be analytically calculated. Also, when muon loses energy during propagation, the Cherenkov angle slowly decreases as well, which changes the area subtended the Cherenkov photons (see Fig. A.2).

4. Precise vertex fitting (MS-fit)

The vertex position is refitted by including also the ring pattern information. The vertex position and particle direction are adjusted to improve the PID likelihood. The final vertex resolution is around 30 cm for 1-ring events.

5. Momentum reconstruction

For each Cherenkov ring, the particle momentum is reconstructed by summing the observed PMT charges inside a cone with a half opening angle of 70° . In case the i -th PMT hit is shared between two or more cones, the charge is separated based on the expected charge contributions from each ring.

The observed p.e. in the n -th ring are corrected by:

$$RTOT_n = \frac{G_{MC}}{G_{data}} \left[\alpha \times \sum_{\substack{\theta_{i,n} < 70^\circ \\ -50ns < t_i < 250ns}} \left(q_{i,n}^{obs} \times \exp\left(\frac{r_i}{L}\right) \times \frac{\cos \Theta_i}{f(\Theta_i)} \right) - \sum_{\theta_{i,n} < 70^\circ} S_i \right], \quad (\text{A.2})$$

where

α : normalization factor,

G_{data}, G_{MC} : relative PMT gain parameter for data and Monte Carlo simulation,

$q_{i,n}^{obs}$: observed charges in the i -th PMT due to the n -th ring,

$\theta_{i,n}$: opening angle between the n -th ring direction and the i -th PMT direction,

Θ_i : Angle of photon arriving direction relative to the i -th PMT,

t_i : time-of-flight subtracted hit time of the i -th PMT position,

L : light attenuation length in water,

r_i : distance from vertex position to the i -th PMT,

$f(\Theta)$: correction function for PMT acceptance, and

S_i : expected charge for the i -th PMT from scattered photons.

$RTOT$ is then converted to momentum using the e/μ conversion table obtained from MC.

6. Decay electron search

When low energy muons stop in the detector, decay electrons are produced which are indicator of μ -like events. They are identified by searching for PMT hit clusters in time (also with some timing and vertex goodness cuts) after the primary neutrino events. Tagged electrons can be classified into three categories: primary-event type where the electron is found within the primary event time window, sub-event type which is outside that time window, and split type in which the energy deposition is split between the primary event and sub-event . The tagging efficiencies are around 96% for μ^+ and 80% for μ^- in SK-IV.

7. Ring number correction

Some of the mis-identified rings have too low momentum or are overlapped with other rings. The ring number correction process compares the i -th ring with the j -th ring, where $i \neq j$. If (I) the i -th ring is of low momentum and overlaps with j -th ring of larger momentum, or (II) the i -th ring is of low momentum and the momentum is very small compared with the j -th ring, the i -th ring is removed.

8. π^0 fitting

As mentioned before, single π^0 production in NC interaction constitutes a large background in the 1-ring e -like samples. This happens when the two gammas from π^0 decay are considerably asymmetric so one gamma is of too small energy to be reconstructed, or the two gamma rings overlap and are reconstructed as one ring only.

A π^0 fitter is applied on the 1-ring e -like events, which assumes the existence of two overlapping gamma rings. The direction of the more energetic gamma is fixed as the reconstructed ring direction. The second ring direction and the energy balance between the two gammas are varied until a best-fit combination is found. The π^0 rejection is done by a cut on the output likelihood value.

A.2 fitQun

fitQun is a maximum likelihood fitter that maximizes the following likelihood function in event reconstruction:

$$L(x) = \prod_j^{\text{unhit}} P_j(\text{unhit}|\mathbf{x}) \prod_i^{\text{hit}} \{1 - P_i(\text{unhit}|\mathbf{x})\} f_q(q_i|\mathbf{x}) f_t(t_i|\mathbf{x}), \quad (\text{A.3})$$

where \mathbf{x} corresponds to the particle track parameters, $P(\text{unhit}|\mathbf{x})$ ($1 - P(\text{unhit}|\mathbf{x})$) is the PMT unhit (hit) probability, and $f_q(q_i|\mathbf{x})$ and $f_t(t_i|\mathbf{x})$ are the probability density functions of observed charge and time respectively. \mathbf{x} can be either a single particle or multi-particle hypothesis, and the collected charges in each PMT are calculated analytically based on the MC generated Cherenkov emission profile, light attenuation factor, PMT acceptance and scattering light contribution.

The reconstruction process is divided into five steps:

1. Vertex pre-fitter
2. Hit clustering
3. Singel-ring fitter
4. π^0 fitter
5. Multi-ring fitter

To begin, a single vertex is first found to avoid the likelihood being stuck at a local minimum. The vertex pre-fitter uses only the PMT hit time information to roughly estimate the vertex position, in a way similar to the first step in *apfit*. Another option is directly using the *apfit* vertex.

Next, in hit clustering, a simple algorithm is used to divide the whole event time window into several “subevents”. Fixing the vertex position as the vertex pre-fitter’s one, the vertex timing is varied to find peaks in the vertex goodness functions. For example, in a stopping muon event with decay electron production, the parent muon production time and the decay electron production time would appear as two separate peaks. A -180 ns to 800 ns time window is defined around each peak to form a subevent (time windows would be merged into one in case of overlapping), and the vertex pre-fitter is performed again for each subevent. The decay electron detection efficiency found in this way is around 88%.

For each subevent, a single-ring fitter is performed to maximize the likelihood function in Eq. A.3 under the single particle hypothesis. There are three possible particle hypothesis: e , μ and π^+ , and the corresponding fitters are applied one by one. Among them, the most special one is the π^+ fitter. While the Cherenkov emission profiles of π^+ are similar to those of μ because of their similar masses, π^+ can easily

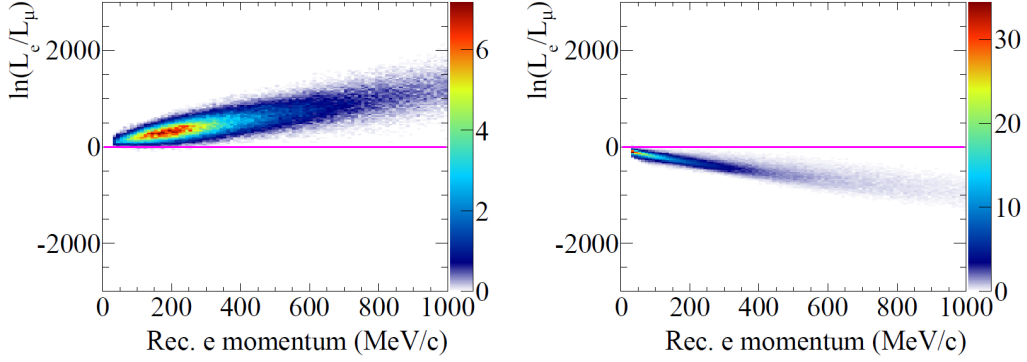


Figure A.3: Likelihood separation of single-ring electron (left) and muon (right) events for SK-IV atmospheric neutrino MC. The magenta lines show the cut criteria for electron-muon separation (Figure taken from [25]).

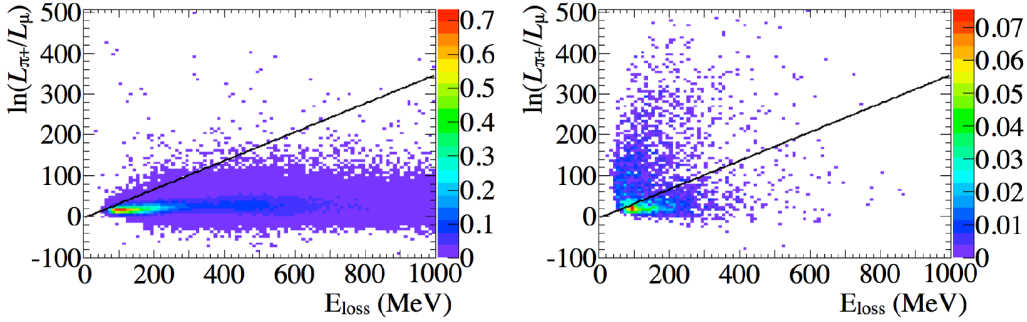


Figure A.4: Likelihood separation of ν_μ charged-current quasi-elastic (left) and $\text{NC}\pi^+$ (right) events for T2K neutrino MC. The black lines show the cut criteria for muon- π^+ separation (Figure taken from [25]).

have hadronic interaction in water which causes scattering or absorption. Thus the π^+ fitter fits for two rings: the “upstream-track” ring before hadronic interaction and the “downstream-track” ring after. The μ fitter result is used as a seed in the upstream-track reconstruction, and the energy loss E_{loss} in the upstream-track is fit, assuming constant energy loss per unit length, to give the downstream-track vertex. The e/μ separation is done by taking the ratio of the log likelihoods $\ln(L_e/L_\mu)$, and the μ/π^+ separation has a two-dimensional cut on $\ln(L_{\pi^+}/L_\mu)$ and E_{loss} . Figs. A.3 and A.4 illustrate the separation powers.

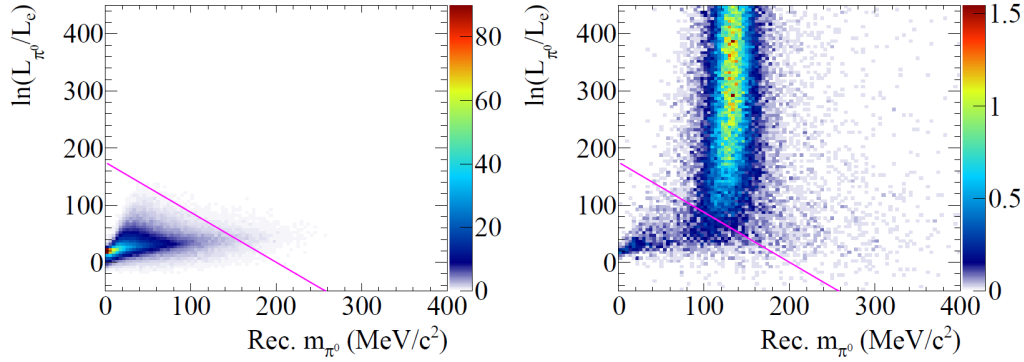


Figure A.5: Likelihood separation of the CC single electron (left) and NC single π^0 (right) events in the SK-IV atmospheric neutrino MC. The magenta lines show the cut criteria for electron- π^0 separation (Figure taken from [25]).

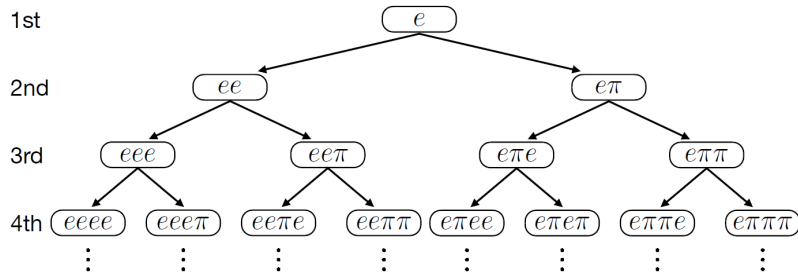


Figure A.6: Schematic diagram of ring counting in the multi-ring fitter of fitQun. The fifth and sixth rings are assumed to be e -like only. This diagram shows the procedure assuming the first ring to be e -like, and the same procedure is repeated for the case of first ring being π^+ -like (Figure taken from [24]).

The π^0 fitter is a dedicated two-ring fitter to identify the $\pi^0 \rightarrow \gamma\gamma$ decay. In each e -like subevent, the e -fit result is acted as the seed for the first gamma ring, and the second gamma ring is searched by minimizing $-\ln L$ with respect to ring directions, momenta and other track parameters. The ratio of the likelihood values L_{π^0}/L_e , as well as the reconstructed π^0 invariant mass, are used to reject π^0 from e -like events (see Fig. A.5).

Finally, the multi-ring fitter is applied only on the first subevent, since subsequent subevents usually contain single particle. As shown in Fig. A.6, a search up

to six rings by doing an exhaustive search for all possible ring candidate combinations. Electrons and gammas are fit by e -hypothesis, while muons and π^+ are fit by upstream-track π^+ hypothesis. Starting from the first ring, additional ring is added assuming the same vertex, and $-\ln L$ is minimized over the two-particle track parameters. The log likelihood ratio $\ln(L_{2R}/L_{1R})$ is evaluate to determine whether the new ring is true or fake. The process repeats until a fake ring or six true rings are found. Once the ring counting is done, the rings are re-ordered by visible energy. The most energetic ring will be merged with lower energy ring(s) if their relative angle is less than 20° . Then all the rings are refitted, in descending order of energy, by the three particle hypothesis (e, μ, π^+) with other rings fixed. If the ring is identified as non-showering (μ/π^+), the most energetic ring is always to assumed to be μ while lower energy rings are π^+ . This is because ν_μ CC events usually have a true muon ring and very rare a true π^+ ring is the most energetic in NC events.

Appendix B

Event rate tables

This section lists the event rates of the eight oscillation samples in the sensitivity study in Section 6.

Event Type	$\nu_\mu \rightarrow \nu_\mu$	$\nu_e \rightarrow \nu_e$	$\bar{\nu}_\mu \rightarrow \bar{\nu}_\mu$	$\bar{\nu}_e \rightarrow \bar{\nu}_e$	$\nu_\mu \rightarrow \nu_e$	$\bar{\nu}_\mu \rightarrow \bar{\nu}_e$	Total
CCQE	175.635	0.004	11.028	0.000	0.022	0.000	186.690
CCMEC	35.525	0.002	1.409	0.000	0.026	0.000	36.961
CC 1π	27.696	0.002	2.616	0.000	0.024	0.000	30.338
CC coh.	0.288	0.000	0.092	0.000	0.000	0.000	0.381
CC other	5.467	0.001	0.406	0.000	0.000	0.000	5.874
NC 1π	5.523	0.116	0.197	0.011	0.000	0.000	5.847
NC coh.	0.000	0.000	0.000	0.000	0.000	0.000	0.000
NC 1γ	0.000	0.000	0.000	0.000	0.000	0.000	0.000
NC other	2.056	0.074	0.131	0.009	0.000	0.000	2.270
Subtotal	252.191	0.199	15.879	0.021	0.072	0.000	
Total			268.361				

Table B.1: Event rate table for FHC $1R\mu$ sample in 3-flavor oscillation analysis.

Event Type	$\nu_\mu \rightarrow \nu_\mu$	$\nu_e \rightarrow \nu_e$	$\bar{\nu}_\mu \rightarrow \bar{\nu}_\mu$	$\bar{\nu}_e \rightarrow \bar{\nu}_e$	$\nu_\mu \rightarrow \nu_e$	$\bar{\nu}_\mu \rightarrow \bar{\nu}_e$	Total
CCQE	0.161	6.306	0.006	0.255	46.282	0.278	53.289
CCMEC	0.030	1.597	0.001	0.043	8.689	0.039	10.399
CC 1π	0.047	0.932	0.003	0.067	4.495	0.047	5.592
CC coh.	0.000	0.008	0.000	0.004	0.034	0.003	0.050
CC other	0.013	0.128	0.000	0.009	0.089	0.003	0.243
NC 1π	1.870	0.042	0.070	0.004	0.000	0.000	1.987
NC coh.	0.528	0.007	0.048	0.003	0.000	0.000	0.586
NC 1γ	0.942	0.017	0.050	0.002	0.000	0.000	1.011
NC other	0.318	0.017	0.021	0.001	0.000	0.000	0.357
Subtotal	3.910	9.054	0.200	0.390	59.589	0.371	
Total							73.514

Table B.2: Event rate table for FHC 1Re sample in 3-flavor oscillation analysis.

Event Type	$\nu_\mu \rightarrow \nu_\mu$	$\nu_e \rightarrow \nu_e$	$\bar{\nu}_\mu \rightarrow \bar{\nu}_\mu$	$\bar{\nu}_e \rightarrow \bar{\nu}_e$	$\nu_\mu \rightarrow \nu_e$	$\bar{\nu}_\mu \rightarrow \bar{\nu}_e$	Total
CCQE	15.293	0.001	29.874	0.001	0.001	0.001	45.171
CCMEC	4.470	0.000	2.838	0.000	0.000	0.000	7.310
CC 1π	3.955	0.000	4.533	0.000	0.001	0.001	8.489
CC coh.	0.047	0.000	0.176	0.000	0.000	0.000	0.223
CC other	0.942	0.000	0.606	0.000	0.000	0.000	1.548
NC 1π	0.420	0.017	0.522	0.014	0.000	0.000	0.973
NC coh.	0.000	0.000	0.002	0.000	0.000	0.000	0.002
NC 1γ	0.000	0.000	0.000	0.000	0.000	0.000	0.000
NC other	0.316	0.016	0.201	0.008	0.000	0.000	0.541
Subtotal	25.443	0.035	38.751	0.023	0.002	0.002	
Total							64.256

Table B.3: Event rate table for RHC 1R μ sample in 3-flavor oscillation analysis.

Event Type	$\nu_\mu \rightarrow \nu_\mu$	$\nu_e \rightarrow \nu_e$	$\bar{\nu}_\mu \rightarrow \bar{\nu}_\mu$	$\bar{\nu}_e \rightarrow \bar{\nu}_e$	$\nu_\mu \rightarrow \nu_e$	$\bar{\nu}_\mu \rightarrow \bar{\nu}_e$	Total
CCQE	0.013	0.509	0.024	0.848	1.027	2.859	5.280
CCMEC	0.003	0.144	0.002	0.113	0.233	0.331	0.825
CC 1π	0.008	0.101	0.007	0.144	0.143	0.334	0.738
CC coh.	0.000	0.001	0.000	0.011	0.001	0.031	0.045
CC other	0.004	0.021	0.001	0.012	0.010	0.007	0.055
NC 1π	0.163	0.007	0.196	0.005	0.000	0.000	0.372
NC coh.	0.048	0.002	0.203	0.003	0.000	0.000	0.256
NC 1γ	0.079	0.004	0.175	0.004	0.000	0.000	0.263
NC other	0.057	0.002	0.027	0.001	0.000	0.000	0.087
Subtotal	0.374	0.792	0.636	1.141	1.415	3.562	
Total	7.920						

Table B.4: Event rate table for RHC 1Re sample in 3-flavor oscillation analysis.

Event Type	$\nu_\mu \rightarrow \nu_\mu$	$\nu_e \rightarrow \nu_e$	$\bar{\nu}_\mu \rightarrow \bar{\nu}_\mu$	$\bar{\nu}_e \rightarrow \bar{\nu}_e$	$\nu_\mu \rightarrow \nu_e$	$\bar{\nu}_\mu \rightarrow \bar{\nu}_e$	Total
CCQE	0.029	0.024	0.001	0.002	0.212	0.003	0.270
CCMEC	0.010	0.022	0.000	0.001	0.160	0.001	0.195
CC 1π	0.076	0.761	0.003	0.004	4.854	0.002	5.699
CC coh.	0.000	0.018	0.000	0.000	0.111	0.000	0.129
CC other	0.038	0.112	0.001	0.003	0.121	0.002	0.276
NC 1π	0.085	0.002	0.005	0.000	0.000	0.000	0.093
NC coh.	0.000	0.000	0.000	0.000	0.000	0.000	0.000
NC 1γ	0.028	0.000	0.001	0.000	0.000	0.000	0.029
NC other	0.206	0.008	0.013	0.001	0.000	0.000	0.228
Subtotal	0.472	0.948	0.024	0.011	5.458	0.008	
Total	6.919						

Table B.5: Event rate table for FHC $\nu_e\text{CC}1\pi^+$ sample in 3-flavor oscillation analysis.

Event Type	$\nu_\mu \rightarrow \nu_\mu$	$\nu_e \rightarrow \nu_e$	$\bar{\nu}_\mu \rightarrow \bar{\nu}_\mu$	$\bar{\nu}_e \rightarrow \bar{\nu}_e$	$\nu_\mu \rightarrow \nu_e$	$\bar{\nu}_\mu \rightarrow \bar{\nu}_e$	Total
CCQE	0.034	0.068	0.002	0.004	0.434	0.002	0.543
CCMEC	0.009	0.015	0.000	0.000	0.044	0.000	0.068
CC 1π	0.221	0.078	0.001	0.005	0.373	0.004	0.683
CC coh.	0.000	0.003	0.000	0.001	0.010	0.001	0.016
CC other	0.072	0.021	0.000	0.002	0.013	0.000	0.108
NC 1π	32.065	0.620	1.119	0.062	0.000	0.000	33.866
NC coh.	8.639	0.145	0.634	0.028	0.000	0.000	9.447
NC 1γ	0.025	0.001	0.001	0.000	0.000	0.000	0.028
NC other	4.273	0.159	0.261	0.021	0.000	0.000	4.714
Subtotal	45.338	1.111	2.019	0.124	0.873	0.007	
Total	49.473						

Table B.6: Event rate table for FHC $2R\pi^0$ sample in 3-flavor oscillation analysis.

Event Type	$\nu_\mu \rightarrow \nu_\mu$	$\nu_e \rightarrow \nu_e$	$\bar{\nu}_\mu \rightarrow \bar{\nu}_\mu$	$\bar{\nu}_e \rightarrow \bar{\nu}_e$	$\nu_\mu \rightarrow \nu_e$	$\bar{\nu}_\mu \rightarrow \bar{\nu}_e$	Total
CCQE	0.002	0.006	0.005	0.009	0.010	0.028	0.060
CCMEC	0.001	0.002	0.000	0.001	0.002	0.001	0.006
CC 1π	0.016	0.008	0.003	0.010	0.010	0.026	0.073
CC coh.	0.000	0.001	0.000	0.003	0.001	0.007	0.012
CC other	0.011	0.003	0.001	0.002	0.001	0.002	0.020
NC 1π	2.168	0.088	3.640	0.078	0.000	0.000	5.973
NC coh.	0.517	0.018	3.308	0.043	0.000	0.000	3.887
NC 1γ	0.003	0.000	0.002	0.000	0.000	0.000	0.005
NC other	0.615	0.028	0.439	0.017	0.000	0.000	1.100
Subtotal	3.333	0.153	7.398	0.163	0.024	0.064	
Total	11.136						

Table B.7: Event rate table for RHC $2R\pi^0$ sample in 3-flavor oscillation analysis.

Event Type	$\nu_\mu \rightarrow \nu_\mu$	$\nu_e \rightarrow \nu_e$	$\bar{\nu}_\mu \rightarrow \bar{\nu}_\mu$	$\bar{\nu}_e \rightarrow \bar{\nu}_e$	$\nu_\mu \rightarrow \nu_e$	$\bar{\nu}_\mu \rightarrow \bar{\nu}_e$	Total
CCQE	2.633	0.000	0.059	0.000	0.000	0.000	2.692
CCMEC	0.000	0.000	0.000	0.000	0.000	0.000	0.000
CC 1π	0.794	0.002	0.007	0.000	0.000	0.000	0.803
CC coh.	0.025	0.000	0.002	0.000	0.000	0.000	0.026
CC other	0.108	0.000	0.003	0.000	0.000	0.000	0.112
NC 1π	17.682	0.361	0.934	0.000	0.000	0.000	18.977
NC coh.	0.000	0.000	0.000	0.000	0.000	0.000	0.000
NC 1γ	0.000	0.000	0.000	0.000	0.000	0.000	0.000
NC other	79.115	1.114	2.561	0.000	0.000	0.000	82.789
Subtotal	100.357	1.477	3.565	0.000	0.000	0.000	
Beam unrelated							2.299
Total							107.698

Table B.8: Event rate table for FHC NC γ de-excitation sample in 3-flavor oscillation analysis.

Event Type	$\nu_\mu \rightarrow \nu_\mu$	$\nu_e \rightarrow \nu_e$	$\bar{\nu}_\mu \rightarrow \bar{\nu}_\mu$	$\bar{\nu}_e \rightarrow \bar{\nu}_e$	$\nu_\mu \rightarrow \nu_e$	$\bar{\nu}_\mu \rightarrow \bar{\nu}_e$	Total
CCQE	175.739	0.004	11.027	0.000	0.021	0.000	186.792
CCMEC	35.538	0.002	1.408	0.000	0.024	0.000	36.972
CC 1π	27.702	0.002	2.616	0.000	0.022	0.000	30.342
CC coh.	0.288	0.000	0.092	0.000	0.000	0.000	0.381
CC other	5.467	0.001	0.406	0.000	0.000	0.000	5.875
NC 1π	5.523	0.116	0.197	0.011	0.000	0.000	5.847
NC coh.	0.000	0.000	0.000	0.000	0.000	0.000	0.000
NC 1γ	0.000	0.000	0.000	0.000	0.000	0.000	0.000
NC other	2.056	0.074	0.131	0.009	0.000	0.000	2.270
Subtotal	252.314	0.199	15.877	0.021	0.067	0.000	
Total							268.478

Table B.9: Event rate table for FHC $1R_\mu$ sample in 3+1 sterile oscillation analysis.

Event Type	$\nu_\mu \rightarrow \nu_\mu$	$\nu_e \rightarrow \nu_e$	$\bar{\nu}_\mu \rightarrow \bar{\nu}_\mu$	$\bar{\nu}_e \rightarrow \bar{\nu}_e$	$\nu_\mu \rightarrow \nu_e$	$\bar{\nu}_\mu \rightarrow \bar{\nu}_e$	Total
CCQE	0.161	6.344	0.006	0.254	42.755	0.304	49.825
CCMEC	0.030	1.605	0.001	0.043	8.071	0.042	9.792
CC 1π	0.047	0.935	0.003	0.067	4.205	0.051	5.308
CC coh.	0.000	0.008	0.000	0.004	0.032	0.004	0.048
CC other	0.013	0.128	0.000	0.009	0.085	0.003	0.240
NC 1π	1.870	0.042	0.070	0.004	0.000	0.000	1.987
NC coh.	0.528	0.007	0.048	0.003	0.000	0.000	0.586
NC 1γ	0.942	0.017	0.050	0.002	0.000	0.000	1.011
NC other	0.318	0.017	0.021	0.001	0.000	0.000	0.357
Subtotal	3.910	9.104	0.200	0.388	55.147	0.404	
Total	69.154						

Table B.10: Event rate table for FHC 1Re sample in 3+1 sterile oscillation analysis.

Event Type	$\nu_\mu \rightarrow \nu_\mu$	$\nu_e \rightarrow \nu_e$	$\bar{\nu}_\mu \rightarrow \bar{\nu}_\mu$	$\bar{\nu}_e \rightarrow \bar{\nu}_e$	$\nu_\mu \rightarrow \nu_e$	$\bar{\nu}_\mu \rightarrow \bar{\nu}_e$	Total
CCQE	15.296	0.001	29.863	0.001	0.001	0.001	45.162
CCMEC	4.471	0.000	2.837	0.000	0.000	0.000	7.309
CC 1π	3.955	0.000	4.532	0.000	0.001	0.001	8.489
CC coh.	0.047	0.000	0.176	0.000	0.000	0.000	0.223
CC other	0.942	0.000	0.606	0.000	0.000	0.000	1.548
NC 1π	0.420	0.017	0.522	0.014	0.000	0.000	0.973
NC coh.	0.000	0.000	0.002	0.000	0.000	0.000	0.002
NC 1γ	0.000	0.000	0.000	0.000	0.000	0.000	0.000
NC other	0.316	0.016	0.201	0.008	0.000	0.000	0.541
Subtotal	25.446	0.035	38.737	0.023	0.002	0.002	
Total	64.246						

Table B.11: Event rate table for RHC 1R μ sample in 3+1 sterile oscillation analysis.

Event Type	$\nu_\mu \rightarrow \nu_\mu$	$\nu_e \rightarrow \nu_e$	$\bar{\nu}_\mu \rightarrow \bar{\nu}_\mu$	$\bar{\nu}_e \rightarrow \bar{\nu}_e$	$\nu_\mu \rightarrow \nu_e$	$\bar{\nu}_\mu \rightarrow \bar{\nu}_e$	Total
CCQE	0.013	0.512	0.024	0.844	0.957	3.179	5.528
CCMEC	0.003	0.144	0.002	0.112	0.219	0.366	0.847
CC 1π	0.008	0.101	0.007	0.144	0.136	0.365	0.761
CC coh.	0.000	0.001	0.000	0.011	0.001	0.035	0.048
CC other	0.004	0.021	0.001	0.012	0.010	0.007	0.055
NC 1π	0.163	0.007	0.196	0.005	0.000	0.000	0.372
NC coh.	0.048	0.002	0.203	0.003	0.000	0.000	0.256
NC 1γ	0.079	0.004	0.175	0.004	0.000	0.000	0.263
NC other	0.057	0.002	0.027	0.001	0.000	0.000	0.087
Subtotal	0.375	0.796	0.636	1.135	1.323	3.952	
Total	8.216						

Table B.12: Event rate table for RHC 1Re sample in 3+1 sterile oscillation analysis.

Event Type	$\nu_\mu \rightarrow \nu_\mu$	$\nu_e \rightarrow \nu_e$	$\bar{\nu}_\mu \rightarrow \bar{\nu}_\mu$	$\bar{\nu}_e \rightarrow \bar{\nu}_e$	$\nu_\mu \rightarrow \nu_e$	$\bar{\nu}_\mu \rightarrow \bar{\nu}_e$	Total
CCQE	0.029	0.025	0.001	0.002	0.196	0.003	0.255
CCMEC	0.010	0.022	0.000	0.001	0.150	0.001	0.184
CC 1π	0.076	0.764	0.003	0.004	4.525	0.002	5.374
CC coh.	0.000	0.018	0.000	0.000	0.103	0.000	0.121
CC other	0.038	0.112	0.001	0.003	0.115	0.002	0.271
NC 1π	0.085	0.002	0.005	0.000	0.000	0.000	0.093
NC coh.	0.000	0.000	0.000	0.000	0.000	0.000	0.000
NC 1γ	0.028	0	0.001	0.000	0.000	0.000	0.029
NC other	0.206	0.008	0.013	0.001	0.000	0.000	0.228
Subtotal	0.472	0.952	0.024	0.011	5.089	0.008	
Total	6.556						

Table B.13: Event rate table for FHC ν_e CC $1\pi^+$ sample in 3+1 sterile oscillation analysis.

Event Type	$\nu_\mu \rightarrow \nu_\mu$	$\nu_e \rightarrow \nu_e$	$\bar{\nu}_\mu \rightarrow \bar{\nu}_\mu$	$\bar{\nu}_e \rightarrow \bar{\nu}_e$	$\nu_\mu \rightarrow \nu_e$	$\bar{\nu}_\mu \rightarrow \bar{\nu}_e$	Total
CCQE	0.034	0.068	0.002	0.004	0.402	0.002	0.512
CCMEC	0.009	0.015	0.000	0.000	0.041	0.000	0.065
CC 1π	0.222	0.079	0.001	0.005	0.348	0.004	0.659
CC coh.	0.000	0.003	0.000	0.001	0.009	0.001	0.015
CC other	0.072	0.021	0.000	0.002	0.012	0.000	0.108
NC 1π	32.065	0.620	1.119	0.062	0.000	0.000	33.866
NC coh.	8.639	0.145	0.634	0.028	0.000	0.000	9.447
NC 1γ	0.025	0.001	0.001	0.000	0.000	0.000	0.028
NC other	4.273	0.159	0.261	0.021	0.000	0.000	4.714
Subtotal	45.338	1.112	2.019	0.124	0.813	0.008	
Total	49.414						

Table B.14: Event rate table for FHC $2R\pi^0$ sample in 3+1 sterile oscillation analysis.

Event Type	$\nu_\mu \rightarrow \nu_\mu$	$\nu_e \rightarrow \nu_e$	$\bar{\nu}_\mu \rightarrow \bar{\nu}_\mu$	$\bar{\nu}_e \rightarrow \bar{\nu}_e$	$\nu_\mu \rightarrow \nu_e$	$\bar{\nu}_\mu \rightarrow \bar{\nu}_e$	Total
CCQE	0.002	0.006	0.005	0.009	0.009	0.031	0.062
CCMEC	0.001	0.002	0.000	0.001	0.002	0.001	0.006
CC 1π	0.016	0.008	0.003	0.010	0.010	0.029	0.075
CC coh.	0.000	0.001	0.000	0.003	0.000	0.008	0.012
CC other	0.011	0.003	0.001	0.002	0.001	0.002	0.020
NC 1π	2.168	0.088	3.640	0.078	0.000	0.000	5.973
NC coh.	0.517	0.018	3.308	0.043	0.000	0.000	3.887
NC 1γ	0.003	0.000	0.002	0.000	0.000	0.000	0.005
NC other	0.615	0.028	0.439	0.017	0.000	0.000	1.100
Subtotal	3.333	0.153	7.398	0.163	0.023	0.071	
Total	11.141						

Table B.15: Event rate table for RHC $2R\pi^0$ sample in 3+1 sterile oscillation analysis.

Event Type	$\nu_\mu \rightarrow \nu_\mu$	$\nu_e \rightarrow \nu_e$	$\bar{\nu}_\mu \rightarrow \bar{\nu}_\mu$	$\bar{\nu}_e \rightarrow \bar{\nu}_e$	$\nu_\mu \rightarrow \nu_e$	$\bar{\nu}_\mu \rightarrow \bar{\nu}_e$	Total
CCQE	2.633	0.000	0.059	0.000	0.000	0.000	2.692
CCMEC	0.000	0.000	0.000	0.000	0.000	0.000	0.000
CC 1π	0.795	0.002	0.007	0.000	0.000	0.000	0.804
CC coh.	0.025	0.000	0.002	0.000	0.000	0.000	0.026
CC other	0.108	0.000	0.003	0.000	0.000	0.000	0.112
NC 1π	17.682	0.361	0.934	0.000	0.000	0.000	18.977
NC coh.	0.000	0.000	0.000	0.000	0.000	0.000	0.000
NC 1γ	0.000	0.000	0.000	0.000	0.000	0.000	0.000
NC other	79.115	1.114	2.561	0.000	0.000	0.000	82.789
Subtotal	100.358	1.477	3.565	0.000	0.000	0.000	
Beam unrelated			2.299				
Total			107.699				

Table B.16: Event rate table for FHC NC γ de-excitation sample in 3+1 sterile oscillation analysis.

Appendix C

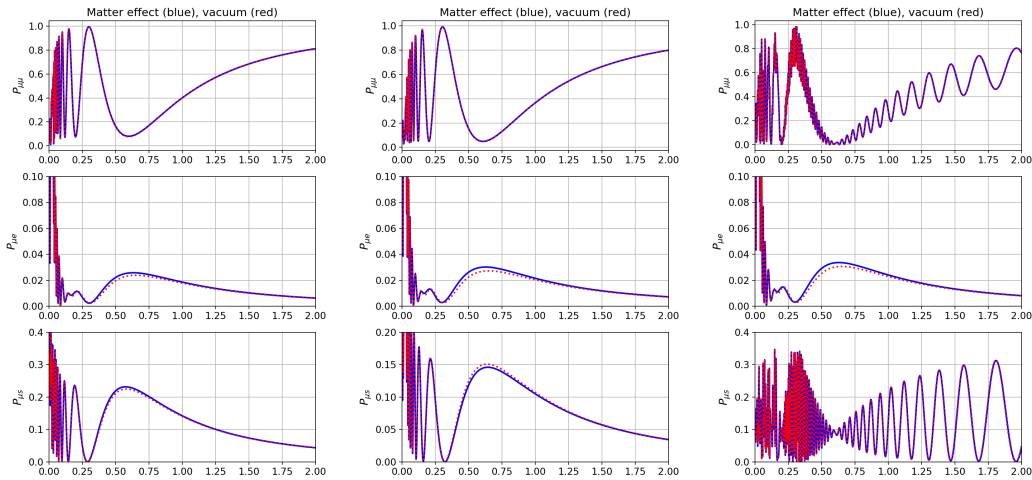
Sterile oscillation probability with matter effect

In Sec. 6.2, we use the sterile oscillation probability in vacuum in the oscillation analysis. There are concerns that whether the Earth matter would have some resonance effect on the oscillation, especially when $\Delta m_{41}^2 \approx \Delta m_{31}^2$. In this section, we check whether the matter effect has significant impacts on the oscillation probability.

To calculate the sterile oscillation probability with matter effect, we use the Python open-source project NuCraft[178]. One important reason to choose NuCraft is that it supports arbitrary numbers of neutrino flavors, including sterile neutrinos, and matter effects with a configurable Earth model. The solution is obtained by numerically solving the Schrödinger equation and can achieve a high enough numerical accuracy.

In the actual computation, we propagate ν_μ from the Earth's surface vertically down to the neutrino detector at a depth of 295 km, which mimics the T2K-SK baseline. Two scenarios are considered: constant Earth matter density of 2.6 kg/cm^3 ,

and $0. \text{kg}/\text{cm}^3$ (vacuum). We choose three sets of parameter values on the $\sin^2 \theta_{24}$ - Δm_{41}^2 plane: $\{0.3, 10^{-4} \text{eV}^2\}$, $\{0.2, 2.51 \times 10^{-3} \text{eV}^2\}$ and $\{0.1, 0.1 \text{eV}^2\}$, which roughly corresponds to the 90% exclusion limit at three different Δm_{41}^2 regimes, and examine the difference in P_{osc} with and without matter effect. As shown in Fig. C.1, matter effect only induces tiny changes to $P_{\mu e}$ and $P_{\mu s}$, and has little effect on our analysis.



$$(a) \{ \sin^2 \theta_{24}, \Delta m_{41}^2 \} \\ = \{ 0.3, 10^{-4} \text{eV}^2 \}$$

$$(b) \{ \sin^2 \theta_{24}, \Delta m_{41}^2 \} \\ = \{ 0.2, 2.51 \times 10^{-3} \text{eV}^2 \}$$

$$(c) \{ \sin^2 \theta_{24}, \Delta m_{41}^2 \} \\ = \{ 0.1, 0.1 \text{eV}^2 \}$$

Figure C.1: P_{osc} with and without matter effect. Unless specified, all oscillation parameters are the same as in Table 6.2.

Appendix D

Differences between NH and IH at

$$\Delta m_{41}^2 \sim \Delta m_{31}^2$$

In Sec.6.2, we see that the $\sin^2 \theta_{24}$ sensitivity curves differ quite a lot when $\Delta m_{41}^2 \sim \Delta m_{31}^2$. To better understand this result, we plot out P_{osc} with $\sin^2 \theta_{24} = 0.2$, $\Delta m_{41}^2 = m_{31}^2 = 2.509 \times 10^{-3} \text{eV}^2$ (other parameters are the same as in Table 6.2). From Fig. D.1, we can clearly observe that there are sizable differences between NH and IH, especially for $P_{\mu s}$.

To realize the difference, we can write out P_{osc} explicitly. Neglecting the Δm_{21}^2 oscillation terms and assuming $\theta_{34} = 0$, P_{osc} can be approximated as:

$$\begin{aligned} P_{\mu\mu} \approx & 1 - 4 \cos^2 \theta_{13} \sin^2 \theta_{23} \cos^4 \theta_{24} (\cos^2 \theta_{23} + \sin^2 \theta_{13} \sin^2 \theta_{23}) \sin^2 \frac{\Delta m_{31}^2 L}{4E} \\ & - \sin^2 2\theta_{24} (\cos^2 \theta_{23} + \sin^2 \theta_{13} \sin^2 \theta_{23}) \sin^2 \frac{\Delta m_{41}^2 L}{4E} \\ & - \cos^2 \theta_{13} \sin^2 \theta_{23} \sin^2 2\theta_{24} \sin^2 \frac{\Delta m_{43}^2 L}{4E}, \end{aligned} \quad (\text{D.1})$$

$$P_{\mu e} \approx \sin^2 2\theta_{13} \cos^2 \theta_{24} \sin^2 \theta_{23} \sin^2 \frac{\Delta m_{31}^2}{4E}, \quad (\text{D.2})$$

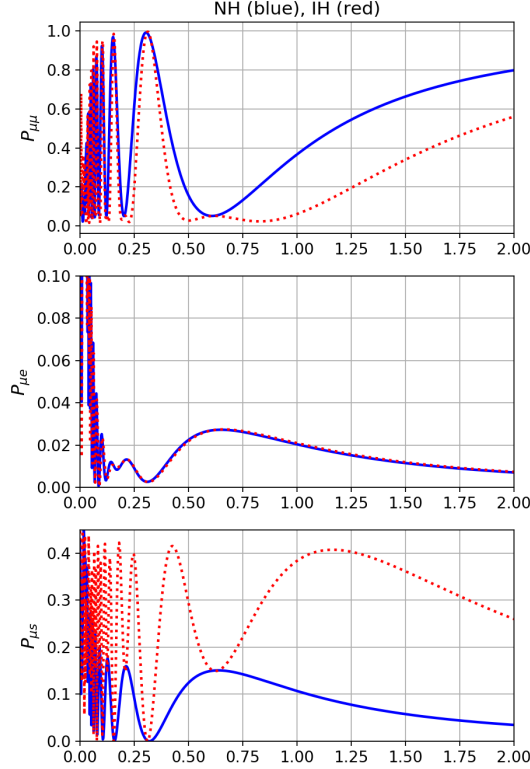


Figure D.1: P_{osc} with $\sin^2 \theta_{24} = 0.2$, $\Delta m_{41}^2 = \Delta m_{31}^2 = 2.509 \times 10^{-3} \text{eV}^2$ for NH and IH.

$$\begin{aligned}
 P_{\mu s} \approx \sin^2 2\theta_{24} \{ & -(\cos^2 \theta_{23} + \sin^2 \theta_{13} \sin^2 \theta_{23}) \cos^2 \theta_{13} \sin^2 \theta_{23} \sin^2 \frac{\Delta m_{31}^2 L}{4E} \\
 & + (\cos^2 \theta_{23} + \sin^2 \theta_{13} \sin^2 \theta_{23}) \sin^2 \frac{\Delta m_{41}^2 L}{4E} \\
 & + \cos^2 \theta_{13} \sin^2 \theta_{23} \sin^2 \frac{\Delta m_{43}^2 L}{4E} \}. \quad (\text{D.3})
 \end{aligned}$$

When $\Delta m_{41}^2 \approx \Delta m_{31}^2$, $\sin^2 \frac{\Delta m_{43}^2 L}{4E} \approx 0$ for NH while $\sin^2 \frac{\Delta m_{43}^2 L}{4E} \approx \sin^2 \frac{2\Delta m_{31}^2 L}{4E}$ for IH. This extra oscillation term with double frequency and amplitude $\cos^2 \theta_{13} \sin^2 \theta_{23} \sin^2 2\theta_{24}$ could modify the oscillation pattern significantly, as illustrated in Fig. D.1. This explains why the exclusion limit of $\sin^2 \theta_{24}$ differs between NH and IH around this

Δm_{41}^2 region.

Appendix E

Effects of θ_{14} , δ_{14} and δ_{24} on the fit

In the sterile oscillation fit performed in Sec.6.2, we assume $\theta_{14} = \delta_{14} = \delta_{24} = 0$. While this is the usual way similar experiments like MINOS present their results, it would be interesting to see how the fit results would change if we release this condition.

If we allow θ_{14} , δ_{14} and δ_{24} to vary from zero, it would affect the mixing matrix mostly in the “sterile row” U_{si} . The full form of U_{si} without any approximation is:

$$U_{s1} = -s_{12}(-c_{23}c_{34}e^{i\delta_{24}}s_{24}+s_{23}s_{34})+c_{12}(-c_{13}c_{24}c_{34}e^{i\delta_{14}}s_{14}-e^{i\delta_{13}}s_{13}(-c_{34}e^{i\delta_{24}}s_{23}s_{24}-c_{23}s_{34})), \quad (\text{E.1})$$

$$U_{s2} = c_{12}(-c_{23}c_{34}e^{i\delta_{24}}s_{24}+s_{23}s_{34})+s_{12}(-c_{13}c_{24}c_{34}e^{i\delta_{14}}s_{14}-e^{i\delta_{13}}s_{13}(-c_{34}e^{i\delta_{24}}s_{23}s_{24}-c_{23}s_{34})), \quad (\text{E.2})$$

$$U_{s3} = -c_{24}c_{34}e^{-i\delta_{13}+i\delta_{14}}s_{13}s_{14} + c_{13}(-c_{34}e^{i\delta_{24}}s_{23}s_{24} - c_{23}s_{34}), \quad (\text{E.3})$$

$$U_{s4} = c_{14}c_{24}c_{34}. \quad (\text{E.4})$$

Consider the third element, U_{s3} . Given fixed values of the standard 3-flavor

parameters and θ_{24} , if we choose the values of θ_{14} , δ_{14} and δ_{24} carefully, we can possibly make $U_{s3} \approx 0$. Therefore any Δm_{31}^2 or Δm_{43}^2 oscillation may be made very small in the $P(\nu_\mu \rightarrow \nu_s)$ channel which suppresses the NC disappearance amplitude. Also, how large the suppression could be would depend on the relative size of s_{14} and s_{24} . From Daya Bay Experiment[179], constraints of $\sin^2 \theta_{14} < 0.01 - 0.1$ have been set over a range of Δm_{41}^2 . We may therefore focus on this $\sin^2 \theta_{14}$ region. In particular, Daya Bay has released its χ^2 map¹. We may define a region of “Daya Bay constraint” of $\sin^2 \theta_{14}$ by requiring

$$\chi^2(\theta_{14}, \Delta m_{41}^2) - \chi^2(3\nu) < 2.3, \quad (\text{E.5})$$

where $\chi^2(3\nu)$ is the χ^2 of the fit in the 3-flavor model. Fig. E.1 shows this “Daya Bay constraint” as a function of Δm_{41}^2 .

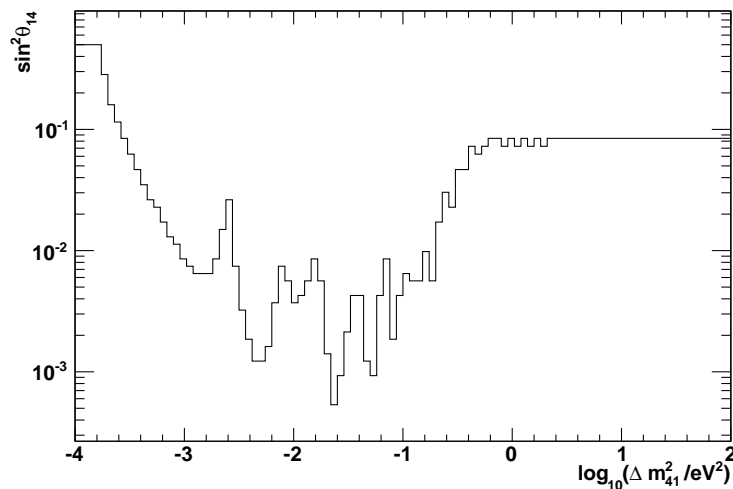


Figure E.1: “Daya Bay constraint” as a function of Δm_{41}^2 .

¹https://wiki.bnl.gov/dayabay/index.php?title=Daya_Bay's_Sterile_Neutrino_Results_in_2016

Below we perform the same sterile oscillation fit as in Sec.6.2, but with free θ_{14} , δ_{14} and δ_{24} . In particular, we do the fit with 4 scenarios on θ_{14} : $\sin^2 \theta_{14} = 0$, $\sin^2 \theta_{14} \leq 0.01$, $\sin^2 \theta_{14} \leq 0.1$ and $\sin^2 \theta_{14} \leq$ “Daya Bay constraint”. Fig. E.2 shows the results on the $\sin^2 \theta_{24}$ - Δm_{41}^2 plane. This mostly changes the constraints of $\sin^2 \theta_{24}$ in the region of $\Delta m_{41}^2 \lesssim \Delta m_{31}^2$, especially at $\Delta m_{41}^2 \approx \Delta m_{31}^2$. The reason is as explained: the Δm_{31}^2 and Δm_{43}^2 oscillation of $P(\nu_\mu \rightarrow \nu_s)$ is suppressed which removes the strongest sterile signature in the NC samples.

When $\Delta m_{41}^2 \approx \Delta m_{31}^2$, the situation is more interesting. The non-zero θ_{14} can reduce the size of $U_{\mu 3} = c_{13}c_{24}s_{23} - e^{-i\delta_{13}+i\delta_{14}-i\delta_{24}}s_{13}s_{14}s_{24}$, where $U_{\mu 4} = c_{14}e^{-i\delta_{24}}s_{24}$ can come in to replace its role as Δm_{41}^2 and Δm_{31}^2 oscillations are nearly degenerate.

On the other hand, for large Δm_{41}^2 , the NC signal is dominated by the fast Δm_{41}^2 oscillation where $U_{\mu 4}$ and $U_{s 4}$ are only slightly modified by a factor of c_{14} , so the fitting results do not change much.

We may present this as a complementary study to the results Sec.6.2.

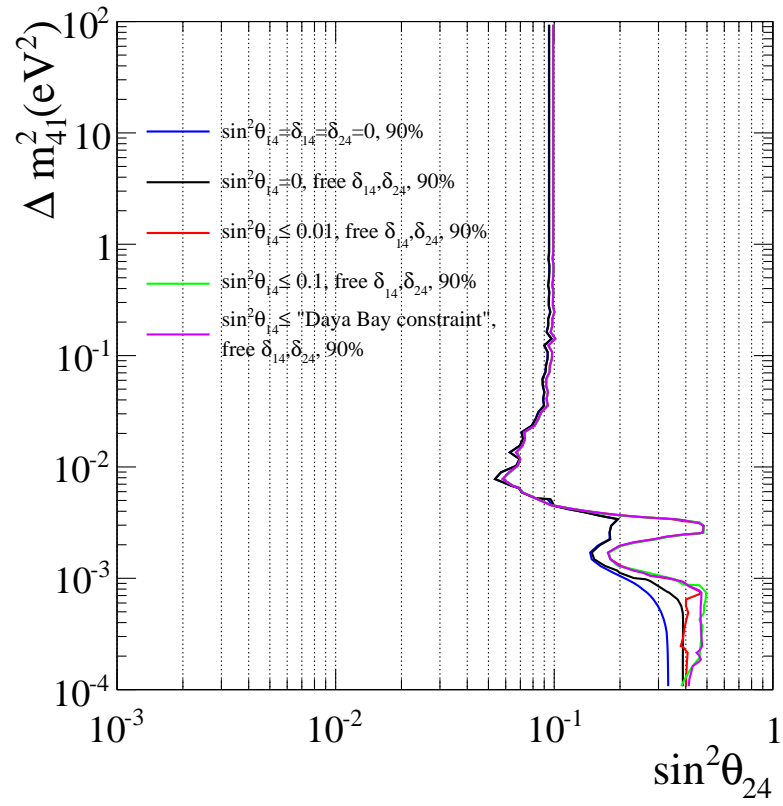


Figure E.2: Asimov sensitivity 2D confidence level contours assuming NH showing the possible effects of θ_{14} , δ_{14} and δ_{24} .

Appendix F

Setting Exclusion limits of sterile parameters with the Gaussian CL_s Method

In Ch. 6, we set the exclusion limits of the oscillation parameters with the fixed $\Delta\chi^2$ method. This method is known to have problems when the fitted parameters are close to their physical boundaries, e.g. $\sin^2\theta_{24} = \sin^2\theta_{34} = 0$, and the confidence intervals (CI) constructed might not have the correct coverage. We may compute the correct CI using the Feldman-Cousins unified approach [180], but in general it is a very computational-expensive method because of the large number of MC samples needed for each grid point. Here we would like to try a much simpler way called the Gaussian CL_s Method which is explained very detailedly in [181].

In the Gaussian CL_s Method, we consider pairs of non-nested hypotheses: the standard 3-flavor oscillation model $H_0 : \beta = \beta_0 = \{\sin^2\theta_{i4} = 0\}$, and the 3+1 sterile oscillation model $H_1 : \beta = \beta_1 = \{\sin^2\theta_{i4}, \Delta m_{41}^2\}$, one pair at a time.

Below we introduce a test statistic, $\Delta T(\beta_0, \beta_1; x) = \Delta T(x)$, for testing H_0 versus H_1 with the data x . We first modify the likelihood functions in Eq.5.17 into:

$$T_{H_0}(\beta_0, x; o, f) = -2 \log(\mathcal{L}(x, N_{\text{pred}}, o(\beta_0), f)), \quad (\text{F.1})$$

$$T_{H_1}(\beta_1, x; o, f) = -2 \log(\mathcal{L}(x, N_{\text{pred}}, o(\beta_1), f)). \quad (\text{F.2})$$

The subscript H_0 (H_1) means that we use the 3-flavor (sterile) oscillation model in the event rate calculation.

Then we minimize the modified likelihood functions over nuisance parameters $\lambda(o, f)$ to obtain $T_{H_0}^{\min}(x) = \min_{\lambda} T_{H_0}$ and $T_{H_1}^{\min}(x) = \min_{\lambda} T_{H_1}$. The test statistic ΔT is defined as the difference:

$$\Delta T(x) = T_{H_1}^{\min}(x) - T_{H_0}^{\min}(x). \quad (\text{F.3})$$

At the first glance, $\Delta T(x)$ may be similar to the usual $\Delta\chi^2(x)$, but in fact they are different concepts because $\Delta T(x)$ involves the best-fit under two different models H_0 (3-flavor) and H_1 (3+1 sterile), while $\Delta\chi^2(x)$ involves the best-fit and the full parameter space of H_1 .

Next we consider the Asimov data set $x_{H_0}^{\text{Asimov}}$ under H_0 . Assuming H_0 is the correct hypothesis, we define

$$\begin{aligned} \overline{\Delta T_{H_0}} &= \Delta T(x_{H_0}^{\text{Asimov}}) \\ &= T_{H_1}^{\min}(x_{H_0}^{\text{Asimov}}) - T_{H_0}^{\min}(x_{H_0}^{\text{Asimov}}) \\ &= T_{H_1}^{\min}(x_{H_0}^{\text{Asimov}}). \end{aligned} \quad (\text{F.4})$$

Similarly, let $x_{H_1}^{\text{Asimov}}$ be the Asimov data set under H_1 , we have

$$\begin{aligned}
 \overline{\Delta T_{H_1}} &= \Delta T(x_{H_1}^{\text{Asimov}}) \\
 &= T_{H_1}^{\min}(x_{H_1}^{\text{Asimov}}) - T_{H_0}^{\min}(x_{H_1}^{\text{Asimov}}) \\
 &= -T_{H_0}^{\min}(x_{H_1}^{\text{Asimov}}).
 \end{aligned}
 \tag{F.5}$$

Ref. [181] shows that with the following 3 conditions satisfied, $\Delta T(X)$ under hypothesis H follows approximately a Gaussian distribution with mean $\overline{\Delta T_H}$ and standard deviation $2\sqrt{|\overline{\Delta T_H}|}$, where H could be either H_0 or H_1 :

CD1. The parameter space of the nuisance parameters are continuous and the model likelihood function is a smooth function within the parameter space.

CD2. The data size is large enough (the total number of events is greater than 100).

CD3. The predictions by the best model under the null hypothesis H_0 and the alternative hypothesis H_1 are relatively small.

We define the CL_s value as:

$$\text{CL}_s(x) = \frac{1 - p_1}{1 - p_0},
 \tag{F.6}$$

where $1 - p_1$ ($1 - p_0$) is the probability that a single experiment will yield a $\Delta T(X)$ value larger than $\Delta T(x)$ when H_1 (H_0) is true. With this definition, a CL_s value close to zero would favor H_0 against H_1 , while it needs to be much larger than one to have H_1 favored against H_0 . The exclusion space is typically defined as the set of parameter value with CL_s value smaller than $\alpha = 0.05$ [182].

With CD1,2,3 satisfied, we may use $\overline{\Delta T_H}$ to calculate the probability:

$$1 - p_0 \approx \frac{1 + \text{Erf} \left(\frac{\overline{\Delta T_{H_0}} - \Delta T(x)}{\sqrt{8|\overline{\Delta T_{H_0}}|}} \right)}{2}, \quad (\text{F.7})$$

$$1 - p_1 \approx \frac{1 + \text{Erf} \left(\frac{\overline{\Delta T_{H_1}} - \Delta T(x)}{\sqrt{8|\overline{\Delta T_{H_1}}|}} \right)}{2}, \quad (\text{F.8})$$

where $\text{Erf}(s) = \frac{2}{\sqrt{\pi}} \int_0^s e^{-t^2} dt$ is the Gaussian error function.

Therefore the CL_s value can be approximated by

$$\text{CL}_s \approx \frac{1 + \text{Erf} \left(\frac{\overline{\Delta T_{H_1}} - \Delta T(x)}{\sqrt{8|\overline{\Delta T_{H_1}}|}} \right)}{1 + \text{Erf} \left(\frac{\overline{\Delta T_{H_0}} - \Delta T(x)}{\sqrt{8|\overline{\Delta T_{H_0}}|}} \right)}. \quad (\text{F.9})$$

Fig. F.1 shows the exclusion limits of our sterile oscillation analysis drawn by the CL_s method, using the same configuration in Sec. 6.2. The CL_s 95% exclusion limit is a bit tighter than the fixed $\Delta\chi^2$ 90% limit, which is as expected because the CL_s test statistic ΔT is designed for distinguishing the differences between the new physics hypotheses (sterile oscillation with $\sin^2 \theta_{i4} > 0$) and the Standard Model (3-flavor oscillation with $\sin^2 \theta_{i4} = 0$). So when the true $\sin^2 \theta_{i4}$ is indeed zero, a strong limits can be set. On the other hand, if the true $\sin^2 \theta_{i4}$ is deviated from zero a lot (the difference between H_0 and H_1 is large), CD3 is violated and the CL_s method is less useful.

As discussed in [181], although the CL_s method is a restricted method that aims at setting upper limits only, its simplicity makes it a popular approach to present searches for new physics beyond the Standard Model. Also, the CL_s method can set comparable exclusion limits as the Feldman-Cousins approach on the parameter space when the new physics hypotheses are close to the Standard Model, which meets

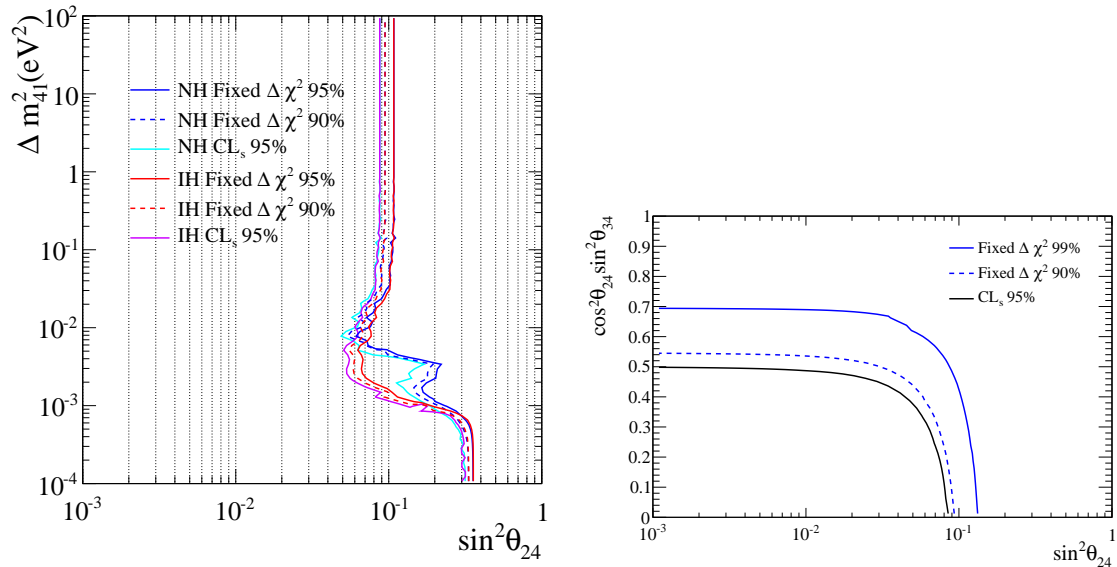
(a) Δm_{41}^2 - $\sin^2 \theta_{24}$ exclusion limits.(b) $\cos^2 \theta_{24} \sin^2 \theta_{34}$ - $\sin^2 \theta_{24}$ exclusion limits.

Figure F.1: Exclusion limits of the sterile parameters drawn by CL_s and fixed $\Delta\chi^2$ methods.

our needs in the sterile neutrino search. It might be good to present the CL_s limits together with the fixed $\Delta\chi^2$ limits as a cross-check of results.

Appendix G

Fitting non-Asimov data sets

The Asimov data set fit in Ch. 6 estimates the median sensitivity to the oscillation parameters. Here we fit for non-Asimov data sets to test the stability of the fitter.

First, for 2500 non-Asimov data sets, we determined the global best-point point for each data set by minimizing the likelihood function in Eq. 5.17 with respect to all oscillation parameters. Fig. G.1 shows the best fit χ^2 distributions for both 3+1 sterile and 3-flavor oscillation models. For the sterile model, NH and IH has similar best fit χ^2 , while 3-flavor model has slightly larger ones, especially for IH. Fig. G.2 shows the best fit standard parameter values. While there are certain shifts of the distributions, it mostly agrees with the true values. Fig. G.3 shows the best fit $\sin^2 \theta_{24}$ - $\sin^2 \theta_{24}$ distribution. Basically the best fit points concentrate around the 0,0 region, with a small probability spreading out.

Next, we fit for several non-Asimov data sets to see the variations of the sensitivity curves. Table G.1 lists the event rates of four non-Asimov data sets. Among them, set 1 is the most special: it has event rates smaller than nominal for every sample, while other data sets have more “random” fluctuations in the event rates. Figs. G.4

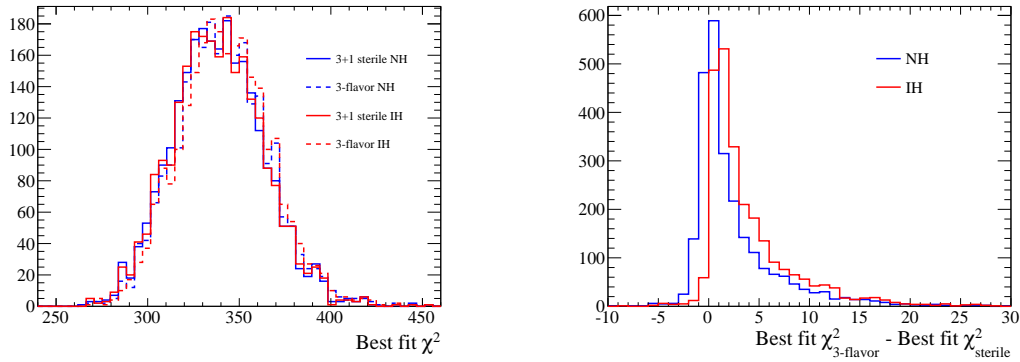


Figure G.1: Best fit χ^2 distributions of both 3+1 sterile and 3-flavor oscillation models for 2500 non-Asimov data sets.

Data set	1R μ		1Re		$\nu_e\text{CC}1\pi^+$	2R π^0		NC γ de-excitation
	FHC	RHC	FHC	RHC	FHC	FHC	RHC	FHC
Asimov	268.4	64.3	73.5	7.9	6.9	49.5	11.3	107.7
non-Asimov 1	190	40	67	8	4	37	10	78
non-Asimov 2	275	69	66	10	7	46	8	99
non-Asimov 3	321	74	56	6	6	58	17	85
non-Asimov 4	254	54	82	9	6	37	6	119

Table G.1: Event rates of four non-Asimov data sets.

and G.5 show the exclusion limits of the non-Asimov data sets, drawn by the fixed $\Delta\chi^2$ or CL_s method. As expected, non-Asimov set 1 prefers non-zero θ_{24}/θ_{34} , while others have limits quite similar to the Asimov sensitivity. Within small statistical or systematical fluctuations, the fitter is stable enough to give reasonable results.

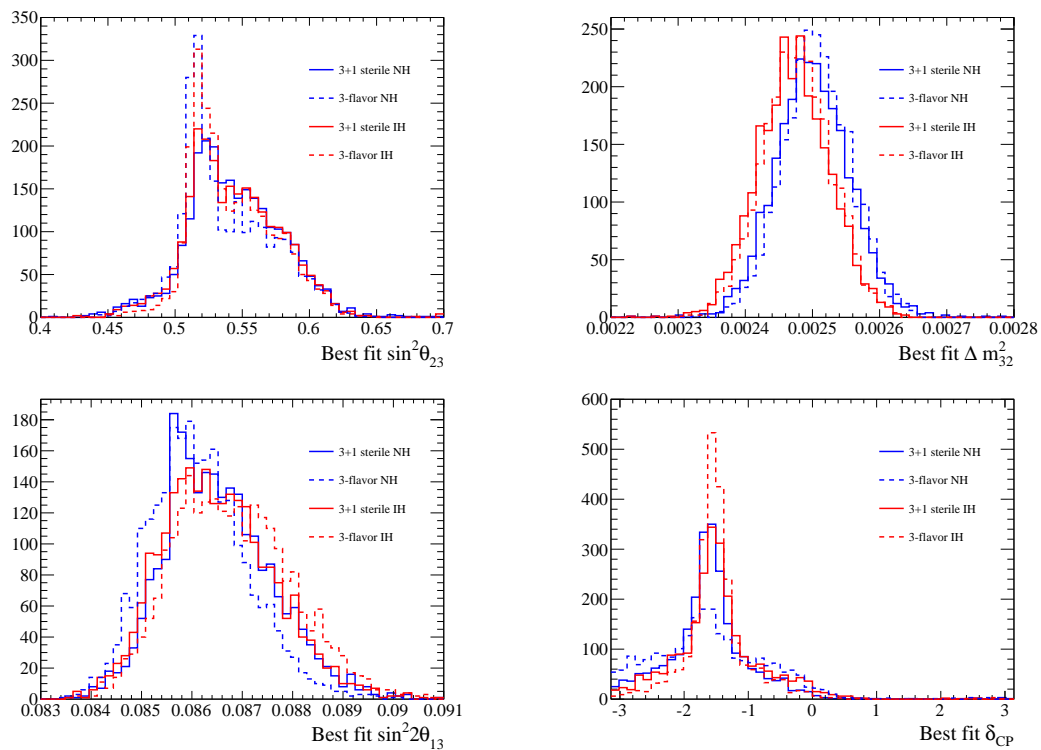


Figure G.2: Best fit standard oscillation parameters for 2500 non-Asimov data sets.

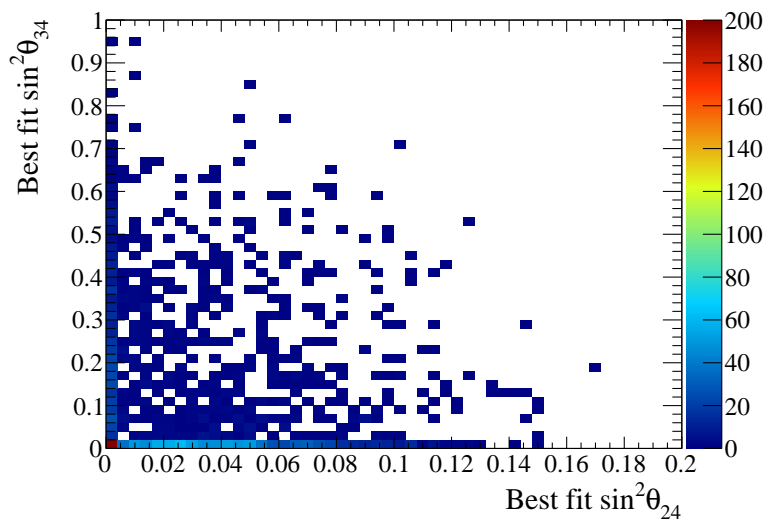


Figure G.3: Best fit $\sin^2 \theta_{24}$ - $\sin^2 \theta_{34}$ distribution for 2500 non-Asimov data sets.

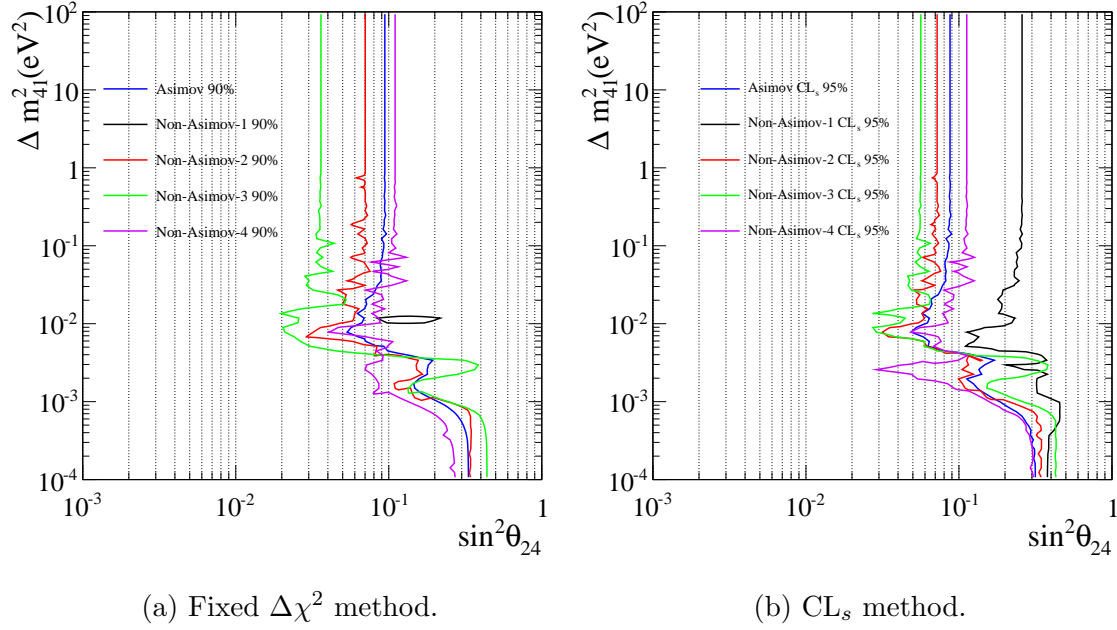


Figure G.4: Exclusion limits in the Δm_{41}^2 - $\sin^2 \theta_{24}$ plane from the Asimov and non-Asimov data sets, assuming NH.

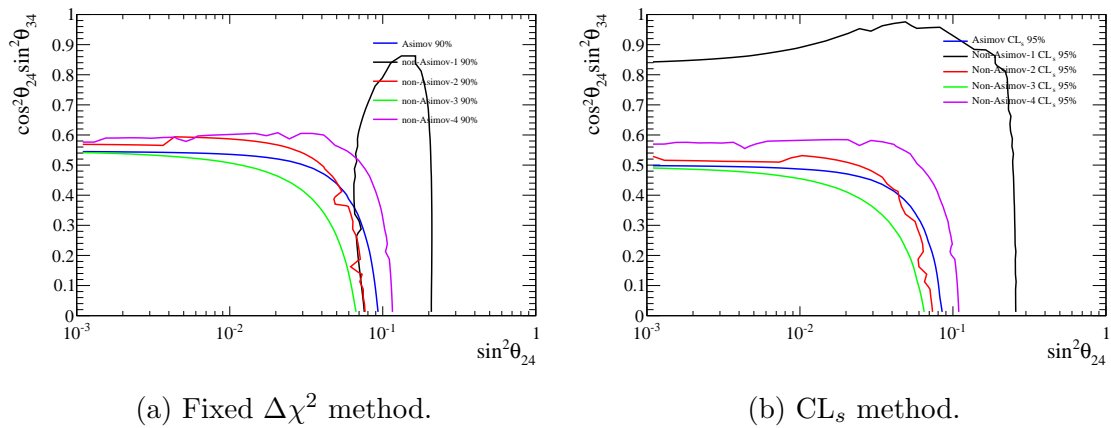


Figure G.5: Exclusion limits in the $\cos^2 \theta_{24} \sin^2 \theta_{34}$ - $\sin^2 \theta_{24}$ plane from the Asimov and non-Asimov data sets, assuming NH.

Appendix H

Valid Δm_{41}^2 parameter space

In the sensitivity study and data fit of the sterile analysis, we limit our fits in regions below $\Delta m_{41}^2 = 0.3\text{eV}^2$. This cut is determined by the value of Δm_{41}^2 beyond which the near detectors (ND) start to see sterile oscillation.

Our oscillation measurement strategy is to use the ND data to predict the non-oscillated event rates at far detector, and fit for the oscillation parameters from the event rate spectral distortions. Since both the non-oscillated event rates and the systematic parameters are determined by the ND BANFF fit, we cannot simply remove the BANFF constraints and claim the result is valid. In an even deeper level, many of the pre-BANFF fit neutrino cross-section parameters come from oscillation experiments with near detectors at a distance from sources, so they can also be affected by sterile oscillation. To solve these issues, T2K is developing a “more general” cross-section model which is potential free of these artefacts. But before this and the related short baseline sterile analysis are done, we have decided not to provide any result in the problematic region.

To see how we determine the cut value, Fig. H.1 shows, e.g. $P(\nu_\mu \rightarrow \nu_\mu)$ at ND

at 0.6 GeV (the neutrino beam peak), as a function of Δm_{41}^2 with $\sin^2 \theta_{24} = 0.1$. We can see sub-percent changes beyond 0.3 eV^2 . We also performed a test study by using $P_{SK}(\nu_\mu \rightarrow \nu_\mu)/P_{ND}(\nu_\mu \rightarrow \nu_\mu)$ and $P_{SK}(\nu_e \rightarrow \nu_e)/P_{ND}(\nu_e \rightarrow \nu_e)$ in event rate calculation. The changes to sensitivity are shown in Fig. H.2, which is insignificant below 0.3 eV^2 . This shows that our cut is well-justified.

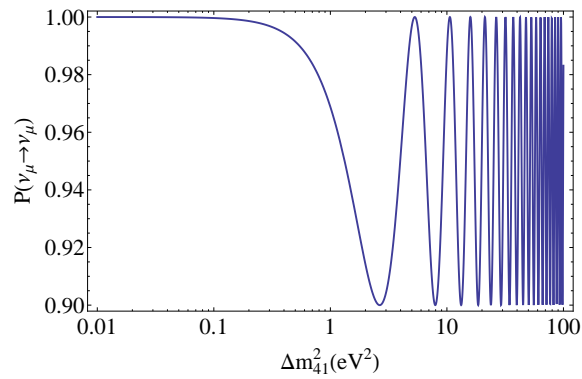


Figure H.1: $P(\nu_\mu \rightarrow \nu_\mu)$ at ND at 0.6 GeV, as a function of Δm_{41}^2 with $\sin^2 \theta_{24} = 0.1$.

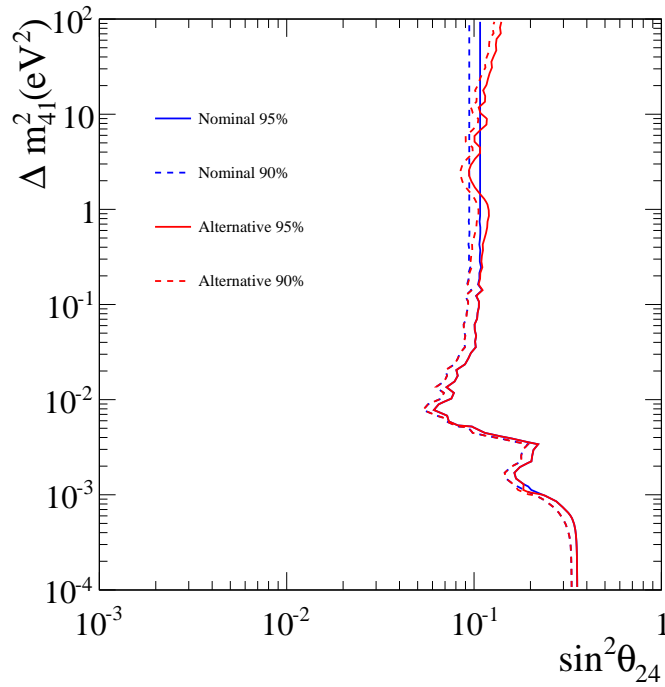


Figure H.2: Asimov sensitivity 2D confidence level contours in Δm_{41}^2 vs. $\sin^2 \theta_{24}$, assuming NH. The blue lines show the nominal sterile analysis, and the red lines show a test study of using $P_{SK}(\nu_\mu \rightarrow \nu_\mu)/P_{ND}(\nu_\mu \rightarrow \nu_\mu)$ and $P_{SK}(\nu_e \rightarrow \nu_e)/P_{ND}(\nu_e \rightarrow \nu_e)$ in event rate calculation. This illustrates that our sterile fit is valid below $\Delta m_{41}^2 = 0.3\text{eV}^2$ where the ND sees little sterile oscillation.

Appendix I

Event spectra at sterile exclusion limits

To illustrate how the sterile exclusion limits are set by the oscillation samples, we show the event spectra at three specific points on the $\sin^2 \theta_{24}$ - Δm_{41}^2 plane: Point #1 $\{0.3, 10^{-4}\text{eV}^2\}$, Point #2 $\{0.2, 2.51 \times 10^{-3}\text{eV}^2\}$ and Point #3 $\{0.1, 0.1\text{eV}^2\}$, which roughly corresponds to the 90% exclusion limit at three different Δm_{41}^2 regimes. We can clearly see the sterile effects on the samples: excess at small Δm_{41}^2 and deficit at large Δm_{41}^2 for $1R\mu$ samples, and varying amount of deficit for ν_e and NC samples.

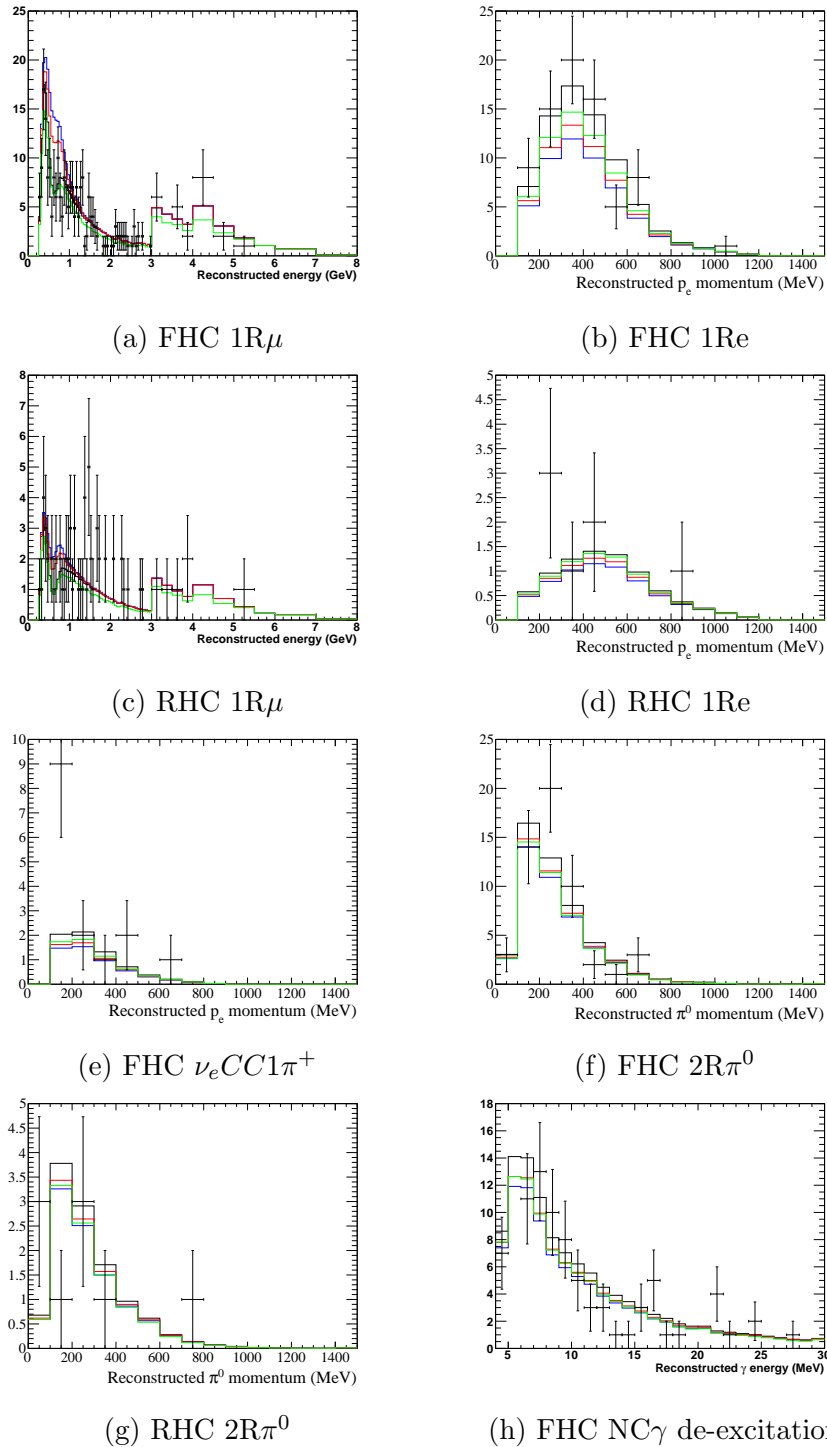


Figure I.1: Asimov event spectra (black lines) together event spectra at Points #1 (blue), #2 (red) and #3 (green), assuming NH, overlaid on data points (black points). The ν_e spectra are projected on the electron momentum p_e .

Appendix J

List of abbreviations and symbols

1Re	Charged-current 1-ring e -like samples
1R μ	Charged-current 1-ring μ -like samples
2R π^0	Neutral-current 2-ring π^0 -like samples
2p2h	(2 particle-2 hole) Multiple nucleon interaction
ν MSM	Neutrino Minimal Standard Model
apfit	Reconstruction algorithm in SK
fitQun	Reconstruction algorithm in SK
p.e.	photo-electrons
BeRPA	Bernstein parameterization of random phase approximation
BANFF fit	Neutrino flux and cross-section fit by the Beam And ND280 Flux extrapolation task Force
BONSAI	Low energy event reconstruction tool in SK

BSM	Beyond Standard Model
CC interaction	Charged-current interaction
CC1 π	Charged-current interactions associated with single-pion resonant production
CC coherent	Charged-current coherent pion production
CCQE	Charged-current quasi-elastic interaction
CP	Charge-parity
FC	(Event) Fully contained in ID
FHC	Forward Horn Current (neutrino beam mode)
FSI	Final state interactions
FV	Fiducial volume of detector
ID	Inner detector of SK
IH	Neutrino inverted mass hierarchy ($m_3 < m_1 < m_2$)
INGRID	Interactive Neutrino GRID (near detector of T2K)
KS test	Kolmogorov-Smirnov test
LE events	Low energy events
NC γ de-excitation	Neutral current sample with gamma de-excitation events
NC interaction	Neutral-current interaction
NC1 π	Neutral-current interactions associated with single-pion resonant production

NC1 γ	Neutral-current interactions with single gamma production
NC coherent	Neutral-current coherent pion production
NCQE	Neutral-current quasi-elastic interaction
ND280	Main near detector in T2K
NEUT	Neutrino interaction generator used in SK and T2K
NH	Neutrino normal mass hierarchy ($m_1 < m_2 < m_3$)
OD	Outer detector of SK
PMNS matrix	Pontecorvo-Maki-Nakagawa-Sakata neutrino mixing matrix
PMT	Photomultiplier tube
POT	Proton-on-target
RFG	Relativistic Fermi gas model
RHC	Reverse Horn Current (antineutrino beam mode)
RPA	Random phase approximation
SF	Spectral function model
SI	Secondary interactions
SK	Super-Kamiokande
SKDETSIM	Detector simulator of Super-Kamiokande
Xsec parameters	Neutrino interaction and cross-section interaction parameters
θ_c	Cherenkov opening angle

θ_{ij}	Neutrino mixing angle
$U_{\alpha i}$	Neutrino mixing matrix element
Δm_{ij}^2	Neutrino mass splittings $m_i^2 - m_j^2$
δ_{CP}	CP-violating phase
n_{hitac}	Number of PMT hits in the largest outer detector hit cluster
$wall$	Closest distance between vertex and detector wall
$towall$	Particle track length in ID
E_{ν}^{rec}	Reconstructed neutrino energy
E_{vis}	Sum of reconstructed particle momentum of each Cherenkov ring
$ovaQ$	Goodness of fit in BONSAI
N_{30}	Maximum number of PMT hits in 30 ns time window

Bibliography

- [1] K. Abe *et al.* (T2K), Phys. Rev. **D91**, 051102 (2015), arXiv:1410.8811 [hep-ex].
- [2] K. Okumura, Physics Procedia **61**, 619 (2015), 13th International Conference on Topics in Astroparticle and Underground Physics, TAUP 2013.
- [3] A. Gando *et al.* (KamLAND Collaboration), Phys. Rev. D **88**, 033001 (2013).
- [4] J. N. Bahcall, A. M. Serenelli, and S. Basu, Astrophys. J. Suppl. **165**, 400 (2006), arXiv:astro-ph/0511337 [astro-ph].
- [5] G. Bellini *et al.* (Borexino Collaboration), Phys. Rev. D **82**, 033006 (2010).
- [6] R. Davis, D. S. Harmer, and K. C. Hoffman, Phys. Rev. Lett. **20**, 1205 (1968).
- [7] J. N. Abdurashitov *et al.* (SAGE Collaboration), Phys. Rev. C **80**, 015807 (2009).
- [8] M. Altmann *et al.*, Physics Letters B **616**, 174 (2005).
- [9] G. Bellini *et al.* (Borexino Collaboration), Phys. Rev. Lett. **107**, 141302 (2011).
- [10] K. Abe *et al.* (Super-Kamiokande Collaboration), Phys. Rev. D **94**, 052010 (2016).

-
- [11] R. Wendell (Super-Kamiokande), *Proceedings, 26th International Conference on Neutrino Physics and Astrophysics (Neutrino 2014): Boston, Massachusetts, United States, June 2-7, 2014*, AIP Conf. Proc. **1666**, 100001 (2015), arXiv:1412.5234 [hep-ex] .
- [12] P. Adamson *et al.* (NOvA), Phys. Rev. **D93**, 051104 (2016), arXiv:1601.05037 [hep-ex] .
- [13] P. Adamson *et al.* (MINOS), Phys. Rev. Lett. **112**, 191801 (2014), arXiv:1403.0867 [hep-ex] .
- [14] M. G. Aartsen *et al.* (IceCube), Phys. Rev. **D91**, 072004 (2015), arXiv:1410.7227 [hep-ex] .
- [15] L. Haegel (T2K), in *2017 European Physical Society Conference on High Energy Physics (EPS-HEP 2017) Venice, Italy, July 5-12, 2017* (2017) arXiv:1709.04180 [hep-ex] .
- [16] F. P. An *et al.* (Daya Bay), Phys. Rev. **D95**, 072006 (2017), arXiv:1610.04802 [hep-ex] .
- [17] A. Bhardwaj, A. Das, P. Konar, and A. Thalapillil, (2018), arXiv:1801.00797 [hep-ph] .
- [18] K. Abe *et al.*, Nuclear Instruments and Methods in Physics Research Section A: Accelerators, Spectrometers, Detectors and Associated Equipment **659**, 106 (2011).
- [19] K. Abe *et al.* (T2K Collaboration), Phys. Rev. D **87**, 012001 (2013).

-
- [20] K. Abe *et al.* (T2K), Phys.Rev. **D96**, 092006 (2017), arXiv:1707.01048 [hep-ex] .
- [21] N. Abgrall *et al.*, Nuclear Instruments and Methods in Physics Research Section A: Accelerators, Spectrometers, Detectors and Associated Equipment **637**, 25 (2011).
- [22] Y. Itow *et al.* (T2K), in *Neutrino oscillations and their origin. Proceedings, 3rd International Workshop, NOON 2001, Kashiwa, Tokyo, Japan, December 508, 2001* (2001) pp. 239–248, arXiv:hep-ex/0106019 [hep-ex] .
- [23] K. Abe *et al.*, Nucl. Instrum. Meth. **A737**, 253 (2014), arXiv:1307.0162 [physics.ins-det] .
- [24] Y. Suda, “Search for proton decay using an improved event reconstruction algorithm in super-kamiokande,” Ph.D. Thesis, University of Tokyo, 2017.
- [25] S. Tobayama, “An analysis of the oscillation of atmospheric neutrinos,” Ph.D. Thesis, University of British Columbia, 2016.
- [26] L. Haegel, “Measurement of neutrino oscillation parameters using neutrino and antineutrino data of the t2k experiment,” Ph.D. Thesis, University of Geneva, 2017.
- [27] R. Akutsu *et al.*, T2K-TN-317 (2017).
- [28] K. Huang *et al.*, T2K-TN-244 (2016).
- [29] K. Ueno, T2K-TN-058 (2012).
- [30] J. Imber *et al.*, T2K-TN-326 (2017).

-
- [31] A. Missert, T2K-TN-318 (2017).
- [32] P. Adamson *et al.* (MINOS), Submitted to: Phys. Rev. Lett. (2017), arXiv:1710.06488 [hep-ex] .
- [33] P. Adamson *et al.* (MINOS Collaboration), Phys. Rev. Lett. **117**, 151803 (2016).
- [34] M. G. Aartsen *et al.* (IceCube Collaboration), Phys. Rev. Lett. **117**, 071801 (2016).
- [35] K. Abe *et al.* (Super-Kamiokande), Phys. Rev. **D91**, 052019 (2015), arXiv:1410.2008 [hep-ex] .
- [36] F. Dydak *et al.*, Physics Letters B **134**, 281 (1984).
- [37] I. E. Stockdale *et al.*, Phys. Rev. Lett. **52**, 1384 (1984).
- [38] K. B. M. Mahn *et al.*, Phys. Rev. D **85**, 032007 (2012).
- [39] S. Gariazzo, C. Giunti, M. Laveder, Y. F. Li, and E. M. Zavatin, Journal of Physics G: Nuclear and Particle Physics **43**, 033001 (2016).
- [40] M. G. Aartsen *et al.* (IceCube), Phys. Rev. **D95**, 112002 (2017), arXiv:1702.05160 [hep-ex] .
- [41] H. Nishino, “Search for nucleon decay into charged antilepton plus meson in super-kamiokande,” Ph.D. Thesis, University of Tokyo, 2009.
- [42] T. Mclachlan, “Study of the oscillation of neutrinos and anti-neutrinos and of non-standard neutrino interactions with the atmospheric data in super-kamiokande,” Ph.D. Thesis, University of Tokyo, 2015.

-
- [43] C. Patrignani and P. D. Group, Chinese Physics C **40**, 100001 (2016).
- [44] P. de Perio *et al.*, T2K-TN-032 (2011).
- [45] W. Ma *et al.*, T2K-TN-321 (2017).
- [46] F. Reines, C. L. Cowan, F. B. Harrison, A. D. McGuire, and H. W. Kruse, Phys. Rev. **117**, 159 (1960).
- [47] G. Danby, J.-M. Gaillard, K. Goulianos, L. M. Lederman, N. Mistry, M. Schwartz, and J. Steinberger, Phys. Rev. Lett. **9**, 36 (1962).
- [48] M. L. Perl *et al.*, Phys. Rev. Lett. **35**, 1489 (1975).
- [49] K. Kodama *et al.*, Physics Letters B **504**, 218 (2001).
- [50] B. Pontecorvo, Sov. Phys. JETP **6**, 429 (1957).
- [51] B. Pontecorvo, Sov. Phys. JETP **7**, 172 (1958).
- [52] Z. Maki, M. Nakagawa, and S. Sakata, Progress of Theoretical Physics **28**, 870 (1962).
- [53] M. Nakagawa, H. Okonogi, S. Sakata, and A. Toyoda, Prog. Theor. Phys. **30**, 727 (1963).
- [54] S. Eliezer and A. R. Swift, Nuclear Physics B **105**, 45 (1976).
- [55] H. Fritzsch and P. Minkowski, Phys. Lett. **B62**, 72 (1976).
- [56] S. M. Bilenky and B. Pontecorvo, Sov. J. Nucl. Phys. **24**, 316 (1976).

-
- [57] S. M. Bilenky and B. Pontecorvo, *Lettere Nuovo Cimento* **17** (1976) 569-574, In **Pontecorvo, B.: Selected scientific works** 321-326, Lett. Nuovo Cim. **17**, 569 (1976).
- [58] T. Asaka and M. Shaposhnikov, Phys. Lett. **B620**, 17 (2005), arXiv:hep-ph/0505013 [hep-ph] .
- [59] T. Asaka, S. Blanchet, and M. Shaposhnikov, Phys. Lett. **B631**, 151 (2005), arXiv:hep-ph/0503065 [hep-ph] .
- [60] A. Boyarsky, O. Ruchayskiy, and M. Shaposhnikov, Ann. Rev. Nucl. Part. Sci. **59**, 191 (2009), arXiv:0901.0011 [hep-ph] .
- [61] Q. R. Ahmad *et al.* (SNO Collaboration), Phys. Rev. Lett. **89**, 011301 (2002).
- [62] Y. Fukuda *et al.* (Super-Kamiokande Collaboration), Phys. Rev. Lett. **81**, 1562 (1998).
- [63] K. Eguchi *et al.* (KamLAND Collaboration), Phys. Rev. Lett. **90**, 021802 (2003).
- [64] L. Wolfenstein, Phys. Rev. D **17**, 2369 (1978).
- [65] V. Barger, K. Whisnant, and R. J. N. Phillips, Phys. Rev. Lett. **45**, 2084 (1980).
- [66] S. P. Mikheev and A. Yu. Smirnov, Sov. J. Nucl. Phys. **42**, 913 (1985).
- [67] S. P. Mikheev and A. Yu. Smirnov, Nuovo Cim. **C9**, 17 (1986).

-
- [68] K. Hirata, T. Kajita, M. Koshiba, M. Nakahata, S. Ohara, Y. Oyama, N. Sato, A. Suzuki, M. Takita, Y. Totsuka, T. Kifune, T. Suda, K. Nakamura, K. Takahashi, T. Tanimori, K. Miyano, M. Yamada, E. Beier, L. Feldscher, E. Frank, W. Frati, S. Kim, A. Mann, F. Newcomer, R. V. Berg, W. Zhang, and B. Cortez, *Physics Letters B* **205**, 416 (1988).
- [69] J. H. Choi *et al.* (RENO), *Phys. Rev. Lett.* **116**, 211801 (2016), arXiv:1511.05849 [hep-ex] .
- [70] Y. Abe *et al.* (Double Chooz), *Journal of High Energy Physics* **01**, 163 (2016), arXiv:1510.08937 [hep-ex] .
- [71] C. Giganti (T2K), in *Prospects in Neutrino Physics (NuPhys2017) London, United Kingdom, December 20-22, 2017* (2018) arXiv:1803.11513 [hep-ex] .
- [72] P. Adamson *et al.* (NOvA), *Phys. Rev. Lett.* **118**, 231801 (2017), arXiv:1703.03328 [hep-ex] .
- [73] A. Timmons, *Adv. High Energy Phys.* **2016**, 7064960 (2016), arXiv:1511.06178 [hep-ex] .
- [74] K. Abe *et al.* (Super-Kamiokande), *Phys. Rev.* **D97**, 072001 (2018), arXiv:1710.09126 [hep-ex] .
- [75] K. Abe *et al.*, (2011), arXiv:1109.3262 [hep-ex] .
- [76] K. Abe *et al.* (Hyper-Kamiokande), *PTEP* **2018**, 063C01 (2018), arXiv:1611.06118 [hep-ex] .
- [77] R. Acciarri *et al.* (DUNE), (2016), arXiv:1601.05471 [physics.ins-det] .

- [78] P. Minkowski, *Physics Letters B* **67**, 421 (1977).
- [79] T. Yanagida, *Proceedings: Workshop on the Unified Theories and the Baryon Number in the Universe: Tsukuba, Japan, February 13-14, 1979*, Conf. Proc. **C7902131**, 95 (1979).
- [80] M. Gell-Mann, P. Ramond, and R. Slansky, *Supergravity Workshop Stony Brook, New York, September 27-28, 1979*, Conf. Proc. **C790927**, 315 (1979), arXiv:1306.4669 [hep-th] .
- [81] S. L. Glashow, in *Quarks and Leptons*, edited by M. Lévy, J.-L. Basdevant, D. Speiser, J. Weyers, R. Gastmans, and M. Jacob (Springer US, Boston, MA, 1980) pp. 687–713.
- [82] R. N. Mohapatra and G. Senjanović, *Phys. Rev. Lett.* **44**, 912 (1980).
- [83] F. R. Klinkhamer and N. S. Manton, *Phys. Rev. D* **30**, 2212 (1984).
- [84] M. Loewenstein, A. Kusenko, and P. L. Biermann, *Astrophys. J.* **700**, 426 (2009), arXiv:0812.2710 [astro-ph] .
- [85] A. Boyarsky, D. Malyshev, A. Neronov, and O. Ruchayskiy, *Mon. Not. Roy. Astron. Soc.* **387**, 1345 (2008), arXiv:0710.4922 [astro-ph] .
- [86] A. Boyarsky, D. Iakubovskiy, O. Ruchayskiy, and V. Savchenko, *Mon. Not. Roy. Astron. Soc.* **387**, 1361 (2008), arXiv:0709.2301 [astro-ph] .
- [87] E. Figueroa-Feliciano *et al.* (XQC), *Astrophys. J.* **814**, 82 (2015), arXiv:1506.05519 [astro-ph.CO] .

-
- [88] A. Boyarsky, J. Lesgourgues, O. Ruchayskiy, and M. Viel, *JCAP* **0905**, 012 (2009), arXiv:0812.0010 [astro-ph] .
- [89] A. Boyarsky, J. Lesgourgues, O. Ruchayskiy, and M. Viel, *Phys. Rev. Lett.* **102**, 201304 (2009), arXiv:0812.3256 [hep-ph] .
- [90] E. J. Chun, A. S. Joshipura, and A. Yu. Smirnov, *Phys. Rev.* **D54**, 4654 (1996), arXiv:hep-ph/9507371 [hep-ph] .
- [91] J. Barry, W. Rodejohann, and H. Zhang, *JHEP* **07**, 091 (2011), arXiv:1105.3911 [hep-ph] .
- [92] C.-S. Chen and R. Takahashi, *Eur. Phys. J.* **C72**, 2089 (2012), arXiv:1112.2102 [hep-ph] .
- [93] A. Kusenko, F. Takahashi, and T. T. Yanagida, *Phys. Lett.* **B693**, 144 (2010), arXiv:1006.1731 [hep-ph] .
- [94] C. Froggatt and H. Nielsen, *Nuclear Physics B* **147**, 277 (1979).
- [95] H. Zhang, *Phys. Lett.* **B714**, 262 (2012), arXiv:1110.6838 [hep-ph] .
- [96] J. Heeck and H. Zhang, *JHEP* **05**, 164 (2013), arXiv:1211.0538 [hep-ph] .
- [97] C. Athanassopoulos *et al.* (LSND), *Phys. Rev. Lett.* **77**, 3082 (1996), arXiv:nucl-ex/9605003 [nucl-ex] .
- [98] A. Aguilar-Arevalo *et al.* (LSND), *Phys. Rev.* **D64**, 112007 (2001), arXiv:hep-ex/0104049 [hep-ex] .
- [99] G. Mention *et al.*, *Phys. Rev.* **D83**, 073006 (2011), arXiv:1101.2755 [hep-ex] .

-
- [100] J. N. Abdurashitov *et al.*, Phys. Rev. **C73**, 045805 (2006), arXiv:nucl-ex/0512041 [nucl-ex] .
- [101] C. Giunti, M. Laveder, Y. F. Li, Q. Y. Liu, and H. W. Long, Phys. Rev. **D86**, 113014 (2012), arXiv:1210.5715 [hep-ph] .
- [102] P. A. R. Ade *et al.* (Planck), Astron. Astrophys. **594**, A13 (2016), arXiv:1502.01589 [astro-ph.CO] .
- [103] H. Harari and M. Leurer, Physics Letters B **181**, 123 (1986).
- [104] A. Palazzo, Modern Physics Letters A **28**, 1330004 (2013), arXiv:1302.1102 [hep-ph] .
- [105] G. Battistoni, F. Cerutti, A. Fassò, A. Ferrari, S. Muraro, J. Ranft, S. Roesler, and P. R. Sala, AIP Conference Proceedings **896**, 31 (2007), <https://aip.scitation.org/doi/pdf/10.1063/1.2720455> .
- [106] R. Brun, F. Bruyant, F. Carminati, S. Giani, M. Maire, A. McPherson, G. Patrick, and L. Urban, *GEANT: Detector Description and Simulation Tool; Oct 1994*, CERN Program Library (CERN, Geneva, 1993) long Writeup W5013.
- [107] C. Zeitnitz and T. A. Gabriel, in *Proceedings of International Conference on Calorimetry in High Energy Physics*, edited by F. Elsevier Science B.V., Talahassee.
- [108] J. R. A. Fasso, A. Ferrari and P. R. Sala, in *Proceedings of International Conference on Calorimetry in High Energy Physics*.
- [109] N. Abgrall *et al.* (The NA61/SHINE Collaboration), Phys. Rev. C **84**, 034604 (2011).

-
- [110] N. Abgrall *et al.* (NA61/SHINE Collaboration), *Phys. Rev. C* **85**, 035210 (2012).
- [111] N. Abgrall *et al.* (NA61/SHINE Collaboration), *The European Physical Journal C* **76**, 84 (2016).
- [112] S. Agostinelli *et al.*, *Nuclear Instruments and Methods in Physics Research Section A: Accelerators, Spectrometers, Detectors and Associated Equipment* **506**, 250 (2003).
- [113] A. Cervera-Villanueva, J. Gómez-Cadenas, and J. Hernando, *Nuclear Instruments and Methods in Physics Research Section A: Accelerators, Spectrometers, Detectors and Associated Equipment* **534**, 180 (2004), proceedings of the IXth International Workshop on Advanced Computing and Analysis Techniques in Physics Research.
- [114] R. Brun and F. Rademakers, *Nuclear Instruments and Methods in Physics Research Section A: Accelerators, Spectrometers, Detectors and Associated Equipment* **389**, 81 (1997), new Computing Techniques in Physics Research V.
- [115] A. A. Aguilar-Arevalo *et al.* (MiniBooNE), *Nucl. Instrum. Meth.* **A599**, 28 (2009), arXiv:0806.4201 [hep-ex] .
- [116] L. Aliaga *et al.* (MINERvA), *Nucl. Instrum. Meth.* **A743**, 130 (2014), arXiv:1305.5199 [physics.ins-det] .
- [117] Y. Hayato, *Proceedings, 1st International Workshop on Neutrino-nucleus interactions in the few GeV region (NuInt 01): Tsukuba, Japan, December 13-16, 2001*, *Nucl. Phys. Proc. Suppl.* **112**, 171 (2002), [,171(2002)].

-
- [118] C. L. Smith, *Physics Reports* **3**, 261 (1972).
- [119] R. Smith and E. Moniz, *Nuclear Physics B* **43**, 605 (1972).
- [120] O. Benhar and A. Fabrocini, *Phys. Rev. C* **62**, 034304 (2000).
- [121] J. Nieves, I. R. Simo, and M. J. V. Vacas, *Phys. Rev. C* **83**, 045501 (2011).
- [122] C. H. Albright, C. Quigg, R. E. Shrock, and J. Smith, *Phys. Rev. D* **14**, 1780 (1976).
- [123] K. Abe *et al.*, *Phys. Rev. Lett.* **56**, 1107 (1986).
- [124] D. Rein and L. M. Sehgal, *Annals of Physics* **133**, 79 (1981).
- [125] M. Glück, E. Reya, and A. Vogt, *The European Physical Journal C - Particles and Fields* **5**, 461 (1998).
- [126] A. Bodek and U. K. Yang, in *2nd International Workshop on Neutrino-Nucleus Interactions in the Few GeV Region (NuInt 02) Irvine, California, December 12-15, 2002* (2003) arXiv:hep-ex/0308007 [hep-ex] .
- [127] P. Musset and J.-P. Vialle, *Physics Reports* **39**, 1 (1978).
- [128] J. E. Kim, P. Langacker, M. Levine, and H. H. Williams, *Rev. Mod. Phys.* **53**, 211 (1981).
- [129] T. Sjostrand, (1994), arXiv:hep-ph/9508391 [hep-ph] .
- [130] S. Barlag *et al.* (Amsterdam-Bologna-Padua-Pisa-Saclay-Turin), *Z. Phys.* **C11**, 283 (1982), [Erratum: *Z. Phys.*C14,281(1982)].
- [131] D. Rein and L. M. Sehgal, *Nuclear Physics B* **223**, 29 (1983).

-
- [132] R. Gran, J. Nieves, F. Sanchez, and M. J. V. Vacas, *Phys. Rev. D* **88**, 113007 (2013).
- [133] R. D. Woods and D. S. Saxon, *Phys. Rev.* **95**, 577 (1954).
- [134] L. Salcedo, E. Oset, M. Vicente-Vacas, and C. Garcia-Recio, *Nuclear Physics A* **484**, 557 (1988).
- [135] K. Nakamura and P. D. Group, *Journal of Physics G: Nuclear and Particle Physics* **37**, 075021 (2010).
- [136] H. W. Bertini, *Phys. Rev.* **C6**, 631 (1972).
- [137] S. J. Lindenbaum and R. M. Sternheimer, *Phys. Rev.* **105**, 1874 (1957).
- [138] O. Benhar, N. Farina, H. Nakamura, M. Sakuda, and R. Seki, *Phys. Rev. D* **72**, 053005 (2005).
- [139] A. M. Ankowski, O. Benhar, T. Mori, R. Yamaguchi, and M. Sakuda, *Phys. Rev. Lett.* **108**, 052505 (2012).
- [140] O. Benhar, A. Fabrocini, S. Fantoni, and I. Sick, *Nuclear Physics A* **579**, 493 (1994).
- [141] B. Frois and I. Sick, *Modern topics in electron scattering* (World Scientific, 1991).
- [142] M. Leuschner, J. R. Calarco, F. W. Hersman, E. Jans, G. J. Kramer, L. Lapikás, G. van der Steenhoven, P. K. A. de Witt Huberts, H. P. Blok, N. Kalantar-Nayestanaki, and J. Friedrich, *Phys. Rev. C* **49**, 955 (1994).
- [143] F. Ajzenberg-Selove, *Nuclear Physics A* **523**, 1 (1991).

-
- [144] K. Kobayashi *et al.*, (2006), arXiv:nucl-ex/0604006 [nucl-ex] .
- [145] M. Yosoi *et al.*, Nuclear Physics A **738**, 451 (2004), proceedings of the 8th International Conference on Clustering Aspects of Nuclear Structure and Dynamics.
- [146] M. Yosoi, H. Akimune, I. Daito, H. Ejiri, H. Fujimura, M. Fujiwara, K. Hara, K. Hara, T. Ishikawa, M. Itoh, *et al.*, Physics of Atomic Nuclei **67**, 1810 (2004).
- [147] M. Smy (SUPER-KAMIOKANDE), in *Proceedings, 30th International Cosmic Ray Conference (ICRC 2007): Merida, Yucatan, Mexico, July 3-11, 2007*, Vol. 5 (2007) pp. 1279–1282.
- [148] E. Wang, L. Alvarez-Ruso, Y. Hayato, K. Mahn, and J. Nieves, Phys. Rev. D **92**, 053005 (2015).
- [149] C. Berger and L. M. Sehgal, Phys. Rev. D **79**, 053003 (2009).
- [150] R. Wendell, “Prob3++ software for computing three flavor neutrino oscillation probabilities,” (2012).
- [151] V. Barger, K. Whisnant, S. Pakvasa, and R. J. N. Phillips, Phys. Rev. D **22**, 2718 (1980).
- [152] A. M. Dziewonski and D. L. Anderson, Physics of the Earth and Planetary Interiors **25**, 297 (1981).
- [153] G. M. Radecky, V. E. Barnes, D. D. Carmony, A. F. Garfinkel, M. Derrick, E. Fernandez, L. Hyman, G. Levman, D. Koetke, B. Musgrave, P. Schreiner,

- R. Singer, A. Snyder, S. Toaff, S. J. Barish, A. Engler, R. W. Kraemer, K. Miller, B. J. Stacey, R. Ammar, D. Coppage, D. Day, R. Davis, N. Kwak, and R. Stump, *Phys. Rev. D* **25**, 1161 (1982).
- [154] M. Derrick, E. Fernandez, L. Hyman, G. Levman, D. Koetke, B. Musgrave, P. Schreiner, R. Singer, A. Snyder, S. Toaff, S. J. Barish, A. Engler, R. W. Kraemer, B. J. Stacey, R. Ammar, D. Coppage, D. Day, R. Davis, N. Kwak, R. Stump, V. E. Barnes, D. D. Carmony, A. F. Garfinkel, and G. M. Radecky, *Phys. Rev. D* **23**, 569 (1981).
- [155] T. Kitagaki, H. Yuta, S. Tanaka, A. Yamaguchi, K. Abe, K. Hasegawa, K. Tama, S. Kunori, Y. Otani, H. Hayano, H. Sagawa, K. Akatsuka, K. Furuno, N. J. Baker, A. M. Cnops, P. L. Connolly, S. A. Kahn, H. G. Kirk, M. J. Murtagh, R. B. Palmer, N. P. Samios, M. Tanaka, M. Higuchi, and M. Sato, *Phys. Rev. D* **34**, 2554 (1986).
- [156] N. J. Baker, A. M. Cnops, P. L. Connolly, S. A. Kahn, M. J. Murtagh, R. B. Palmer, N. P. Samios, and M. Tanaka, *Phys. Rev. D* **23**, 2495 (1981).
- [157] K. Furuno, A. Suzuki, T. Kitagaki, M. Etou, H. Sagawa, K. B. McConnell Mahn, E. J. Jeon, and M. Sakuda, in *2nd International Workshop on Neutrino-Nucleus Interactions in the Few GeV Region (NuInt 02) Irvine, California, December 12-15, 2002* (2003).
- [158] C. Bronner *et al.*, T2K-TN-161 (2013).
- [159] P. de Perio *et al.*, T2K-TN-113 (2012).
- [160] P. A. Rodrigues, *Proceedings, 8th International Workshop on Neutrino-Nucleus*

- Interactions in the Few GeV Region (NuInt 12): Rio de Janeiro, Brazil, October 22-27, 2012*, AIP Conf. Proc. **1663**, 030006 (2015), arXiv:1402.4709 [hep-ex] .
- [161] A. M. Ankowski, M. B. Barbaro, O. Benhar, J. A. Caballero, C. Giusti, R. González-Jiménez, G. D. Megias, and A. Meucci, Phys. Rev. **C92**, 025501 (2015), arXiv:1506.02673 [nucl-th] .
- [162] A. M. Ankowski, *8th International Workshop on Neutrino-Nucleus Interactions in the Few GeV Region (NuInt 12) Rio de Janeiro, Brazil, October 22-27, 2012*, AIP Conf. Proc. **1663**, 080002 (2015), arXiv:1304.4714 [hep-ph] .
- [163] A. A. Aguilar-Arevalo *et al.* (MiniBooNE Collaboration), Phys. Rev. D **82**, 092005 (2010).
- [164] J. O. Johnson and T. A. Gabriel, (1987), 10.2172/6080059.
- [165] J. Johnson and T. Gabriel, 10.2172/5567506.
- [166] W. Coleman and T. Armstrong, 10.2172/4096131.
- [167] S. S. Wilks, Ann. Math. Statist. **9**, 60 (1938).
- [168] K. A. Olive *et al.* (Particle Data Group. Berkeley), Chin. Phys. C **38**, 090001 (2014), all tables, listings, and reviews (and errata) are also available on the Particle Data Group website: <http://pdg.lbl.gov>.
- [169] Y. Koshio *et al.*, RCNP Experiment E487 (2016).
- [170] A. Blondel, M. Yokoyama, and M. Zito (T2K Collaboration), *The T2K-ND280 upgrade proposal*, Tech. Rep. CERN-SPSC-2018-001. SPSC-P-357 (CERN, Ge-

- neva, 2018) this proposal is the follow-up of the Expression of Interest EOI-15 submitted to SPSC in January 2017.
- [171] M. Antonova *et al.*, *Proceedings, 2017 International Workshop on Neutrinos from Accelerators (NuFact17): Uppsala University Main Building, Uppsala, Sweden, September 25-30, 2017*, PoS **NuFact2017**, 078 (2018), arXiv:1704.08079 [physics.ins-det] .
- [172] S. Aoki *et al.* (The NINJA Collaboration), “Proposal for precise measurement of neutrino-water cross-section in ninja physics run,” P71, Proposal for the 25th J-PARC PAC meeting.
- [173] S. Bhadra *et al.* (nuPRISM), (2014), arXiv:1412.3086 [physics.ins-det] .
- [174] S. Bhadra *et al.*, “Proposal for the nuprism experiment in the j-parc neutrino beamline,” P61, Proposal for the 22th J-PARC PAC meeting.
- [175] C. Andreopoulos *et al.*, (2016), arXiv:1606.08114 [physics.ins-det] .
- [176] K. Abe *et al.* (Hyper-Kamiokande), (2018), arXiv:1805.04163 [physics.ins-det] .
- [177] E. R. Davies, *Machine vision: theory, algorithms, practicalities* (Elsevier, 2004).
- [178] M. Wallraff and C. Wiebusch, *Comput. Phys. Commun.* **197**, 185 (2015), arXiv:1409.1387 [astro-ph.IM] .
- [179] F. P. An *et al.* (Daya Bay Collaboration), *Phys. Rev. Lett.* **117**, 151802 (2016).
- [180] G. J. Feldman and R. D. Cousins, *Phys. Rev. D* **57**, 3873 (1998).

- [181] X. Qian, A. Tan, J. J. Ling, Y. Nakajima, and C. Zhang, Nucl. Instrum. Meth. **A827**, 63 (2016), arXiv:1407.5052 [hep-ex] .
- [182] L. Lyons, Ann. Appl. Stat. **2**, 887 (2008).